MONASH University

Deciphering the structural evolution of orogens through numerical modelling

Ben Steven Knight
MESci

A thesis submitted for the degree of
Doctor of Philosophy
at Monash University in 2021
School of Earth, Atmosphere & Environment
Faculty of Science

Copyright

Abstract

Mountains form due to the closure of oceanic basins and the collision of continental crust. Due to the timescales over which mountains form, the various processes occurring during mountain building cannot be observed directly. Numerical models recreate the mountain building process to provide insights into how different processes operating influence the evolution of the mountain belt. The multiple processes operating include erosion and sedimentation that redistributes material, deformation of the crust in response to convergence, and internal heating, which is a product of heat producing elements in the crust. The aim of this thesis is to use numerical models to contribute to the understanding of mountain building and how the various processes outlined above influence the evolution. To do so, each process is investigated individually to mitigate feedback between processes and determine the influence of each on the evolution of the orogen. The models show that each process can dramatically alter the structural evolution of the orogen when dominant and produces a unique structure.

The models provide insights into the evolution of mountain ranges found within the Alpide belt, which stretches from Europe to Asia. The Alpide belt contains the European Alps, Zagros mountains and the Himalayas, with each mountain range showing different deformation styles and structures. The models provide insights into the different deformation styles, highlighting the influence of the convergence velocity and crustal thickness on the internal structure of each mountain range. The evolution of the Himalayas is investigated extensively, focusing on the formation of salients and recesses at the front of the orogen as well as the structural evolution of the Himalayan orogen and Tibetan plateau. The models show that the major structures found in the Himalayas and Tibet are a direct result of the kinematic and thermal evolution.

Plain language summary

When continents collide, mountains form. The rocks found within mountains undergo a range of processes that alter the shape, size, and internal structure of the mountains as the continents continue colliding. The processes investigated in this thesis include erosion and sedimentation, internal heating of the crust due to the presence of heat producing elements and deformation of the crust due to convergence. When modelling mountain building, these processes are usually incorporated together, which hinders the insights into each process due to feedback between them. The aim of this thesis is to investigate each process individually to better understand the influence of each on the structures found in mountains. The findings presented in this thesis have implications for understanding mountain building, showing each process can dramatically alter the internal structure when dominant and produce a unique structure.

Publications during enrolment

Knight, B.S., Capitanio, F.A., Weinberg, R.F., 2021. Convergence velocity controls on the structural evolution of orogens. Tectonics 40(9), e2020TC006570. https://doi.org/10.1029/2020TC006570

Knight, B.S., Davies, J.H., Capitanio, F.A., 2021. Timescales of successful and failed subduction: insights from numerical modelling. Geophysical Journal International 225, 261–276. https://doi.org/10.1093/gji/ggaa410

Thesis including published works declaration

I hereby declare that this thesis contains no material which has been accepted for the award of any other degree or diploma at any university or equivalent institution and that, to the best of my knowledge and belief, this thesis contains no material previously published or written by another person, except where due reference is made in the text of the thesis.

This thesis includes one original paper published in peer reviewed journals and three chapters formatted as papers that have not been submitted. The core theme of the thesis is the study of orogenesis, providing insights into the structural evolution of the Himalayas and Tibet. The ideas, development and writing up of all the papers in the thesis were the principal responsibility of myself, the student, working within the School of Earth, Atmosphere and Environment under the supervision of Associate Professor Fabio A. Capitanio and Professor Roberto F. Weinberg.

(The inclusion of co-authors reflects the fact that the work came from active collaboration between researchers and acknowledges input into team-based research.)

In the case of 4 chapters my contribution to the work involved the following:

Thesis Chapter	**Publication Title**	**Status** *(published, in press, accepted or returned for revision, submitted)*	**Nature and % of student contribution**	**Co-author name(s) Nature and % of Co-author's contribution***	**Co-author(s), Monash student Y/N***
3	*Convergence velocity controls on the structural evolution of orogens*	*Accepted*	*75%. Concept, data processing & analysis and writing first draft*	*1) Fabio Capitanio, input into manuscript 15%* *2) Roberto Weinberg, input into manuscript 10%*	*No* *No*
4	*Time dependent processes on the structural evolution of orogenic wedges*	*Not submitted*	*75%. Concept, data processing & analysis and writing first draft*	*1) Fabio Capitanio, input into manuscript 15%* *2) Roberto Weinberg, input into manuscript 10%*	*No* *No*
5	*The role of surface processes and rheology in the formation of salients and recesses*	*Not submitted*	*80%. Concept, data processing & analysis and writing first draft*	*1) Fabio Capitanio, input into manuscript 10%* *2) Roberto Weinberg, input into manuscript 10%*	*No* *No*
6	*Fast-to-slow convergence reconciles the long-term evolution of the Himalayan orogen*	*Not submitted*	*70%. Concept, data processing & analysis and writing first draft*	*1) Fabio Capitanio, input into manuscript 15%* *2) Roberto Weinberg, input into manuscript 10%* *3) Luca Dal Zilio, input into manuscript 5%*	*No* *No* *No*

I have renumbered sections of submitted or published papers to generate a consistent presentation within the thesis.

Student signature: **Date:** 10/12/2021

The undersigned hereby certify that the above declaration correctly reflects the nature and extent of the student's and co-authors' contributions to this work. In instances where I am not the responsible author I have consulted with the responsible author to agree on the respective contributions of the authors.

Main Supervisor signature: **Date:** 10/12/2021

Acknowledgements

Inevitability I will forget to thank a whole host of people but here is my attempt to recognise everyone that has helped me during my PhD.

Firstly, I'd like to thank Fabio for the opportunity to pursue a doctoral degree at Monash and all that comes with it, as without his funding I wouldn't be submitting this body of work. Fabio has been much more than just a supervisor over the last four years, he's also been a great friend, mentor and all-round good guy who has always been there to help. I would also like to thank Roberto for all his help and guidance over the last four years, always pointing out points I had overlooked, helping to get the most out of each research chapter. A shout out to my panel for their help and guidance at each milestone which has kept me on track over the years, so thank you Peter, Sandy, Marty, and Chris.

Next, I'd like to thank all the staff at Monash who have let me teach as part of their academic units, all the other TA's I have shared a classroom with and all the students who I have had the pleasure of teaching. A big thanks to Marion, Ruth, Adam, Anja, Dietmar, Jimbo, Fabio, Andy, and Mel for letting me teach a wide range of topics and develop a whole new set of skills! The pinnacle of my teaching career (so far) was the field trip to NZ in February 2020 (right before covid!), so a big thanks to Andy and Mel! I'd also like to thank all the support staff at the university, including Emily, Christine, Yuzhou, Rob, and Silvana for all their help over the last four years.

I'd also like to thank all the other PhD candidates at Monash, it's been a tough year and a half but it's great to see everyone still conducting great research! There are a few individuals I'd also like to include, as these people have made my experience at Monash an enjoyable one. A big shout out to all occupants of office 252 past and present, including Mitch, Drew, Alexander, Angus and Ella for making coming into the office so fun, all the coffee breaks, chats and games made the days in the office go past so quickly! I'd also like

to thank Marianne & Saskia for all the morning coffees, as I'd be a zombie for the day without one! Thanks to Matt and Jonas who made house sharing a great experience, I've heard some horror stories so you two were a blessing! A big shout out to Jonas who made the 2020 lockdown with all the coffee breaks, dinners, and TV series we managed to get through! Thanks to the Monday crew too who made the worst day of the week one of the best especially host Newfie Chris for always cooking up an amazing dinner. Also a big shoutout to Zinger Box/RIPON/RIPW/RIPP for the games to get through lockdown!

I'd also like to thank Monash University SC for helping me get back in to football (soccer) after a couple of years out, with the pinnacle being crowned state league 4 champions in my first year in the team. The club influenced my time greatly here in Melbourne so thanks to all involved, including coach/president Ned, head coach Vasey, team manager Nick and Mr. Monash Patto. There's been too many teammates over the years to name them all, but thanks to all of you for making my time in Melbourne.

Thanks to everyone who made the trip out to Australia from the UK to come and visit, it's a long journey so I appreciate the effort you all made to come and see me and Australia! Lastly, I'd like to thank my Mum, Dad and brothers Craig and Harvey for all the support throughout the years to peruse my dreams! A big thanks to Mum for all the help and support, although I'm on the other side of the planet you've always been there for me, so thank you!

To whoever is reading this, grab a beverage of choice and I hope you enjoy!

Acknowledgement of Country

I acknowledge and pay my respects to the Boonwurrung and Wurundjeri peoples who are the Traditional Custodians of the Land this research was conducted on. I pay my respects to the Elders past, present and emerging of the Kulin Nation and extend that respect to all Aboriginal Australians and Torres Strait Islanders. They have never ceded sovereignty and remain strong in their enduring connection to land, water, and culture.

Table of contents

TABLE OF CONTENTS ..... **XIII**

LIST OF FIGURES ..... **XVI**

LIST OF TABLES ..... **XXI**

CHAPTER 1 ..... **1**

1.1. UNDERSTANDING OROGENESIS 2
1.1.1. Plastic crust and critical taper theory *2*
1.1.2. Visco-plastic crust on the evolution of wedges *5*
1.1.3. Dimensional analysis of orogenic wedges *6*
1.1.3.1. The Ramberg number 6
1.1.3.2. The erosion number 9
1.2. THESIS OVERVIEW 9
1.3. REFERENCES 12

CHAPTER 2 ..... **18**

2.1. GOVERNING EQUATIONS 19
2.1.1. Conservation of mass *19*
2.1.2. Conservation of momentum *20*
2.1.3. Conservation of energy *20*
2.2. CONSTITUTIVE LAWS 20
2.2.1. Creep law *20*
2.2.2. Plastic rheology *21*
2.2.3. Composite rheology *22*
2.3. NUMERICAL METHOD 22
2.4. BOUNDARY CONDITIONS 23
2.5. SURFACE PROCESSES 24
2.5.1. Linear hillslope diffusion *25*
2.5.2. Velocity-dependent surface processes *26*
2.6. MODEL LIMITATIONS 27
2.6.1. Setup and boundary conditions *27*
2.6.2. Rheology *27*
2.6.3. Surface processes *28*
2.6.4. Parameter investigation *28*
2.7. COMPUTATIONAL PERFORMANCE 29
2.7.1. Strong scaling *29*
2.7.2. Weak scaling *31*
2.8. REFERENCES 33

CHAPTER 3 ..... **37**

ABSTRACT 38
3.1. INTRODUCTION 39
3.2. MODELLING APPROACH 41
3.2.1. Governing equations *41*
3.2.2. Constitutive laws *41*
3.2.3. Model Setup *45*
3.2.4. Scaling laws: viscous and plastic wedges *47*
3.3. RESULTS 52
3.3.1. CT20: Thin crust models *54*
3.3.1.1. CT20-1: Thin crust-slow convergence 54
3.3.1.2. CT20-10: Thin crust-fast convergence 55
3.3.2. CT25: Intermediate crust thickness models *56*
3.3.2.1. CT25-1: Intermediate crust-slow convergence 56
3.3.2.2. CT25-10: Intermediate crust-fast convergence 57

3.3.3. CT30: Thick crust models ... *59*
3.3.3.1. CT30-1: Thick crust-slow convergence ... 59
3.3.3.2. CT30-10: Thick crust-fast convergence ... 60
3.4. Discussion ... 61
3.4.1. Orogenic wedge models: from plastic to viscous wedges ... *61*
3.4.2. Orogenic wedges in nature ... *66*
3.4.3. Model Limitations ... *70*
3.5. Conclusions ... 71
3.6. Acknowledgements ... 72
3.7. References ... 73

CHAPTER 4 ... 82

Abstract ... 83
4.1. Introduction ... 84
4.2. Methods ... 86
4.2.1. Governing equations ... *86*
4.2.2. Rheology ... *87*
4.2.3. Surface processes ... *88*
4.2.4. Model setup ... *90*
4.3. Results ... 92
4.3.1. Role of internal heating ... *93*
4.3.2. Role of surface processes ... *96*
4.4. Discussion ... 98
4.4.1. The role of internal heating on orogenic wedge structure ... *98*
4.4.2. The role of surface processes on orogenic wedge structure ... *101*
4.4.3. Model limitations ... *104*
4.5. Conclusions ... 105
4.6. References ... 107

CHAPTER 5 ... 112

Abstract ... 113
5.1. Introduction ... 114
5.2. Modelling approach ... 116
5.2.1. Model Setup ... *117*
5.2.2. Rheological laws ... *119*
5.2.3. Surface processes ... *121*
5.3. Results ... 122
5.3.1. 2D models ... *124*
5.3.2. 3D models ... *129*
5.3.2.1. Role of lateral variation in rheology ... 129
5.3.2.2. Role of lateral variation in surface processes ... 131
5.4. Discussion ... 134
5.4.1. Role of crustal strength on the formation of salients and recesses ... *134*
5.4.2. Surface processes on salients and recesses ... *136*
5.4.3. Identifying the causes of salients and recesses in nature ... *137*
5.4.4. Model limitations ... *141*
5.5. Conclusions ... 142
5.6. References ... 143

CHAPTER 6 ... 149

Abstract ... 150
6.1. Introduction ... 151
6.2. Methods ... 155
6.2.1. Rheology ... *155*
6.2.2. Surface processes ... *157*
6.2.3. Model setup ... *158*
6.3. Results ... 161

6.3.1. Constant convergence velocity models ... *163*
6.3.1.1. Fast Convergence model - CV10 ... 163
6.3.1.2. Slow Convergence model – CV2 ... 166
6.3.2. Fast-to-slow convergence ... *169*
6.3.2.1. DV10-2 (10 – 2 cm yr^{-1}) ... 169
6.3.3. Influence of different processes during orogenesis ... *172*
6.3.3.1. Role of internal heating ... 172
6.3.3.2. Role of surface processes ... 175
6.3.3.3. Role of crustal density ... 176
6.4. Discussion ... 177
6.4.1. The role of velocity on the long-term structural evolution ... *177*
6.4.2. Insights into the processes occurring in the Himalayas and Tibet over time ... *179*
6.4.2.1. Uplift of Tibetan Plateau ... 180
6.4.2.2. Formation of the Himalayan FAT belt ... 181
6.4.3. Model limitations ... *187*
6.5. Conclusions ... 188
6.6. References ... 189

CHAPTER 7 ... 198

7.1. Thesis summary ... 199
7.1.1. Convergence velocity on the structure of orogens ... *199*
7.1.2. The role of time-dependent processes on the structural evolution of orogens ... *200*
7.1.3. The formation of salients and recesses in the Himalayas ... *201*
7.2. Future work on orogenesis ... 202
7.3. Concluding remarks ... 203
7.4. References ... 205

List of figures

Figure 1.1: Evolution of a critical taper model with a flat base and rigid backstop. a, b & c represent the Mohr circles (left) that correspond to points in the crust (right). A) Initial wedge development, where the surface slope is below the critical taper angle (as the basal slope is flat) and must increase to reach the critical taper. B) Wedge is on the verge of failure everywhere as the critical taper angle has been achieved. C) Wedge is in an over-critical state as the slope is too high, the wedge must widen through lengthening at the front due to the rigid backstop to re-gain the critical taper angle. 3

Figure 1.2: A) Critical taper model, where material accretes at a rigid backstop and deformation is concentrated to the left of the backstop. B) S-point model, where a velocity discontinuity occurs at the centre of the model, creating deformation on both the sides of the discontinuity. 4

Figure 1.3: Schematic drawing of an orogenic wedge showing the internal stresses acting on the wedge (green) direction of applied convergence (red) and parameters of the crust (black). v_{conv} = convergence velocity, alpha = surface angle, beta = basal angle, h = crustal thickness, ρ = crustal density, η = viscosity of the crust, fc = friction coefficient of the crust. 6

Figure 1.4: Rm number over a range of 1 to 10 cm yr^{-1} convergence velocities. A) Showing the influence of crustal thickness with a constant viscosity (10^{21} Pa s), with an increase in crustal thickness increasing the value of Rm_v at a low convergence velocity, whilst also shifting the curve to the right. B) Influence of crustal viscosity on Rm for a crustal thickness of 25 km, with an increase in viscosity decreasing the value of Rm for a given convergence velocity and reduces the range of Rm. 8

Figure 2.1: An example of hillslope diffusion of an elevated region at given time intervals between 0 and 1 Myr (10^6 yr). 26

Figure 2.2: Strong scaling tests for 2D models. A) number of processors against time. B) processors increase factor against speed up factor. The strong scaling shows how the total model time speeds up initially before plateauing at around 8 processors. 30

Figure 2.3: Strong scaling tests for 3D models. A) number of processors against time. B) processors increase factor against speed up factor. The strong scaling shows how the total model time decreases before plateauing at around 512 processors in 3D. 31

Figure 2.4: Weak scaling tests for 2D models. A) number of processors against time. B) processors increase factor against speed up factor. The weak scaling shows how the total model time increases between 4 and 16 CPUs, suggesting the increase is due to communication time between processors rather than calculations within the model. 32

Figure 3.1: A) Initial model setup of case CT25, with an initial crustal thickness of 25 km (see Table 2). Temperature contours are given at 200℃ intervals. The black box (x > 700 km & x < 1100 km, y < 20km & y > -150 km) portrays the area shown in subsequent figures that display model evolution. The convergence velocity profile on the left displays the velocity boundary condition, with convergence applied to the crust and lithosphere. An inflow-outflow condition is applied across the sticky air, whilst the velocity decreases to 0 from the bottom of the lithosphere to the bottom of the domain. B) Strength profile for CT20, CT25 and CT30, where $\dot{\varepsilon}_{II} = 10^{-13} s^{-1}$. C) Strength profile for CT25, showing the influence of strain weakening on the strength profile. D) Strength profile for CT25 showing the influence of varying strain rate. E) Initial temperature profile for all models, with a geothermal gradient of 25 °C km^{-1} for the first 10 km and then 12 °C km^{-1} until a temperature of 1300 °C is reached at the lithosphere-asthenosphere boundary (LAB) at a depth of 97.5 km. 46

Figure 3.2: Schematic drawing of the orogenic wedge, highlighting where the stresses are acting on the wedge. The key length scales, the length (λc) and thickness (h) are shown, which are used to deduce the balance of horizontal and vertical forces acting on the wedge. 51

Figure 3.3: Evolution of end member cases in CT20. A) Evolution of the material and B) accumulated plastic strain and velocity vectors at a given time for CT20-1. C) Evolution of the material and D) accumulated plastic strain and velocity vectors at a given time for CT20-10. The inverted triangles at the top of the figures mark the edge of the orogen determined by the point at which strain is 0.5. The red line denotes the base of the crust/Moho. 55

Figure 3.4: Evolution of end member cases in CT25. A) Evolution of the material and B) accumulated plastic strain and velocity vectors at a given time for CT25-1. C) Evolution of the material and D) accumulated plastic strain and velocity vectors at a given time for CT25-10. The inverted triangles at the top of the figures mark the

edge of the orogen determined by the point at which strain is 0.5. The red line denotes the base of the crust/Moho. 58

Figure 3.5: Evolution of end member cases in CT30. A) Evolution of the material and B) accumulated plastic strain and velocity vectors at a given time for CT30-1. C) Evolution of the material and D) accumulated plastic strain and velocity vectors at a given time for CT30-10. The inverted triangles at the top of the figures mark the edge of the orogen determined by the point at which strain is 0.5. The red line denotes the base of the crust/Moho. 60

Figure 3.6: A) Wedge length (λc) against change in crustal thickness (Δh). Symbols represent the initial crustal thickness (h_0), given in (C) and numbers represent the velocity whilst colour represents the dominant deformation mechanism. At 435km of convergence, the geometry of the wedge defines three groups: viscous, visco-plastic, and plastic. B)$\frac{\lambda_c}{\Delta h}$ and the effective friction coefficient (fce) as a function of convergence velocity (v_{conv}) showing a decrease in $\frac{\lambda_c}{\Delta h}$ corresponds to an increase in fce as velocity increases until the plastic limit is reached at ~$\frac{1}{f_c}$. The dotted line represents the estimated plastic lower stress limiter of the crust, where$\frac{\lambda_c}{\Delta h} \sim \frac{1}{f_c}$ = 3.3. C) Wedge characterisation as a function of initial crustal thickness (h_0) or initial Moho temp (T_0) and convergence velocity. 62

Figure 3.7: Evolution of $\frac{\lambda_c}{\Delta h}$ over the total convergence for A) CT20, B) CT25, C) CT30. Solid lines – plastic wedge, dash dotted lines – visco-plastic wedge, dotted lines – viscous wedge, as outlined in Figure 3.6C. The diagrams show how $\frac{\lambda_c}{\Delta h}$ evolves over time, that changes with convergence velocity. This cyclical change is particularly well-defined in (A) and records a stepwise lengthening of the orogeny followed by slow thickening. The $\frac{\lambda_c}{\Delta h}$ values increase with increasing initial crustal thickness, from (A) to (C). Most cases in (B) and all in (C) record a strong increase of $\frac{\lambda_c}{\Delta h}$ between 250 and 300 km of convergence. At this point the curves diverge, with the slow convergence models rising more significantly. This divergence indicates the increased role of the viscous lower crust causing the widening of the orogen. This change is more marked for (C) than for (B) and absent in (A). Evolution of change in thickness against length of the wedge for D) CT20, E) CT25, F) CT30 displaying the cyclical pattern for plastic wedges and smooth evolution for viscous wedges that reach a critical crustal thickness. 64

Figure 3.8: A) Crustal thickness map from CRUST1.0 (Laske et al., 2013) used to determine the change in thickness (Δh) along each profile between the foreland and orogenic wedge. X marks the spot where each measurement of crustal thickness is taken. λc is obtained from published work on each orogenic wedge (Zagros - Nissen et al. (2011); European Alps - Rosenberg et al. (2015), Himalayas - Roy and Purohit (2018)). B) Ratio of $\frac{\lambda_c}{\Delta h}$ taken from multiple profiles across each orogenic wedge, with marker colour corresponding to the profile colour in (A). Values of f_c^e from published work on orogenic wedge strength for comparison with values determined by eq 18. The estimated values from eq. 3.18 are within the range suggested from previously published work (Zagros - Nankali (2011), Vernant and Chéry (2006); European Alps - Hagke et al. (2014), Dielforder (2017); Himalayas - Dielforder (2017), Dielforder et al. (2020), Wallis et al. (2015), Dal Zilio et al. (2019)). 69

Figure 4.1: A) Initial model setup, with an initial crustal thickness of 25 km. Temperature contours are given at 200℃ intervals. The black box (x > 500 km and x < 1100 km, y < 20km and y > -150 km) portrays the area shown in subsequent figures that display model evolution. B) Strength profile for varying strain rates and the initial temperature distribution across the crust and mantle. 91

Figure 4.2: Comparison of structure from the material, between no internal heating and an internal heating rate for different convergence velocities after 435 km of convergence. A) CT25-1, B) CT25-10, C) CT25-1-1.8H_r, D) CT25-10-1.8H_r. E) CT25-1-3.6H_r, F) CT25-10-3.6H_r, G) Topography for A), C) and E). H) Topography for B) and D) and F). The topography shows how the elevation decreases due to the influence of internal heating, with the influence stronger in CT25-1-IH compared to CT25-10-IH due to the time dependency. VE = 40 x is the vertical exaggeration. 93

Figure 4.3: Similar to Figure 4.2 but showing plastic strain distribution between no internal heating and an internal heating rate for different convergence velocities after 435 km of convergence. A) CT25-1, B) CT25-10, C) CT25-1-1.8H_r, D) CT25-10-1.8H_r. E) CT25-1-3.6H_r, F) CT25-10-3.6H_r. The white line in each plot denotes the boundary between the crust and mantle. G) Plastic strain profiles taken at a y = -10 km for A), C) and E). H) Plastic strain profiles taken at a y = -10 km for B), D) and F). Results show that with increasing internal heating, the depth of the brittle ductile transition shallows. At low velocity and high internal heating (CT25-1-3.6H_r) no plastic strain occurs in the upper crust and instead convergence is accommodated through viscous deformation. 95

Figure 4.4: Comparison of internal structure from the material, with no erosion (A and B) and a hillslope diffusion rate to the surface (C-F). A) CT25-1. B) CT25-10. C) CT25-1-D300. D) CT25-10-D300. E) CT25-1-D300. F) CT25-10-D3000. G) Topography of models presented in A), C) and E). H) Topography of models presented in B), D) and F), showing how the diffusive surface smooths topography and reduces the height of the orogen. The smoothing of topography is most pronounced in the slow convergence models, occurring over a wider area compared to the fast convergence models, reflecting the time dependency of a diffusive surface. Surface processes also impede the outward growth of wedge, concentrating deformation close to the centre and promote exhumation, which is more apparent in the slow convergence velocity models. VE = 40 x is the vertical exaggeration. 96

Figure 4.5: Comparison of plastic strain between models with no erosion (A and B) and a hillslope diffusion rate to the surface (C-F). A) CT25-1. B) CT25-10. C) CT25-1-D300. D) CT25-10-D300. E) CT25-1-D300. F) CT25-10-D3000. The white line in each plot denotes the boundary between the crust and mantle. G) Plastic strain of models presented in A), C) and E) at y = -10 km. H) Plastic strain of models presented in B), D) and F) at y = -10 km. The plastic strain shows how increasing the surface diffusivity restricts the wedge width, reduces the number of shear zones (based on the amount of strain localisation) and concentrates deformation at the centre of the wedge. The back-thrust in E) is well-defined in the profile presented in G). 98

Figure 4.6: Horizontal temperature profile at y = -24 km for all models presented in the internal heating section after 435 km of convergence. The high convergence velocity models have a similar temperature, whilst a large difference (~400 °C) is observed between CT25-1 (~600 °C) and CT25-1-3.6H_r (~1000 °C) due to more heat being produced over the time to reach 435 km of convergence in the low convergence velocity models. 99

Figure 4.7: Evolution of strain at y = -10 km to highlight the influence of surface processes on strain localisation in the crust. A) CT25-1, B) 25-10, C) CT25-1-D300, D) CT25-10-D300, E) CT25-1-D3000, F) CT25-10-D3000. 101

Figure 4.8: Evolution of selected particles to highlight the depth at which material is exhumed from. A) CT25-1, B) CT25-10, C) CT25-1-D300, D) CT25-10-D300, E) CT25-1-D3000, F) CT25-10-D3000. No exhumation takes place in A, B or D. Material is exhumed from a depth of ~10 km in C, ~30 km in E and ~14 km in F. This highlights that most exhumation takes place in the low velocity model with a high surface diffusivity rate due to the amount of time to reach 435 km, with material eroded as fast as uplift occurs, resulting in the exhumation of deep crustal material along a single back thrust. 103

Figure 5.1: A) Initial 2D model setup of case 03fc. Temperature contours are given at 200 ℃ intervals. The black box (x > 700 km & x < 1100 km, y < 20km & y > -150 km) portrays the area shown in subsequent figures that display model evolution. B) 1D strength and temperature profile of the crust and mantle. The strength profiles have a constant strain rate ($\dot{\varepsilon}_{II} = 10^{-14}\ s^{-1}$) with different friction coefficients, with increasing friction coefficient resulting in a thicker viscous layer at the base of the crust. 118

Figure 5.2: Material plots for models with different f_c values with no surface processes (A - D) or with slow (E – H) or fast (I – L) surface processes (SSP and FSP, respectively) after 450 km of convergence (t = 22.5 Myr). A clear transition from plastic-dominated features (stacking of the entire crust) in 01fc to viscous-dominated features (folding of crust) as in 04fc can be seen when looking left to right. SSP representing v_e = 0.5 mm yr^{-1} & v_s =0.05 mm yr^{-1} whilst FSP represents v_e = 1 mm yr^{-1} & v_s = 0.1 mm yr^{-1}. Regarding surface processes, the internal structural is very similar with and without surface processes, however surface processes do promote exhumation at the centre of the wedge. 124

Figure 5.3: Strain plots for models with different f_c values with no surface processes (A - D) or with slow (E – H) or fast (I – L) surface processes (SSP and FSP, respectively) after 450 km of convergence (t = 22.5 Myr). A clear transition from plastic-dominated features (stacking of the entire crust), as seen in 01fc, to viscous-dominated features (folding of crust), as seen in 04fc, is observed. SSP represents v_e = 0.5 mm yr^{-1} & v_s =0.05 mm yr^{-1} whilst FSP represents v_e = 1 mm yr^{-1} & v_s = 0.1 mm yr^{-1}. surface processes, do not alter the overall internal structure much, but do reduce the distance between high strain zones and reduce the length of the wedge. 125

Figure 5.4: Evolution of orogens front (solid line) and rear (dotted line) position, based on the position of elevated topography (where y first exceeds 200 m at the orogens front and rear), for all 2D models. A) No surface processes, B) SSP models, c) FSP models. The distance between the front and back of the orogen represents the orogens width The model results show that both rheology and surface processes influence the width of the orogeny. The influence of rheology on orogen width increases as the amount of convergence increases. 126

Figure 5.5: Comparison of topography due to A) rheology and B) surface processes after 450 km of convergence. Profiles taken from Fig. 3. In A) a large distance is observed at the front of the wedge between 01fc and 02fc of ~70 km, whilst erosion and sedimentation reduce the wedge with by ~50 km at the back of the wedge and ~10 km at the front of the wedge. 127

Figure 5.6: A) Plot of surface topography, B) lateral flow at a depth of ~4 km below the surface and 2D profiles of material (C and E) and accumulated plastic strain (D and D) for 01fc-04fc-3D after 450 km of convergence. The dotted lines in (A) represent the profiles taken to measure the evolution of topography in Figure 5.7 and the location of the profiles of material (C and E) and strain (D and F). The topography highlights how the location of peak topography is discontinuous along strike, with a salient forming where rheological strength is low (z > 150 km) and a recess forming where rheological strength is high (z < 150 km). 130

Figure 5.7: Evolution of orogens front (solid line) and rear (dotted line) over 450 km of convergence for 01fc-04fc-3D. The y axis represents the x-coordinate where the topography first (front - solid) or last (back - dotted) exceeds a height of 200 m. The grey lines represent the evolution of the topography at z = 80 km where the crust has a friction coefficient of 0.4 (04fc) and blue is measured at z = 220 km where the crust has a friction coefficient of 0.1 (01fc). The model highlights a similar evolution to the 2D models (Figure 5.4A), with the topographic fronts diverging throughout convergence to form a salient (blue) and recess (grey) in the 3D models. 131

Figure 5.8: A) Plot of surface topography and B) lateral flow direction at a depth of ~4 km below the surface. 2D profiles of material (C and E) and accumulated plastic strain (D and F) for 01fc-SP-3D after 450 km of convergence. The dotted lines in (A) represent the profiles taken to measure the evolution of topography in Figure 5.9 and the 2D profiles of material (C and E) and strain (D and F). The topography highlights how the location of peak topography is continuous along strike, with a salient forming where the orogen is wide due to slow erosion rates (z > 150 km) and a recess forming where the orogen is narrow due to fast erosion rates (z < 150 km). 132

Figure 5.9: Evolution of orogens front (solid line) and rear (dotted line) over 450 km of convergence for 01fc-SP-3D, where the constant fc throughout but the erosion & sedimentation rates vary laterally. The y axis represents the x-coordinate where the topography first (front - solid) or last (back - dotted) exceeds a height of 200 m. The blue lines represent the evolution of the topography at z = 80 km where slow erosion and sedimentation rates (SSP) are applied and cyan is measured at z = 220 km, where the fast erosion and sedimentation rates (FSP) are applied. SSP represents v_e = 0.5 mm yr^{-1} & v_s =0.05 mm yr^{-1} whilst FSP represents v_e = 1 mm yr^{-1} & v_s = 0.1 mm yr^{-1} .The model highlights a similar evolution to the 2D models (Figure 5.4), with the topographic fronts diverging to form a salient (blue) and recess (grey) in the 3D models. The outward propagation of the orogen front occurs at different amounts of convergence due to varying erosion and sedimentation rates, resulting in periods where the fronts of both orogens are at a similar position (e.g. at ~375 km of convergence). 133

Figure 5.10: A) Topography from EarthEnv-DEM90 (Robinson et al., 2014) and B) free air gravity anomalies from WGM2012 (Balmino et al., 2012) of the Himalayan arc between 85 and 92 °E, along with the small circle arc from Bendick and Bilham (2001) that is centred at 92.6 °E, 42.4 °N with a radius of 1696 km. Two salients (S1 & S2) and recesses (R1 & R2) are marked along the orogen front but show very different topographic and free-air gravity anomaly features. The black lines represent country boundaries. 139

Figure 6.1: A) Schematic evolution of the Himalayas and Tibet, highlighting the formation of key structures at different times, based on various previous schematic diagrams of the evolution of the major structures (e.g. Elliott et al., 2016; Herman et al., 2010; Nelson et al., 1996; Searle, 2015; Streule et al., 2010). IYSZ – Indus Yarlung Suture Zone, NHD – Northern Himalayan Domes, MHT – Main Himalayan Thrust, STD – South Tibetan Detachment, MCT – Main Central Thrust, MBT – Main Boundary Thrust, MFT – Main Frontal Thrust, LHS – Lesser Himalayan Sequence, TSS – Tethyan Sedimentary Sequence, GHCS – Greater Himalayan Crystalline Sequence. B) Evolution of convergence, trench and plate velocity, modified from Capitanio et al. (2010). The convergence velocity (v_{conv}) is the sum of the plate velocity (v_{plate}) and trench velocity (v_{trench})..... 152

Figure 6.2: A) Model setup. The convergence velocity is applied to the left boundary, the top boundary is free slip, the right boundary no slip and the bottom boundary is unconstrained. The left, top and right boundaries have zero heat flux, whilst the temperature of the bottom boundary is unconstrained. The black box marks the area that is plotted in subsequent figures. LM = lithospheric mantle. B) Strength and temperature profile displaying the difference in strength between crust A/B (quartzite) and C (diabase). C) Total convergence against time to show how each model reaches 2000 km of convergence over the duration of the model: CV10 – fast model (10 cm yr^{-1}) for 20 Myr, CV2 – slow model (2 cm yr^{-1}) for 100 Myr, DV10-2 – decreasing velocity model (10 to 2 cm yr^{-1}) over 50 Myr. 159

Figure 6.3: Evolution of material and passive tracers in CV10, with material plots also including temperature contours, velocity vectors and passive tracers. Boxes above material plots highlight the horizontal strain rate (□xx) and vertical velocity (vy) at y = -15 km. Boxes to the right of the material show the pressure-temperature paths of the passive tracers. A) Phase 1 – formation of initial wedge above weak zone. B) Phase 2 – migration toward the back wall and lengthening of the orogen and Phase 4 - where underthrusting of crust

A below crust B occurs and return flow forms at the front of the orogen. C & D) Phase 3 – doming of the crust and exhumation of deep crustal material. E) Topography at the same intervals presented in A-D. The topography shows the different stages, with topography narrow in phase 1 before widening and forming a plateau in phase 2 and 3. During phase 4, the orogen continues to widen, with a sharp topographic gradient at the front of the orogen. *163*

Figure 6.4: Evolution of material and passive tracers in CV2, with material plots also including temperature contours, velocity vectors and passive tracers. Boxes above material plots highlight the horizontal strain rate (ε_{xx}) and vertical velocity (v_y) at y = -15 km. Boxes to the right of the material show the pressure-temperature paths of the passive tracers. A) – D) highlight that the orogen migrates backward throughout and primarily accommodates convergence through thickening and folding of the crust. E) Topography at the same intervals presented in A-D, with the topographic height continuously increasing and migrating backward throughout the evolution of the model. A large decrease in length and increase in crustal thickness is observed between 56 and 81 Myr, concentrated in Crust B which undergoes intense shortening forming tight folds. *166*

Figure 6.5: Evolution of material and passive tracers in DV10-2, with material plots also including temperature contours, velocity vectors and passive tracers. Boxes above material plots highlight the horizontal strain rate (ε_{xx}) and vertical velocity (v_y) at y = -15 km. Boxes to the right of the material show the pressure-temperature paths of the passive tracers. A) Phase 1 – formation of initial wedge above weak zone. B) Phase 2 – migration toward the back wall and lengthening of the orogen & Phase 3 - with underthrusting of crust A below crust B and return flow at the front of the orogen. C) Phase 4 - flattening of the slab, large exhumation event and relaxing of the isotherms. D) Phase 5 – FAT belt development at the front of the orogen. E) Topography at the same intervals presented in A-D. The topography shows the different stages, with phase 1 (5 Myr) very narrow before widening and forming a plateau in phase 2 and 3 (15 Myr). During phase 4 (35 Myr), the orogen lengthens slightly, before extending mainly at the front during FAT development in phase 5 (50 Myr). *169*

Figure 6.6: Comparison of models after 2000 km of convergence with differing amounts of internal heating rates in the crust. Left – H_r = 0.5 μW m^{-3}, centre - H_r = 1 μW m^{-3}, right - H_r = 2.25 μW m^{-3}. Fast convergence models (v_{conv} = 10 cm yr^{-1}) are along the top (A – C), slow convergence models (v_{conv} = 2 cm yr^{-1}) are along the middle (D – E) and fast-to-slow convergence models (v_{conv} = 10 to 2 cm yr^{-1}) are along the bottom (G - I). The models show that increasing the internal heating rate influences the internal structure as it becomes the main heating mechanism, outweighing structures that form due to advection and diffusion, resulting in similar structures regardless of convergence velocity when high enough, observed when H_r = 2.25 μW m^{-3} (right column). *172*

Figure 6.7: Comparison of models after 2000 km of convergence without surface processes (left) and with a surface diffusivity rate of 150 m^2 yr^{-1}(centre) and 300 m^2 yr^{-1} (right). Fast convergence models (v_{conv} = 10 cm yr^{-1}) are along the top, slow convergence models (v_{conv} = 2 cm yr^{-1}) are along the middle and fast-to-slow convergence models (v_{conv} = 10 to 2 cm yr^{-1}) are along the bottom. The models show that a surface processes, represented by a diffusive surface, do not have a major influence on the final structure of the orogen. The only major difference is the deposition of sediments across the plateau and within the fold-and-thrust belt, as well as the advection of sediments deep within the wedge in the return flow region. *175*

Figure 6.8: Comparison of models after 2000 km of convergence with varying crustal density. Left - ρ_0 = 2700 kg m^{-3}, centre - ρ_0 = 2800 kg m^{-3}, right - ρ_0 = 2900 kg m^{-3}. Fast convergence models (v_{conv} = 10 cm yr^{-1}) are along the top (A - C), slow convergence models (v_{conv} = 2 cm yr^{-1}) are along the middle (D – F) and fast-to-slow convergence models (v_{conv} = 10 to 2 cm yr^{-1}) are along the bottom (G – I). The models show that changes in the crustal density do not influence the overall structure of the orogen, with only minor localised variations in structure observed. *176*

Figure 6.9: Underthrusting of crust A and the formation of a viscous lower crust to form the Tibetan Plateau in DV10-2. Top – material, bottom – viscosity. *181*

Figure 6.10: Temperature vs time diagram to compare geochronological data from the Himalayas presented in Searle (2015) with model results. Both show peak metamorphic temperatures between 20 and 25 Ma before decreasing due to the rapid exhumation and subsequent cooling of the partial molten mid-crust, as observed in phase 4 of DV10-2. ..... *184*

Figure 6.11: Comparison of topography at the front of the orogen between the model (DV10-2 – orange line) and nature (topography – blue line). The model matches the overall topographic shape, whilst there are discrepancies in the plateau height of ~2 km. The topography was determined between points (81, 27) and (87, 37) in the WGS84 reference frame. *187*

List of tables

Table 2.1: Optimum number of processors based on strong and weak scaling analysis and trial and error of model runs. 32

Table 3.1: Initial material properties used for the visco-plastic rheology. ρ is density at the surface. A is the pre-exponential factor, n, is the stress exponent, V is the activation volume, E is the activation energy, f_c is the friction coefficient, φ is the internal friction angle, C is the cohesion at the surface, ρ_0 is the density of the crust at the surface and R (=8.314462) is the gas constant. Subscript w represents the weakened value. 44

*Table 3.2: Experiments described in the text. Cases are labelled according to initial crustal thickness and velocity where CT20-1 indicates a crustal thickness of 20km and velocity of 1 cm/yr. *Main deformation mechanism is determined by the internal structure and aspect ratio after 435 km of convergence. 53*

Table 4.1: Initial material properties used for the visco-plastic rheology. ρ is density at the surface. A is the pre-exponential factor, n, is the stress exponent, E is the activation energy, f_c is the friction coefficient, C is the cohesion at the surface and α is the coefficient of thermal expansion. 88

Table 4.2: Case names with the parameters modified for each model. 1 Watt (W) is equal to 1 kg m^2 s^{-3} 92

Table 5.1: Initial material properties used for the visco-plastic rheology. ρ is density at the surface. A is the pre-exponential factor, n, is the stress exponent, E is the activation energy, f_c is the friction coefficient, C is the cohesion at the surface and α is the coefficient of thermal expansion. 120

Table 5.2: Experiments described in the text. Cases are labelled according to the friction coefficient, where 03fc represents a friction coefficient (f_c) of 0.3 with no surface processes. -SSP represents slow, and -FFP represents fast, surface processes. 123

Table 6.1: Initial material properties used for the viscoplastic rheology. ρ is the density at the surface. A is the pre-exponential factor, n, is the stress exponent, E is the activation energy, f_c is the friction coefficient, C is the cohesion at the surface and α is the coefficient of thermal expansion. 156

Table 6.2: Model name, total time, velocity condition and additional processes. 161

Chapter 1

Introduction

Mountains are one of the most remarkable features of the Earth. Mountain ranges, or orogens, are the product of plate tectonics and form due to the convergence of buoyant, continental crust, with the process known as orogenesis. Subduction leads to an orogeny, resulting in the rise of mountains after the closure of oceans to form elevated regions of topography that can exceed over 8 km in height above sea level. This is most notably represented by *Chomolungma* (Mount Everest) in the Himalayas, the tallest mountain (above sea level, MSL) in the world, which stands at height of 8847.43 m MSL (Angus-Leppan, 1982; Chen et al., 2006; de Graaff-Hunter, 1955).

The internal structure of an orogen is a product of the deformation history of the region and crustal strength. On geological timescales over which orogenesis occurs, the strength of the crust and mantle is determined by the rheology, which is controlled by two primary deformation mechanisms: (1) the frictional-plastic properties of the crust, which occurs at low temperatures, usually close to the surface, and (2) the viscous-ductile rheology of the crust, which occurs at higher temperatures deeper within the crust (Burov and Watts, 2006; Burov, 2011). The deformation mechanisms are important in understanding the structural evolution of orogens, however early studies neglected the role of viscous rheology and focused on purely frictional-plastic materials.

1.1. Understanding orogenesis

1.1.1. Plastic crust and critical taper theory

A major development in the understanding of the structural evolution of orogens is attributed to the development of the critical taper theory (Chapple, 1978; Dahlen, 1990, 1984; Dahlen and Barr, 1989; Davis et al., 1983) of Mohr-Coulomb wedges. The critical taper theory assumes plastic-only deformation, with the crust initially thickening to increase the stress acting on the crust for the shear stress to reach the failure envelope of the crust (Figure 1.1A). Once the shear stress within the crust has increased sufficiently to reach the

failure envelope, a constant angle between the slope (α) and the basal décollement (β), when on an inclined plane, are maintained to keep the internal material on the verge of failure everywhere (Dahlen, 1984; Davis et al., 1983) (Figure 1.1B) and maintain the critical taper ($\theta_c \equiv \alpha + \beta$). However, if the material reaches an over-critical state (Figure 1.1C), the orogen must lengthen to reduce the vertical load and re-equilibrate the stresses acting on the wedge to maintain the critical taper angle. The critical taper for a dry, cohesionless, sandy material is represented as (Dahlen, 1990; Graveleau et al., 2012):

$$\theta_c = \left(\frac{1 - f_c}{1 + f_c}\right)\left(f_{c_b} + \beta\right) \tag{1.1}$$

where f_c is the internal friction coefficient of the wedge and f_{c_b} is the basal friction coefficient.

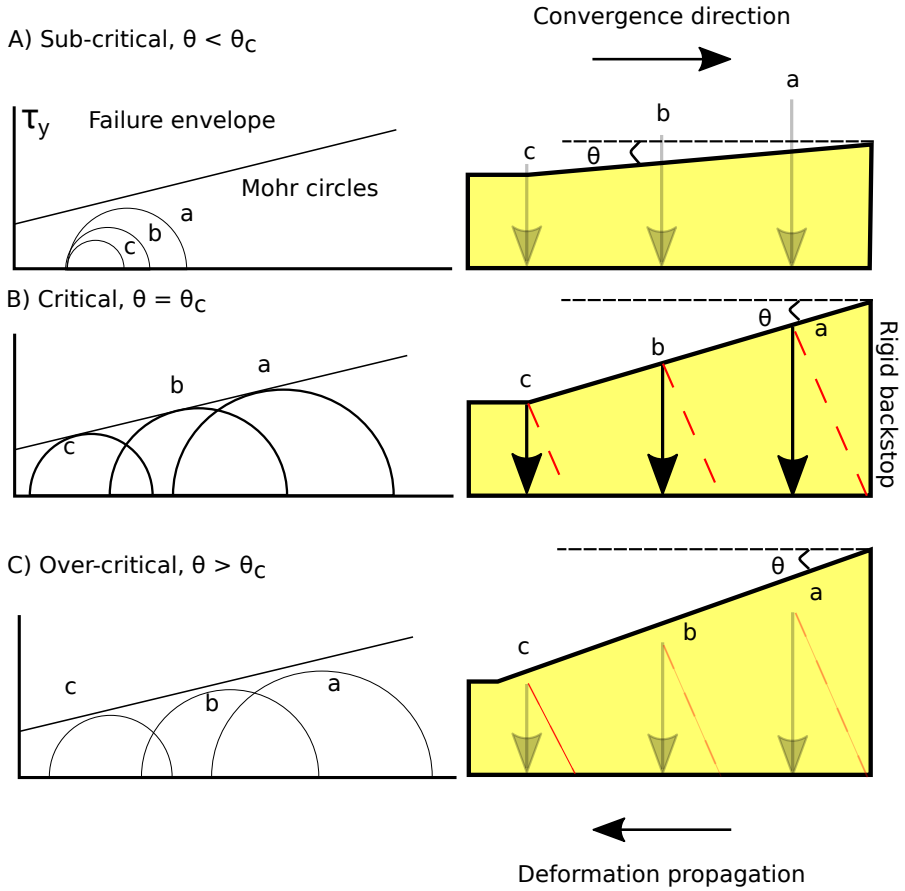

Figure 1.1: Evolution of a critical taper model with a flat base and rigid backstop. a, b & c represent the Mohr circles (left) that correspond to points in the crust (right). A) Initial wedge development, where the surface slope is below the critical taper angle (as the basal slope is flat) and must increase to reach the critical taper. B) Wedge is on the verge of failure everywhere as the critical taper angle has been achieved. C) Wedge is in an over-critical state as the slope is too high, the wedge must widen through lengthening at the front due to the rigid backstop to re-gain the critical taper angle.

Due to the timescales at which orogens evolve over, orogenesis cannot be observed directly, with both laboratory analogue (e.g. Graveleau et al., 2012; Gutscher et al., 1996; Luth et al., 2010; Mulugeta and Koyi, 1992; Schreurs et al., 2006; Verschuren et al., 1996) and numerical (e.g. Dal Zilio et al., 2020; Ruh, 2017; Ruh et al., 2014, 2013, 2012) models utilised to investigate the evolution of orogens within the critical taper framework. Early models utilised a rigid backstop which caused material to accrete at the backstop (Figure 1.2A). As outlined by eq. 1.1, the controlling factor on the critical taper is the internal and basal friction coefficient, representing strength, of the deforming material.

The critical taper theory assumes a plastic-only rheology. However, over the timescales that orogens form, the crust and mantle also deforms as a viscous fluid (Platt, 1986). This led to the critical taper models being superseded by the S-point wedge model (Beaumont et al., 1996a; Willett et al., 1993), where the S-point represents a discontinuity in the velocity condition that is applied to the base of one plate (Figure 1.2B). This creates deformation on both sides of the discontinuity, creating structural styles more synonymous to orogenic wedges in nature when compared to the early critical taper models that utilised a rigid backstop.

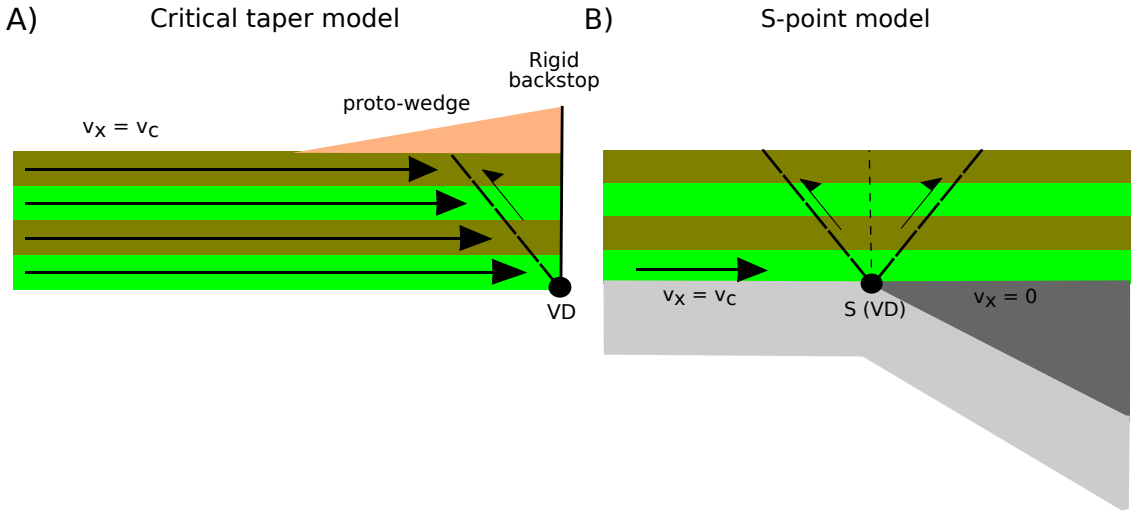

Figure 1.2: A) Critical taper model, where material accretes at a rigid backstop and deformation is concentrated to the left of the backstop. B) S-point model, where a velocity discontinuity occurs at the centre of the model, creating deformation on both the sides of the discontinuity.

1.1.2. Visco-plastic crust on the evolution of wedges

The first numerical models developed by Willett et al. (1993) were S-point models and included both plastic and viscous rheology, with the viscous rheology incorporating the influence of temperature and strain rates on the model evolution. During the evolution of the model, a change from a plastic to viscous lower crust occurred due to crustal thickening and increasing temperatures at the base of the crust, favouring viscous deformation over plastic (Willett et al., 1993). This change from plastic to viscous rheology resulted in a decrease in overall crustal strength, causing a decrease in crustal thickness and an increase in wedge length. Willett et al. (1993) also postulated the role of convergence velocity on the geometry of the orogen due to the inclusion of viscous rheology, that is rate dependent.

Various numerical models which do not have a constrained basal condition like the S-point models have been used to investigate the influence of rheology on the structural evolution of orogens (e.g. Burg and Gerya, 2005; Chen et al., 2017; Faccenda et al., 2008; Jammes and Huismans, 2012; Vogt et al., 2017b, 2017a; Willett, 1999b). However, the heterogeneous nature of the composition of the continental crust and uncertainties in the geotherm means similar structures can be obtained from numerical models that use different parameters but produce a similar strength profile. For example, a low geothermal gradient and quartzite rheology can produce a similar strength profile and structural style comparable to a high geothermal gradient and a feldspar rheology (Beaumont et al., 1996b).

Other numerical studies have focussed on processes that influence the strength of the crust and lithosphere on the evolution of orogens. These processes include, but are not limited to, the rate at which the crust collides (convergence rate) and the subsequent induced strain rates (e.g. Burov, 2011; Faccenda et al., 2008; Rossetti et al., 2000; Vogt et al., 2017b), surface processes (e.g. Avouac and Burov, 1996; Dal Zilio et al., 2020; Jammes and Huismans, 2012; Vogt et al., 2017a; Whipple and Meade, 2004; Willett, 1999a), and

internal temperature, through the initial geotherm (e.g. Ellis, 1988; Vogt et al., 2017a) or internal heating due to radiogenic heat producing elements in sediments, the crust and mantle (Faccenda et al., 2008a, 2009). Although these studies utilise different approaches to alter the rheology, whilst also introducing various complexities in each study, the fundamental parameter controlling the evolution of the orogen is the strength of the crust as it dictates the crustal thickness that can be supported and the width of the orogen. A low strength produces a thin and wide orogen, whilst a high strength produces a narrow and thick orogen (Chen et al., 2017a; Pusok and Kaus, 2015; Ruh et al., 2012, 2014).

1.1.3. Dimensional analysis of orogenic wedges

1.1.3.1. The Ramberg number

The primary stresses controlling the development of the wedge are the resistance to deformation (strength) in response to excess gravitational stresses (England and McKenzie, 1982; Ramberg, 1967; Stüwe, 2007; Weijermars and Schmeling, 1986). This was first presented by Ramberg (1967) and subsequently termed the Ramberg number (Rm) by Weijermars and Schmeling (1986). Rm is similar to the Argand number (Ar) (England and McKenzie, 1982; Pusok and Kaus, 2015; Willett, 1999a), however the formulations are slightly different.

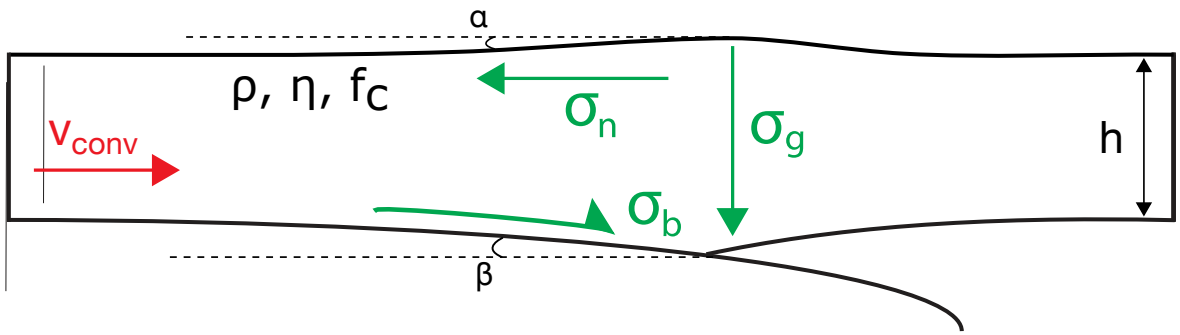

Figure 1.3: Schematic drawing of an orogenic wedge showing the internal stresses acting on the wedge (green) direction of applied convergence (red) and parameters of the crust (black). v_{conv} = convergence velocity, alpha = surface angle, beta = basal angle, h = crustal thickness, ρ = crustal density, η = viscosity of the crust, f_c = friction coefficient of the crust.

During the early stages of orogenesis, the gravitational (vertical) and internal (horizontal) stresses evolve to reach an equilibrium, and then attempt to remain

proportionate. This is similar to the evolution of the critical taper angle ($\alpha + \beta$), as outlined in eq. 1.1, with the taper angle increasing until reaching equilibrium, with the critical angle then remaining relatively constant.

Rm, for a viscous fluid, is expressed as (Medvedev, 2002; Pusok and Kaus, 2015; Ramberg, 1967; Weijermars and Schmeling, 1986):

$$Rm_v \sim \frac{\rho_{crust} g h^2}{\eta_{crust} \mathrm{v}_{conv}} \tag{1.2}$$

where ρ_{crust} is the density and η_{crust} is the viscosity of the crust, g represents gravity, h is the thickness of the crust and v_{conv} represents the convergence velocity. If all values remain constant in eq. 1.2, an increase in either the convergence velocity or viscosity decreases the value of Rm. A low Rm number implies a high resistance to deformation where the wedge can support high gravitational stresses, resulting in a thick and narrow wedge (Medvedev, 2002; Pusok and Kaus, 2015; Vanderhaeghe et al., 2003; Willett, 1999a). However, for a plastic, dry and cohesionless crust, Rm is expressed as:

$$Rm_p \sim \frac{\rho_{crust} g h}{(\rho_{crust} g h) f_c} \sim \frac{1}{f_c} \tag{1.3}$$

where f_c is the friction coefficient. In eq. 1.3 the Rm number decreases with increasing f_c, representing an increase in wedge strength, resulting in an increase in wedge thickness and decrease in wedge length. Eq. 1.3 is independent of convergence velocity and instead dependent on the friction coefficient of the deforming material, similar to the critical taper angle (eq. 1.1). When combined for a visco-plastic rheology, as utilised throughout this thesis, Rm becomes:

$$Rm \sim \min\left(Rm_p, Rm_v\right) \tag{1.4}$$

as the weakest deformation mechanism controls the internal deformation of the crust.

The calculated values of Rm for different crustal thicknesses are presented in Figure 1.4A, showing that an increase in crustal thickness, whilst all over parameters remain the

same, results in an increase in Rm_v for a given convergence velocity. This is due to the convergence velocity being distributed across a thicker crust, resulting in a lower average strain rate across the crust, causing an increase in Rm_v. As the convergence velocity increases, the strain rates in the crust increase due to a fixed crustal thickness, resulting in a decrease in Rm_v (Figure 1.4). However, Rm_p does not vary with convergence velocity or crustal thickness as it is only dependent on the inverse of the friction coefficient (Figure 1.4A). Figure 1.4B shows the influence of the crustal viscosity, and thus strength, with a lower viscosity crust showing a larger range of Rm_v over the range of convergence velocities tested. At a lower viscosity, the crust is much more sensitive to changes in convergence velocity, however when viscosity is high, the crust has a higher internal resistance to deformation and is insensitive to changes in velocity.

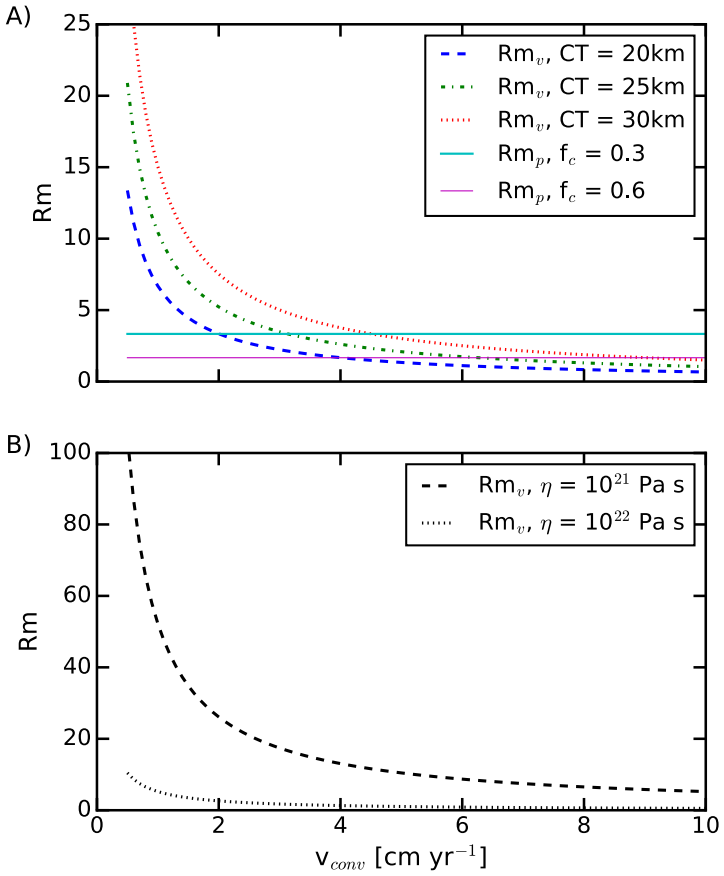

Figure 1.4: Rm number over a range of 1 to 10 cm yr^{-1} convergence velocities. A) Showing the influence of crustal thickness with a constant viscosity (10^{21} Pa s), with an increase in crustal thickness increasing the value of Rm_v at a low convergence velocity, whilst also shifting the curve to the right. B) Influence of crustal viscosity on Rm for a crustal thickness of 25 km, with an increase in viscosity decreasing the value of Rm for a given convergence velocity and reduces the range of Rm.

1.1.3.2. The erosion number

The evolution of the wedge is also influenced by surface processes. Erosion and sedimentation redistribute material, with erosion reducing the vertical gravitational load acting on the wedge. This results in a reduction in wedge length, concentrating deformation at the centre of the wedge and promoting exhumation (Dal Zilio et al., 2020; Jammes and Huismans, 2012; Kaus et al., 2008) whilst also extending the duration of activity on faults (Avouac and Burov, 1996; Dal Zilio et al., 2020; Ellis et al., 2001; Jammes and Huismans, 2012; Jaquet et al., 2017; Selzer et al., 2008). If erosion rates exceed uplift rates, exhumation is concentrated along a single back thrust (Beaumont et al., 1996b; Willett, 1999b), whilst also producing a smoothed topography (Avouac and Burov, 1996).

The role of erosion is encapsulated by the non-dimensional erosion number (Ne) (Willett, 1999), which shows that the total amount of eroded material is proportional to the product of the erodibility of the material (k) and the layer thickness (h) and inversely proportional to the convergence velocity (v_{conv}):

$$Ne = \frac{kh}{v_{conv}} \tag{1.5}$$

When Ne → ∞ due to either material that can be eroded quickly or extremely low convergence rates, no topography can exist as it is either eroded instantaneously or there is no convergence to create topography (Willett, 1999). Ne → 0 also occurs due to strong material that resists erosion or a high convergence velocity, where topography develops quickly and the erosion rate cannot remove the material.

1.2. Thesis overview

The aim of this thesis is to apply the insights outlined above to the evolution of orogenic wedges. Instead of using a constant viscosity and crustal density, we utilise a

lithospheric scale model with a rheology that incorporates both non-linear viscous and depth-dependent plastic rheology to better replicate the deformation of the crust. This thesis investigates:

1. The role of convergence velocity and crustal thickness on the structural evolution of orogens, providing constraints to determine the deformation mechanisms accommodating convergence in the Himalayas, European Alps and the Zagros (chapter 3).
2. How internal heating and surface processes influence the structural evolution of orogens, highlighting their time-dependency (chapter 4).
3. The role of lateral variations in strength on the formation of salients and recesses, with insights into the causes of salients and recesses along the Himalayan arc (chapter 5).
4. How the decrease in convergence velocity between India and Asia since collision ~50 Ma influenced the formation of the Himalayan fold-and-thrust belt and Tibetan Plateau (chapter 6).

The first three research chapters (3 – 5) investigate each key parameter independently to determine how each influences the structural evolution of the orogen. This differs to previous studies that typically incorporate all these processes in one model which then hinders the understanding of each parameter that is modified due to non-linear feedbacks. Chapter 6 then investigates long-term convergence, replicating the convergence history between India and Asia.

Each research chapter is presented as a stand-alone article, an accepted format for the PhD thesis at Monash University. Although each chapter is unique, there is repetition in the introduction and methods sections due to similar methods and model setups used.

Chapter 3 has recently been accepted for publication in *Tectonics*, whilst Chapters 4, 5 and 6 have not yet been submitted for publication.

1.3. References

Angus-Leppan, P.V., 1982. The height of Mount Everest. Surv. Rev. 26, 367–385. https://doi.org/10.1179/sre.1982.26.206.367

Avouac, J.P., Burov, E.B., 1996. Erosion as a driving mechanism of intracontinental mountain growth. J. Geophys. Res. Solid Earth 101, 17747–17769. https://doi.org/10.1029/96JB01344

Beaumont, C., Ellis, S., Hamilton, J., Fullsack, P., 1996a. Mechanical model for subduction-collision tectonics of Alpine-type compressional orogens. Geology 24, 675–678. https://doi.org/10.1130/0091-7613(1996)024<0675:MMFSCT>2.3.CO;2

Beaumont, C., Kamp, P.J.J., Hamilton, J., Fullsack, P., 1996b. The continental collision zone, South Island, New Zealand: Comparison of geodynamical models and observations. J. Geophys. Res. Solid Earth 101, 3333–3359. https://doi.org/10.1029/95JB02401

Burg, J.-P., Gerya, T.V., 2005. The role of viscous heating in Barrovian metamorphism of collisional orogens: thermomechanical models and application to the Lepontine Dome in the Central Alps. J. Metamorph. Geol. 23, 75–95. https://doi.org/10.1111/j.1525-1314.2005.00563.x

Burov, E., Watts, A.B., 2006. The long-term strength of continental lithosphere : “jelly sandwich” or “crème brûlée” ? Geol. Soc. Am. Bull. 16(1), 4–10. https://doi.org/10.1130/1052-5173

Burov, E.B., 2011. Rheology and strength of the lithosphere. Mar. Pet. Geol. 28, 1402–1443. https://doi.org/10.1016/j.marpetgeo.2011.05.008

Chapple, W.M., 1978. Mechanics of thin-skinned fold-and-thrust belts. GSA Bull. 89, 1189–1198. https://doi.org/10.1130/0016-7606(1978)89<1189:MOTFB>2.0.CO;2

Chen, J., Yuan, J., Guo, C., Zhang, Y., Zhang, P., 2006. Progress in technology for the 2005 height determination of Qomolangma Feng (Mt. Everest). Sci. China Ser. D 49, 531–538. https://doi.org/10.1007/s11430-006-0531-1

Chen, L., Capitanio, F.A., Liu, L., Gerya, T.V., 2017. Crustal rheology controls on the Tibetan plateau formation during India-Asia convergence. Nat. Commun. 8, 15992. https://doi.org/10.1038/ncomms15992

Dahlen, F.A., 1984. Noncohesive critical Coulomb wedges: An exact solution. J. Geophys. Res. Solid Earth 89, 10125–10133. https://doi.org/10.1029/JB089iB12p10125

Dahlen, F.A., 1990. Critical Taper Model of Fold-And-Thrust Belts and Accretionary Wedges. Annu. Rev. Earth Planet. Sci. 18, 55–99. https://doi.org/10.1146/annurev.ea.18.050190.000415

Dahlen, F.A., Barr, T.D., 1989. Brittle frictional mountain building: 1. Deformation and mechanical energy budget. J. Geophys. Res. Solid Earth 94, 3906–3922. https://doi.org/10.1029/JB094iB04p03906

Dal Zilio, L., Ruh, J., Avouac, J.-P., 2020. Structural Evolution of Orogenic Wedges: Interplay Between Erosion and Weak Décollements. Tectonics 39, e2020TC006210. https://doi.org/10.1029/2020TC006210

Davis, D., Suppe, J., Dahlen, F.A., 1983. Mechanics of fold-and-thrust belts and accretionary wedges. J. Geophys. Res. Solid Earth 88, 1153–1172. https://doi.org/10.1029/JB088iB02p01153

de Graaff-Hunter, J., 1955. Various Determinations over a Century of the Height of Mount Everest. Geogr. J. 121, 21–26. https://doi.org/10.2307/1791803

Ellis, M., 1988. Lithospheric Strength in Compression: Initiation of Subduction, Flake Tectonics, Foreland Migration of Thrusting, and an Origin of Displaced Terranes. J. Geol. 96, 91–100.

Ellis, S., Wissing, S., Pfiffner, A., 2001. Strain localization as a key to reconciling experimentally derived flow-law data with dynamic models of continental collision. Int. J. Earth Sci. 90, 168–180. https://doi.org/10.1007/s005310000151

England, P., McKenzie, D., 1982. A thin viscous sheet model for continental deformation. Geophys. J. Int. 70, 295–321. https://doi.org/10.1111/j.1365-246X.1982.tb04969.x

Faccenda, M., Gerya, T.V., Chakraborty, S., 2008. Styles of post-subduction collisional orogeny: Influence of convergence velocity, crustal rheology and radiogenic heat production. Lithos 103, 257–287. https://doi.org/10.1016/j.lithos.2007.09.009

Faccenda, M., Minelli, G., Gerya, T.V., 2009. Coupled and decoupled regimes of continental collision: Numerical modeling. Earth Planet. Sci. Lett. 278, 337–349. https://doi.org/10.1016/j.epsl.2008.12.021

Graveleau, F., Malavieille, J., Dominguez, S., 2012. Experimental modelling of orogenic wedges: A review. Tectonophysics 538, 1–66. https://doi.org/10.1016/j.tecto.2012.01.027

Gutscher, M.-A., Kukowski, N., Malavieille, J., Lallemand, S., 1996. Cyclical behavior of thrust wedges: Insights from high basal friction sandbox experiments. Geology 24, 135–138. https://doi.org/10.1130/0091-7613(1996)024<0135:CBOTWI>2.3.CO;2

Jammes, S., Huismans, R.S., 2012. Structural styles of mountain building: Controls of lithospheric rheologic stratification and extensional inheritance. J. Geophys. Res. Solid Earth 117. https://doi.org/10.1029/2012JB009376

Jaquet, Y., Duretz, T., Grujic, D., Masson, H., Schmalholz, S.M., 2017. Formation of orogenic wedges and crustal shear zones by thermal softening, associated topographic evolution and application to natural orogens. Tectonophysics. https://doi.org/10.1016/j.tecto.2017.07.021

Kaus, B.J.P., Steedman, C., Becker, T.W., 2008. From passive continental margin to mountain belt: Insights from analytical and numerical models and application to Taiwan. Phys. Earth Planet. Inter., Recent Advances in Computational Geodynamics: Theory, Numerics and Applications 171, 235–251. https://doi.org/10.1016/j.pepi.2008.06.015

Konstantinovskaya, E., Malavieille, J., 2011. Thrust wedges with décollement levels and syntectonic erosion: A view from analog models. Tectonophysics 502, 336–350. https://doi.org/10.1016/j.tecto.2011.01.020

Luth, S., Willingshofer, E., Sokoutis, D., Cloetingh, S., 2010. Analogue modelling of continental collision: Influence of plate coupling on mantle lithosphere subduction, crustal deformation and surface topography. Tectonophysics, Quantitative modelling of geological processes 484, 87–102. https://doi.org/10.1016/j.tecto.2009.08.043

Malavieille, J., 2010. Impact of erosion, sedimentation, and structural heritage on the structure and kinematics of orogenic wedges: Analog models and case studies. GSA Today 4–10. https://doi.org/10.1130/GSATG48A.1

Medvedev, S., 2002. Mechanics of viscous wedges: Modeling by analytical and numerical approaches. J. Geophys. Res. Solid Earth 107, ETG 9-1. https://doi.org/10.1029/2001JB000145

Mulugeta, G., Koyi, H., 1992. Episodic accretion and strain partitioning in a model sand wedge. Tectonophysics 202, 319–333. https://doi.org/10.1016/0040-1951(92)90117-O

Platt, J.P., 1986. Dynamics of orogenic wedges and the uplift of high-pressure metamorphic rocks. Geol. Soc. Am. Bull. 97, 1037. https://doi.org/10.1130/0016-7606(1986)97<1037:DOOWAT>2.0.CO;2

Pusok, A.E., Kaus, B.J.P., 2015. Development of topography in 3-D continental-collision models. Geochem. Geophys. Geosystems 16, 1378–1400. https://doi.org/10.1002/2015GC005732

Ramberg, H., 1967. Model Experimentation of the Effect of Gravity on Tectonic Processes. Geophys. J. R. Astron. Soc. 14, 307–329. https://doi.org/10.1111/j.1365-246X.1967.tb06247.x

Rossetti, F., Faccenna, C., Ranalli, G., Storti, F., 2000. Convergence rate-dependent growth of experimental viscous orogenic wedges. Earth Planet. Sci. Lett. 178, 367–372. https://doi.org/10.1016/S0012-821X(00)00082-0

Ruh, J.B., 2017. Effect of fluid pressure distribution on the structural evolution of accretionary wedges. Terra Nova 29, 202–210. https://doi.org/10.1111/ter.12263

Ruh, J.B., Gerya, T., Burg, J.-P., 2013. High-resolution 3D numerical modeling of thrust wedges: Influence of décollement strength on transfer zones. Geochem. Geophys. Geosystems 14, 1131–1155. https://doi.org/10.1002/ggge.20085

Ruh, J.B., Gerya, T., Burg, J.-P., 2014. 3D effects of strain vs. velocity weakening on deformation patterns in accretionary wedges. Tectonophysics 615–616, 122–141. https://doi.org/10.1016/j.tecto.2014.01.003

Ruh, J.B., Kaus, B.J.P., Burg, J.-P., 2012. Numerical investigation of deformation mechanics in fold-and-thrust belts: Influence of rheology of single and multiple décollements. Tectonics 31. https://doi.org/10.1029/2011TC003047

Schreurs, G., Buiter, S.J.H., Boutelier, D., Corti, G., Costa, E., Cruden, A.R., Daniel, J.-M., Hoth, S., Koyi, H.A., Kukowski, N., Lohrmann, J., Ravaglia, A., Schlische, R.W., Withjack, M.O., Yamada, Y., Cavozzi, C., Ventisette, C.D., Brady, J.A.E., Hoffmann-Rothe, A., Mengus, J.-M., Montanari, D., Nilforoushan, F., 2006. Analogue benchmarks of shortening and extension experiments. Geol. Soc. Lond. Spec. Publ. 253, 1–27. https://doi.org/10.1144/GSL.SP.2006.253.01.01

Selzer, C., Buiter, S.J.H., Pfiffner, O.A., 2007. Sensitivity of shear zones in orogenic wedges to surface processes and strain softening. Tectonophysics 437, 51–70. https://doi.org/10.1016/j.tecto.2007.02.020

Selzer, C., Buiter, S.J.H., Pfiffner, O.A., 2008. Numerical modeling of frontal and basal accretion at collisional margins. Tectonics 27. https://doi.org/10.1029/2007TC002169

Stüwe, K., 2007. Geodynamics of the lithosphere: an introduction, 2nd ed. ed. Springer, Berlin ; New York.

Vanderhaeghe, O., Medvedev, S., Fullsack, P., Beaumont, C., Jamieson, R.A., 2003. Evolution of orogenic wedges and continental plateaux: insights from crustal thermal-mechanical models overlying subducting mantle lithosphere. Geophys. J. Int. 153, 27–51. https://doi.org/10.1046/j.1365-246X.2003.01861.x

Verschuren, M., Nieuwland, D., Gast, J., 1996. Multiple detachment levels in thrust tectonics: Sandbox experiments and palinspastic reconstruction. Geol. Soc. Lond. Spec. Publ. 99, 227–234. https://doi.org/10.1144/GSL.SP.1996.099.01.17

Vogt, K., Matenco, L., Cloetingh, S., 2017a. Crustal mechanics control the geometry of mountain belts. Insights from numerical modelling. Earth Planet. Sci. Lett. 460, 12–21. https://doi.org/10.1016/j.epsl.2016.11.016

Vogt, K., Willingshofer, E., Matenco, L., Sokoutis, D., Gerya, T., Cloetingh, S., 2017b. The role of lateral strength contrasts in orogenesis: A 2D numerical study. Tectonophysics. https://doi.org/10.1016/j.tecto.2017.08.010

Weijermars, R., Schmeling, H., 1986. Scaling of Newtonian and non-Newtonian fluid dynamics without inertia for quantitative modelling of rock flow due to gravity (including the concept of rheological similarity). Phys. Earth Planet. Inter. 43, 316–330. https://doi.org/10.1016/0031-9201(86)90021-X

Whipple, K.X., Meade, B.J., 2004. Controls on the strength of coupling among climate, erosion, and deformation in two-sided, frictional orogenic wedges at steady state. J. Geophys. Res. Earth Surf. 109. https://doi.org/10.1029/2003JF000019

Willett, S., Beaumont, C., Fullsack, P., 1993. Mechanical model for the tectonics of doubly vergent compressional orogens 4.

Willett, S.D., 1999a. Rheological dependence of extension in wedge models of convergent orogens. Tectonophysics 305, 419–435. https://doi.org/10.1016/S0040-1951(99)00034-7

Willett, S.D., 1999b. Orogeny and orography: The effects of erosion on the structure of mountain belts. J. Geophys. Res. Solid Earth 104, 28957–28981. https://doi.org/10.1029/1999JB900248

Chapter 2

Modelling approach

2.1. Governing equations

The numerical modelling in this thesis is based on the finite element, particle in-cell (PIC) framework Underworld2 (Beucher et al., 2019a; Moresi et al., 2003a, 2007a). To solve the conservation of mass, momentum, and energy equations, Underworld2 uses the Boussinesq approximation for an incompressible, visco-plastic fluid under Stokes flow in a 2D Cartesian box. Stokes flow, or the Navier-Stokes equation, in fluid mechanics is a partial differential equation (PDE) that describes the flow of incompressible fluids.

The Boussinesq approximation (BA) of stokes flow is used when modelling tectonic settings as the BA assumes density variations are small so they can be ignored everywhere except in the buoyancy term in the momentum equation (van Zelst et al., 2021). This is a result of the Prandlt (Pr) and Reynolds (Re) numbers, where the Pr number represents the ratio of kinematic viscosity (momentum diffusion) over thermal diffusion (Turcotte and Schubert, 2002) and the Re number represents the inertial forces (the product of density, thickness and velocity) over the resistance to flow, i.e. the viscosity of a fluid (Turcotte and Schubert, 2002). The controlling factor of both Pr and Re is the viscosity (η), where $Pr \propto \eta$ and $Re \propto \frac{1}{\eta}$, which results in a high Pr and low Re number. The high viscosity of the crust and mantle and resulting high Pr and low Re values means inertial forces can be neglected in Stokes flow when modelling tectonic settings as the high viscosity inhibits the influence of inertial forces (Turcotte and Schubert, 2002). The extended BA is used in Underworld2 as it includes the option of additional heating mechanisms (e.g. internal heating).

2.1.1. Conservation of mass

The BA assumes that changes to the flow that arise due to compression are considered as a perturbation to the incompressible flow. This is sufficiently incorporated by applying an incompressible constraint on velocity (v):

$$\frac{\partial v_i}{\partial x_i} = 0 \tag{2.1}$$

2.1.2. Conservation of momentum

The conservation of momentum, under the assumption of negligible inertia, is expressed as:

$$\frac{\partial \tau_{ij}}{\partial x_j} - \frac{\partial P}{\partial x_i} + \rho(P,T,C)g_i = 0 \tag{2.2}$$

where τ_{ij} is the stress tensor, P is the lithostatic pressure, ρ is the density, which is dependent on the pressure (P), temperature (T) and composition (C) and g_i is the (vertical) gravity component.

2.1.3. Conservation of energy

The energy conservation is enforced by the following:

$$\frac{\partial T}{\partial t} = \frac{\partial}{\partial x_i}\kappa\left(\frac{\partial T}{\partial x_i}\right) - v_i\frac{\partial T}{\partial x_i} + H_r \tag{2.3}$$

where changes in temperature over time ($\frac{\partial T}{\partial t}$) are a result of thermal diffusion ($\frac{\partial}{\partial x_i}\kappa\left(\frac{\partial T}{\partial x_i}\right)$), thermal advection ($v_i\frac{\partial T}{\partial x_i}$) and internal heating ($H_r$). The inclusion of internal heating in the conservation of energy represents the extended BA.

2.2. Constitutive laws

Critical to this thesis is the use of a non-linear, temperature- and rate-dependent visco-plastic rheology.

2.2.1. Creep law

The viscous deformation of rocks is determined through a temperature-, pressure- and strain rate-dependent power law equation, which allows defining dislocation and diffusion viscosities:

$$\eta_{diff/disl} = \frac{1}{2} A^{-\frac{1}{n}} \dot{\varepsilon}_{II}^{\frac{1-n}{n}} exp\left(\frac{E + PV}{nRT_r}\right) \quad (2.4)$$

where η is the viscosity, A is the pre-exponential factor, n is the stress exponent, E is the activation energy, P is the lithostatic pressure, V the activation volume, R the gas constant, T_r is the temperature at a given position and $\dot{\varepsilon}_{II}$ $(= (0.5\, \dot{\varepsilon}_{ij} \dot{\varepsilon}_{ij})^{0.5})$ is the square root of the second invariant of the strain rate tensor ($\dot{\varepsilon}_{ij}$) at a given position. Diffusion creep is neglected in the crust due to the low temperatures and high strain rates. The bulk average grain size of the crust, which is on the order of mm scale, also makes dislocation creep the dominant viscous deformation mechanism in the crust (Ranalli and Adams, 2013). For simplicity, we ignore the influence of grain size and water fugacity on deformation mechanisms, which can result in large variations in viscosity alone (e.g. Dannberg et al., 2017; Ranalli, 1982).

2.2.2. Plastic rheology

Plasticity is implemented in the model through a Drucker-Prager yield criterion (Spiegelman et al., 2016), which is limits the maximum stresses in the crust (eq. 2.5.1) which is then used to produce an effective viscosity for plastic flow (eq. 2.5.2):

$$\tau_y = C\cos(\varphi) + P\sin(\varphi) \quad (2.5.1)$$

$$\eta_p = \frac{\tau_y}{2\dot{\varepsilon}_{ii}} \quad (2.5.2)$$

where τ_y is the yield stress, C is the cohesion at the surface, $\sin(\varphi)$ $(= f_c)$ is the friction coefficient, φ is the internal friction angle and P represents the lithostatic pressure. Plastic strain-weakening of the crust is implemented through a function of the integrated material plastic strain (ε), where the cohesion (C) and internal friction angle (φ) are reduced linearly (C_w, φ_w) with strain between 0.5 (ε_{min}) and 1.5 (ε_{max}) before reaching the weakened value when $\varepsilon \geq \varepsilon_{max}$:

$$C = \begin{cases} \mathrm{C} & if\ \varepsilon \leq\ \varepsilon_{min} \\ C + \dfrac{(C - C_w)}{(\varepsilon_{min} - \varepsilon_{max})}(\varepsilon - \varepsilon_{min}), & if\ \varepsilon_{min} <\ \varepsilon <\ \varepsilon_{max} \\ C_w, & if\ \varepsilon \geq\ \varepsilon_{max} \end{cases} \quad (2.6.1)$$

$$\varphi = \begin{cases} \varphi & if\ \varepsilon \leq\ \varepsilon_{min} \\ \varphi + \dfrac{(\varphi - \varphi_w)}{(\varepsilon_{min} - \varepsilon_{max})}(\varepsilon - \varepsilon_{min}), & if\ \varepsilon_{min} <\ \varepsilon <\ \varepsilon_{max} \\ \varphi_w, & if\ \varepsilon \geq\ \varepsilon_{max} \end{cases} \quad (2.6.2)$$

Plastic strain (ε) is the time-integrated strain rate second invariant ($\dot{\varepsilon}_{II}$) in areas deforming in the plastic regime, updated and stored on the particles. This method of weakening is similar to previously published work (e.g. Ruh et al., 2012; Vogt et al., 2017).

2.2.3. Composite rheology

Under the assumption of a Maxwell body rheology, the viscosity (η) for each material is the minimum viscosity yielded by each deformation mechanism:

$$\eta_{crust} = \min(\eta_p, \eta_{disl}) \quad (2.7.1)$$

$$\eta_{mantle} = \min(\eta_p, \eta_{disl}, \eta_{diff}) \quad (2.7.2)$$

Viscosity is subsequently limited in the model between 10^{19} Pa s and 10^{24} Pa s. Elasticity may alter the short-term stress distribution within the model, however it is not accounted for as the visco-plastic rheology utilised provides a sufficient first-order estimate on the long-term stress evolution of orogenic wedges over geological timescales (Kaus et al., 2008; Vogt et al., 2017a).

2.3. Numerical method

The governing equations and the constitutive laws outlined above are solved on a regularly spaced grid in a Eulerian configuration. Within the Eulerian grid are Lagrangian particles that are used to track material properties throughout the evolution of the model, which is known as the particle-in-cell (PIC) method.

Underworld2 utilises the multigrid method to discretise the domain to solve the Boussinesq approximation for stokes flow (Moresi et al., 2003a, 2007a). The discretisation of the mesh reduces the problem size, resulting in the BA being reduced to a set of linear equations that can be solved in form of combinations of polynomial expressions (van Zelst et al., 2021). The multigrid method determines the stokes flow by first solving for the pressure using the Schur complement matrix, before backsolving for the velocity, producing the complete solution.

Underworld2 uses Q_1P_0 elements by default, which utilises quadrilateral elements that use linear functions for velocity and a discontinuous constant pressure (Crameri et al., 2012). In the solution, material particles are used to determine the unknowns in the system that are required to approximate the BA. Due to this, no direct interpolation is required between the particles and the mesh (Crameri et al., 2012). The solver time for the multigrid method is proportional to the number of unknowns in the system (Moresi et al., 2003a, 2007a), which is typically the velocity components, pressure and temperature for geodynamic problems.

2.4. Boundary conditions

The boundary conditions vary between chapters and are outlined in the methods section of each chapter. Here, we outline the different types of boundary conditions utilised in each model.

In all models the convergence velocity (v_x) is applied to the left side wall. The convergence velocity is applied across the crust and lithospheric mantle, before decreasing from v_{conv} at the lithosphere asthenosphere boundary to 0 at the bottom of the left side wall. Across the sticky air layer is an inflow/flow condition that allows sticky air to escape at the top of the box. Due to the imposed convergence, new sticky air is introduced into the box,

which must be removed otherwise the top of the box becomes filled with sticky air that stops topography developing. On the left side wall the vertical velocity (v_y) is unconstrained.

No velocity conditions are defined on the bottom boundary (unconstrained), allowing for inflow and outflow of material, implying the model overlies an infinite space filled by an inviscid fluid (Gerya, 2009). This, coupled with the inflow and outflow condition across the sticky air on the left side wall, is required as new material is introduced due to the applied convergence velocity on the left side wall, with the in-flowing material being balanced by out-flow of material along these boundaries. The depth of the bottom boundary varies between each research chapter, with the domain dimensions described in the methods section. The right-side wall boundary condition also varies, with either a free slip ($v_x = 0$) or no slip condition applied ($v_x, v_y = 0$), which stops outflow on the right-side wall. Each model also uses a free-slip condition on the top ($v_y = 0$) boundary to stop material escaping vertically. In 3D, the front and back boundaries are also set to free-slip.

To allow topography to develop, a 'sticky air' layer is included between the top of the crust and the top boundary, with a low viscosity (10^{19} Pa s) and density (1 kg m^{-3}) which minimizes shear stresses at the surface and creates a pseudo free surface (Crameri et al., 2012; Schmeling et al., 2008; Vogt et al., 2017a). The thickness of the sticky air layer varies between chapters, with the thickness stated in the methods section of each research chapter.

2.5. Surface processes

In this thesis, surface processes have been implemented within the Underworld2 UWGeodynamics (v2.10.0b) framework (Beucher et al., 2020). Although not used in each chapter, surface processes are an important part of orogenesis, altering the forces acting on the wedge.

In all implementations of surface processes, the passive tracers are first advected with the particles to determine the new surface position. The particles are then interpolated back to the initial x coordinate on the regularly spaced line (2D) or xz coordinate of a grid (3D) that is defined during model setup, with the surface processes then applied to the particle to determine the new height of the surface and for erosion or sedimentation to take place.

2.5.1. Linear hillslope diffusion

Linear hillslope diffusion (D) has been implemented, which is the rate at which variations in topography diffuse over. The 2D evolution of the surface topography (h) is modelled assuming the short-range transport of material as a linear flux (q_s) which is proportional to the surface slope (Avouac, 1993; Culling, 1960):

$$q_s = -D\frac{dh}{dx} \tag{2.8}$$

where *D* is the surface diffusion constant, expressed as a unit area over unit time ($m^2\ yr^{-1}$), that determines the amount of erosion and sedimentation taking place at the surface. As the surface of the model is represented as a line (1D), the change in surface height over time ($\frac{dh}{dt}$) is reduced to (Gerya, 2009):

$$\frac{dh}{dt} = \frac{dq_s}{dx} \tag{2.9}$$

Where v_y is the uplift velocity, v_x is the horizontal velocity and $\frac{dh}{dx}$ is the vertical height difference between adjacent particles that track the surface. An example of linear hillslope diffusion is given in Figure 2.1, displaying how an elevated region erodes over 1 Myr. As the diffusive surface is implemented over a line, it is only currently available in 2D models.

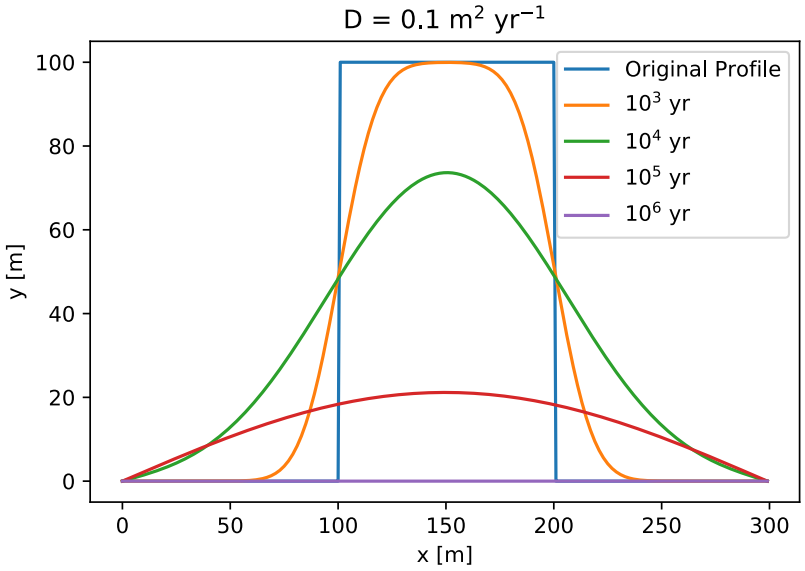

Figure 2.1: An example of hillslope diffusion of an elevated region at given time intervals between 0 and 1 Myr (10^6 yr).

2.5.2. Velocity-dependent surface processes

An alternative approach to surface processes is the use of a sedimentation and erosion rate, where the surface evolves according to the following transport equation (Gerya, 2009):

$$\frac{dh}{dt} = v_s - v_e \tag{2.10}$$

Where v_e and v_s are the erosion and sedimentation rates, respectively. To limit erosion to uplifted areas and sedimentation to basins, a condition is imposed based on the horizontal position (y) of the surface tracking particle compared to the original surface (y_0) (Gerya, 2009):

$$v_s = 0\ m\ yr^{-1}, v_e = v_e\ when\ y > y_0 \tag{2.11}$$

$$v_e = 0\ m\ yr^{-1}, v_s = v_s\ when\ y < y_0 \tag{2.12}$$

The velocity surface processes outlined above have been implemented in both 2D and 3D within UWGeodynamics framework (v2.10.0b).

2.6. Model limitations

2.6.1. Setup and boundary conditions

The setup utilised in this thesis attempts to replicate the upper 300 km of the Earth, which includes the air, crust, lithosphere and upper mantle, this approach is beneficial over sandbox models which only replicate the deformation within the crust and neglects stresses that arise due to the evolving mantle structure. The model incorporates a lower boundary that is unconstrained to allow outflow whilst a velocity condition is imposed on the left sidewall. In these models, the stresses within the wedge evolve in response to convergence and changes in the subduction angle, however this is initially controlled by the angle of the weak zone embedded in the lithosphere. This approach is beneficial over S-point models, where the velocity discontinuity is fixed whilst it can migrate over time in this approach due to evolving stresses.

The open lower boundary condition included in the model setup does not accurately simulate mantle dynamics, where a viscosity increase between the upper and lower mantle which has been shown to stall subducting slabs and alter surface dynamics (Garel et al., 2014; Crameri et al., 2017). The stresses exerted on the wedge due mantle flow are also not accurately represented in this approach as a velocity condition is also imposed across the mantle and do not arise self-consistently, which would be the case when incorporating mantle convection. However, mantle convection models require a large domain to replicate the entire mantle and usually have a lower resolution (larger cell size) to reduce computational time. The lower resolution would then hinder the insights on crustal processes which require a high resolution to capture structures that form during orogenesis.

2.6.2. Rheology

A viscoplastic rheology is utilised throughout this thesis to replicate both brittle and ductile deformation that occurs during orogenesis (Platt, 1986). The numerical approach

utilised does not encapsulate purely brittle deformation, but it is replicated by pseudo-plastic deformation which results in viscous flow. This is a main drawback of numerical methods against sandbox models, which replicate the brittle deformation of the crust well to form faults. However, the approach used in this thesis does include strain weakening which results in localised areas of high strain and the formation of crustal scale shear zones when modelled at a high enough resolution. Benchmarks between numerical models and sandbox models have shown that the overall evolution of numerical and sandbox models are similar (Buiter et al., 2006).

Elasticity has been shown to alter the short-term stress distribution numerical models that simulate orogenesis. However, elasticity is not included in these models as the visco-plastic rheology utilised provides a sufficient first-order estimate on the long-term stress evolution of orogenic wedges over geological timescales (Kaus et al., 2008; Vogt et al., 2017).

2.6.3. Surface processes

Surface processes are implemented through either an erosion and sedimentation rate or a diffusive rate. Both these approaches assume a constant rate throughout the evolution of the model, whilst in nature erosion rates have previously been recorded to scale with topography, with erosion rates highest at highest elevations, with a non-linear relationship between topographic height and erosion rates (Montgomery and Brandon, 2002) due to hillslope and stream processes (Avouac and Burov, 1996). However, the inclusion of these processes is required to determine the influence surface processes has on the structural evolution of orogens.

2.6.4. Parameter investigation

The models employed throughout the thesis differ from previous studies as each parameter is investigated independently. This is beneficial as it develops a baseline

understanding of how each parameter alters the structural evolution of orogens independently. However, all these processes are operating in nature at the same time and feedbacks occur between each parameter, further altering the structural evolution. The work presented in this thesis can then be used in future studies to fully understand how each parameter influences the evolution of orogens when all parameters are included in modelling of orogens.

2.7. Computational performance

Strong scaling is defined as how the solution time varies with the number of processors for a fixed total problem size, whereas **weak scaling** where both the number of processors and problem size are increased by the same factor (van Zelst et al., 2021).

2.7.1. Strong scaling

In general, as the number of CPUs increases, a decrease in the total time should occur if the problem size is fixed. For ideal strong scaling, the solution time is inversely proportional to the number of processors (van Zelst et al., 2021). Strong scaling analysis in 2D was performed on a base resolution of 128 x 32, as the model has an aspect ratio of 4:1 (x:y). In 3D, models were performed on a base resolution of 128 x 32 x 32 as the 3D models have an aspect ratio of 4:1:1 (x:y:z).

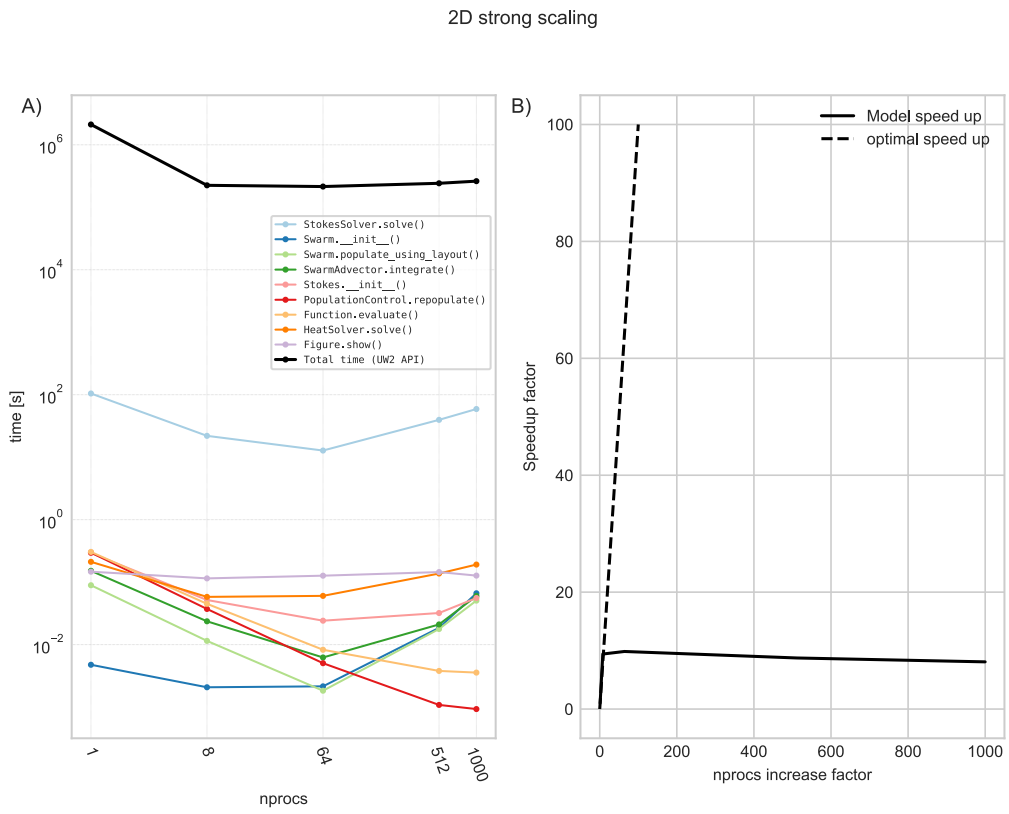

Figure 2.2: Strong scaling tests for 2D models. A) number of processors against time. B) processors increase factor against speed up factor. The strong scaling shows how the total model time speeds up initially before plateauing at around 8 processors.

Our results found that peak performance occurs between 8 and 64 CPUs in 2D, with a further increase in the number of CPUs not decreasing the solution time (Figure 2.2). This roughly corresponds to the number of CPUs per node on the Gadi HPC system, which has 24 CPUs per node on the 'normal' nodes (Intel Xeon Cascade Lake) whilst the 'normalsl' nodes have 16 CPUs per node (Intel Xeon Skylake). The limiting factor on duration above the node CPU limit is communication between nodes rather than the model time itself.

As the computational resources required to solve 3D models increases by a factor of 2^3, a dramatic increase in the number of CPUs is required to perform strong scaling analysis. In 3D, our results show peak performance ~512 CPUs (Figure 2.3A), after which total run time plateaus. From Figure 2.3, this is due to the decrease in time for most operations being countered by an increase in time for the advection of the particles (swarmAdvector.integrate()).

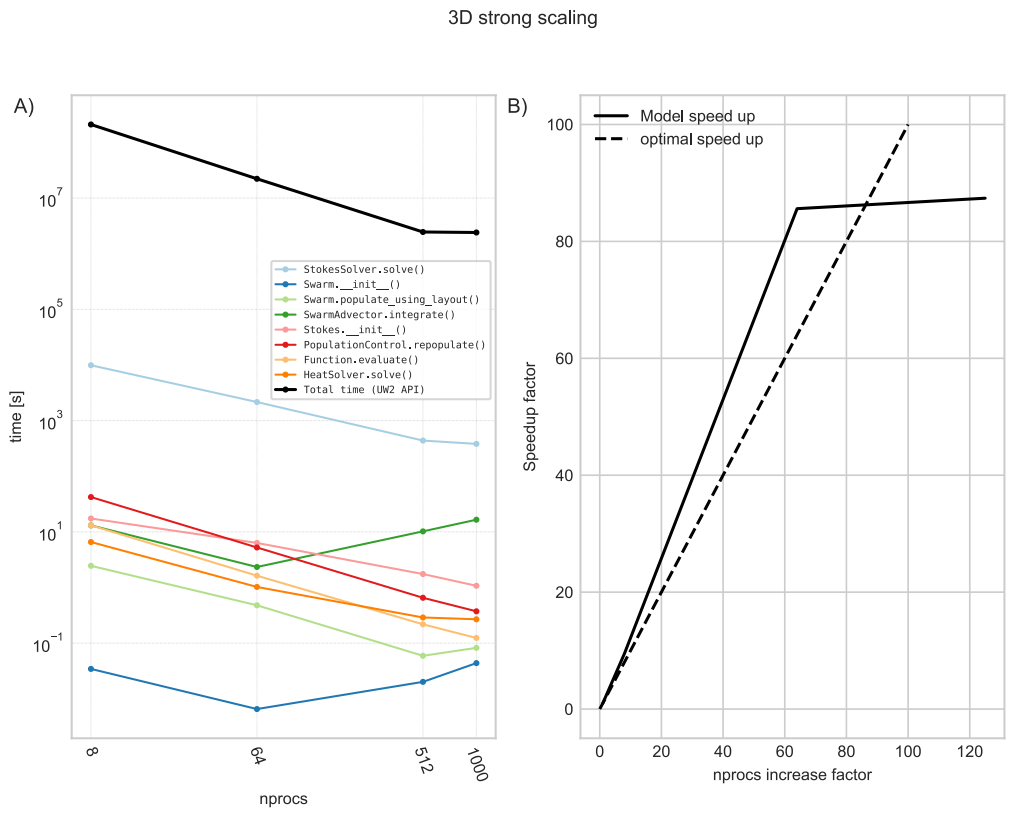

Figure 2.3: Strong scaling tests for 3D models. A) number of processors against time. B) processors increase factor against speed up factor. The strong scaling shows how the total model time decreases before plateauing at around 512 processors in 3D.

2.7.2. Weak scaling

To achieve an ideal weak scaling relationship, the solution time should remain constant as the problem scales with the number of processors, which should result in the same computational power required per processor (van Zelst et al., 2021). However, this is complicated when running models on multiple nodes which takes more time than if all processes were occurring on a single node. Our weak scaling results suggest the optimum number of processors in 2D is between 4 and 16 processors (Figure 2.4A). After this point, a decrease in speed occurs (Figure 2.4A-B), mostly due to an increase in time of the stokes solver and heat solver functions (Figure 2.4A). Similar to the strong scaling, peak performance of the 2D models occurs at the CPU limit per node, as above this limit communication between nodes becomes the bottle-neck, slowing down the time to solve.

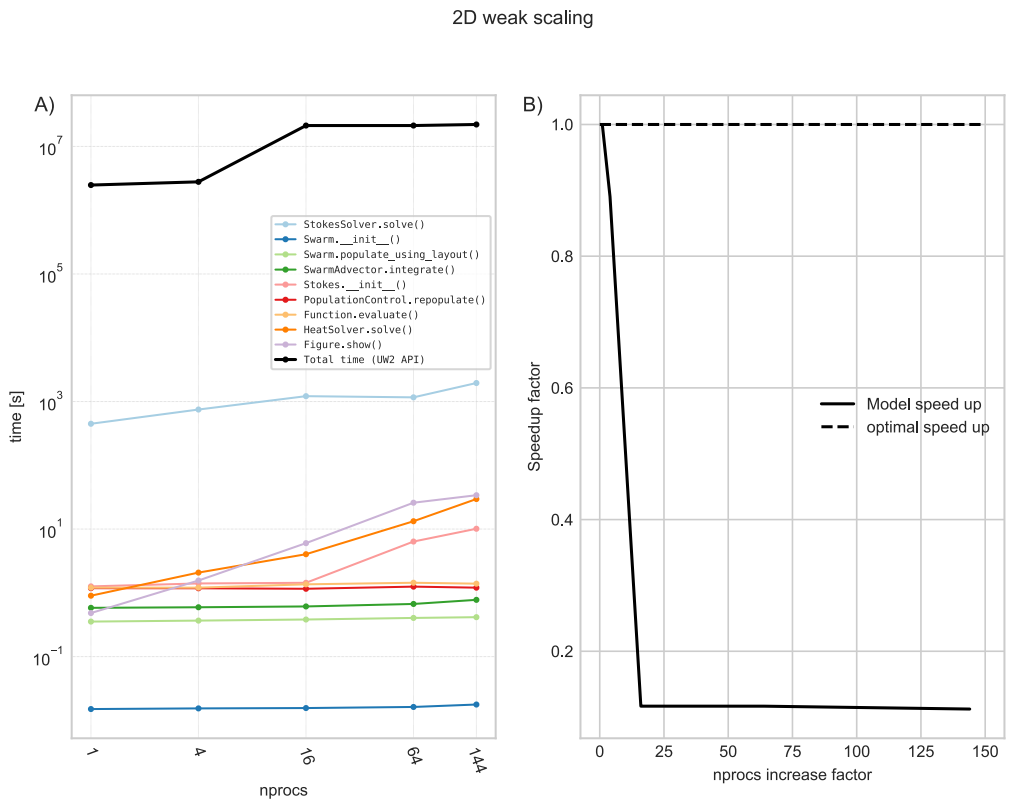

Figure 2.4: Weak scaling tests for 2D models. A) number of processors against time. B) processors increase factor against speed up factor. The weak scaling shows how the total model time increases between 4 and 16 CPUs, suggesting the increase is due to communication time between processors rather than calculations within the model.

Table 2.1: Optimum number of processors based on strong and weak scaling analysis and trial and error of model runs.

Model dimensions	*No. of processors*
2	12
3	512

2.8. References

Avouac, J.-P., 1993. Analysis of scarp profiles: Evaluation of errors in morphologic dating. J. Geophys. Res. Solid Earth 98, 6745–6754. https://doi.org/10.1029/92JB01962

Avouac, J.P., Burov, E.B., 1996. Erosion as a driving mechanism of intracontinental mountain growth. J. Geophys. Res. Solid Earth 101, 17747–17769. https://doi.org/10.1029/96JB01344

Beucher, R., Moresi, L., Giordani, J., Mansour, J., Sandiford, D., Farrington, R., Mondy, L., Mallard, C., Rey, P., Duclaux, G., kaluza, O., Laik, A., Morón, S., 2020. UWGeodynamics: A teaching and research tool for numerical geodynamic modelling. Zenodo. https://doi.org/10.5281/zenodo.4248184

Beucher, R., Moresi, L., Giordani, J., Mansour, J., Sandiford, D., Farrington, R., Mondy, L., Mallard, C., Rey, P., Duclaux, G., Kaluza, O., Laik, A., Morón, S., 2019. UWGeodynamics: A teaching and research tool for numerical geodynamic modelling. J. Open Source Softw. 4, 1136. https://doi.org/10.21105/joss.01136

Buiter, S.J., Babeyko, A.Y., Ellis, S., Gerya, T.V., Kaus, B.J., Kellner, A., Schreurs, G. and Yamada, Y., 2006. The numerical sandbox: comparison of model results for a shortening and an extension experiment. Geological Society, London, Special Publications, 253(1), pp.29-64.

Crameri, F., Lithgow-Bertelloni, C.R. and Tackley, P.J., 2017. The dynamical control of subduction parameters on surface topography. Geochemistry, Geophysics, Geosystems, 18(4), pp.1661-1687.

Crameri, F., Schmeling, H., Golabek, G.J., Duretz, T., Orendt, R., Buiter, S.J.H., May, D.A., Kaus, B.J.P., Gerya, T.V., Tackley, P.J., 2012. A comparison of numerical surface topography calculations in geodynamic modelling: an evaluation of the 'sticky air' method: Modelling topography in geodynamics. Geophys. J. Int. 189, 38–54. https://doi.org/10.1111/j.1365-246X.2012.05388.x

Culling, W.E.H., 1960. Analytical Theory of Erosion. J. Geol. 68, 336–344.

Dannberg, J., Eilon, Z., Faul, U., Gassmöller, R., Moulik, P., Myhill, R., 2017. The importance of grain size to mantle dynamics and seismological observations. Geochem. Geophys. Geosystems 18, 3034–3061. https://doi.org/10.1002/2017GC006944

Garel, F., Goes, S., Davies, D.R., Davies, J.H., Kramer, S.C. and Wilson, C.R., 2014. Interaction of subducted slabs with the mantle transition-zone: A regime diagram from

2-D thermo-mechanical models with a mobile trench and an overriding plate. Geochemistry, Geophysics, Geosystems, 15(5), pp.1739-1765.

Gerya, T., 2009. Introduction to Numerical Geodynamic Modelling. Cambridge University Press, Cambridge. https://doi.org/10.1017/CBO9780511809101

Kaus, B.J.P., Steedman, C., Becker, T.W., 2008. From passive continental margin to mountain belt: Insights from analytical and numerical models and application to Taiwan. Phys. Earth Planet. Inter., Recent Advances in Computational Geodynamics: Theory, Numerics and Applications 171, 235–251. https://doi.org/10.1016/j.pepi.2008.06.015

Montgomery, D.R., Brandon, M.T., 2002. Topographic controls on erosion rates in tectonically active mountain ranges. Earth Planet. Sci. Lett. 201, 481–489. https://doi.org/10.1016/S0012-821X(02)00725-2

Moresi, L., Dufour, F., Mühlhaus, H.-B., 2003. A Lagrangian integration point finite element method for large deformation modeling of viscoelastic geomaterials. J. Comput. Phys. 184, 476–497. https://doi.org/10.1016/S0021-9991(02)00031-1

Moresi, L., Quenette, S., Lemiale, V., Mériaux, C., Appelbe, B., Mühlhaus, H.-B., 2007. Computational approaches to studying non-linear dynamics of the crust and mantle. Phys. Earth Planet. Inter. 163, 69–82. https://doi.org/10.1016/j.pepi.2007.06.009

Platt, J.P., 1986. Dynamics of orogenic wedges and the uplift of high-pressure metamorphic rocks. Geol. Soc. Am. Bull. 97, 1037. https://doi.org/10.1130/0016-7606(1986)97<1037:DOOWAT>2.0.CO;2

Ranalli, G., 1982. Deformation maps in grain-size-stress space as a tool to investigate mantle rheology. Phys. Earth Planet. Inter. 29, 42–50.

Ranalli, G., Adams, M., 2013. Rheological contrast at the continental Moho: Effects of composition, temperature, deformation mechanism, and tectonic regime. Tectonophysics, Moho: 100 years after Andrija Mohorovicic 609, 480–490. https://doi.org/10.1016/j.tecto.2012.10.037

Ruh, J.B., Kaus, B.J.P., Burg, J.-P., 2012. Numerical investigation of deformation mechanics in fold-and-thrust belts: Influence of rheology of single and multiple décollements. Tectonics 31. https://doi.org/10.1029/2011TC003047

Schmeling, H., Babeyko, A.Y., Enns, A., Faccenna, C., Funiciello, F., Gerya, T., Golabek, G.J., Grigull, S., Kaus, B.J.P., Morra, G., Schmalholz, S.M., van Hunen, J., 2008. A benchmark comparison of spontaneous subduction models—Towards a free surface.

Phys. Earth Planet. Inter., Recent Advances in Computational Geodynamics: Theory, Numerics and Applications 171, 198–223. https://doi.org/10.1016/j.pepi.2008.06.028

Spiegelman, M., May, D.A., Wilson, C.R., 2016. On the solvability of incompressible Stokes with viscoplastic rheologies in geodynamics. Geochem. Geophys. Geosystems 17, 2213–2238. https://doi.org/10.1002/2015GC006228

Turcotte, D.L., Schubert, G., 2002. Geodynamics, 2nd ed. Cambridge University Press, Cambridge. https://doi.org/10.1017/CBO9780511807442

van Zelst, I., Crameri, F., Pusok, A.E., Glerum, A., Dannberg, J., Thieulot, C., 2021. 101 Geodynamic modelling: How to design, carry out, and interpret numerical studies. Solid Earth Discuss. 1–80. https://doi.org/10.5194/se-2021-14

Vogt, K., Matenco, L., Cloetingh, S., 2017. Crustal mechanics control the geometry of mountain belts. Insights from numerical modelling. Earth Planet. Sci. Lett. 460, 12–21. https://doi.org/10.1016/j.epsl.2016.11.016

Willett, S.D., 1999. Orogeny and orography: The effects of erosion on the structure of mountain belts. Journal of Geophysical Research: Solid Earth, 104, 28957-28981. https://doi.org/10.1029/1999JB900248

Chapter 3

Convergence velocity controls on the structural evolution of orogens

Authors: Ben S. Knight, Fabio A. Capitanio, Roberto F. Weinberg

Affiliation:

School of Earth, Atmosphere & Environment, Monash University, Clayton, 3800

Accepted for publication in *Tectonics* (2021), doi: 10.1029/2020TC006570

Abstract

The collision of continental crust results in the formation of orogenic wedges to accommodate convergence. We use 2D thermo-mechanical models to address the growth of visco-plastic orogenic wedges, focusing on the structural evolution over time. We find that when the shear stress at the base of the crust is below the yield stress then the viscous behaviour dictates the evolution, with the wedge structure and geometry influenced by the convergence velocity. In contrast, when the shear stress is equal to or above the yield stress across the entire wedge then the plastic behaviour controls the evolution, with the structural style and geometry independent of convergence velocity. The models highlight the controls of the basal décollement rheology on the deformation style of the orogenic wedge. We find that for increasing crustal thickness, the velocity required to transition from viscous- to visco-plastic- and then to plastic-dominated wedges increases. We determine empirically how the viscous deformation influences the wedge strength and estimate an effective friction coefficient based on the geometry of the entire wedge. The models allow inferences on the dominant deformation mechanism currently accommodating convergence in the Zagros, Himalayas and European Alps when estimating the effective friction coefficient from the geometry, showing the relevant role of rate-dependent viscous deformation in each orogenic wedge.

3.1. Introduction

During plate convergence and collision, deformation of the continental crust is accommodated by the formation of an orogenic wedge. Key to the different structural styles of orogenic wedges is the rheology, determining whether deformation is predominantly accommodated by either brittle-plastic or viscous-ductile deformation. Early studies into orogenic wedges focused on brittle-plastic deformation, using the critical taper approach (e.g. Dahlen, 1990, 1988, 1984; Dahlen and Barr, 1989; Davis et al., 1983; Platt, 1986), while other studies (e.g. Beaumont et al., 1996; Medvedev, 2002; Piccolo et al., 2017; Vanderhaeghe et al., 2003; Vogt et al., 2017a, 2017b; Willett, 1999) demonstrate that some or all of convergence may be accommodated by viscous-ductile deformation, first hypothesized by Platt (1986). The dominance of plastic or viscous deformation is critical to the structural evolution of orogenic wedges.

At crustal scale, plastic deformation favours localised deformation and stacking of crustal layers, while strain rate-dependent viscous flow favours diffuse deformation (Pfiffner, 2017; Poblet and Lisle, 2011). These rheological end members may co-exist, with structures related to both deformation mechanisms present in orogenic wedges, which may have occurred at the same, or different, times throughout the evolution of the orogenic wedge (Mouthereau et al., 2007; Pfiffner, 2017). The dominant deformation mechanism is a consequence of the rheological behaviour of the crust under convergence, determined by the depth of the brittle-ductile (BD) transition in the crust.

Previous studies have shown how the geotherm of the crust alters the BD transition and subsequent structural evolution (Ellis, 1988; Vogt et al., 2017a), where a decrease in the geothermal gradient results in the deepening of the BD transition. The depth of the BD transition is also determined by the composition of the crust (Burov, 2011; Chen et al.,

2017b; Jammes and Huismans, 2012; Medvedev, 2002; Piccolo et al., 2017; Vanderhaeghe et al., 2003; Vogt et al., 2017a, 2017c), with a ‘stiffer’ viscous rheology increasing the plastic domain and deepening the BD transition for a constant friction coefficient. Comparably, a decrease in friction coefficient increases the depth of the BD transition for a given viscous rheology. Convergence velocity also controls the depth of the BD transition through induced strain rates, with larger strain rates resulting in the deepening of the BD transition, increasing the amount of crust under plastic deformation (Burov, 2011; Gerya, 2009). While these previous studies have provided insights into factors influencing the structural evolution of orogenic wedges, the influence of convergence velocity has not been comprehensively investigated.

The aim of this study is to improve the understanding on the influence of convergence velocity on the structural evolution of orogenic wedges. We use a 2D thermo-mechanical numerical model to investigate the role of convergence velocity and crustal thickness on the dominant deformation mechanism and resulting structural styles of orogenic wedges. By addressing these parameters, we encompass the thermo-mechanical conditions influencing the crustal rheology, due to its strain-rate and temperature dependency, highlighting the role of each on the structural evolution of orogenic wedges. We compare the results with nature to estimate the wedge strength and determine the role of viscous deformation in accommodating convergence in the Zagros, Himalayas and European Alps. The outcomes emphasize the role of rate-dependent viscous rheology on the estimated strength of the wedge and resultant structural style.

3.2. Modelling approach

3.2.1. Governing equations

We model plate convergence and collision as the viscous flow of a fluid with an infinite Prandtl number and a low Reynolds number. The conservation of mass, momentum and energy equations are solved for an incompressible, visco-plastic fluid in a 2D Cartesian box using the finite element, particle-in-cell (PIC) code Underworld2 (Beucher et al., 2019b; Moresi et al., 2007b, 2003b). Underworld2 allows the tracking of distinct materials and their properties through Lagrangian particles within a Eulerian finite element grid (PIC method).

The conservation of mass, momentum and energy are solved using the Boussinesq approximation of an incompressible Stokes flow in a two-dimensional Cartesian geometry (Moresi et al., 2007b, 2003b):

$$\frac{\partial v_i}{\partial x_i} = 0 \tag{3.1}$$

$$\frac{\partial \tau_{ij}}{\partial x_j} - \frac{\partial P}{\partial x_i} = -\rho g_i \tag{3.2}$$

$$\frac{\partial T}{\partial t} + v_i \frac{\partial T}{\partial x_i} = \frac{\partial}{\partial x_i} \kappa \left(\frac{\partial T}{\partial x_i} \right) \tag{3.3}$$

Where x_i represents the coordinate system, τ_{ij} is the deviatoric stress tensor, P the pressure, v_i is the velocity, T is the temperature, ρ is the density, g is gravity, t represents time and κ is the thermal diffusivity.

3.2.2. Constitutive laws

Critical to our study is the use of a non-linear, temperature- and rate-dependent visco-plastic rheology. The viscous deformation of rocks is calculated using a temperature,

pressure and strain rate dependent power law equation, with dislocation and diffusion creep determined through a generic relationship between stress and strain rate for each mechanism:

$$\eta_{diff,disl} = \frac{1}{2} A^{-\frac{1}{n}} \dot{\varepsilon}_{II}^{\frac{1-n}{n}} exp\left(\frac{E + PV}{nRT_r}\right) \quad (3.4)$$

where η is the viscosity, A is the pre-exponential factor, n is the stress exponent, E is the activation energy, P is the lithostatic pressure, V the activation volume, R the gas constant, T_r is the temperature at a given position and $\dot{\varepsilon}_{II} = (\frac{1}{2}\dot{\varepsilon}_{ij}\dot{\varepsilon}_{ij})^{0.5}$ is the square root of the second invariant of the strain rate tensor ($\dot{\varepsilon}_{ij}$) at a given position. The value for each parameter is presented in Table 3.1. The deviatoric stress tensor and the strain rate tensor ($\dot{\varepsilon}_{ij}$) are related by $\tau_{ij} = 2\eta\dot{\varepsilon}_{ij}$, where η is the viscosity and subscript *i* and *j* represent the tensor indices.

Diffusion creep is included in the mantle but neglected in the crust due to the low temperature and high strain rates within the crust. The bulk average grain size of the crust, which is on the order of mm scale, also makes dislocation creep the dominant viscous deformation mechanism in the crust (Ranalli and Adams, 2013). For simplicity, we use a constant grain size for the viscous rheology, referring the readers to previously published work on the influence of grain size on viscous deformation (e.g. Dannberg et al., 2017; Ranalli, 1982).

Plasticity is implemented in the model through a Drucker-Prager yield criterion (Spiegelman et al., 2016), which is used to limit the maximum stresses in the crust that results in an effective viscosity for the plastic flow (η_p):

$$\tau_y = C\cos(\varphi) + P\sin(\varphi) \quad (3.5.1)$$

$$\eta_p = \frac{\tau_y}{2\dot{\varepsilon}_{II}} \tag{3.5.2}$$

where τ_y is the yield stress, C is the cohesion at the surface, φ is the internal friction angle, where $\sin(\varphi)$ represents the friction coefficient (f_c) and *P* is the lithostatic pressure.

Plastic strain-weakening of the crust is also included, where the cohesion (C) and internal friction angle (φ) are reduced linearly between plastic strain (ε) values 0.5 (ε_{min}) and 1.5 (ε_{max}) before reaching the weakened value when $\varepsilon \geq \varepsilon_{max}$:

$$C = \begin{cases} \mathrm{C} & if\ \varepsilon \leq \varepsilon_{min} \\ C + \dfrac{(C - C_w)}{(\varepsilon_{min} - \varepsilon_{max})}(\varepsilon - \varepsilon_{min}), & if\ \varepsilon_{min} < \varepsilon < \varepsilon_{max} \\ C_w, & if\ \varepsilon \geq \varepsilon_{max} \end{cases} \tag{3.6.1}$$

$$\varphi = \begin{cases} \varphi & if\ \varepsilon \leq \varepsilon_{min} \\ \varphi + \dfrac{(\varphi - \varphi_w)}{(\varepsilon_{min} - \varepsilon_{max})}(\varepsilon - \varepsilon_{min}), & if\ \varepsilon_{min} < \varepsilon < \varepsilon_{max} \\ \varphi_w, & if\ \varepsilon \geq \varepsilon_{max} \end{cases} \tag{3.6.2}$$

Plastic strain is the time-integrated strain rate second invariant ($\dot{\varepsilon}_{II}$) in areas deforming in the plastic regime, which is updated and stored on the particles. This method of weakening is similar to previously published methods (e.g. Ruh et al., 2012; Vogt et al., 2017a). The influence of strain weakening on the strength profile of the crust is visible in Figure 3.1C.

The effective viscosity (η) for each layer is then determined through the minimum viscosity of each deformation mechanism:

$$\eta_{crust} = \min(\eta_p, \eta_{disl}) \tag{3.7}$$

$$\eta_{mantle} = \min(\eta_p, \eta_{disl}, \eta_{diff}) \tag{3.8}$$

Viscosity is subsequently limited in the model between 10^{19} Pa s and 10^{24} Pa s. Maximum strain rates in the model reach ~10^{-14} s^{-1}, which produce a viscosity >10^{19} Pa s for the

rheology used (Table 3.1). Elasticity may alter the short-term stress distribution within the model, however it is not included as the visco-plastic rheology utilised provides a sufficient first-order estimate on the long-term stress evolution of orogenic wedges over geological timescales (Kaus et al., 2008; Vogt et al., 2017a).

Table 3.1: Initial material properties used for the visco-plastic rheology. ρ is density at the surface. A is the pre-exponential factor, n, is the stress exponent, V is the activation volume, E is the activation energy, f_c is the friction coefficient, φ is the internal friction angle, C is the cohesion at the surface, ρ_0 is the density of the crust at the surface and R (=8.314462) is the gas constant. Subscript w represents the weakened value.

	Crust	**Mantle**		**Weak Zone**	
Rheology	*Quartzite*[a]	*Olivine*[b]		*Wet Olivine* [b]	
Symbol	*Dislocation*	*Dislocation*	*Diffusion*	*Dislocation*	*Diffusion*
A (MPa^{-n} s^{-1})	1.1×10^{-34}	1.1×10^{5}	1.5×10^{9}	1.6×10^{3}	2.5×10^{7}
n	*4.0*	*3.5*	*1.0*	*3.5*	*1.0*
E ($J\ mol^{-1}$)	2.23×10^{5}	5.30×10^{5}	3.75×10^{5}	5.20×10^{5}	3.75×10^{5}
V ($m^3\ mol^{-1}$)	*0*	6.0×10^{-6}	6.0×10^{-6}	2.3×10^{-5}	1.0×10^{-5}
R ($J\ mol^{-1}\ K^{-1}$)	*8.3144621*	*8.3144621*	*8.3144621*	*8.3144621*	*8.3144621*
C - C_w (Pa)	10^7 - 10^6	10^7		10^7 - 10^6	
f_c – f_{cw}	*0.3 - 0.15*	*0.6*		*0.1 - 0.05*	
φ	17.5	36.9		5.74	
φ_w	8.62	36.9		2.87	
ρ_0 ($kg\ m^{-3}$)	*2700*	*3300*		*3300*	

[a](Gleason and Tullis, 1995) [b](Hirth and Kohlstedt, 2003)

3.2.3. Model Setup

The model (Figure 3.1A) is designed to simulate continental collision, where an orogenic wedge is formed above a pre-existing weakness as the crust converges and detaches from the subducting mantle lithosphere. The model domain is two-dimensional, with a length of 1200 km and depth of 300 km. A uniform grid is used, with a distribution of 512 × 128 nodal points giving a cell length of 2.34 km, with 30 particles per cell. Timesteps are determined by using (half of) the Courant–Friedrichs–Lewy (CFL) condition. A cell width of 2.34 km results in timesteps of ~117,000 years for a convergence velocity of 1 cm yr^{-1} and 11,700 years at a convergence velocity of 10 cm yr^{-1}.

The initial configuration is that of a homogenous crust with a 45° dipping weak zone within the mantle lithosphere at x = 700 km, representing a pre-existing subduction zone (Figure 3.1A). The weak zone has a wet olivine rheology and low friction coefficient whilst the surrounding lithospheric mantle has a dry olivine rheology and high friction coefficient, localising deformation above the weak zone. To allow the evolution of topography, a 30 km 'sticky air' layer is included with a low viscosity (10^{19} Pa s) and density (1 kg m^{-3}) which minimizes shear stresses at the surface and creates a pseudo free surface (Crameri et al., 2012; Schmeling et al., 2008; Vogt et al., 2017a). A quartzite rheology is applied to the crust (Table 1), with the thickness of the crust varied between 20, 25 and 30 km. A single crustal layer is used to better constrain the influence of the visco-plastic rheology and brittle-ductile transition on the structural evolution that may be impeded when multiple rheological layers are used.

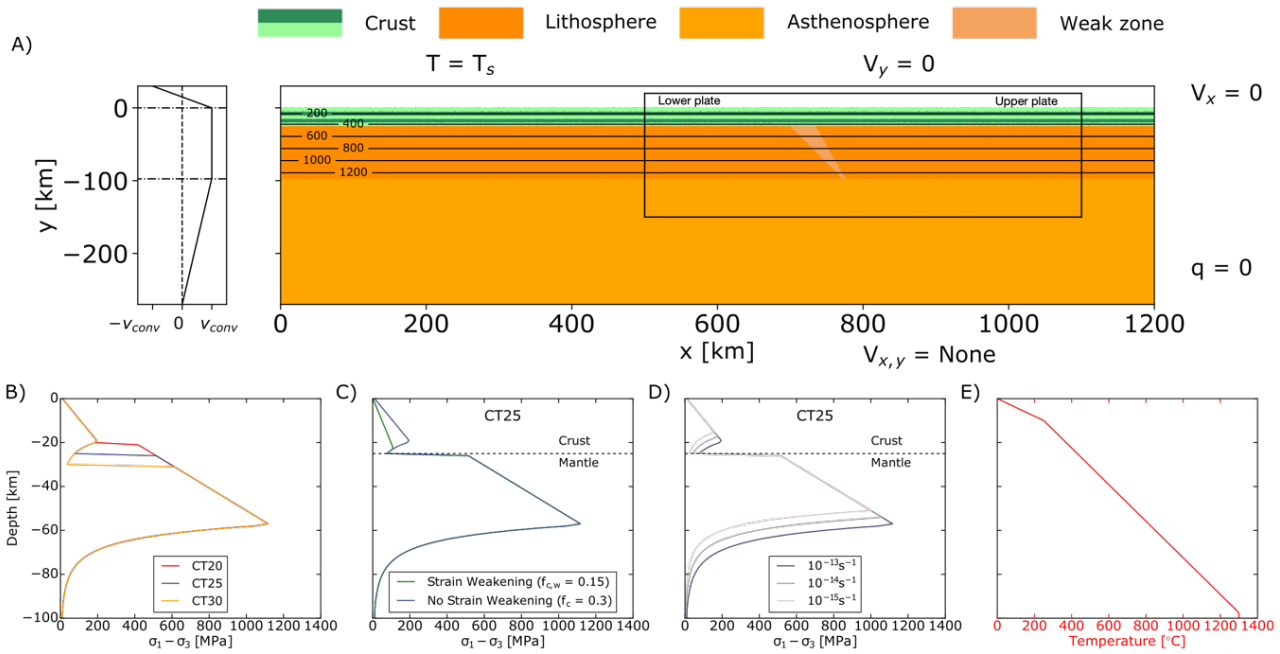

Figure 3.1: A) Initial model setup of case CT25, with an initial crustal thickness of 25 km (see Table 2). Temperature contours are given at 200 °C intervals. The black box (x > 700 km & x < 1100 km, y < 20km & y > -150 km) portrays the area shown in subsequent figures that display model evolution. The convergence velocity profile on the left displays the velocity boundary condition, with convergence applied to the crust and lithosphere. An inflow-outflow condition is applied across the sticky air, whilst the velocity decreases to 0 from the bottom of the lithosphere to the bottom of the domain. B) Strength profile for CT20, CT25 and CT30, where $\dot{\varepsilon}_{II} = 10^{-13} s^{-1}$. C) Strength profile for CT25, showing the influence of strain weakening on the strength profile. D) Strength profile for CT25 showing the influence of varying strain rate. E) Initial temperature profile for all models, with a geothermal gradient of 25 °C km^{-1} for the first 10 km and then 12 °C km^{-1} until a temperature of 1300 °C is reached at the lithosphere-asthenosphere boundary (LAB) at a depth of 97.5 km.

A constant temperature (T = 0 °C) is applied to the top boundary, with no heat flux across the side walls. The initial internal temperature distribution follows a geothermal gradient of 25 °C km^{-1} for the first 10 km and then 12 °C km^{-1} until a temperature of 1300 °C is reached at the lithosphere-asthenosphere boundary (LAB) at a depth of 97.5 km. We neglect adiabatic gradients and keep the underlying mantle at 1300 ˚C. The geotherm is constant across all models, where an increase in crustal thickness results in a higher Moho temperature. This alters the strength profile, by swapping a strong upper mantle for a weak (viscous) lower crust (Figure 3.1B-D).

The model uses a free-slip condition on the right (v_x = 0) and top (v_y = 0) boundaries. The velocity is unconstrained at the base, allowing for inflow and outflow of material, implying the model overlies an infinite space with an inviscid fluid (Gerya, 2009) at a depth of 270 km. The convergence velocity is applied on the left wall, with velocity (v_{conv}) varied

between 1 and 10 cm yr^{-1}. The velocity condition is applied across the crust and mantle lithosphere, which induces convergence. Below the lithosphere (y < - 97.5 km), the velocity linearly decreases from the convergence velocity at base of the lithosphere to zero at the bottom of the left wall. Above the crust, an inflow/outflow is prescribed across the sticky air layer (y >0 km) to allow topography to develop (Figure 3.1A, left panel).

The range of velocities tested in this study are within the range of present-day plate velocities (Goes et al., 2008; Zahirovic et al., 2015). A range of crustal thickness are also tested, compatible with reconstructed original margin thicknesses at the onset of collision, from a thinned continental margin to a typical undeformed continental crust (Bott, 1980; Capitanio et al., 2010). To highlight the role of convergence velocity, we keep other parameters constant, e.g. the geothermal gradient and rheology, which would otherwise alter the depth of the brittle-ductile transition (Burov, 2011).

All models are run for the same amount of convergence (~435 km) similar to the amount of shortening accommodated in the Eastern Himalayan Fold-and-Thrust belt (DeCelles et al., 2002). As models are run for the same amount of convergence, the time varies by a factor of 10 between end-member cases (convergence velocities of 1 and 10 cm yr^{-1}). Due to this, we ignore other rate-dependent processes (e.g. surface processes, internal heating) which, if included, would have increasing influence on structure as the duration increases.

3.2.4. Scaling laws: viscous and plastic wedges

The evolution of orogenic wedges has been explored extensively using scaling derived from forces acting on an orogenic wedge. Different approaches exist addressing either the evolution of a Coulomb plastic wedge (Dahlen, 1990, 1988, 1984; Dahlen and Barr, 1989; Davis et al., 1983; Willett, 1999a) or a Newtonian viscous wedge (England and

McKenzie, 1982; Medvedev, 2002; Pusok and Kaus, 2015; Ramberg, 1967; Royden, 1996; Vanderhaeghe et al., 2003; Willett, 1999a). Both approaches are based on the balance of forces acting on a wedge at equilibrium:

$$\int_0^h \sigma_g \, dz + \int_0^h \sigma_n \, dz + \int_0^{\lambda_c} \sigma_b \, dx = 0 \tag{3.9}$$

Where σ_g is the gravitational stress, σ_n is the internal normal compressive stress and σ_b is the shear stress at the base of the wedge along the basal décollement. The stresses acting on the wedge are integrated over a length scale, which are the thickness (h) and the wedge length (λ_c), to determine the force balance (Figure 3.2).

In the critical taper approach, the wedge is considered to be on the verge of failure everywhere internally ($\sigma_n \to 0$). Therefore, the wedge geometry is controlled by the equilibrium between gravitational load and basal décollement shear stress ($\frac{\sigma_g}{\sigma_b}$) (Dahlen, 1990, 1984; Davis et al., 1983; Willett, 1999a). This force balance has also been applied to viscous wedges as either the Argand (Ar) or Ramberg (Rm) number (England and McKenzie, 1982; Pusok and Kaus, 2015; Ramberg, 1967; Royden, 1996; Willett, 1999a), where $\frac{\sigma_g}{\sigma_b}$ represent the resistance to deformation in response to excess gravitational stresses (England and McKenzie, 1982; Ramberg, 1967; Stüwe, 2007).

In the visco-plastic rheology addressed here, the shear stress along the basal décollement is approximated by the dominant deformation mechanism:

$$\sigma_b \sim (\sigma_1 - \sigma_3) \sim \min\{\sigma_b(plastic), \sigma_b(viscous)\} \tag{3.10}$$

When the stress within the wedge and at the base is at or exceeds the yield stress limit ($\sigma_b \geq \tau_y$), the shear stress along the basal décollement can be approximated through the plastic stress (Willett, 1999a):

$$\sigma_b(plastic) \sim C\cos(\varphi) + (\rho_{crust} g h) f_c \quad (3.11)$$

Instead, when the shear stress along the basal décollement is below the yield stress limit ($\sigma_b < \tau_y$), then the basal décollement stress can be approximated through the viscous stress (England and McKenzie, 1982; Ramberg, 1967):

$$\sigma_b(viscous) \sim \eta_{crust} \frac{\mathrm{v}_{conv}}{h} \quad (3.12)$$

Where η_{crust} is the viscosity of the crust, v_{conv} is the convergence velocity and h is the thickness of the crust.

The gravitational stress (σ_g) is the product of crustal density (ρ_c), gravity (g) and thickness of the crust (h):

$$\sigma_g \sim \rho_{crust} g h \quad (3.13)$$

When substituting eq. 3.11 and eq. 3.13, for the plastic rheology, $\frac{\sigma_g}{\sigma_b}$ becomes:

$$\frac{\sigma_g}{\sigma_b(plastic)} \sim \frac{\rho_{crust} g h}{C\cos\,(\varphi) + (\rho_{crust} g h) f_c} \sim \frac{1}{f_c} \quad (3.14)$$

The plastic stress $\sigma_b(plastic)$ shows no dependency on velocity, and eq. 3.14 instead is controlled by the friction coefficient (f_c) as the influence of cohesion is negligible compared to lithostatic pressure at the base of the crust (Willett, 1999a).

Instead, when substituting eq. 3.12 and 3.13, for the viscous stress, $\frac{\sigma_g}{\sigma_b}$ becomes:

$$\frac{\sigma_g}{\sigma_b(viscous)} \sim \frac{\rho_{crust} g h^2}{\eta_{crust} \mathrm{v}_{conv}} \quad (3.15)$$

Which includes the convergence velocity (v_{conv}). An increase in v_{conv}, whilst all other variables remain constant, results in a decrease in $\frac{\sigma_g}{\sigma_{b(viscous)}}$.

When combining both for the visco-plastic rheology utilised here (eq. 3.10), $\frac{\sigma_g}{\sigma_b}$ becomes:

$$\frac{\sigma_g}{\sigma_b} = \min\left(\frac{\rho_{crust} g h^2}{\eta_{crust} \mathrm{v}_{conv}}, \frac{1}{f_c}\right) \tag{3.16}$$

σ_b is difficult to determine analytically due to the non-Newtonian viscous rheology used, with strain rates and viscosities within the wedge varying across space and time, while σ_g is difficult to determine due to the temperature-dependent density that varies in space and time. Instead, σ_g and σ_b are determined empirically within the model by using the characteristic lengths (Figure 3.2), to approximate the ratio of $\frac{\sigma_g}{\sigma_b}$:

$$\frac{\sigma_g}{\sigma_b} \sim \frac{\lambda_c}{\Delta h} \tag{3.17}$$

The characteristic lengths are the change in crustal thickness (Δh), which represents the excess gravitational stresses acting vertically on the wedge, and wedge length (λ_c) which represents the (resistance to) lateral growth of the wedge (Medvedev, 2002; Vanderhaeghe et al., 2003). These length scales encapsulate how the wedge accommodates convergence, regardless of the dominant deformation mechanism. The wedge either increases in thickness (Δh) due to resistance to internal deformation (σ_b) or lengthens (λ_c) to reduce the gravitational load (σ_g), resulting in internal deformation.

Using eq. 3.16 and eq. 3.17, the length scales can be used to estimate the effective friction coefficient (f_c^e) of the entire wedge:

$$\frac{1}{f_c^e} \sim \frac{\lambda_c}{\Delta h}, \therefore f_c^e = \frac{\Delta h}{\lambda_c} \quad (3.18)$$

Deviations between f_c^e and f_c arise due to the combined visco-plastic rheology (eq. 3.16). The larger the deviation, the increasing influence of the viscous rheology.

The wedge thickness (h) is measured by the thickness of the crust above the deepest point within the wedge (Figure 3.2). The change in thickness (Δh) is defined as the difference between wedge thickness (h) and initial thickness h_0, that is $\Delta h = h - h_0$. The length of the wedge (λ_c) is measured by determining the location at the front and back of the wedge where strain is 0.5 at a depth of 10 km, representing the location of active deformation front on the upper and lower plates.

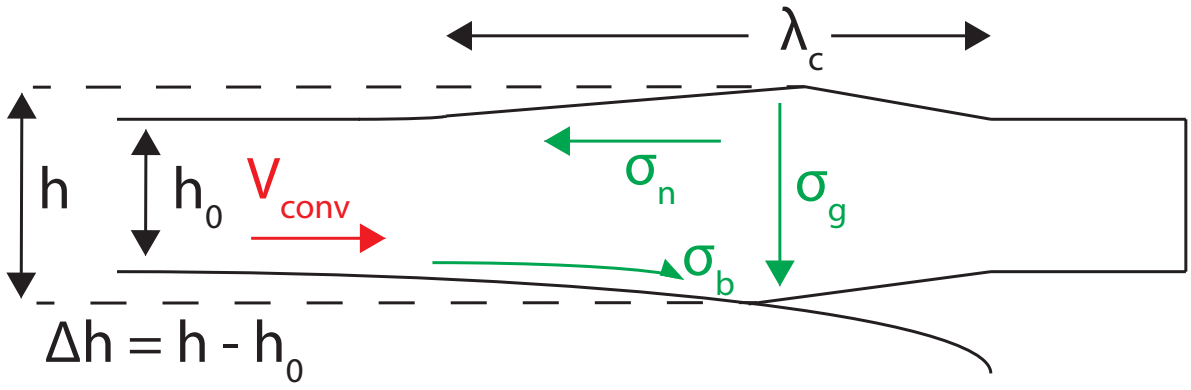

Figure 3.2: Schematic drawing of the orogenic wedge, highlighting where the stresses are acting on the wedge. The key length scales, the length (λ_c) and thickness (h) are shown, which are used to deduce the balance of horizontal and vertical forces acting on the wedge.

The ratio of λ_c over Δh provides a diagnostic to determine the controlling deformation mechanism on the wedge as the wedge evolves over time. The yield stress acts as a stress limiter for the crust with a visco-plastic rheology (eq. 3.6.1). If the stress across the wedge is below the yield stress ($\sigma_b < \tau_y$), then the geometry is controlled by the viscous stress ($\frac{\sigma_g}{\sigma_b(viscous)}$), and $\frac{\lambda_c}{\Delta h}$ varies with convergence velocity (eq. 3.15). If internal stresses within the wedge are equal or greater than the yield stress ($\sigma_b \geq \tau_y$), then the behaviour is dictated by

the plastic stress ($\frac{\sigma_g}{\sigma_{b(plastic)}}$), and a constant value of $\frac{\lambda_c}{\Delta h}$ is expected, that is independent of convergence velocity or crustal thickness and instead dependent on the inverse of the friction coefficient (eq. 3.14).

To summarise, a constant value of $\frac{\lambda_c}{\Delta h}$, independent of convergence velocity and crustal thickness, is indicative of a plastic wedge. Instead, when $\frac{\lambda_c}{\Delta h}$ varies due to the convergence velocity, the wedge is influenced by the viscous rheology. The velocity at which the wedge transitions from a viscous to plastic dominated wedge varies depending on the initial crustal thickness.

3.3. Results

The models are presented in order of increasing crustal thickness. A range of velocities were tested (Table 3.2) and analysed for the discussion, while only two end member cases for each crustal thickness are presented in detail in the results section. The results focus on the structural evolution of the wedge and the differences in the wedge geometry, captured by its length and change in thickness, whilst also quantifying the strain rates, which are proportional to convergence velocity, and the accumulated plastic strain.

*Table 3.2: Experiments described in the text. Cases are labelled according to initial crustal thickness and velocity where CT20-1 indicates a crustal thickness of 20km and velocity of 1 cm/yr. *Main deformation mechanism is determined by the internal structure and aspect ratio after 435 km of convergence.*

Case Name	*Convergence velocity (v_{conv}) [cm yr^{-1}]*	*Initial crustal thickness (h_0) [km]*	*Initial Moho temperature (T_0) [^{o}C]*	*Main deformation mechanism**
CT20-1	1	20	370	Plastic
CT20-2	2	20	370	Plastic
CT20-4	4	20	370	Plastic
CT20-6	6	20	370	Plastic
CT20-8	8	20	370	Plastic
CT20-10	10	20	370	Plastic
CT25-1	1	25	430	Visco-plastic
CT25-2	2	25	430	Visco-plastic
CT25-4	4	25	430	Visco-plastic
CT25-6	6	25	430	Visco-plastic
CT25-8	8	25	430	Plastic
CT25-10	10	25	430	Plastic
CT30-1	1	30	490	Viscous
CT30-2	2	30	490	Viscous
CT30-4	4	30	490	Viscous
CT30-6	6	30	490	Visco-plastic
CT30-8	8	30	490	Visco-plastic
CT30-10	10	30	490	Visco-plastic

3.3.1. CT20: Thin crust models

In CT20 models (Figure 3.3), the internal structure of the wedge is similar for each case, independent of velocity, producing shear zones that extend to the base of the crust, resulting in the stacking of crust. This is due to plasticity being the primary deformation mechanism, as the brittle ductile transition occurs close to the base of the crust (Figure 3.1B) with plastic deformation independent of convergence velocity.

3.3.1.1. CT20-1: Thin crust-slow convergence

CT20-1 has an initial crustal thickness of 20 km and a convergence velocity of 1 cm yr^{-1} (Figure 3.3A-B). Initially, conjugate shear zones develop above the plate interface before deformation begins to propagate outwards on the lower plate, after ~15 Myr (Figure 3.3Ai & Figure 3.3Bi). Shear zones develop within the crust, resulting in progressive crustal stacking, which can be seen by the localised bands of high strain in the crust (Figure 3.3Bi-iii), all of which are linked to a basal décollement. As convergence continues, deformation remains concentrated near to the centre of the wedge, as seen by the distribution of strain (Figure 3.3Bii). Strain rates along the décollement and shear zones within the wedge are similar at ~$2x10^{-14}$ s^{-1}. The upper plate's crust and lithospheric mantle are coupled and act as a rigid backstop, concentrating deformation on the lower plate (Figure 3.3Aiii), while some strain accumulates on the upper plate. Progressive crustal stacking is accommodated between the shear zones, which are illustrated by the high amounts of plastic strain (Figure 3.3Bi-iii), above the plate interface, developing into a thick and narrow wedge, with a thickness of ~85 km and a wedge length of 190 km after 435 km of convergence. Shear zones are evenly spaced ~30 km apart, with dips that shallow outwards from the centre of the wedge due to stacking (Figure 3.3Biii).

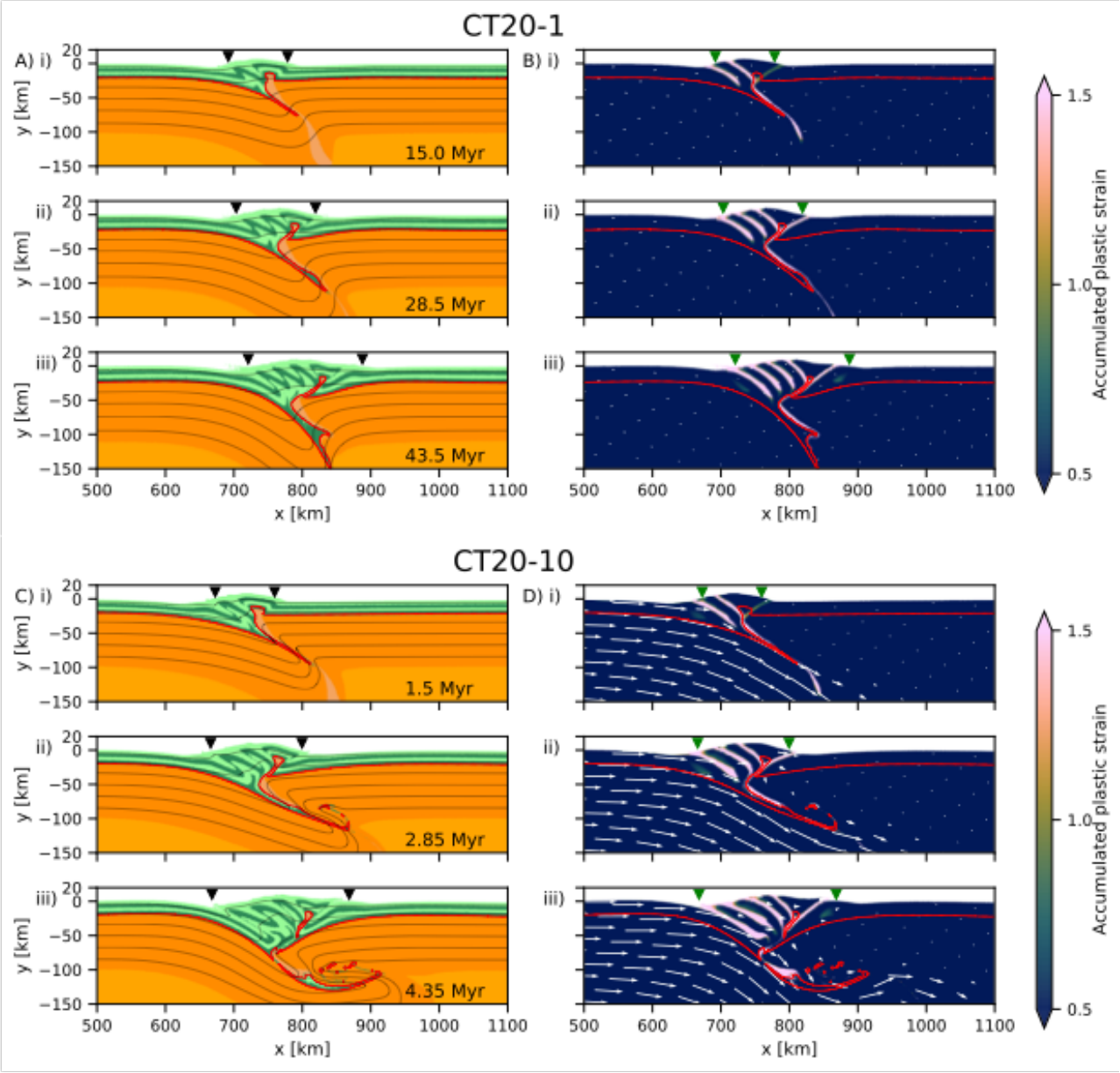

Figure 3.3: Evolution of end member cases in CT20. A) Evolution of the material and B) accumulated plastic strain and velocity vectors at a given time for CT20-1. C) Evolution of the material and D) accumulated plastic strain and velocity vectors at a given time for CT20-10. The inverted triangles at the top of the figures mark the edge of the orogen determined by the point at which strain is 0.5. The red line denotes the base of the crust/Moho.

3.3.1.2. CT20-10: Thin crust-fast convergence

The evolution of CT20-10 (Figure 3.3C-D) is similar in structural style to CT20-1 (Figure 3.3A-B). Throughout the evolution, a main frontal shear zone is active and progressively migrates outwards, widening the orogen and stacking the crust as convergence progresses. The stacking of crust occurs along shear zones that develop within the crust, highlighted by the high amounts of plastic strain (Figure 3.3D). In the upper plate,

deformation localizes along a single shear zone that dips towards the orogeny interior, with strain accumulating near to the centre of the wedge (Figure 3.3D). Deformation is concentrated on the lower plate, with the upper plate and crust remaining relatively undeformed. Underthrusting of the upper plate beneath the orogenic wedge (Figure 3.3C) is also observed, creating a 'V' geometry at the base of the wedge. The strain rates at the centre of the wedge are much larger than in CT20-1, reaching an order of magnitude higher at ~2 x 10^{-13} s^{-1}. Although strain rates are higher, the overall structural style is similar to CT20-1. A similar geometry to CT20-1 is also attained, with CT20-10 reaching a wedge thickness of ~90 km and a length of 200 km after 435 km of convergence.

The similar structures developed in the fast and slow convergence CT20 models show that the structures are not influenced by the convergence velocity. This is a consequence of the dominantly plastic, strain-rate independent regime due to the thinner and, therefore, colder crust.

3.3.2. CT25: Intermediate crust thickness models

The structural style in CT25 (Figure 3.4) models varies with velocity, resulting in either high strain localisation at high velocity (CT25-10) or a wide, diffuse wedge with some strain localisation in the upper crust at low velocity (CT25-1). This is due to a viscous lower crust in CT25-1, caused by the higher Moho temperatures and low convergence velocity, introducing dependency on convergence velocity on the structural evolution.

3.3.2.1. CT25-1: Intermediate crust-slow convergence

The onset of collision in CT25-1 is initially characterised by the localisation of deformation above the weak zone. The wedge initially thickens, with deformation localising on the conjugate shear zones above the weak zone (Figure 3.4A-B). A décollement develops at the base of the crustal layer, with strain rates of ~10^{-14} s^{-1}. This décollement

propagates in both the upper and lower plate over a wide area, decoupling the crust and mantle. This décollement allows strain to accumulate over a wider area (Figure 3.4B) compared to CT20 (Figure 3.3B).

Deformation propagates outward on the lower plate after 15 Myr (Figure 3.4B) along the viscous décollement, which also facilitates deformation of the upper plate, widening the wedge. Deformation at the base of the crust is diffused, with strain rates of ~10^{-14} s^{-1} along the décollement and 10^{-15} s^{-1} along shear zones in the crust. As the wedge front propagates the deformation remains diffused in the lower crust, with some shear zones developing in the upper crust (Figure 3.4Bi-iii). The crust is characterised by shear zones ~30 km apart that extend to mid-crustal depths, whilst near to the base of the crust, viscous deformation is dominant, allowing deformation over a wide area, with crust thickened to ~70 km and a wedge length of ~235 km after 435 km of convergence, making this wedge thinner and wider than those observed in CT20.

3.3.2.2. CT25-10: Intermediate crust-fast convergence

The initial evolution of CT25-10 (Figure 3.4C) is similar to CT25-1 (Figure 3.4A), with deformation localising above a lithospheric weak zone in conjugate shear zones. However, these conjugate shear zones extend to near the base of the crust (Figure 3.4Di), whilst the conjugate shear zones in CT25-1 stop at mid-crustal depths (Figure 3.4Bi). After ~1.5 Myr, deformation extends onto the lower plate, with a second shear zone developing, whilst the upper plate remains relatively undeformed (Figure 3.4Ci & Di). The wedge appears to be more narrow and thicker than CT25-1 after the same amount of convergence. The high velocity also results in coupling the crust and mantle that concentrates deformation on the lower plate, similar to CT20 (Figure 3.4D).

After 4.35 Myr, the crust has thickened to ~90 km and lengthened to ~210 km after 435 km of convergence. This wedge has dimensions that are similar to CT20, with shear zones that dip toward the centre of the wedge (Figure 3.4D). Underthrusting of the upper plate beneath the wedge (Figure 3.4C) is also observed, creating a V-shape geometry of crust at the base of the wedge.

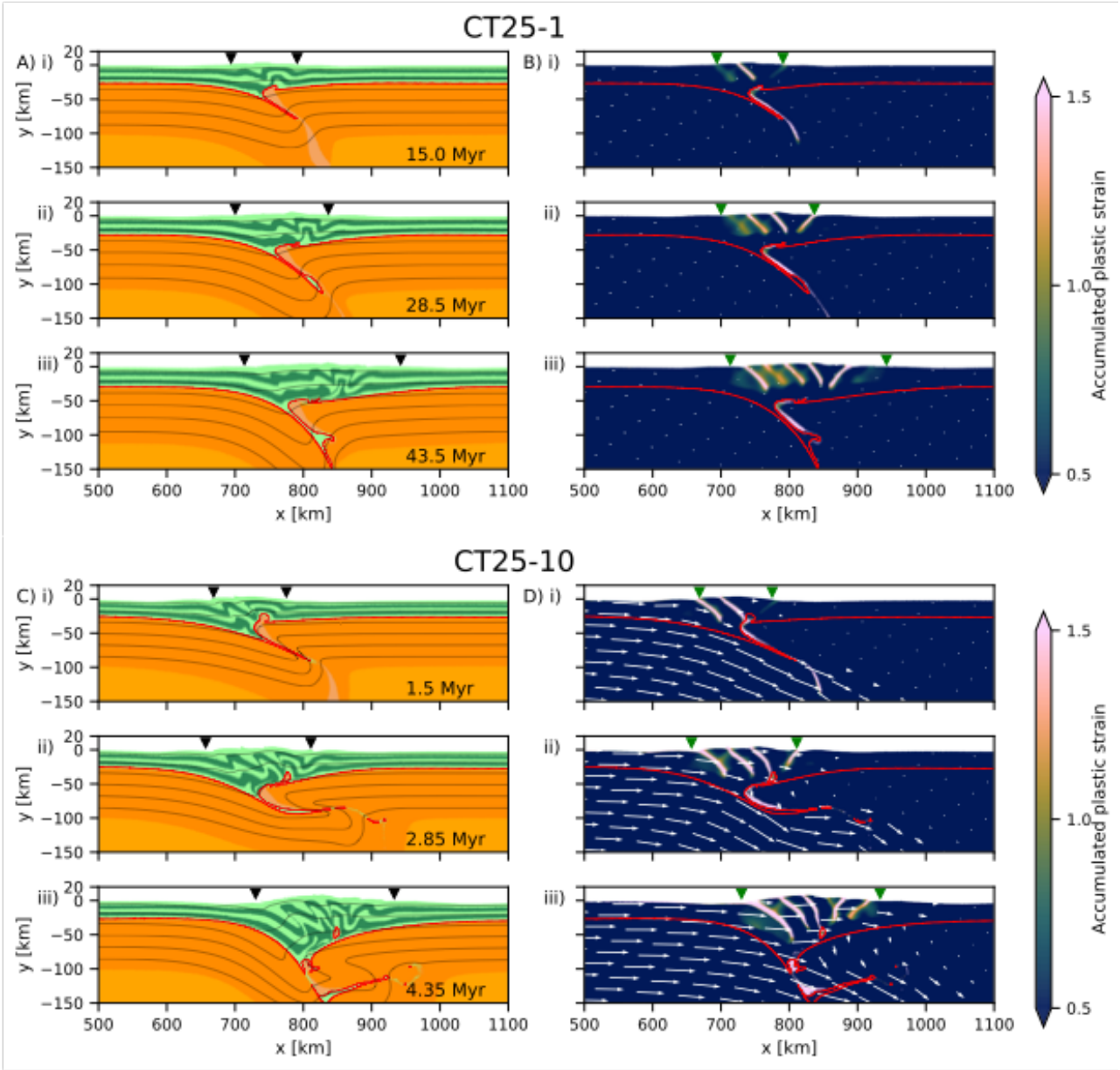

Figure 3.4: Evolution of end member cases in CT25. A) Evolution of the material and B) accumulated plastic strain and velocity vectors at a given time for CT25-1. C) Evolution of the material and D) accumulated plastic strain and velocity vectors at a given time for CT25-10. The inverted triangles at the top of the figures mark the edge of the orogen determined by the point at which strain is 0.5. The red line denotes the base of the crust/Moho.

3.3.3. CT30: Thick crust models

The structural style in CT30 (Figure 3.5) varies depending on the convergence velocity. In CT30, models are characterised by viscous thickening of the crust at low velocity. At increasing velocity, increasing strain localisation takes place and is combined with crustal scale folds developing throughout the crust.

3.3.3.1. CT30-1: Thick crust-slow convergence

The evolution of CT30-1 (Figure 3.5A) is noticeably different from the previous models as no visible shear zones develop and no strain localisation takes place in the crust above the décollement (Figure 3.5B). The higher Moho temperature, due to an increase in crustal thickness, allows for an effective decoupling of the crust from the mantle due to the weak, viscous décollement, similar to CT25-1. However, the viscous lower crust is thicker compared to CT25-1, and is able to accommodate the majority of convergence, with minimal amounts of plastic strain accumulation (Figure 3.5B). Strain rates in the upper crust are ~10^{-15} $s^{-1,}$ with some folding above the weak zone due to the initial deformation at the onset of collision. This folding begins to migrate onto the upper plate after 15 Myr (Figure 3.5Ai). There is minor crustal thickening, with a flat and wide orogenic wedge forming due to the viscous décollement. The deformation fronts spread outwards from the centre, with migration far into the upper and lower plates along the viscous basal décollement, with decoupling of the crust and mantle. The wedge is ~60 km thick and ~290 km in length after 435 km of convergence, much thinner and wider than previous cases.

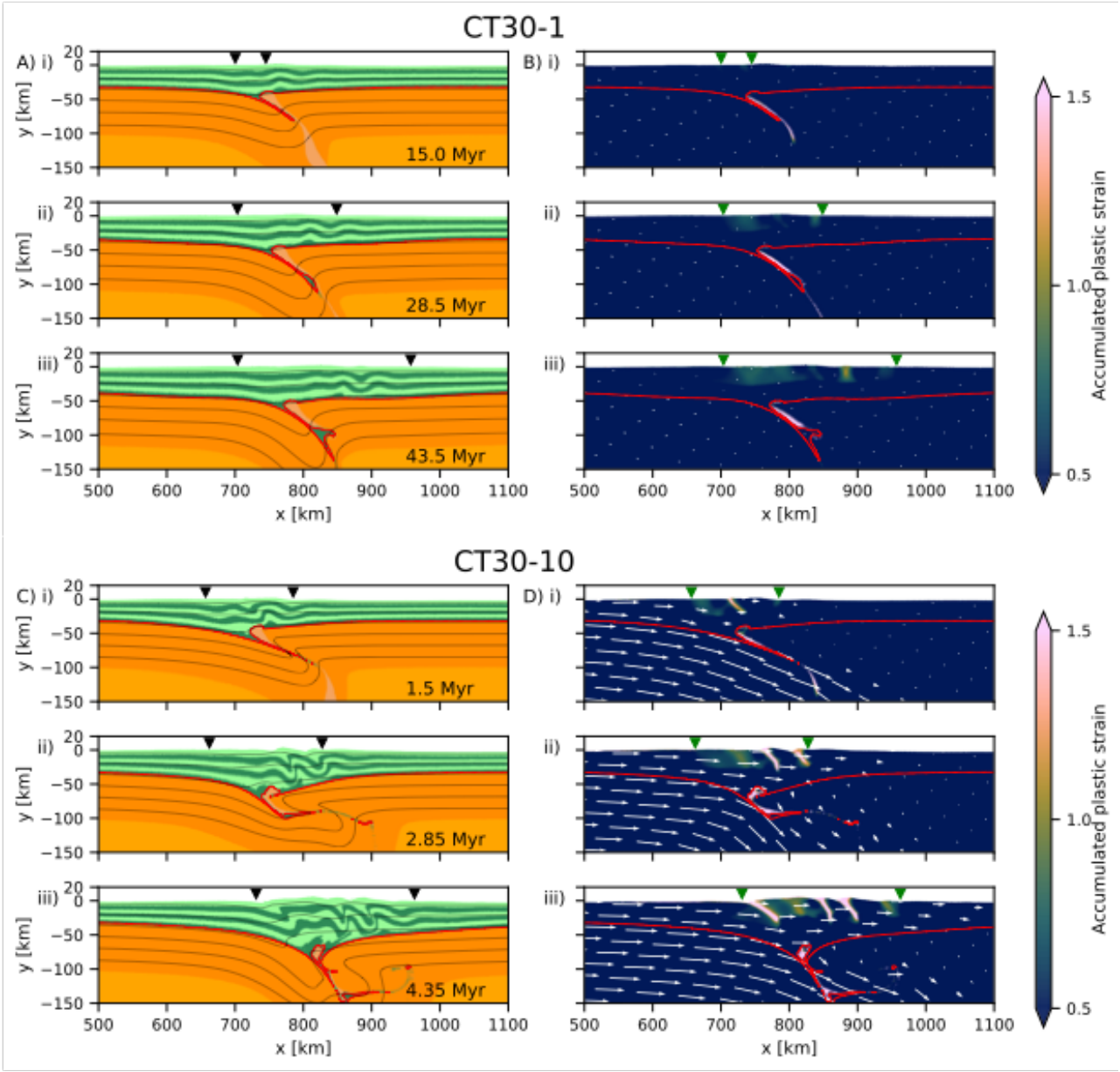

Figure 3.5: Evolution of end member cases in CT30. A) Evolution of the material and B) accumulated plastic strain and velocity vectors at a given time for CT30-1. C) Evolution of the material and D) accumulated plastic strain and velocity vectors at a given time for CT30-10. The inverted triangles at the top of the figures mark the edge of the orogen determined by the point at which strain is 0.5. The red line denotes the base of the crust/Moho.

3.3.3.2. CT30-10: Thick crust-fast convergence

The higher convergence velocity in CT30-10 results in a different internal structure (Figure 3.5C) compared to CT30-1 (Figure 3.5A), with higher amplitude folds occurring within the crust and higher amounts of plastic strain accumulation (Figure 3.5D). The faster convergence leads to higher strain rates, reaching ~10^{-13} s^{-1} along the basal décollement, 10^{-14} s^{-1} along shear zones in the upper crust and ~10^{-15} s^{-1} in the surrounding regions. The

high Moho temperature in CT30 result in viscous deformation dominating along the décollement whilst strain localisation occurs in the plastic upper crust to create shear zones, as seen by plastic strain accumulating above mid-crustal levels (Figure 3.5D). The strain distribution in Figure 3.5D shows both diffuse and localised deformation, with folding and some areas of high amounts of plastic strain. Diffuse strain rates in the upper crust result in large folds forming after ~2.85 Myr, with additional shear zones forming at ~4.35 Myr. Viscous shear at the base of the crust accommodates the wedge migration onto the upper plate at ~4.35 Myr, creating a second shear zone in the upper plate. The crust thickens to ~75 km near the weak zone and attains a length of ~230 km after 435 km of convergence, thicker and narrower than CT30-1, with a similar in geometry to CT25-1. Some underthrusting of the upper plate beneath the orogenic wedge (Figure 3.5C) occurs due to the high velocity, encapsulating some weak zone material within the orogenic wedge.

3.4. Discussion

3.4.1. Orogenic wedge models: from plastic to viscous wedges

To determine the structural style for each model, we used K-mean clustering on the length and change in thickness (Figure 3.6A) after 435 km of convergence. Three distinct clusters can be seen in Figure 3.6A, which are grouped by centroids that are used to cluster data points to define each wedge category. These categories are then used in Figure 3.6B to determine the corresponding $\frac{\lambda_c}{\Delta h}$ for each category: (1) plastic wedges, that are narrow and thick, with a low $\frac{\lambda_c}{\Delta h}$ (<3.3); (2) viscous wedges, that are wide and thin, resulting in a high $\frac{\lambda_c}{\Delta h}$ (>5.5) and (3) visco-plastic wedges, where the wedge has an intermediate $\frac{\lambda_c}{\Delta h}$ between the viscous and plastic wedges (Figure 3.6B). These groups are then used to determine the resulting type of wedge based on the initial crustal thickness and convergence velocity (Figure 3.6C).

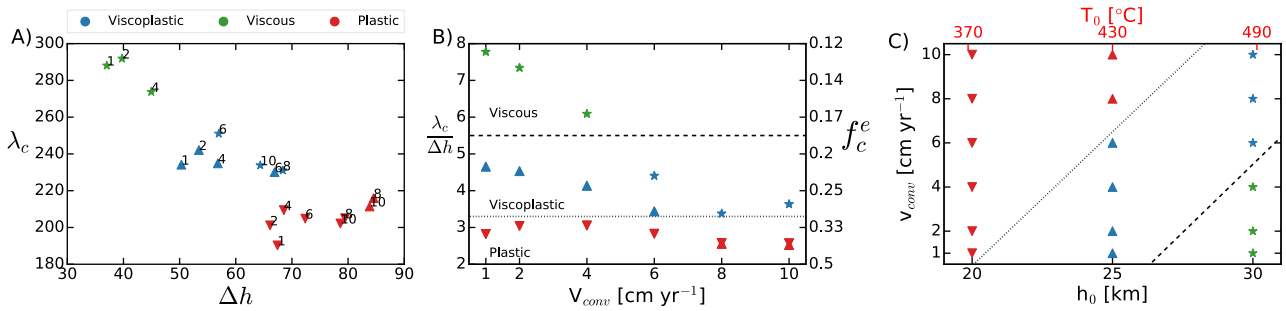

Figure 3.6: A) Wedge length (λ_c) against change in crustal thickness (Δh). Symbols represent the initial crustal thickness (h_0), given in (C) and numbers represent the velocity whilst colour represents the dominant deformation mechanism. At 435km of convergence, the geometry of the wedge defines three groups: viscous, visco-plastic, and plastic. B) $\frac{\lambda_c}{\Delta h}$ and the effective friction coefficient (f_c^e) as a function of convergence velocity (v_{conv}) showing a decrease in $\frac{\lambda_c}{\Delta h}$ corresponds to an increase in f_c^e as velocity increases until the plastic limit is reached at $\sim\frac{1}{f_c}$. *The dotted line represents the estimated plastic lower stress limiter of the crust, where $\frac{\lambda_c}{\Delta h} \sim \frac{1}{f_c}$ = 3.3. C) Wedge characterisation as a function of initial crustal thickness (h_0) or initial Moho temp (T_0) and convergence velocity.*

Plastic wedges show similar structures across a range of velocities as they deform at stresses equal to or exceeding the yield stress (Willett, 1999a). Plastic wedges grow in a cyclical pattern once the initial pop-up structure forms, growing in thickness and then lengthening (Figure 3.7A & Figure 3.7D), similar to analogue experiments into orogenic wedge evolution (Koyi and Vendeville, 2003; Mulugeta and Koyi, 1992). This is a result of plastic deformation being independent of strain rate and instead controlled by the yield stress, which acts as a maximum stress limiter of the visco-plastic crust.

During the formation of plastic wedges, the lithospheric mantle and upper plate are coupled and act as a rigid backstop, remaining relatively undeformed, in agreement with published work (Calignano et al., 2015; Chen et al., 2017b; Faccenda et al., 2008b; Jammes and Huismans, 2012; Piccolo et al., 2017; Vogt et al., 2017c, 2017a; Willingshofer et al., 2013). This results in stresses transmitted vertically in the wedge and concentrates deformation at the front of the wedge (Royden, 1996), where crustal-scale shear zones form which dip towards the core of the orogen. This is observed in all cases in CT20 and CT25 where v_{conv} >6 cm yr^{-1} as these wedges obtain a similar geometry (Figure 3.6A) and structure regardless of crustal thickness or convergence velocity as the entire wedge is deforming in the plastic regime.

The effective friction coefficient (f_c^e) is estimated using eq. 3.18 and presented in Figure 3.6B, with values ranging between 0.3 and 0.4 based on the λ_c and Δh measurements. The value of f_c^e is closer to f_c rather than f_{cw}, highlighting that the f_c for the crust controls the geometry rather than f_{cw}, which only occurs in localised areas of high strain.

The values of f_c^e are slightly larger than the prescribed f_c value of 0.3. This discrepancy is due to over-estimations in crustal thickness that is caused by crustal material coupled to the subducting lithosphere (Figure 3.7). However, values of f_c^e for plastic wedges remains relatively constant when compared to the variations in f_c^e for viscous and visco-plastic wedges (Figure 3.6B). The wedge geometry (Figure 3.6A) and the internal structure for plastic wedges is similar after 435 km of convergence, emphasising that the structural evolution is independent of convergence velocity and crustal thickness, as predicted by eq. 3.14.

In contrast, orogenic wedges that vary in internal structure and geometry in response to variations in convergence velocity and crustal thicknesses is due to the stress at the base of the crust being below the yield stress (Willett, 1999a), deforming viscously, showing velocity dependency in the evolution of the wedge, as predicted by eq. 3.15. Viscous-dominated wedges are wide and thin, with negligible strain localisation in the upper crust and minor crustal thickening. This is due to the decoupling of crust and mantle, resulting in stresses transmitted horizontally and the lateral flow of the crust with minor changes in crustal thickness (Royden, 1996).

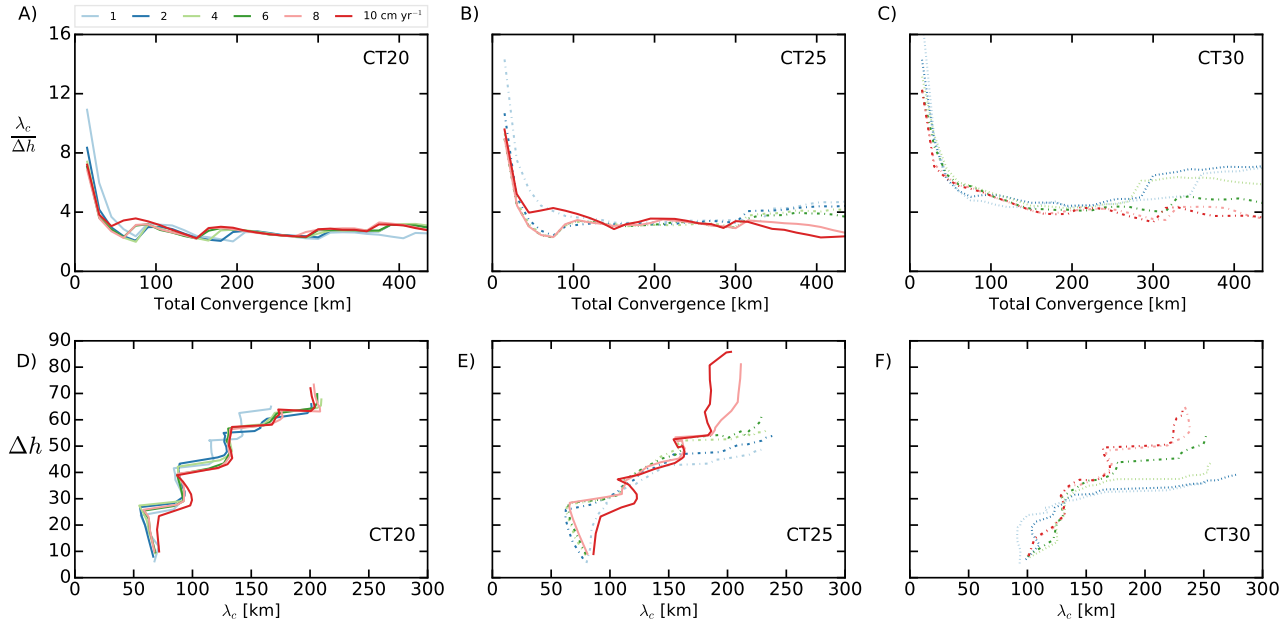

Figure 3.7: Evolution of $\frac{\lambda_c}{\Delta h}$ over the total convergence for A) CT20, B) CT25, C) CT30. Solid lines – plastic wedge, dash dotted lines – visco-plastic wedge, dotted lines – viscous wedge, as outlined in Figure 3.6C. The diagrams show how $\frac{\lambda_c}{\Delta h}$ evolves over time, that changes with convergence velocity. This cyclical change is particularly well-defined in (A) and records a stepwise lengthening of the orogeny followed by slow thickening. The $\frac{\lambda_c}{\Delta h}$ values increase with increasing initial crustal thickness, from (A) to (C). Most cases in (B) and all in (C) record a strong increase of $\frac{\lambda_c}{\Delta h}$ between 250 and 300 km of convergence. At this point the curves diverge, with the slow convergence models rising more significantly. This divergence indicates the increased role of the viscous lower crust causing the widening of the orogen. This change is more marked for (C) than for (B) and absent in (A). Evolution of change in thickness against length of the wedge for D) CT20, E) CT25, F) CT30 displaying the cyclical pattern for plastic wedges and smooth evolution for viscous wedges that reach a critical crustal thickness.

Viscous wedges are observed in CT30 where v_{conv} <6 cm yr^{-1}. As v_{conv} decreases, $\frac{\lambda_c}{\Delta h}$ also decreases due to an increase in length and decrease in change in crustal thickness, as expected from eq. 3.15. Viscous wedges reach a critical thickness at ~300 km of convergence, where a large increase in $\frac{\lambda_c}{\Delta h}$ is observed (Figure 3.7B-C). Before this point, each wedge has a similar evolution as the crust is able to support the growing crustal thickness. At ~300 km of convergence (Figure 3.7E-F) the wedge reaches a critical thickness, with the wedge then lengthening to accommodate convergence. The critical thickness decreases whilst the wedge length increases with decreasing convergence velocity (Figure 3.7E-F) and is due to the overall crustal strength. This is similar to sand-box studies that show a critical thickness can be reached when the basal f_c (and thus strength) is low (Bose et al., 2009), resulting in a relatively stable thickness, with the wedge then

accommodating convergence laterally. f_c^e is calculated at 435 km of convergence (Figure 3.6B), with viscous wedges displaying an f_c^e <0.18, estimated from eq. 3.18.

A similar relationship between $\frac{\lambda_c}{\Delta h}$ and v_{conv} is also observed in visco-plastic wedges (Figure 3.6B-C), demonstrating that the basal décollement rheology controls the evolution, in agreement with the scaling analysis. Visco-plastic wedges have an internal structure that incorporates features of both viscous and plastic wedge, with viscous deformation observed within the lower crust whilst strain localisation is observed in the upper crust. The dual structural style is observed in CT30 where v_{conv} >4 cm yr^{-1} and CT25 where v_{conv} ≤6 cm yr^{-1} (Figure 3.6C). Visco-plastic wedges also reach a critical thickness at ~300 km of convergence, similar to viscous wedges (Figure 3.7B-C & Figure 3.7E-F), as the wedge reaches a critical thickness and lengthens to continue to accommodate convergence. The effective friction coefficient (f_c^e) of the visco-plastic wedge shows a range between 0.18 and 0.3 (Figure 3.6B).

The ratio of vertical stress (σ_g) to the basal stress (σ_b), estimated by $\frac{\lambda_c}{\Delta h}$, is similar to orogenic wedges characterised by Ramberg (Rm) and Argand (Ar) numbers in previously published work (e.g. England and McKenzie, 1982; Medvedev, 2002; Pusok and Kaus, 2015; Ramberg, 1967; Vanderhaeghe et al., 2003; Willett, 1999) and can be compared. These studies have shown a low Rm or Ar represents a strong crust, which results in a narrow and thick wedge geometry that resists lateral flow, similar to the evolution of plastic wedges in our visco-plastic models. Conversely, A high value of Rm or Ar is representative of a weak crust that flows laterally easily in response to applied forces, with no significant increase in crustal thickness (Royden, 1996; Stüwe, 2007), similar to the viscous wedges shown in this study.

The estimation of wedge strength, presented as the effective friction coefficient (f_c^e) (Figure 3.6B), from the model suggests that increasing influence of viscous deformation for a given friction coefficient results in a decrease in the overall crustal strength and the estimated value of f_c^e.

3.4.2. Orogenic wedges in nature

The ongoing deformation in each area of the Alpine-Himalayan orogenic belt is driven by convergence that results in the outward growth of deformation and lengthening of the wedge, as well as a change in thickness between the foreland and the orogenic wedge. The length of each orogen is acquired from previously published work (Zagros - Hatzfeld et al., 2003; McQuarrie et al., 2003; Paul et al., 2006; European Alps - Grad and Tiira, 2009), whilst the change in thickness is obtained from the CRUST1.0 dataset (Laske et al., 2013), with multiple profiles taken across each orogen (Figure 3.8A). Assessing the length (λ_c) and change in thickness (Δh) between the foreland, where thickness is smallest, and the orogen centre, where thickness is greatest, for the each orogen can offer insights into the strength of each orogenic wedge and the dominant deformation mechanism currently operating. In critical taper studies, wedge strength is commonly expressed by the (effective) friction coefficient (f_c^e), which can be determined using eq. 3.18.

In nature, f_c^e has previously been calculated for the entire orogenic wedges (Figure 3.8B) (Dal Zilio et al., 2019; Dielforder, 2017; Dielforder et al., 2020; Hagke et al., 2014; Nankali, 2011; Vernant and Chéry, 2006; Wallis et al., 2015), producing values much lower than the friction coefficient of rocks (~0.6) obtained from laboratory experiments (Byerlee, 1978). Using the scaling analysis, the dominant deformation mechanism currently accommodating convergence can be determined using eq. 3.18. If $f_c^e < f_c$ for the entire

wedge, then, according to our results, there is a viscous component accommodating convergence.

In the Alpine-Himalayan orogenic belt, which stretches from the East Asia to Western Europe, there are three main sections: the Himalayas, Zagros and European Alps. The internal structures are the result of the unique convergent history of each orogenic wedge and the overall wedge strength. Each orogeny was preceded by the closure of the Tethys ocean during the Mesozoic, resulting in the collision of a thinned margin (Zagros - Agard et al., 2011; Mouthereau et al., 2007; European Alps - Butler, 2013; Handy et al., 1999; Mohn et al., 2014; Himalayas - DeCelles et al., 2002). According to our results, the collision of thin crust (CT20) results in the stacking of the entire crust to the Moho. This may explain why similar structures displaying crustal stacking are observed close to the suture zone at the centre of the Zagros, European Alps and Himalayan orogenic wedges, but the subsequent structural style varies significantly between each wedge.

In the Zagros, we use a length of 300 km (Nissen et al., 2011) and a change in thickness of between 12 km and 15 km depending on the profile (Figure 3.8A). This results in f_c^e for the Zagros ranging between ~0.05 and ~0.035 (Figure 3.8B). From our results, a low value of f_c^e suggests a predominantly viscous wedge accommodating convergence. Previous studies on the Zagros wedge suggest a f_c^e <0.05, is required to match GPS slip rates from the model with those observed within the Zagros orogenic wedge when using lithospheric scale numerical models (Nankali, 2011; Vernant and Chéry, 2006). The inclusion of thick sedimentary packages that include low viscosity salt layers reduce the overall wedge strength (Paul et al., 2006), resulting in a low wedge strength. The region also has an average crystalline crustal thickness of ~35 km (Hatzfeld et al., 2003) and ~10 km of sedimentary cover (McQuarrie, 2004; Nissen et al., 2011), producing an average crustal thickness of ~45 km (Paul et al., 2006), with our results suggesting a thicker crust favouring

viscous deformation. This is in agreement with previous studies, which deduced convergence in the Zagros is accommodated primarily by diffuse deformation (Paul et al., 2006) at low velocities (McQuarrie et al., 2003).

Critical taper analysis by Hagke et al. (2014) in the European Alps suggest an f_c^e <0.2 in shale-dominated areas, and f_c^e <0.1 in evaporite-dominated areas, whilst higher values of f_c^e of 0.4 – 0.7 have been proposed for the crystalline units, whilst Dielforder (2017) estimates f_c^e of 0.065 for the entire wedge from critical taper analysis. The data presented in Figure 3.8B, using a length of to 200 km (Rosenberg et al., 2015) and change in thickness of between 20 km and 35 km (Figure 3.8A) suggest f_c^e ranges between 0.1 and 0.175 for the European Alps (Figure 3.8B), in agreement with the range of f_c^e suggested by Hagke et al. (2014). These values of f_c^e suggests both viscous and plastic deformation accommodating convergence in the European Alps.

The Himalayan orogenic wedge length increases from 150 km in the East to 350 km in the West (Roy and Purohit, 2018), whilst the change in thickness varies between 36 and 43 km (Figure 3.8A). This results in an f_c^e of. ~0.2 in the East to ~0.1 in the West (Figure 3.8B). Previous studies into the Himalayan wedge strength suggest an estimated value of f_c^e between 0.07 and 0.25 (Dielforder, 2017; Dielforder et al., 2020; Wallis et al., 2015; Dal Zilio et al., 2019), in agreement with our estimation. Erosion has been previously stated to cause the discrepancy in length and not strain rates, both of which increase eastward (Hirschmiller et al., 2014). However, if some convergence is being accommodated viscously, an increase in strain rates to the East would also cause the wedge length to decrease eastward.

The range of f_c^e for the entire wedge determined from wedge length and change in crustal thickness is within the range of f_c^e presented by other studies that use critical taper

analysis (Figure 3.8B). This advocates the length and change in thickness can be used to approximate the overall wedge strength that produces results that are similar to the critical taper approach.

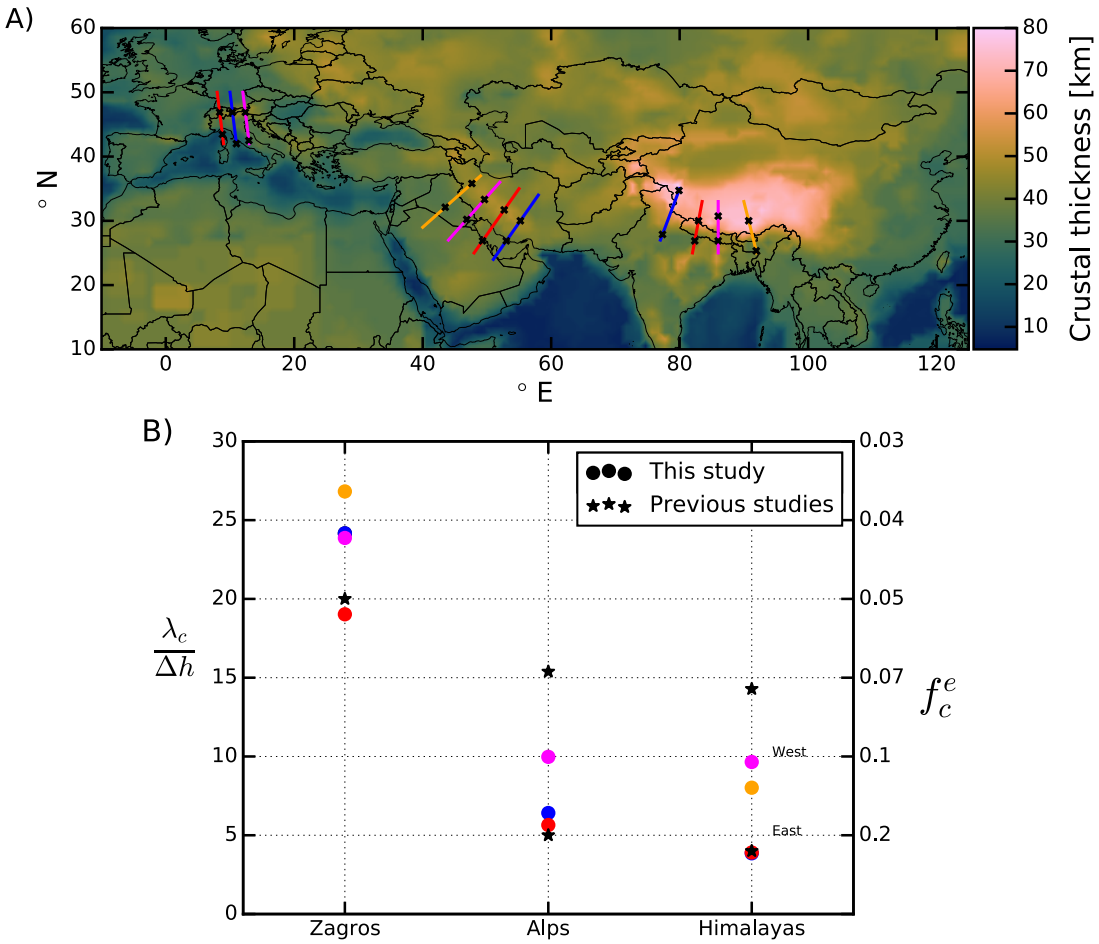

Figure 3.8: A) Crustal thickness map from CRUST1.0 (Laske et al., 2013) used to determine the change in thickness (Δh) along each profile between the foreland and orogenic wedge. X marks the spot where each measurement of crustal thickness is taken. λ_c is obtained from published work on each orogenic wedge (Zagros - Nissen et al. (2011); European Alps - Rosenberg et al. (2015), Himalayas - Roy and Purohit (2018)). B) Ratio of $\frac{\lambda_c}{\Delta h}$ taken from multiple profiles across each orogenic wedge, with marker colour corresponding to the profile colour in (A). Values of f_c^e from published work on orogenic wedge strength for comparison with values determined by eq 18. The estimated values from eq. 3.18 are within the range suggested from previously published work (Zagros - Nankali (2011), Vernant and Chéry (2006); European Alps - Hagke et al. (2014), Dielforder (2017); Himalayas - Dielforder (2017), Dielforder et al. (2020), Wallis et al. (2015), Dal Zilio et al. (2019)).

The values of f_c^e calculated in Figure 3.8 for the Zagros, European Alps and Himalayas are all below the value of f_c equal to 0.6 obtained by Byerlee (1978) and below f_c equal to 0.3 used in the models. According to the results, the discrepancy between f_c^e and f_c for the entire wedge can arise due to the influence of viscous rheology on the overall wedge strength. Increasing influence of viscous rheology, for a constant friction coefficient,

results in a decrease in the overall strength of orogenic wedges and decreases the estimated f_c^e. As the overall wedge strength decreases, the wedge preferentially favours lengthening over thickening to accommodate convergence as the wedge is unable to support a large change in crustal thickness. The minimum value of f_c^e obtained from nature (0.033) is lower than that obtained from the models (0.12). The discrepancy in this value is most likely due to the thickness of crust entering the orogenic wedge and the strength of the crust, with the crustal thickness in the Zagros foreland basin ~45 km (Figure 3.8A; Nissen et al., 2011; Paul et al., 2006) whilst only up to 30 km crustal thickness was tested in the models, whilst the crust in the Zagros also contains very weak salt layers. The thicker crust and low strength salt layers results in an increase in a very weak crust, decreasing f_c^e.

The values of $\frac{\lambda_c}{\Delta h}$ (Figure 3.8B) for the Zagros ranges between ~27 and 19, whilst for the Alps the range is 10 to 6.5 and Himalayas is ~4 in the East to ~9 in the West. This is in agreement with range of values of Ar suggested by England and McKenzie (1982) of between 0 to 30, which encompasses the range of rheological behaviours observed on Earth. However, we advocate a lower limit dictated by the inverse of the friction coefficient (eq. 3.14) whilst the upper limit is determined by the viscous rheology (eq. 3.15). Using f_c ~0.6 (Byerlee, 1978), we propose a range of Ar between 1.67 to 30 encompasses the range of rheological behaviours observed on Earth.

3.4.3. Model Limitations

The evolution of orogenic wedges in nature is inherently three dimensional and incorporates a wide range of complexities that include rheological heterogeneities and structural inheritance, both of which can vary laterally as well as vertically and influence the structural evolution. The structural evolution is also a product of the convergence history, with a convergence velocity that may vary over time, as observed in the Himalayas

(Zahirovic et al., 2012), all of which are not addressed here. However, our model provides insights on how the convergence velocity and crustal thickness influence the structural evolution of orogenic wedges due to the feedback between the convergence velocity, temperature, and viscous rheology.

3.5. Conclusions

We use 2D thermo-mechanical modelling to show how convergence velocity and crustal thickness control the dominant deformation mechanism and influence the structures observed in visco-plastic orogenic wedges. We find the structure of viscous wedges are influenced by the convergence velocity, whilst the structure of plastic wedges is independent of velocity and instead is controlled by the friction coefficient, with transition from plastic to viscous occurring at a threshold velocity for a given initial crustal thickness. As velocity increases, the wedge geometry ($\frac{\lambda_c}{\Delta h}$) decreases due to the viscous rheology until reaching the velocity limit set by the plastic rheology, then remaining constant. According to our models, the length over change in thickness ($\frac{\lambda_c}{\Delta h}$) decreases from >5.5 for viscous wedges to 5.5 – 3.3 for visco-plastic wedges and ~3.3 for plastic wedges when f_c is equal to 0.3.

In nature, the approximation of wedge strength can also be determined using the length and change in thickness of the wedge. The estimated value of f_c^e for the entire wedge for the Zagros, Himalayas and Alps is lower than f_c predicted from laboratory experiments. These values are too low to be explained by purely plastic behaviour and instead suggest these values are best explained by a more relevant role of viscous deformation than previously thought. These findings highlight the important role of viscous deformation on the structural evolution of orogenic wedges.

3.6. Acknowledgements

We acknowledge the provision of resources and services from the National Computational Infrastructure (NCI), which is supported by the Australian Government. This research was also supported by Australian Research Council grant FT170100254 (to FAC). BSK was supported by a Monash University Faculty of Science DIPR scholarship. CRUST1.0 is available from Laske et al. (2013). A setup file for CT25-1 is available online (doi: 10.5281/zenodo.4760310), where the crustal thickness and convergence velocity can be modified to test any of the cases. We thank Jonas Ruh and an anonymous reviewer for in depth reviews and associate editor Luca Dal Zilio for additional comments, all of which improved the quality of the manuscript.

3.7. References

Agard, P., Omrani, J., Jolivet, L., Whitechurch, H., Vrielynck, B., Spakman, W., Monié, P., Meyer, B., Wortel, R., 2011. Zagros orogeny: a subduction-dominated process. Geol. Mag. 148, 692–725. https://doi.org/10.1017/S001675681100046X

Beaumont, C., Ellis, S., Hamilton, J., Fullsack, P., 1996. Mechanical model for subduction-collision tectonics of Alpine-type compressional orogens. Geology 24, 675–678. https://doi.org/10.1130/0091-7613(1996)024<0675:MMFSCT>2.3.CO;2

Beucher, R., Moresi, L., Giordani, J., Mansour, J., Sandiford, D., Farrington, R., Mondy, L., Mallard, C., Rey, P., Duclaux, G., Kaluza, O., Laik, A., Morón, S., 2019. UWGeodynamics: A teaching and research tool for numerical geodynamic modelling. J. Open Source Softw. 4, 1136. https://doi.org/10.21105/joss.01136

Bose, S., Mandal, N., Mukhopadhyay, D.K., Mishra, P., 2009. An unstable kinematic state of the Himalayan tectonic wedge: Evidence from experimental thrust-spacing patterns. J. Struct. Geol. 31, 83–91. https://doi.org/10.1016/j.jsg.2008.10.002

Bott, M.H.P., 1980. Mechanisms of Subsidence at Passive Continental Margins, in: Dynamics of Plate Interiors. American Geophysical Union (AGU), pp. 27–35. https://doi.org/10.1029/GD001p0027

Burov, E.B., 2011. Rheology and strength of the lithosphere. Mar. Pet. Geol. 28, 1402–1443. https://doi.org/10.1016/j.marpetgeo.2011.05.008

Butler, R.W.H., 2013. Area balancing as a test of models for the deep structure of mountain belts, with specific reference to the Alps. J. Struct. Geol. 52, 2–16. https://doi.org/10.1016/j.jsg.2013.03.009

Byerlee, J., 1978. Friction of rocks. Pure Appl. Geophys. 116, 615–626. https://doi.org/10.1007/BF00876528

Calignano, E., Sokoutis, D., Willingshofer, E., Gueydan, F., Cloetingh, S., 2015. Asymmetric vs. symmetric deep lithospheric architecture of intra-plate continental orogens. Earth Planet. Sci. Lett. 424, 38–50. https://doi.org/10.1016/j.epsl.2015.05.022

Capitanio, F.A., Morra, G., Goes, S., Weinberg, R.F., Moresi, L., 2010. India–Asia convergence driven by the subduction of the Greater Indian continent. Nat. Geosci. 3, 136–139. https://doi.org/10.1038/ngeo725

Chen, L., Capitanio, F.A., Liu, L., Gerya, T.V., 2017. Crustal rheology controls on the Tibetan plateau formation during India-Asia convergence. Nat. Commun. 8, 15992. https://doi.org/10.1038/ncomms15992

Crameri, F., Schmeling, H., Golabek, G.J., Duretz, T., Orendt, R., Buiter, S.J.H., May, D.A., Kaus, B.J.P., Gerya, T.V., Tackley, P.J., 2012. A comparison of numerical surface topography calculations in geodynamic modelling: an evaluation of the 'sticky air' method: Modelling topography in geodynamics. Geophys. J. Int. 189, 38–54. https://doi.org/10.1111/j.1365-246X.2012.05388.x

Dahlen, F.A., 1984. Noncohesive critical Coulomb wedges: An exact solution. J. Geophys. Res. Solid Earth 89, 10125–10133. https://doi.org/10.1029/JB089iB12p10125

Dahlen, F.A., 1988. Mechanical energy budget of a fold-and-thrust belt. Nature 331, 335–337. https://doi.org/10.1038/331335a0

Dahlen, F.A., 1990. Critical Taper Model of Fold-And-Thrust Belts and Accretionary Wedges. Annu. Rev. Earth Planet. Sci. 18, 55–99. https://doi.org/10.1146/annurev.ea.18.050190.000415

Dahlen, F.A., Barr, T.D., 1989. Brittle frictional mountain building: 1. Deformation and mechanical energy budget. J. Geophys. Res. Solid Earth 94, 3906–3922. https://doi.org/10.1029/JB094iB04p03906

Dal Zilio, L., Dinther, Y. van, Gerya, T., Avouac, J.-P., 2019. Bimodal seismicity in the Himalaya controlled by fault friction and geometry. Nat. Commun. 10, 48. https://doi.org/10.1038/s41467-018-07874-8

Dannberg, J., Eilon, Z., Faul, U., Gassmöller, R., Moulik, P., Myhill, R., 2017. The importance of grain size to mantle dynamics and seismological observations. Geochem. Geophys. Geosystems 18, 3034–3061. https://doi.org/10.1002/2017GC006944

Davis, D., Suppe, J., Dahlen, F.A., 1983. Mechanics of fold-and-thrust belts and accretionary wedges. J. Geophys. Res. Solid Earth 88, 1153–1172. https://doi.org/10.1029/JB088iB02p01153

DeCelles, P.G., Robinson, D.M., Zandt, G., 2002. Implications of shortening in the Himalayan fold-thrust belt for uplift of the Tibetan Plateau. Tectonics 21, 12-1-12–25. https://doi.org/10.1029/2001TC001322

Dielforder, A., 2017. Constraining the strength of megathrusts from fault geometries and application to the Alpine collision zone. Earth Planet. Sci. Lett. 474, 49–58. https://doi.org/10.1016/j.epsl.2017.06.021

Dielforder, A., Hetzel, R., Oncken, O., 2020. Megathrust shear force controls mountain height at convergent plate margins. Nature 582, 225–229. https://doi.org/10.1038/s41586-020-2340-7

Ellis, M., 1988. Lithospheric Strength in Compression: Initiation of Subduction, Flake Tectonics, Foreland Migration of Thrusting, and an Origin of Displaced Terranes. J. Geol. 96, 91–100.

England, P., McKenzie, D., 1982. A thin viscous sheet model for continental deformation. Geophys. J. Int. 70, 295–321. https://doi.org/10.1111/j.1365-246X.1982.tb04969.x

Faccenda, M., Gerya, T.V., Chakraborty, S., 2008. Styles of post-subduction collisional orogeny: Influence of convergence velocity, crustal rheology and radiogenic heat production. Lithos 103, 257–287. https://doi.org/10.1016/j.lithos.2007.09.009

Gerya, T., 2009. Introduction to Numerical Geodynamic Modelling. Cambridge University Press, Cambridge. https://doi.org/10.1017/CBO9780511809101

Gleason, G.C., Tullis, J., 1995. A flow law for dislocation creep of quartz aggregates determined with the molten salt cell. Tectonophysics, 30 Years of Tectonophysics a Special Volume in Honour of Gerhard Oertel 247, 1–23. https://doi.org/10.1016/0040-1951(95)00011-B

Goes, S., Capitanio, F.A., Morra, G., 2008. Evidence of lower-mantle slab penetration phases in plate motions. Nature 451, 981–984. https://doi.org/10.1038/nature06691

Grad, M., Tiira, T., 2009. The Moho depth map of the European Plate. Geophys. J. Int. 176, 279–292. https://doi.org/10.1111/j.1365-246X.2008.03919.x

Hagke, C. von, Oncken, O., Evseev, S., 2014. Critical taper analysis reveals lithological control of variations in detachment strength: An analysis of the Alpine basal detachment (Swiss Alps). Geochem. Geophys. Geosystems 15, 176–191. https://doi.org/10.1002/2013GC005018

Handy, M.R., Franz, L., Heller, F., Janott, B., Zurbriggen, R., 1999. Multistage accretion and exhumation of the continental crust (Ivrea crustal section, Italy and Switzerland). Tectonics 18, 1154–1177. https://doi.org/10.1029/1999TC900034

Hatzfeld, D., Tatar, M., Priestley, K., Ghafory-Ashtiany, M., 2003. Seismological constraints on the crustal structure beneath the Zagros Mountain belt (Iran). Geophys. J. Int. 155, 403–410. https://doi.org/10.1046/j.1365-246X.2003.02045.x

Hirschmiller, J., Grujic, D., Bookhagen, B., Coutand, I., Huyghe, P., Mugnier, J.L., Ojha, T., 2014. What controls the growth of the Himalayan foreland fold-and-thrust belt? Geology 42, 247–250. https://doi.org/10.1130/g35057.1

Hirth, G., Kohlstedt, D., 2003. Rheology of the upper mantle and the mantle wedge: A view from the experimentalists, in: Eiler, J. (Ed.), Geophysical Monograph Series. American Geophysical Union, Washington, D. C., pp. 83–105. https://doi.org/10.1029/138GM06

Jammes, S., Huismans, R.S., 2012. Structural styles of mountain building: Controls of lithospheric rheologic stratification and extensional inheritance. J. Geophys. Res. Solid Earth 117. https://doi.org/10.1029/2012JB009376

Kaus, B.J.P., Steedman, C., Becker, T.W., 2008. From passive continental margin to mountain belt: Insights from analytical and numerical models and application to Taiwan. Phys. Earth Planet. Inter., Recent Advances in Computational Geodynamics: Theory, Numerics and Applications 171, 235–251. https://doi.org/10.1016/j.pepi.2008.06.015

Koyi, H.A., Vendeville, B.C., 2003. The effect of décollement dip on geometry and kinematics of model accretionary wedges. J. Struct. Geol. 25, 1445–1450. https://doi.org/10.1016/S0191-8141(02)00202-X

Laske, G., Masters, G., Ma, Z., Pasyanos, M., 2013. Update on CRUST1.0 - A 1-degree Global Model of Earth's Crust. Presented at the EGU General Assembly Conference Abstracts, pp. EGU2013-2658.

McQuarrie, N., 2004. Crustal scale geometry of the Zagros fold–thrust belt, Iran. J. Struct. Geol. 26, 519–535. https://doi.org/10.1016/j.jsg.2003.08.009

McQuarrie, N., Stock, J.M., Verdel, C., Wernicke, B.P., 2003. Cenozoic evolution of Neotethys and implications for the causes of plate motions. Geophys. Res. Lett. 30. https://doi.org/10.1029/2003GL017992

Medvedev, S., 2002. Mechanics of viscous wedges: Modeling by analytical and numerical approaches. J. Geophys. Res. Solid Earth 107, ETG 9-1. https://doi.org/10.1029/2001JB000145

Mohn, G., Manatschal, G., Beltrando, M., Haupert, I., 2014. The role of rift-inherited hyper-extension in Alpine-type orogens. Terra Nova 26, 347–353. https://doi.org/10.1111/ter.12104

Moresi, L., Dufour, F., Mühlhaus, H.-B., 2003. A Lagrangian integration point finite element method for large deformation modeling of viscoelastic geomaterials. J. Comput. Phys. 184, 476–497. https://doi.org/10.1016/S0021-9991(02)00031-1

Moresi, L., Quenette, S., Lemiale, V., Mériaux, C., Appelbe, B., Mühlhaus, H.-B., 2007. Computational approaches to studying non-linear dynamics of the crust and mantle. Phys. Earth Planet. Inter. 163, 69–82. https://doi.org/10.1016/j.pepi.2007.06.009

Mouthereau, F., Tensi, J., Bellahsen, N., Lacombe, O., Boisgrollier, T.D., Kargar, S., 2007. Tertiary sequence of deformation in a thin-skinned/thick-skinned collision belt: The Zagros Folded Belt (Fars, Iran). Tectonics 26. https://doi.org/10.1029/2007TC002098

Mulugeta, G., Koyi, H., 1992. Episodic accretion and strain partitioning in a model sand wedge. Tectonophysics 202, 319–333. https://doi.org/10.1016/0040-1951(92)90117-O

Nankali, H.R., 2011. Slip rate of the Kazerun Fault and Main Recent Fault (Zagros, Iran) from 3D mechanical modeling. J. Asian Earth Sci. 41, 89–98. https://doi.org/10.1016/j.jseaes.2010.12.009

Nissen, E., Tatar, M., Jackson, J.A., Allen, M.B., 2011. New views on earthquake faulting in the Zagros fold-and-thrust belt of Iran. Geophys. J. Int. 186, 928–944. https://doi.org/10.1111/j.1365-246X.2011.05119.x

Paul, A., Kaviani, A., Hatzfeld, D., Vergne, J., Mokhtari, M., 2006. Seismological evidence for crustal-scale thrusting in the Zagros mountain belt (Iran). Geophys. J. Int. 166, 227–237. https://doi.org/10.1111/j.1365-246X.2006.02920.x

Pfiffner, O.A., 2017. Thick-Skinned and Thin-Skinned Tectonics: A Global Perspective. Geosciences 7, 71. https://doi.org/10.3390/geosciences7030071

Piccolo, A., Faccenda, M., Carosi, R., Montomoli, C., Visonà, D., 2017. Crustal strength control on structures and metamorphism in collisional orogens. Tectonophysics. https://doi.org/10.1016/j.tecto.2017.09.018

Platt, J.P., 1986. Dynamics of orogenic wedges and the uplift of high-pressure metamorphic rocks. Geol. Soc. Am. Bull. 97, 1037. https://doi.org/10.1130/0016-7606(1986)97<1037:DOOWAT>2.0.CO;2

Poblet, J., Lisle, R.J., 2011. Kinematic evolution and structural styles of fold-and-thrust belts. Geol. Soc. Lond. Spec. Publ. 349, 1–24. https://doi.org/10.1144/SP349.1

Pusok, A.E., Kaus, B.J.P., 2015. Development of topography in 3-D continental-collision models. Geochem. Geophys. Geosystems 16, 1378–1400. https://doi.org/10.1002/2015GC005732

Ramberg, H., 1967. Model Experimentation of the Effect of Gravity on Tectonic Processes. Geophys. J. R. Astron. Soc. 14, 307–329. https://doi.org/10.1111/j.1365-246X.1967.tb06247.x

Ranalli, G., 1982. Deformation maps in grain-size-stress space as a tool to investigate mantle rheology. Phys. Earth Planet. Inter. 29, 42–50.

Ranalli, G., Adams, M., 2013. Rheological contrast at the continental Moho: Effects of composition, temperature, deformation mechanism, and tectonic regime. Tectonophysics, Moho: 100 years after Andrija Mohorovicic 609, 480–490. https://doi.org/10.1016/j.tecto.2012.10.037

Rosenberg, C.L., Berger, A., Bellahsen, N., Bousquet, R., 2015. Relating orogen width to shortening, erosion, and exhumation during Alpine collision. Tectonics 34, 1306–1328. https://doi.org/10.1002/2014TC003736

Roy, A.B., Purohit, R., 2018. Chapter 17 - The Himalayas: Evolution Through Collision, in: Roy, A.B., Purohit, R. (Eds.), Indian Shield. Elsevier, pp. 311–327. https://doi.org/10.1016/B978-0-12-809839-4.00018-7

Royden, L., 1996. Coupling and decoupling of crust and mantle in convergent orogens: Implications for strain partitioning in the crust. J. Geophys. Res. Solid Earth 101, 17679–17705. https://doi.org/10.1029/96JB00951

Ruh, J.B., Kaus, B.J.P., Burg, J.-P., 2012. Numerical investigation of deformation mechanics in fold-and-thrust belts: Influence of rheology of single and multiple décollements. Tectonics 31. https://doi.org/10.1029/2011TC003047

Schmeling, H., Babeyko, A.Y., Enns, A., Faccenna, C., Funiciello, F., Gerya, T., Golabek, G.J., Grigull, S., Kaus, B.J.P., Morra, G., Schmalholz, S.M., van Hunen, J., 2008. A benchmark comparison of spontaneous subduction models—Towards a free surface. Phys. Earth Planet. Inter., Recent Advances in Computational Geodynamics: Theory, Numerics and Applications 171, 198–223. https://doi.org/10.1016/j.pepi.2008.06.028

Searle, M.P., 2015. Mountain Building, Tectonic Evolution, Rheology, and Crustal Flow in the Himalaya, Karakoram, and Tibet, in: Treatise on Geophysics. Elsevier, pp. 469–511. https://doi.org/10.1016/B978-0-444-53802-4.00121-4

Spiegelman, M., May, D.A., Wilson, C.R., 2016. On the solvability of incompressible Stokes with viscoplastic rheologies in geodynamics. Geochem. Geophys. Geosystems 17, 2213–2238. https://doi.org/10.1002/2015GC006228

Stüwe, K., 2007. Geodynamics of the lithosphere: an introduction, 2nd ed. ed. Springer, Berlin ; New York.

Vanderhaeghe, O., 2012. The thermal–mechanical evolution of crustal orogenic belts at convergent plate boundaries: A reappraisal of the orogenic cycle. J. Geodyn., Geodynamics and Orogenesis 56–57, 124–145. https://doi.org/10.1016/j.jog.2011.10.004

Vanderhaeghe, O., Medvedev, S., Fullsack, P., Beaumont, C., Jamieson, R.A., 2003. Evolution of orogenic wedges and continental plateaux: insights from crustal thermal-mechanical models overlying subducting mantle lithosphere. Geophys. J. Int. 153, 27–51. https://doi.org/10.1046/j.1365-246X.2003.01861.x

Vernant, P., Chéry, J., 2006. Mechanical modelling of oblique convergence in the Zagros, Iran. Geophys. J. Int. 165, 991–1002. https://doi.org/10.1111/j.1365-246X.2006.02900.x

Vogt, K., Matenco, L., Cloetingh, S., 2017a. Crustal mechanics control the geometry of mountain belts. Insights from numerical modelling. Earth Planet. Sci. Lett. 460, 12–21. https://doi.org/10.1016/j.epsl.2016.11.016

Vogt, K., Willingshofer, E., Matenco, L., Sokoutis, D., Gerya, T., Cloetingh, S., 2017b. The role of lateral strength contrasts in orogenesis: A 2D numerical study. Tectonophysics. https://doi.org/10.1016/j.tecto.2017.08.010

Wallis, D., Lloyd, G.E., Phillips, R.J., Parsons, A.J., Walshaw, R.D., 2015. Low effective fault strength due to frictional-viscous flow in phyllonites, Karakoram Fault Zone, NW India. J. Struct. Geol. 77, 45–61. https://doi.org/10.1016/j.jsg.2015.05.010

Willett, S.D., 1999. Rheological dependence of extension in wedge models of convergent orogens. Tectonophysics 305, 419–435. https://doi.org/10.1016/S0040-1951(99)00034-7

Willingshofer, E., Sokoutis, D., Luth, S.W., Beekman, F., Cloetingh, S., 2013. Subduction and deformation of the continental lithosphere in response to plate and crust-mantle coupling. Geology 41, 1239–1242. https://doi.org/10.1130/G34815.1

Zahirovic, S., Müller, R.D., Seton, M., Flament, N., 2015. Tectonic speed limits from plate kinematic reconstructions. Earth Planet. Sci. Lett. 418, 40–52. https://doi.org/10.1016/j.epsl.2015.02.037

Zahirovic, S., Müller, R.D., Seton, M., Flament, N., Gurnis, M., Whittaker, J., 2012. Insights on the kinematics of the India-Eurasia collision from global geodynamic models. Geochem. Geophys. Geosystems 13. https://doi.org/10.1029/2011GC003883

Chapter 4

Time dependent processes on the structural evolution of orogenic wedges

Authors: Ben S. Knight, Fabio A. Capitanio, Roberto F. Weinberg

Affiliation:

School of Earth, Atmosphere & Environment, Monash University, Clayton, 3800

Abstract

The collision of continental crust over geological timescales results in the formation of mountains. Processes operating during orogenesis, such as internal heating or erosion and sedimentation, are usually incorporated into numerical models to replicate these processes operating in nature. However, these processes are typically incorporated as a constant rate, increasing their influence as the time increases. In this study, 2D numerical models are used to show that the structure of the orogen can vary significantly between models with and without erosion and sedimentation or internal heating. Erosion and sedimentation restrict wedge growth and can result in exhumation along a single back thrust if the erosion rate is high enough. Internal heating alters the temperature of the crust, resulting in increasingly viscous structures forming as convergence is ongoing. These processes can obscure insights into other mechanisms operating during orogenesis when included. These results demonstrate that these processes should be carefully considered when modelling any tectonic setting.

4.1. Introduction

Orogenesis is the process in which mountains form due to the convergence of buoyant continental crust over time. The internal structure is a product of the convergence history, thermal and compositional structure of the crust and surface processes opperating during orogenesis.

Surface processes are time-dependent and are usually included in geodynamic models as either a diffusive surface or as an erosion and sedimentation rate (Gerya, 2009). Surface processes erode topography from elevated regions, reducing the gravitational load acting on the wedge, and deposit sediments in peripheral basins. Previous numerical models have shown surface processes promotes prolonged fault activity and strain localisation, restricting outward propagation and concentrate deformation close to the centre of the orogenic wedge (Avouac and Burov, 1996; Dal Zilio et al., 2020; Ellis et al., 2001; Jammes and Huismans, 2012; Jaquet et al., 2017; Piccolo et al., 2017; Selzer et al., 2008) which also promotes exhumation (Dal Zilio et al., 2020; Jammes and Huismans, 2012; Kaus et al., 2008) which may occur along a single back-thrust in extreme cases (Beaumont et al., 1996; Willett, 1999a).

Internal heating is included in geodynamic models as a heating rate, influencing the structural evolution of an orogenic wedge by increasing the temperature of the crust over time. Numerical models have shown that increasing the internal heating rate of sediment increases melt production and reduces the strength of the crust (Faccenda et al., 2008; Piccolo et al., 2017). This is due to the increase in temperature reducing the effective viscosity of the crust (Faccenda et al., 2009; Vanderhaeghe et al., 2003) due to the temperature dependency of the viscous rheology.

Surface processes and internal heating are usually included in models that investigate various tectonic settings, but the influence of each process has not been investigated with respect to the model duration. In this study, we use a 2D numerical model to assess the influence of internal heating and surface processes on the structural evolution of orogenic wedges over time. We run models with different convergence velocities for the same amount of convergence to determine how the strain rate and temperature-dependent viscous rheology and time-dependent processes (internal heating and surface processes) influence the internal structure and topography. To assess the influence of internal heating and surface processes on the structural evolution of the orogen, we compare models that include these processes with models that do not.

We find that the inclusion of internal heating increases the temperature of the wedge, decreasing the depth of the brittle-ductile transition, resulting in a decrease in plastic strain localisation in the upper crust whilst increasing the amount of viscous deformation occurring within the wedge. When internal heating is high, it alters the structural style to create a hot, viscous orogen. Surface processes have a minor influence on the internal structure when the rate of erosion is low, with similar structures observed with and without surface processes. However, when material is eroded quickly, a change in structural style does occur, with deformation concentrated along a single back thrust that exhumes material from deep within the crust. As the duration of the model increases, the influence of both internal heating and surface processes increases as both are incorporated as a constant rate. The value at which the structural style of the orogen changes for both surface processes and internal heating is determined by the convergence velocity.

4.2. Methods

4.2.1. Governing equations

The conservation of mass, momentum and energy equations are solved for an incompressible, visco-plastic fluid in a 2D Cartesian box using the finite element, particle-in-cell (PIC) code Underworld2 (Beucher et al., 2019; Moresi et al., 2007, 2003). Underworld allows the tracking of distinct materials and their properties through Lagrangian particles within a Eulerian finite element grid (PIC method).

The conservation of mass, momentum and energy are solved using the extended Boussinesq approximation of an incompressible Stokes flow in a two-dimensional Cartesian geometry (Moresi et al., 2007, 2003), as the internal heating term is included in the conservation of energy equation (H_r):

$$\frac{\partial v_i}{\partial x_i} = 0 \tag{4.1}$$

$$\frac{\partial \tau_{ij}}{\partial x_j} - \frac{\partial P}{\partial x_i} + \rho g_i = 0 \tag{4.2}$$

$$\frac{\partial T}{\partial t} - \frac{\partial}{\partial x_i} \kappa \left(\frac{\partial T}{\partial x_i} \right) + v_i \frac{\partial T}{\partial x_i} - H_r = 0 \tag{4.3}$$

where x_i represents the coordinate system, τ_{ij} is the stress tensor, *P* the pressure, v_i is the velocity, T is the temperature, ρ is the density, g is gravity, t represents time and κ is the thermal diffusivity.

To investigate the role of internal heating, a homogenous internal heating rate (H_r) of either 0 μW m^{-3}, 1.8 μW m^{-3} or 3.6 μW m^{-3} is applied to the crust. Minimum rates of internal heating are estimated from concentrations of heat producing elements within the crust, with

the values used in this study comparable to current internal heating rates observed at various tectonic settings (Jaupart et al., 2016; Kumar et al., 2009; Mareschal and Jaupart, 2013).

4.2.2. Rheology

The viscous deformation and ductile flow of rocks is dependent on the temperature, pressure, and strain rate power-law constitutive equation. Dislocation and diffusion creep are determined in the model through a general relationship between stress and strain rate for each mechanism:

$$\eta_{diff,disl} = \frac{1}{2} A^{-\frac{1}{n}} \dot{\varepsilon}_{II}^{\frac{1-n}{n}} exp\left(\frac{E + PV}{nRT_r}\right) \quad (4.4)$$

where η is the viscosity, A is the pre-exponential factor, n is the stress exponent, E is the activation energy, P is the lithostatic pressure, V the activation volume, R the gas constant, T_r is the temperature at a given position and $\dot{\varepsilon}_{II} = (\frac{1}{2}\dot{\varepsilon}_{ij}\dot{\varepsilon}_{ij})^{0.5}$ is the square root of the second invariant of the strain rate tensor $\dot{\varepsilon}_{ij}$ at a given position. The value for each parameter is presented in Table 3.1.

Plasticity is also included through a Drucker-Prager yield criterion (Spiegelman et al., 2016), which is used to limit the maximum stresses in the crust and lithospheric mantle that results in an effective viscosity for the plastic flow (η_p):

$$\tau_y = C \cos\varphi + P \sin\varphi \quad (4.5.1)$$

$$\eta_p = \frac{\tau_y}{2\dot{\varepsilon}_{II}} \quad (4.5.2)$$

where τ_y is the yield stress, C is the cohesion at the surface, φ is the internal friction angle, $\sin\varphi$ is the friction coefficient (f_c) and *P* is the lithostatic pressure.

Plastic strain-weakening of the crust is implemented through a function of accumulated plastic strain (ε) within the material, where the cohesive (C) and the internal friction angle (φ) are reduced linearly (C_w, φ_w) with accumulated plastic strain between 0.5 (ε_{min}) and 1.5 (ε_{max}) before reaching the weakened value when $\varepsilon \geq \varepsilon_{max}$, as outlined in Chapter 2.

Table 4.1: Initial material properties used for the visco-plastic rheology. ρ is density at the surface. A is the pre-exponential factor, n, is the stress exponent, E is the activation energy, f_c is the friction coefficient, C is the cohesion at the surface and α is the coefficient of thermal expansion.

	Crust	***Sediment****	***Mantle***		***Weak Zone***	
Rheology	Quartzite[a]	Quartzite[a]	Olivine[b]		Wet Olivine [b]	
Deformation Mechanism	Dislocation	Dislocation	Dislocation	Diffusion	Dislocation	Diffusion
A (MPa^{-n} s^{-1})	1.1×10^{-34}	1.1×10^{-34}	1.1×10^{5}	1.5×10^{9}	1.6×10^{3}	2.5×10^{7}
n	4.0	4.0	3.5	1.0	3.5	1.0
E ($J\ mol^{-1}$)	2.23×10^{5}	2.23×10^{5}	5.30×10^{5}	3.75×10^{5}	5.20×10^{5}	3.75×10^{5}
V ($m^3\ mol^{-1}$)	0	0	6.0×10^{-6}	6.0×10^{-6}	2.3×10^{-5}	1.0×10^{-5}
C, C_w (MPa)	10, 1	10, 1	10		10, 1	
f_c, $f_{c,w}$	0.3, 0.15	0.3, 0.15	0.6		0.1, 0.05	
φ, φ_w (°)	17.5, 8.63	17.5, 8.63	36.9		5.74, 2.87	
ρ_0 ($kg\ m^{-3}$)	2700	1700	3300		3300	
H_r ($\mu W\ m^{-3}$)	0, 1.8, 3.6	0	0, 0.022		0, 0.022	

[a](Gleason and Tullis, 1995) [b](Hirth and Kohlstedt, 2003)

4.2.3. Surface processes

To investigate the role of surface processes during orogenesis, a linear hillslope diffusive (D) surface is used. The 2D evolution of the topography (h) is modelled assuming

the short-range transport of material as a linear flux (q_s) which is proportional to the surface slope ($\frac{dh}{dx}$) (Avouac, 1993; Culling, 1960):

$$q_s = -D\frac{dh}{dx} \tag{4.6}$$

The diffusion constant (D), expressed as a unit area over unit time ($m^2\ yr^{-1}$), determines the amount of erosion and sedimentation taking place at the surface. In 2D, the surface is represented as a line (1D), which reduces the change in surface height over time ($\frac{dh}{dt}$) to:

$$\frac{dh}{dt} = \frac{dq_s}{dx} \tag{4.7}$$

The surface timesteps are smaller than the model CFL condition to allow accurate tracking of the surface. The surface timestep (dt) is determined using one-fifth of the CFL condition and is determined by the value of D. When *D* is equal to 300 $m^2\ yr^{-1}$ and *dx* is equal to 1 km the timesteps are 666.66 years, and when *D* is equal to 3000 $m^2\ yr^{-1}$ timesteps are 66.666 years.

Erosion and sedimentation are implemented through the material particles in the model. As the surface diffuses, new material is embedded beneath the diffused surface as sediment that was previously sticky air, while crust or sediment above the diffused surface is removed and re-assigned as sticky air. We test different values of hillslope diffusion, ranging from D = 0 $m^2\ yr^{-1}$ to D = 3000 $m^2\ yr^{-1}$. The upper limit of 3000 $m^2\ yr^{-1}$ is comparable to the current erosion rates in the Himalayas (Avouac and Burov, 1996; Toussaint et al., 2004), which produces an erosion rate in the order of ~1 mm yr^{-1} for a 400 km wide orogenic wedge with a topography that reaches >1 km in relief (Avouac and Burov, 1996; Burov and Toussaint, 2007).

A linear diffusive surface approach does not accurately represent material transport in orogenic wedges due to neglecting the non-linear influence of hillslope and stream processes that re-distribute material during orogenesis (Avouac and Burov, 1996). However, a linear diffusive surface does produce a volume of sediment that is proportional to the amount eroded. Therefore, the linear diffusion equation enforces the conservation of volume, balancing the deposited sediment and eroded material. The density of the sediments differs from the crustal material, implying that mass and momentum are not strictly conserved and thicknesses are underestimated. This simplification is justified by the focus on the dynamics of the wedge, rather than on realistic surface processes and sedimentary thicknesses.

4.2.4. Model setup

The model is designed to simulate continental collision (Figure 4.1A), where an orogenic wedge forms above a heterogeneity in the mantle lithosphere. The model domain is two-dimensional, with a length (x) of 1200 km and depth (y) of 300 km. The grid is uniformly spaced with 512 x 128 nodal points, producing a resolution of 2.34 km, with each cell in the grid populated with 30 particles. Timesteps are determined by using (half of) the Courant–Friedrichs–Lewy (CFL) condition. A cell width of 2.34 km results in timesteps of ~117,000 years for a convergence velocity of 1 cm yr^{-1} and 11,700 years at a convergence velocity of 10 cm yr^{-1}.

The initial configuration includes a homogenous crust with a 45° dipping weak zone within the mantle lithosphere at x = 700 km, representing a pre-existing suture zone (Figure 4.1A). The weak zone has a wet olivine rheology and low friction coefficient (0.1) whilst the surrounding lithospheric mantle has a dry olivine rheology and high friction coefficient (0.6).

The weak zone introduces a rheological heterogeneity that facilitates lithospheric subduction and localises deformation in the crust above the weak zone.

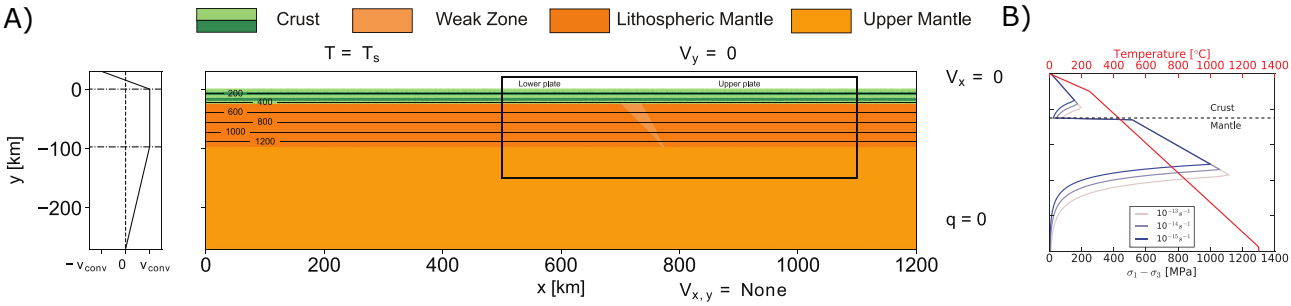

Figure 4.1: A) Initial model setup, with an initial crustal thickness of 25 km. Temperature contours are given at 200°C intervals. The black box (x > 500 km and x < 1100 km, y < 20km and y > -150 km) portrays the area shown in subsequent figures that display model evolution. B) Strength profile for varying strain rates and the initial temperature distribution across the crust and mantle.

To allow the evolution of topography, a 30 km 'sticky air' layer is included with a low viscosity (10^{19} Pa s) and density (1 kg m^{-3}) which minimizes shear stresses at the surface, creating a pseudo free surface (Crameri et al., 2012; Schmeling et al., 2008; Vogt et al., 2017). A quartzite rheology is applied to the crust (Table 4.1), with a single crustal layer used to minimise effects that may arise due to multiple rheological layers.

A constant temperature (T = 0 °C) is applied to the top boundary, with no heat flux across the side walls. The initial internal temperature distribution follows a geothermal gradient of 25 °C km^{-1} for the first 10 km and then 12 °C km^{-1} until a temperature of 1300 °C is reached at the lithosphere-asthenosphere boundary (LAB) at a depth of 97.5 km. We neglect adiabatic gradients and keep the underlying mantle at 1300 ˚C. The geotherm is constant across all models, with alterations in the temperature of the crust due to advection, diffusion, and internal heating.

The model uses a free-slip condition on the right (v_x = 0) and top (v_y = 0) boundaries. The velocity is unconstrained at the base, allowing for inflow and outflow of material, implying the model overlies an infinite space with an inviscid fluid (Gerya, 2009) at a depth of 270 km. The velocity condition is applied on the left wall, with a convergence velocity

(v_{conv}) of either 1 or 10 cm yr^{-1}. The velocity condition is applied across the crust and mantle lithosphere, which induces convergence. Below the lithosphere (y < - 97.5 km) the velocity linearly decreases from the convergence velocity at base of the lithosphere to zero at the bottom of the left wall. Above the crust, an inflow/outflow is prescribed across the sticky air layer (y > 0 km) to allow topography to develop (Figure 4.1A, left panel).

Table 4.2: Case names with the parameters modified for each model. 1 Watt (W) is equal to 1 kg m^2 s^{-3}.

Case Name	*Convergence velocity (v_{conv}) [cm yr^{-1}]*	*Crust internal heating rate (H_r) [μW m^{-3}]*	*Surface diffusion rate (D) [m^2 yr^{-1}]*
CT25-1	1	0	0
CT25-1-1.8H_r	1	1.8	0
CT25-1-3.6H_r	1	3.6	0
CT25-1-D300	1	0	300
CT25-1-D3000	1	0	3000
CT25-10	10	0	0
CT25-10-1.8H_r	10	1.8	0
CT25-10-3.6H_r	10	3.6	0
CT25-10-D300	10	0	300
CT25-10-D3000	10	0	3000

4.3. Results

In this section, the role of internal heating is first presented, outlining the model with no internal heating (H_r = 0 μW m^{-3}), low internal heating (H_r = 1.8 μW m^{-3}) and high internal heating (H_r = 3.6 μW m^{-3}) rates. The final structure and topography of each model is

presented in Figure 4.2 and plastic strain distribution, highlighting shear zones, presented in Figure 4.3. This is repeated for the diffusive surface, where no surface diffusivity (D = 0 m^2 yr^{-1}), low surface diffusivity (D = 300 m^2 yr^{-1}) and high surface diffusivity (D = 3000 m^2 yr^{-1}) rates are investigated. The final structure and topography are presented in Figure 4.4 and plastic strain distribution, highlighting shear zones, presented in Figure 4.5. Each model is run at a slow (1 cm yr^{-1}) or fast (10 cm yr^{-1}) convergence velocity to assess the role of each time-dependent process.

4.3.1. Role of internal heating

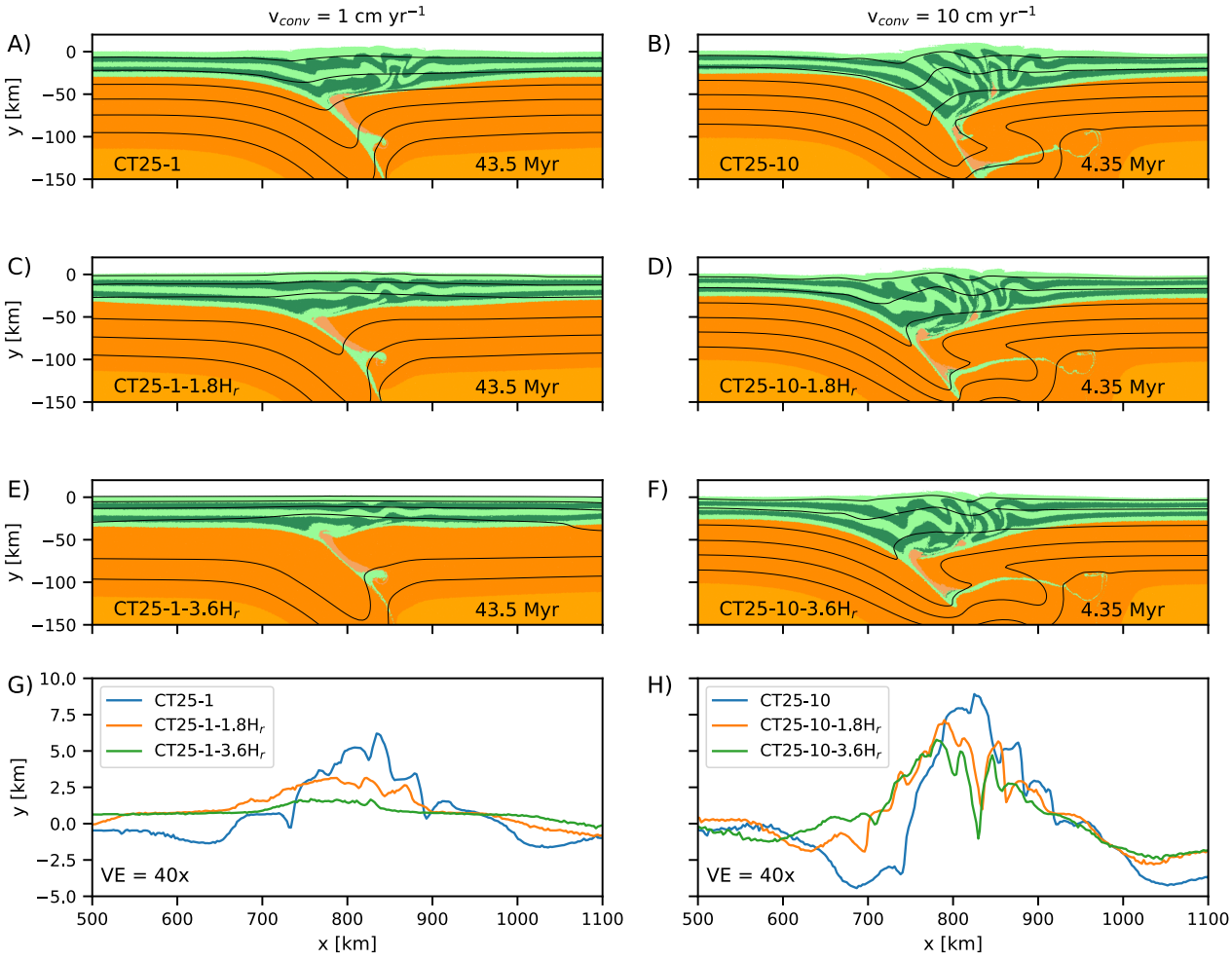

Figure 4.2: Comparison of structure from the material, between no internal heating and an internal heating rate for different convergence velocities after 435 km of convergence. A) CT25-1, B) CT25-10, C) CT25-1-1.8H_r, D) CT25-10-1.8H_r. E) CT25-1-3.6H_r, F) CT25-10-3.6H_r, G) Topography for A), C) and E). H) Topography for B) and D) and F). The topography shows how the elevation decreases due to the influence of internal heating, with the influence stronger in CT25-1-IH compared to CT25-10-IH due to the time dependency. VE = 40 x is the vertical exaggeration.

CT25-1 (Figure 4.2A) has no internal heating and displays some minor crustal stacking in the upper crust, with ductile flow occurring in the lower crust. In CT25-10, crustal stacking also occurs but incorporates most of the crust, with shear zones that extend to near the Moho. Deformation in models without internal heating propagates outward from the centre and do not exhibit exhumation of crust from within the wedge. From these models, an increase in convergence velocity results in an increase in topography (Figure 4.2G-H) and crustal thickness, decrease the wedge length whilst also increasing the amount of crustal stacking. The distribution of plastic strain suggests that the depth of the brittle-ductile transition, highlighted by the depth at which strain accumulation stops, increases with increasing velocity (Figure 4.3A & 4.3B).

Including a low internal heating rate (H_r =1.8 μW m^{-3}) in the low velocity model (CT25-1-1.8H_R; Figure 4.2C) reduces the amount of strain localisation in the upper crust and the depth strain accumulates (Figure 4.3C), whilst also reducing the amount of crustal thickening. A lack of strain localisation is also observed in CT25-1-3.6H_R (Figure 4.3E) with the high internal heating rate results in a much higher geotherm, as seen by the isotherms in Figure 4.2E. In both slow convergence velocity models with internal heating, convergence is primarily accommodated through viscous flow with the wedge which grows laterally.

When a low internal heating rate (H_r =1.8 μW m^{-3}) is applied to the fast velocity model, CT25-10-1.8H_R (Figure 4.2D), variations in structure occur near to the front of the wedge compared to CT25-10, with some ductile flow at the base of the crust, whilst similar structures are visibile at the centre of the wedge. With a high internal heating rate (CT25-10-3.6H_R; H_r =3.6 μW m^{-3}), the structures at the centre of the wedge are similar to the other high velocity models, with crustal stacking involving the entire crust (Figure 4.2F). However, the structures at the front of the wedge change considerably, with large folds developing. This is highlighted by the depth of strain localisation in the crust (Figure 4.3B-F), which

decreases with increasing internal heating rate at the front of the wedge. Changes in topography and wedge length are also observed, with the height of the topography decreasing and wedge length increasing with increasing internal heating rates (Figure 4.2H).

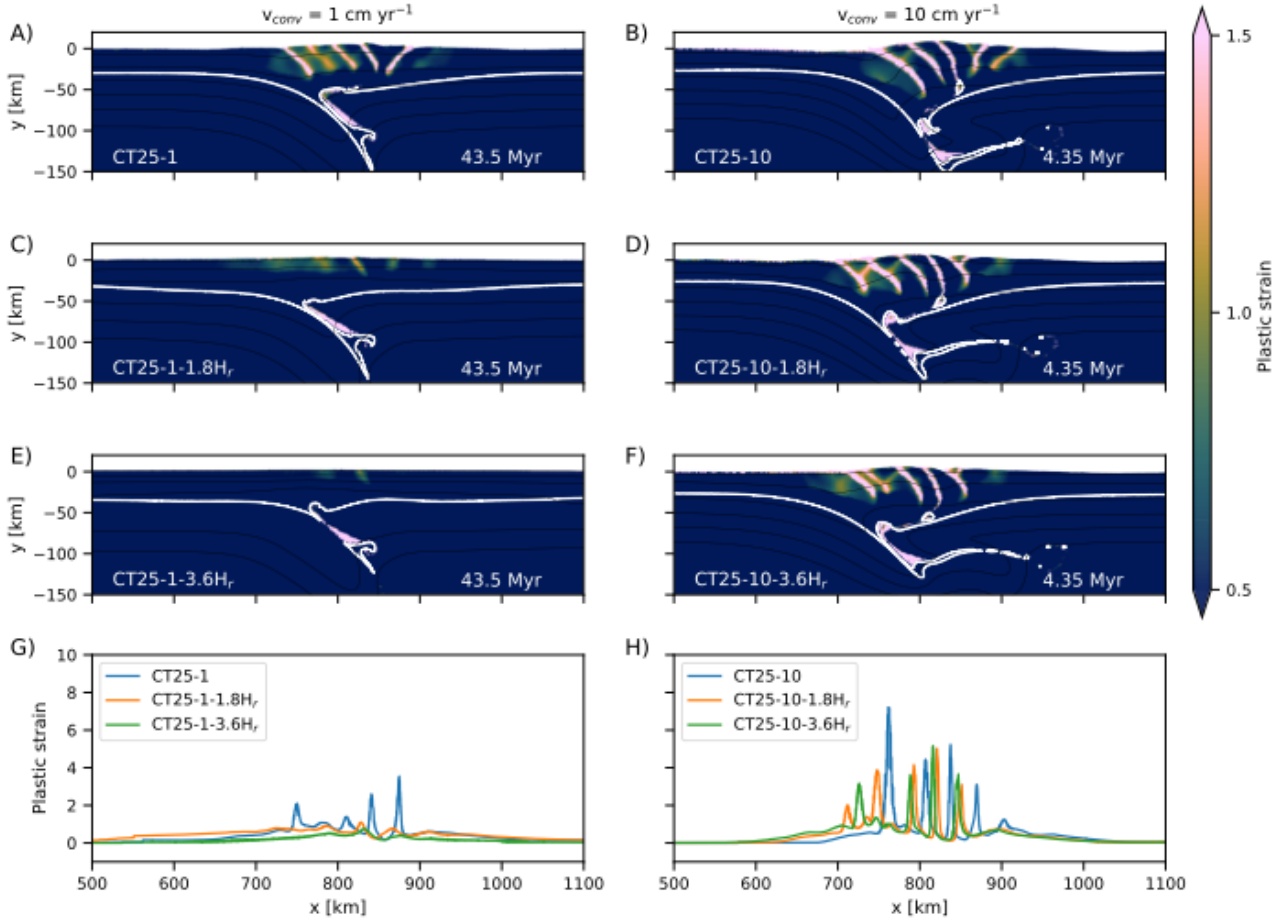

Figure 4.3: Similar to Figure 4.2 but showing plastic strain distribution between no internal heating and an internal heating rate for different convergence velocities after 435 km of convergence. A) CT25-1, B) CT25-10, C) CT25-1-1.8H_r, D) CT25-10-1.8H_r. E) CT25-1-3.6H_r, F) CT25-10-3.6H_r. The white line in each plot denotes the boundary between the crust and mantle. G) Plastic strain profiles taken at a y = -10 km for A), C) and E). H) Plastic strain profiles taken at a y = -10 km for B), D) and F). Results show that with increasing internal heating, the depth of the brittle ductile transition shallows. At low velocity and high internal heating (CT25-1-3.6H_r) no plastic strain occurs in the upper crust and instead convergence is accommodated through viscous deformation.

In general, increasing the internal heating rate leads to a decrease in the height of the topography and a lengthening of the orogen, with the change in the distribution of topography more substantial in the low velocity models (Figure 4.2G) compared to the high velocity models (Figure 4.2H). An increase in internal heating rate also hinders plastic strain localisation in the upper crust (Figure 4.3G-H), with deformation accommodated through viscous flow instead. The influence of internal heating on strain localisation is more

substantial in the low velocity models compared to the high velocity models due to the model duration.

4.3.2. Role of surface processes

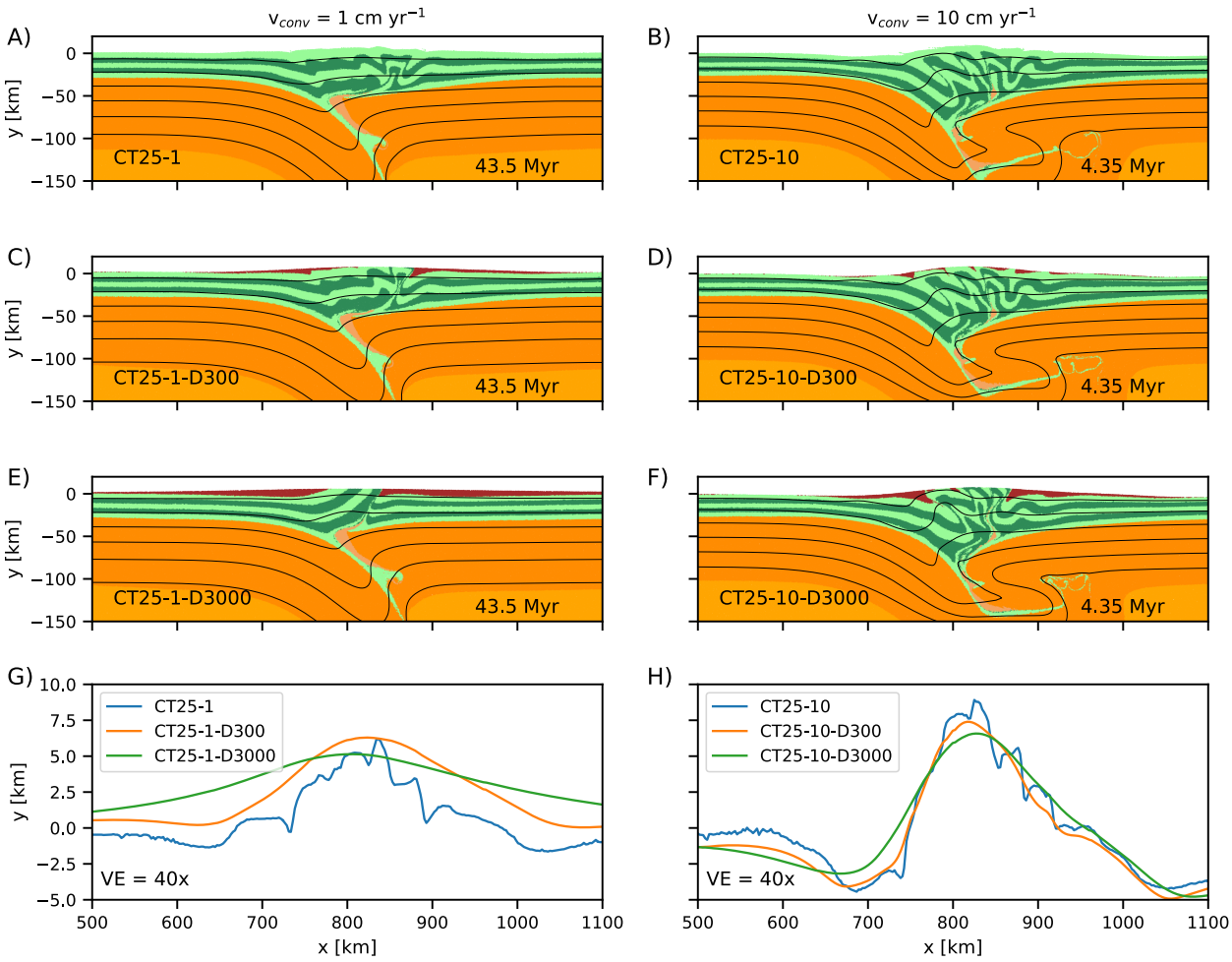

Figure 4.4: Comparison of internal structure from the material, with no erosion (A and B) and a hillslope diffusion rate to the surface (C-F). A) CT25-1. B) CT25-10. C) CT25-1-D300. D) CT25-10-D300. E) CT25-1-D300. F) CT25-10-D3000. G) Topography of models presented in A), C) and E). H) Topography of models presented in B), D) and F), showing how the diffusive surface smooths topography and reduces the height of the orogen. The smoothing of topography is most pronounced in the slow convergence models, occurring over a wider area compared to the fast convergence models, reflecting the time dependency of a diffusive surface. Surface processes also impede the outward growth of wedge, concentrating deformation close to the centre and promote exhumation, which is more apparent in the slow convergence velocity models. VE = 40 x is the vertical exaggeration.

Figure 4.4A & 4.4B display models run without erosion and show the orogenic wedge structure after 435 km of convergence, and are the same as the models presented in Figure 4.2A & 4.2B. Figure 4.4C & 4.4D, where D = 300 m^2 yr^{-1}, show varying amounts of influence of erosion after 435 km of convergence. In CT25-1-D300 (Figure 4.4C), there is ~10 km of material eroded from the material at the centre of the wedge, based on the layers in the

crust. In CT25-10-D300 (Figure 4.4D) there is no exhumation of deep crustal material and displays a very similar structure to CT25-10 (Figure 4.4B). A high convergence rate of 10 cm yr^{-1} results in rapid uplift and formation of structures, which is too fast to be eroded when D = 300 m^2 yr^{-1}. Figure 4.4 & 4.4F present the fast surface diffusion models (D = 3000 m^2 yr^{-1}) with both displaying a large amount of erosion and sedimentation and exhumation of crust at the centre of the wedge. In CT25-10-D3000 (Figure 4.4F), structures at the centre of the orogenic wedge are exhumed from a depth of ~10 km, similar to the depth of exhumed material in CT25-1-D300. The discrete zones that cause crustal stacking at the centre of the wedge in CT25-10-D3000 (Figure 4.4F) appear closer together compared to CT25-10 (Figure 4.4B) and CT25-10-D300 (Figure 4.4D). This is also observed in the distribution of plastic strain, which is concentrated at the centre of the wedge (Figure 4.5F).

In contrast, CT25-1-D3000 (Figure 4.4D) shows large amounts of sedimentation and erosion, with a very smooth topography. In CT25-1-D3000, uplifted material is eroded rapidly, restricting the outward growth of the wedge. This results in deformation being concentrated at the centre of the wedge along a main back thrust, as shown by the distribution of plastic strain in Figure 4.5E. In CT25-1-D3000 a large amount of exhumation occurs, with lower crust that initially started at a depth of ~20 km exposed at the surface in the centre of the wedge.

The strain profiles presented in Figure 4.5G-H shows how the distance between active deformation at the front and back of the wedge decreases with the increasing rate of surface diffusivity for a given convergence rate. The topography (Figure 4.4G-H) shows smoothing with increasing diffusive rate due to the amount of erosion and sedimentation increases that redistributes material across the wedge. The amount of topographic smoothing increases with increasing model duration, with a reduced topographic height and sediment deposited over a wider area in models where v_{conv} = 1 cm yr^{-1} (Figure 4.4G)

compared with models where v_{conv} = 10 cm yr^{-1} (Figure 4.4H) for a given surface diffusivity rate.

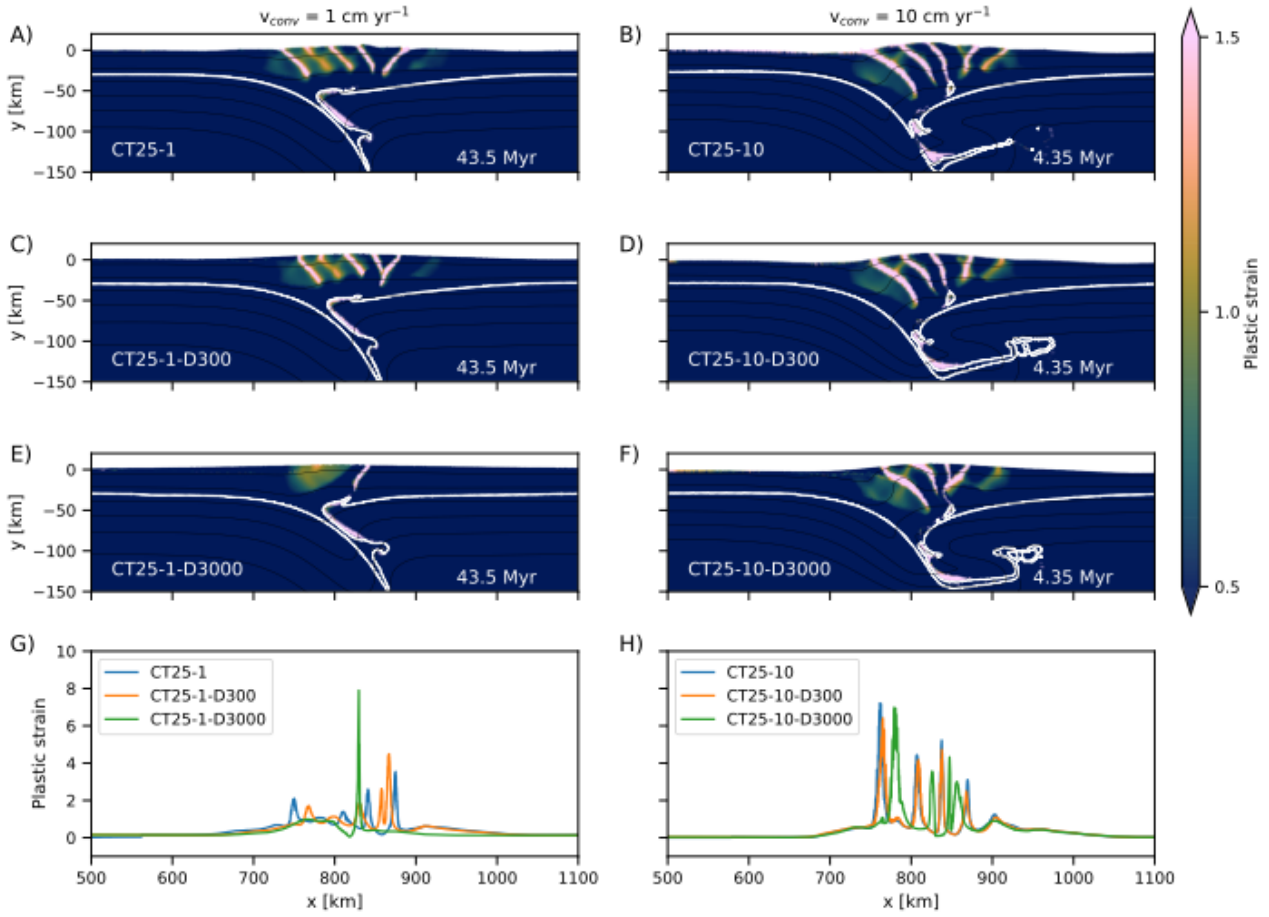

Figure 4.5: Comparison of plastic strain between models with no erosion (A and B) and a hillslope diffusion rate to the surface (C-F). A) CT25-1. B) CT25-10. C) CT25-1-D300. D) CT25-10-D300. E) CT25-1-D300. F) CT25-10-D3000. The white line in each plot denotes the boundary between the crust and mantle. G) Plastic strain of models presented in A), C) and E) at y = -10 km. H) Plastic strain of models presented in B), D) and F) at y = -10 km. The plastic strain shows how increasing the surface diffusivity restricts the wedge width, reduces the number of shear zones (based on the amount of strain localisation) and concentrates deformation at the centre of the wedge. The back-thrust in E) is well-defined in the profile presented in G).

4.4. Discussion

4.4.1. The role of internal heating on orogenic wedge structure

The influence of internal heating on the temperature distribution is shown by the isotherms in Figure 4.2, with isotherms much closer together and closer to the surface when compared to the models without internal heating. Figure 4.6 shows the difference in temperature at y = -24 km between CT25-1-3.6H_r (~700 °C) and CT25-10-3.6H_r (~1000 °C) after 435 km of convergence, highlighting the influence of internal heating on the

temperature within the wedge as the duration of the model increases. The difference in the temperature at y = -24 km between CT25-1 (~600 °C) and CT25-10 (~700 °C) in Figure 4.6 is due to thermal diffusion, which cools the crust over time, although the rate of thermal diffusion is much slower than the internal heating rate, with the latter having the biggest influence on the temperature distribution between the low and high convergence velocity models. Diffusion is another important factor in the temperature distribution and has previously been shown to hinder the subduction in temperature-dependent, buoyancy driven subduction zones (Knight et al., 2021).

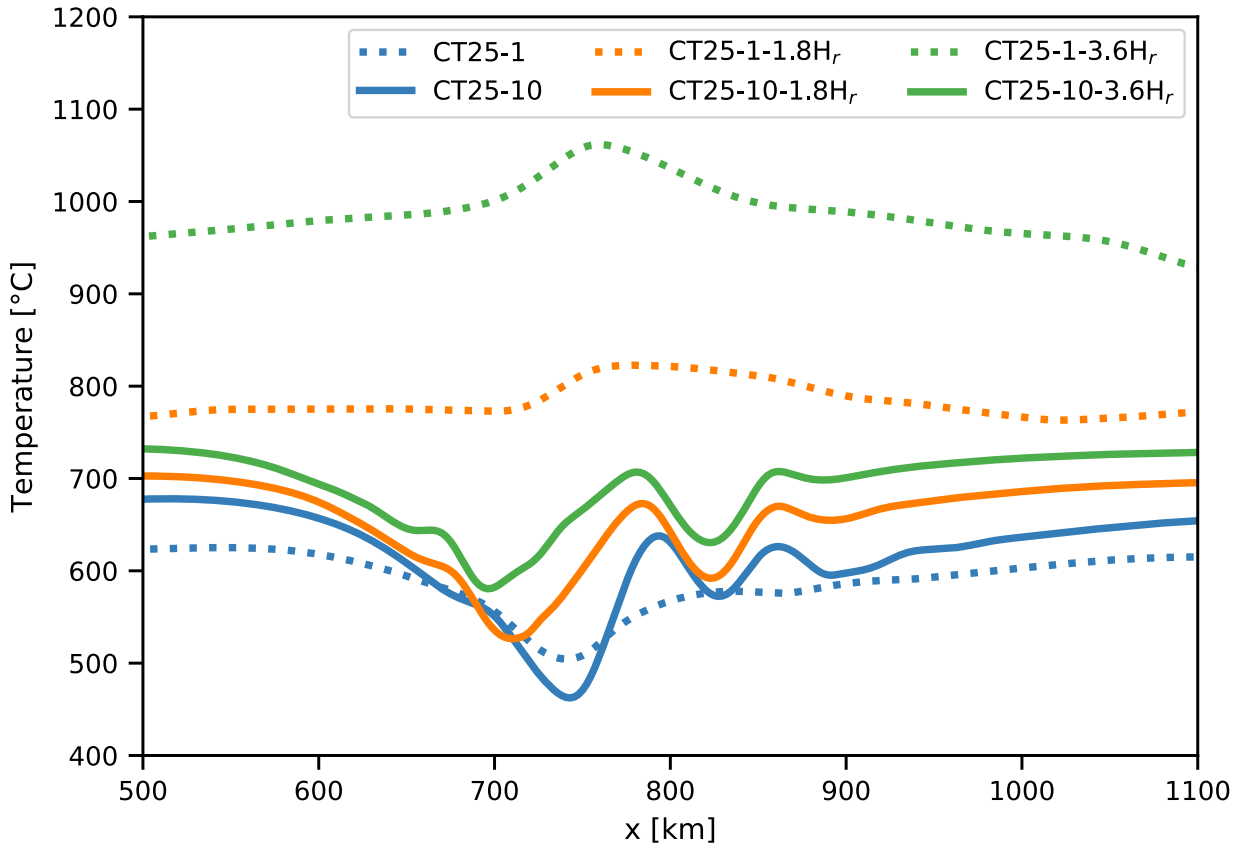

Figure 4.6: Horizontal temperature profile at y = -24 km for all models presented in the internal heating section after 435 km of convergence. The high convergence velocity models have a similar temperature, whilst a large difference (~400 °C) is observed between CT25-1 (~600 °C) and CT25-1-3.6H_r (~1000 °C) due to more heat being produced over the time to reach 435 km of convergence in the low convergence velocity models.

Similar structures at the centre of the wedge are observed in CT25-10 (Figure 4.2B), CT25-10-1.8H_R (Figure 4.2D) and CT25-10-3.6H_R (Figure 4.2F) as the structures form quickly due to the high convergence rate. As convergence is on-going, internal heating rate

begins to increase the temperature of the crust. This results in different structures forming at the front of the wedge between CT25-10, CT25-10-1.8H_R and CT25-10-3.6H_R as the internal temperature distribution changes, with the structures transitioning from crustal stacking in CT20-10 to folding in CT25-10-3.6H_R. In contrast, the low convergence velocity models transition from upper crustal stacking and flow in the lower crust in CT25-1 (Figure 4.2A) to only ductile flow in the crust in CT25-1-1.8H_R (Figure 4.2C) and CT25-1-3.6H_R (Figure 4.2E). This change in structural style is due to the large increase in temperature of the crust through the evolution of the low convergence velocity models (Figure 4.6). To alter the structural style of each wedge, an internal heating rate of <1.8 μW m^{-3} is required at a convergence velocity of 1 cm yr^{-1} and ~3.6 μW m^{-3} at convergence velocity of 10 cm yr^{-1}.

The increase in internal temperature results in an overall decrease in the strength of the wedge, through the temperature-dependent effective viscosity (Vanderhaeghe et al., 2003). This increase in temperature within the wedge favours viscous deformation over plastic, reducing the amount of plastic strain localisation in the upper crust (Figure 4.3). The reduction in wedge strength is also highlighted by the height of topography and length of the wedge after 435 km of convergence, with a decrease in strength resulting in a decrease in topographic height and increase in wedge length (Figure 4.2G-H). The influence of internal heating rate on topography (Figure 4.2G-H) and strain localisation (Figure 4.3G-H) is more pronounced in low velocity models compared to the high velocity models as the increase in temperature inside the wedge is higher due to the longer duration in the low velocity models. These results emphasise the role of internal heating and its influence on wedge strength and structural evolution, with the influence of internal heating increasing over time.

4.4.2. The role of surface processes on orogenic wedge structure

Surface processes reorganise the orogenic wedge over time, altering the timing of growth of the orogenic wedge. In our models, the diffusive surface promotes prolonged fault activity and strain localisation, restricting outward propagation and concentrating deformation in the centre of the orogenic wedge (e.g. Avouac and Burov, 1996; Dal Zilio et al., 2020; Ellis et al., 2001; Jammes and Huismans, 2012; Jaquet et al., 2017; Piccolo et al., 2017; Selzer et al., 2008) whilst also promoting the exhumation of mid to lower crustal material (Dal Zilio et al., 2020; Jammes and Huismans, 2012; Kaus et al., 2008), in agreement with previous studies.

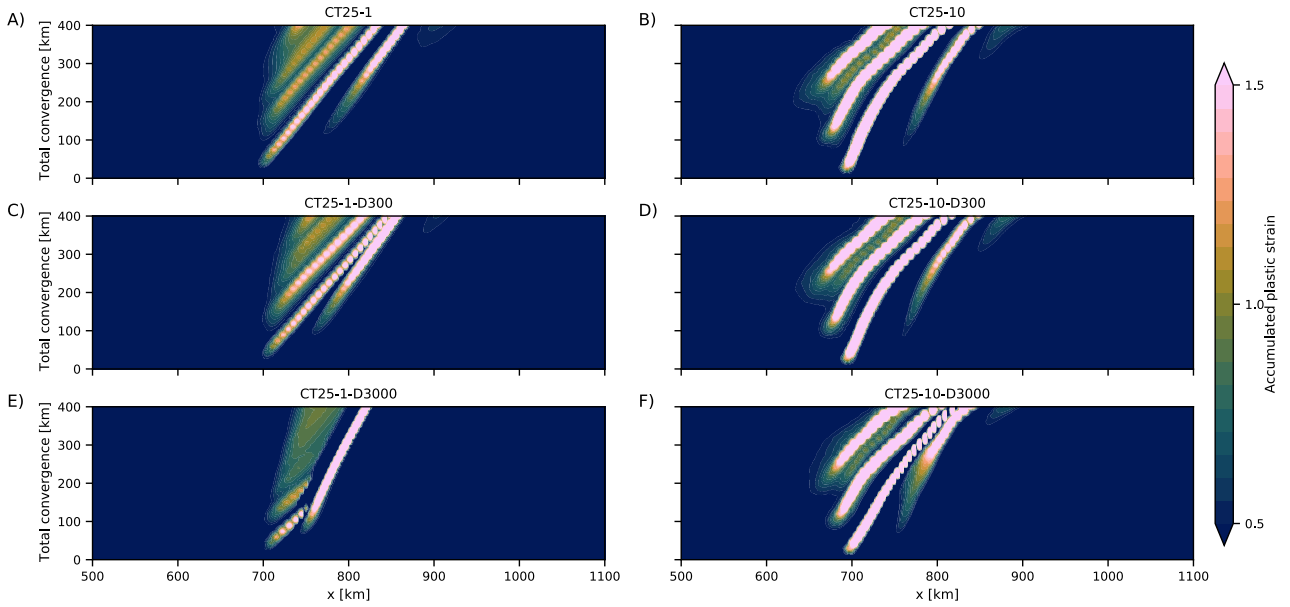

Figure 4.7: Evolution of strain at y = -10 km to highlight the influence of surface processes on strain localisation in the crust. A) CT25-1, B) 25-10, C) CT25-1-D300, D) CT25-10-D300, E) CT25-1-D3000, F) CT25-10-D3000.

Surface processes result in the number of shear zones in the upper crust decreasing with increasing diffusivity rate for a given convergence velocity (Figure 4.5 & Figure 4.7). Figure 4.7 shows that not only do the number of shear zones decrease, but the duration of activity along the active shear zone also increases, in agreement with previous studies (Jaquet et al., 2017; Selzer et al., 2007) as well as increasing the amount of strain accommodated along the shear zone. This increase in shear zone longevity is due surface

processes redistributing material from the centre to the peripheral of the wedge, which reduces the gravitational load acting on the wedge.

To develop a new shear zone, the internal stress and gravitational load must be in disequilibrium, with an excess gravitational load (e.g. Dahlen, 1990; Graveleau et al., 2012). This results in the wedge lengthening and developing a new shear zone to reduce the gravitational load and re-equilibrate. Surface processes redistribute the material, with erosion at the centre of the wedge reducing the gravitational load. This increases the time to reach a disequilibrium and cause the wedge to lengthen compared to models without surface processes, prolonging the duration of activity along the active shear zone. This also results in a decrease in wedge length in models with surface processes compared to those without. In the most extreme case, CT25-1-D3000, the crust is unable to thicken sufficiently for outward propagation to occur, instead deformation is concentrated along a single back thrust that accommodates most of the deformation and is active for the entire duration of the model (Figure 4.7E).

Surface processes also promote exhumation at the centre of the wedge due to the redistribution of material, with the depth of exhumed crust increasing with increasing diffusive rate for a given convergence velocity (Figure 4.8). The depth of exhumed material is higher in the low convergence velocity models due to surface processes having longer to erode material from the centre of the wedge compared to the high convergence models. No exhumation occurs in models without surface processes (Figure 4.8A-B), whilst the most extreme exhumation is observed in CT25-1-D3000 (Figure 4.8E). In CT25-1-D3000 material is initially buried from a depth of ~20 km to ~30 km below the surface before being exhumed, with the material travelling ~250 km from its initial position to where it is exhumed at the surface. In comparison, exhumation of crustal material CT25-10-D3000 is exhumed from a

depth of ~15 km (Figure 4.8F), with the material originating ~100 km from its exhumed position.

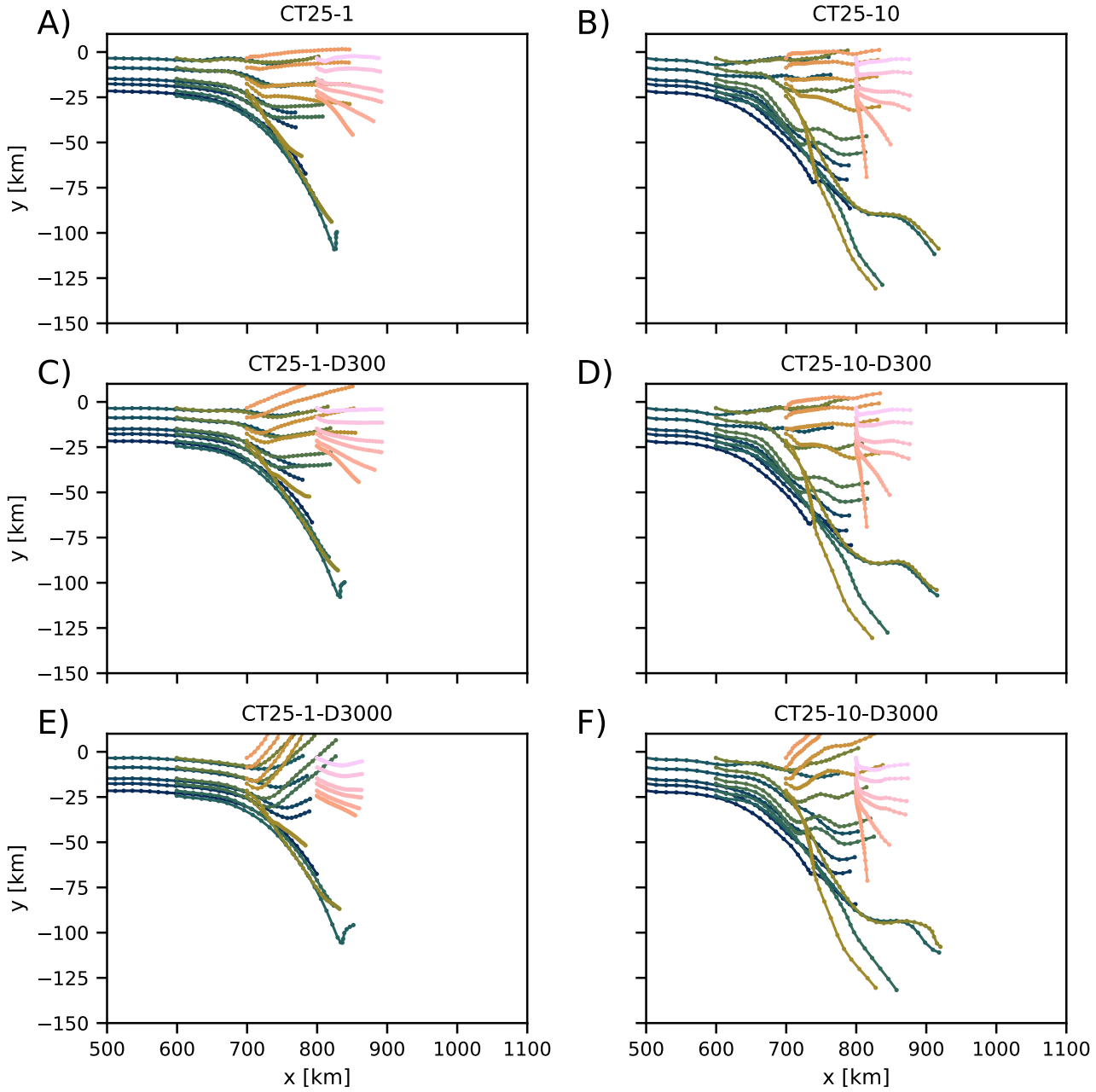

Figure 4.8: Evolution of selected particles to highlight the depth at which material is exhumed from. A) CT25-1, B) CT25-10, C) CT25-1-D300, D) CT25-10-D300, E) CT25-1-D3000, F) CT25-10-D3000. No exhumation takes place in A, B or D. Material is exhumed from a depth of ~10 km in C, ~30 km in E and ~14 km in F. This highlights that most exhumation takes place in the low velocity model with a high surface diffusivity rate due to the amount of time to reach 435 km, with material eroded as fast as uplift occurs, resulting in the exhumation of deep crustal material along a single back thrust.

A drastic change in the internal structure is observed in extreme cases when the removal of material from the wedge interior is similar to uplift rates (Avouac and Burov, 1996; Beaumont et al., 1996; Willett, 1999b), as seen in CT25-1-D3000 (Figure 4.4E). The rapid

removal of material restricts any outward growth of the wedge, concentrating deformation and exhumation along a single back thrust. This results in a wedge with a very smooth topography (Avouac and Burov, 1996) with a reduced topographic high above the deformation zone (Figure 4.4G), with this elevated region related to the very high amounts of exhumation at the centre of the wedge (Willett, 1999a).

These results emphasise the increasing influence of surface processes on the structural evolution of orogenic wedges with increasing time.

4.4.3. Model limitations

Our model is a simplified version of crustal deformation during orogenesis, which does not encapsulate all the complexities occurring in nature. In nature, orogenic wedge formation is inherently 3D, whilst our model is 2D. We assume a homogenous crust, whilst in nature the rheology of the crust within the orogenic wedge can vary both laterally and vertically. We also apply a constant convergence velocity, which may vary over the duration of convergence.

We assume a constant surface diffusivity rate, whilst in nature the rate at which surface processes occur may vary over time and laterally within the orogen due to variations in rock type, erosive processes (e.g. physical/chemical erosion) or climatic conditions. However, our results match previous studies into surface processes (e.g. Avouac and Burov, 1996; Burov and Toussaint, 2007; Ellis et al., 2001; Jammes and Huismans, 2012; Jaquet et al., 2017; Kaus et al., 2008; Selzer et al., 2008, 2007; Willett, 1999b)

To include internal heating in the models, a homogeneous heating rate is applied to the entire crust. However, the internal heating rate may be enhanced or depleted in certain areas of the crust during orogenesis as radiogenic heat producing elements (HPE) are redistributed in the crust through melting and recrystallization. If sufficiently voluminous, the

redistribution of HPE could alter the local temperature and alter how deformation localises within the wedge. However, our results agree with previous studies that show the viscosity, representing strength, of the crust decreases (Faccenda et al., 2009; Vanderhaeghe et al., 2003) as the rate of internal heating increases (Faccenda et al., 2008; Piccolo et al., 2017) due to the temperature dependency of the viscous rheology.

4.5. Conclusions

We use 2D numerical models with a visco-plastic rheology to investigate the influence of rate-dependent (convergence velocity) and time-dependent processes (internal heating, surface processes) on the structural evolution of orogenic wedges can be summarised as follows.

Over long durations or at a high surface diffusivity, surface processes alter the internal structure of the wedge considerably. Erosion concentrates deformation at the centre of the wedge, restrict the distance between the deformation fronts at the front and back of the orogen, reduce the number of shear zones, extend the duration of activity along shear zones, and promotes exhumation compared to models without the inclusion of erosion. As the surface processes are implemented as a constant diffusive rate, the influence of erosion and sedimentation on the distribution of material increases over time for a given diffusivity rate.

Internal heating increases the internal temperature of the crust, resulting in a decrease in the depth of the brittle-ductile transition and a decrease in the wedge viscosity and thus strength. This results in a decrease in plastic strain localisation and restricts the formation of shear zones in the upper crust, with deformation instead accommodated through viscous flow. The reduction is strength results in a decrease in wedge thickness and increase in wedge length compared to models without the inclusion of internal heating. As

Internal heating is also a rate, the influence of internal heating on the structure of the wedge increases as the duration of the model increases. Over long durations or high heating rates, internal heating has a growing influence on the internal wedge structure, promoting increasingly viscous structures to form as the temperature of the crust increases.

Our results highlight that these processes (internal heating and surface processes) should be carefully considered when included in modelling of any tectonic margin, particularly if there are differences in duration.

4.6. References

Avouac, J.-P., 1993. Analysis of scarp profiles: Evaluation of errors in morphologic dating. J. Geophys. Res. Solid Earth 98, 6745–6754. https://doi.org/10.1029/92JB01962

Avouac, J.P., Burov, E.B., 1996. Erosion as a driving mechanism of intracontinental mountain growth. J. Geophys. Res. Solid Earth 101, 17747–17769. https://doi.org/10.1029/96JB01344

Beaumont, C., Kamp, P.J.J., Hamilton, J., Fullsack, P., 1996. The continental collision zone, South Island, New Zealand: Comparison of geodynamical models and observations. J. Geophys. Res. Solid Earth 101, 3333–3359. https://doi.org/10.1029/95JB02401

Beucher, R., Moresi, L., Giordani, J., Mansour, J., Sandiford, D., Farrington, R., Mondy, L., Mallard, C., Rey, P., Duclaux, G., Kaluza, O., Laik, A., Morón, S., 2019. UWGeodynamics: A teaching and research tool for numerical geodynamic modelling. J. Open Source Softw. 4, 1136. https://doi.org/10.21105/joss.01136

Burov, E., Toussaint, G., 2007. Surface processes and tectonics: Forcing of continental subduction and deep processes. Glob. Planet. Change, TOPO-EUROPE: the Geoscience of Coupled Deep Earth-Surface Processes 58, 141–164. https://doi.org/10.1016/j.gloplacha.2007.02.009

Crameri, F., Schmeling, H., Golabek, G.J., Duretz, T., Orendt, R., Buiter, S.J.H., May, D.A., Kaus, B.J.P., Gerya, T.V., Tackley, P.J., 2012. A comparison of numerical surface topography calculations in geodynamic modelling: an evaluation of the 'sticky air' method: Modelling topography in geodynamics. Geophys. J. Int. 189, 38–54. https://doi.org/10.1111/j.1365-246X.2012.05388.x

Culling, W.E.H., 1960. Analytical Theory of Erosion. J. Geol. 68, 336–344.

Dahlen, F.A., 1990. Critical Taper Model of Fold-And-Thrust Belts and Accretionary Wedges. Annu. Rev. Earth Planet. Sci. 18, 55–99. https://doi.org/10.1146/annurev.ea.18.050190.000415

Dal Zilio, L., Ruh, J., Avouac, J.-P., 2020. Structural Evolution of Orogenic Wedges: Interplay Between Erosion and Weak Décollements. Tectonics 39, e2020TC006210. https://doi.org/10.1029/2020TC006210

Ellis, S., Wissing, S., Pfiffner, A., 2001. Strain localization as a key to reconciling experimentally derived flow-law data with dynamic models of continental collision. Int. J. Earth Sci. 90, 168–180. https://doi.org/10.1007/s005310000151

Faccenda, M., Gerya, T.V., Chakraborty, S., 2008. Styles of post-subduction collisional orogeny: Influence of convergence velocity, crustal rheology and radiogenic heat production. Lithos 103, 257–287. https://doi.org/10.1016/j.lithos.2007.09.009

Faccenda, M., Minelli, G., Gerya, T.V., 2009. Coupled and decoupled regimes of continental collision: Numerical modeling. Earth Planet. Sci. Lett. 278, 337–349. https://doi.org/10.1016/j.epsl.2008.12.021

Gerya, T., 2009. Introduction to Numerical Geodynamic Modelling. Cambridge University Press, Cambridge. https://doi.org/10.1017/CBO9780511809101

Gleason, G.C., Tullis, J., 1995. A flow law for dislocation creep of quartz aggregates determined with the molten salt cell. Tectonophysics, 30 Years of Tectonophysics a Special Volume in Honour of Gerhard Oertel 247, 1–23. https://doi.org/10.1016/0040-1951(95)00011-B

Graveleau, F., Malavieille, J., Dominguez, S., 2012. Experimental modelling of orogenic wedges: A review. Tectonophysics 538, 1–66. https://doi.org/10.1016/j.tecto.2012.01.027

Hirth, G., Kohlstedt, D., 2003. Rheology of the upper mantle and the mantle wedge: A view from the experimentalists, in: Eiler, J. (Ed.), Geophysical Monograph Series. American Geophysical Union, Washington, D. C., pp. 83–105. https://doi.org/10.1029/138GM06

Jammes, S., Huismans, R.S., 2012. Structural styles of mountain building: Controls of lithospheric rheologic stratification and extensional inheritance. J. Geophys. Res. Solid Earth 117. https://doi.org/10.1029/2012JB009376

Jaquet, Y., Duretz, T., Grujic, D., Masson, H., Schmalholz, S.M., 2017. Formation of orogenic wedges and crustal shear zones by thermal softening, associated topographic evolution and application to natural orogens. Tectonophysics. https://doi.org/10.1016/j.tecto.2017.07.021

Jaupart, C., Mareschal, J.-C., Iarotsky, L., 2016. Radiogenic heat production in the continental crust. Lithos 262, 398–427. https://doi.org/10.1016/j.lithos.2016.07.017

Kaus, B.J.P., Steedman, C., Becker, T.W., 2008. From passive continental margin to mountain belt: Insights from analytical and numerical models and application to Taiwan. Phys. Earth Planet. Inter., Recent Advances in Computational Geodynamics: Theory, Numerics and Applications 171, 235–251. https://doi.org/10.1016/j.pepi.2008.06.015

Knight, B.S., Davies, J.H., Capitanio, F.A., 2021. Timescales of successful and failed subduction: insights from numerical modelling. Geophys. J. Int. 225, 261–276. https://doi.org/10.1093/gji/ggaa410

Kumar, P.S., Menon, R., Reddy, G.K., 2009. Heat production heterogeneity of the Indian crust beneath the Himalaya: Insights from the northern Indian Shield. Earth Planet. Sci. Lett. 283, 190–196. https://doi.org/10.1016/j.epsl.2009.04.015

Mareschal, J.-C., Jaupart, C., 2013. Radiogenic heat production, thermal regime and evolution of continental crust. Tectonophysics, Moho: 100 years after Andrija Mohorovicic 609, 524–534. https://doi.org/10.1016/j.tecto.2012.12.001

Moresi, L., Dufour, F., Mühlhaus, H.-B., 2003. A Lagrangian integration point finite element method for large deformation modeling of viscoelastic geomaterials. J. Comput. Phys. 184, 476–497. https://doi.org/10.1016/S0021-9991(02)00031-1

Moresi, L., Quenette, S., Lemiale, V., Mériaux, C., Appelbe, B., Mühlhaus, H.-B., 2007. Computational approaches to studying non-linear dynamics of the crust and mantle. Phys. Earth Planet. Inter. 163, 69–82. https://doi.org/10.1016/j.pepi.2007.06.009

Piccolo, A., Faccenda, M., Carosi, R., Montomoli, C., Visonà, D., 2017. Crustal strength control on structures and metamorphism in collisional orogens. Tectonophysics. https://doi.org/10.1016/j.tecto.2017.09.018

Schmeling, H., Babeyko, A.Y., Enns, A., Faccenna, C., Funiciello, F., Gerya, T., Golabek, G.J., Grigull, S., Kaus, B.J.P., Morra, G., Schmalholz, S.M., van Hunen, J., 2008. A benchmark comparison of spontaneous subduction models—Towards a free surface. Phys. Earth Planet. Inter., Recent Advances in Computational Geodynamics: Theory, Numerics and Applications 171, 198–223. https://doi.org/10.1016/j.pepi.2008.06.028

Selzer, C., Buiter, S.J.H., Pfiffner, O.A., 2007. Sensitivity of shear zones in orogenic wedges to surface processes and strain softening. Tectonophysics 437, 51–70. https://doi.org/10.1016/j.tecto.2007.02.020

Selzer, C., Buiter, S.J.H., Pfiffner, O.A., 2008. Numerical modeling of frontal and basal accretion at collisional margins. Tectonics 27. https://doi.org/10.1029/2007TC002169

Spiegelman, M., May, D.A., Wilson, C.R., 2016. On the solvability of incompressible Stokes with viscoplastic rheologies in geodynamics. Geochem. Geophys. Geosystems 17, 2213–2238. https://doi.org/10.1002/2015GC006228

Toussaint, G., Burov, E., Avouac, J.P., 2004. Tectonic evolution of a continental collision zone: A thermomechanical numerical model. Tectonics 23, n/a-n/a. https://doi.org/10.1029/2003TC001604

Vanderhaeghe, O., Medvedev, S., Fullsack, P., Beaumont, C., Jamieson, R.A., 2003. Evolution of orogenic wedges and continental plateaux: insights from crustal thermal-mechanical models overlying subducting mantle lithosphere. Geophys. J. Int. 153, 27–51. https://doi.org/10.1046/j.1365-246X.2003.01861.x

Vogt, K., Matenco, L., Cloetingh, S., 2017. Crustal mechanics control the geometry of mountain belts. Insights from numerical modelling. Earth Planet. Sci. Lett. 460, 12–21. https://doi.org/10.1016/j.epsl.2016.11.016

Willett, S.D., 1999a. Rheological dependence of extension in wedge models of convergent orogens. Tectonophysics 305, 419–435. https://doi.org/10.1016/S0040-1951(99)00034-7

Willett, S.D., 1999b. Orogeny and orography: The effects of erosion on the structure of mountain belts. J. Geophys. Res. Solid Earth 104, 28957–28981. https://doi.org/10.1029/1999JB900248

Chapter 5

The role of surface processes and rheology in the formation of salients and recesses

Authors: Ben S. Knight, Fabio A. Capitanio, Roberto F. Weinberg

Affiliation:

School of Earth, Atmosphere & Environment, Monash University, Clayton, 3800

Abstract

Salients and recesses are prominent features of orogens, visible due to variations in topography along the orogen front. In this study, 2D and 3D thermo-mechanical models are used to investigate the formation of salients and recesses during orogenesis. We test rheological heterogeneities, through varying the friction, and erosion and sedimentation rates along the front of a collisional zone to show that a local increase in either strength or erosion rates results in decreased front advance and the formation of a recess. The increase in frictional properties also alters the internal structural style of the wedge, from predominantly plastic to a style characterised by viscous features. Surface processes do not alter the internal structure but do promote crustal exhumation, whilst restricting the lateral growth of the orogen. We distinguish characteristic topographic features to identify the cause of salients and recesses in nature. When there are lateral variations in rheology, the peak topographic height is offset laterally, with the topography migrating backwards with increasing frictional strength. In contrast, no change in the position of maximum topographic height is observed across the orogen when there are lateral variations in the erosion and sedimentation rates. These results provide a diagnostic to identify the causes of salients and recesses along the Himalayan front. Along with the topography, free-air gravity anomalies are utilised to identify variations in strength, with small recesses in the region related to focused erosion whilst large recesses are attributed to increases in strength.

5.1. Introduction

Mountain belts are distinguishable features of the surface of the Earth. One prominent feature along an orogen front is areas where the high topography either extends into or retracts from the low topography surroundings, characterised as salients and recesses (Miser, 1932). Salients and recesses are observed throughout the Himalayan arc and have previously been attributed to surface processes (Bendick and Bilham, 2001) or lateral variations in rock strength (Koulakov et al., 2015).

At large scale, the Himalayan front forms a near-perfect arc 1800 km in length between 77.2 and 92.1 °E based on either seismicity, topography, or stress state (Bendick and Bilham, 2001). A maximum deviation of ~48 km between the small-circle fit and the topographic front is observed, with the largest deviations associated with large trans-Himalayan river drainage basins (Bendick and Bilham, 2001), highlighting the role of surface processes.

Erosion restricts the wedge width by delaying the outward propagation of deformation (Dal Zilio et al., 2018; Ellis et al., 2001; Jaquet et al., 2017; Liu et al., 2020; Selzer et al., 2007; Vogt et al., 2017a; Willett, 1999a), which results in the formation of a recess where local erosion rates are high compared to low rates in surrounding regions. Localised erosion due to river incision has been attributed to the formation of the Dujiangyan recess in Eastern Tibet (Liu et al., 2020).

At smaller scales (~10 km), multiple salients and recesses have been identified along the Himalayan arc (Macedo and Marshak, 1999). Koulakov et al. (2015) proposed that salients and recesses along the Himalayan front may be the result of variations in strength, causing variations in crustal thickness, based on magnetic and free-air gravity anomalies. It has been argued that the salients and recesses at the front of the Himalayans may be self-

organised, where sections deform unpredictably but at large scale there is a steady-state growth of the orogen (Weinberg, 2016). Koulakov et al. (2015) suggest positive magnetic and free-air gravity anomalies may be the result of igneous bodies below the surface that strengthen the crust, whilst negative gravity and magnetic anomalies may be due to thicker sediments, resulting in a weaker crust.

A similar observation was made by Livani et al. (2018), where the formation of the Cremona salient, the Parma recess, and the Ferrara salient in the northern Apennines was influenced partly by the presence of the Upper Ladinian volcanic edifices, identified from geophysical data, beneath the Parma recess (Livani et al., 2018). These igneous bodies increase the crustal strength, which influences the width and thickness of the orogen, with a high crustal strength resulting in a decrease in the orogen width and increasing the crustal thickness that can be supported (Pusok and Kaus, 2015; Ruh et al., 2014, 2012; Vogt et al., 2017a, 2017b; Willett, 1999b). A high rock strength results in a recess when it is next to a lower strength rock, that forms a salient.

At the crustal scale, the strength of a visco-plastic wedge is altered through the rheology of rocks, that is controlled by the Coulomb plastic strength, through the friction coefficient and cohesive strength, or the viscous rheology, due to the temperature, strain-rate, and composition dependency of the viscous flow. The evolution of Coulomb plastic wedges is dictated by the friction coefficient at the base of the wedge, as the material within the wedge is assumed to be cohesionless and on the verge of failure at all locations, implying that the internal strength of the wedge is negligible (Dahlen, 1990, 1988, 1984; Davis et al., 1983; Willett, 1999b). Previous studies into fold-and-thrust belts (Ruh et al., 2014, 2012) determined that increasing the internal friction angle results in a shorter and thicker wedge, as well as a decrease in the number of shear zones, forming a salient where the friction coefficient and therefore strength is low and recess where the friction coefficient is high.

Similar observations have been made from 2D lithospheric-scale visco-plastic models. In general, an increase in the overall crustal viscosity and strength results in a decrease in wedge width and increase in crustal thickness (Medvedev, 2002; Piccolo et al., 2017; Vanderhaeghe et al., 2003; Vogt et al., 2017b; Willett, 1999b). It is expected that in 3D lateral variations in strength would result in the formation of salients in areas of low strength and recesses in areas of high strength. This has been observed in 3D numerical models of fold-and-thrust belts (Ruh et al., 2014), where the basal decollement strength was varied laterally to form a narrow fold-and-thrust belt where the decollement strength was low and a wide fold-and-thrust belt where strength was high. Similar results have been observed in 3D lithospheric scale models investigating the formation of plateaus (Chen et al., 2017; Pusok and Kaus, 2015).

Although the role of rheology and surface processes have been well studied during orogenesis, the role of each on the formation of salients and recesses has not previously been investigated systematically. Here, we test how the rheology and surface processes interact in the formation of salients and recesses by means of numerical modelling. We first investigate how the friction coefficient and surface processes influence the internal structure and the topography of visco-plastic wedges in 2D, whilst keeping all other parameters the same (e.g. geotherm, viscous rheology, convergence rate) as each of these parameters has previously been shown to alter rock strength (e.g. Ellis, 1988; Vanderhaeghe et al., 2003; Vogt et al., 2017b, 2017a). 3D models are then utilised to assess the topographic response to lateral variations in erosion and sedimentation rates or the rock rheology that results in the formation of salients and recesses.

5.2. Modelling approach

We model the collision of continental crust as a viscous fluid with an infinite Prandtl number at a low Reynolds number. The conservation of mass, momentum and energy equations are

solved for an incompressible fluid through the Boussinesq approximation in both a 2D and 3D Cartesian box using the finite element, particle-in-cell (PIC) code Underworld2 (Beucher et al., 2019; Moresi et al., 2007, 2003). Underworld2 allows the tracking of distinct materials and their properties through Lagrangian particles within a Eulerian finite element grid. More details on the numerical method and governing equations are outlined in Chapter 2.

5.2.1. Model Setup

The model setup (Figure 5.1A) is designed to simulate continental collision, where an orogenic wedge forms above a pre-existing weakness as the lithospheric mantle subducts. The model replicates the air, crust, and mantle over a depth (y) of 300 km and a width of (x) 1200 km. In 3D, the box has a length (z) of 300 km. x-y-z coordinates were set to maintain a constant notation between 2D and 3D models, with x-y coordinates used in 2D and x-y-z in 3D models, where x represents the width, y represents the depth and z represents the length.

A uniform grid is used, with a distribution of 512 × 128 nodal points giving a cell width of 2.34 km, with 30 particles per cell in 2D. In 3D, a 256 x 64 x 64 grid is used with 80 particles per cell. Timesteps are determined by using (half of) the Courant–Friedrichs–Lewy (CFL) condition. Using the CFL condition, a convergence velocity of 2 cm yr^{-1} and a cell width of 2.34 km results in timesteps of ~58,500 years in the 2D models and timesteps of ~117,000 years with a cell width of 4.68 km in the 3D models.

The model uses a free-slip condition on the back ($v_x = 0$) and top ($v_y = 0$) boundaries in 2D and on the left and right ($v_z = 0$) boundaries in 3D. At the base, the boundary is unconstrained, allowing the inflow and outflow of material, implying the model overlies an infinite space constituting of an inviscid fluid at a depth of 270 km. A constant convergence velocity (v_{conv}) of 2 cm yr^{-1} is applied to the left boundary. This velocity is similar to the current

accommodation rate within the Himalayan orogenic wedge (Ader et al., 2012; Stevens and Avouac, 2015). The velocity is applied to the lower plate, on the left wall across the crust and mantle lithosphere, which induces convergence towards the upper plate, to the left of model. Below the lithosphere (y < -97.5 km), the velocity linearly decreases from 2 cm yr^{-1} to zero at the bottom of the left wall. Above the crust, an inflow/outflow is prescribed across the sticky air layer (y > 0 km) to allow topography to develop (Figure 5.1A, left panel).

The temperature of the top boundary is kept constant (T = 0 °C), with no heat flux across the side walls. The internal temperature follows a geothermal gradient of 25 °C km^{-1} for the first 10 km and then 12 °C km^{-1} until a temperature of 1300 °C is reached at the lithosphere-asthenosphere boundary (LAB) at a depth of 97.5 km. We neglect adiabatic gradients and keep the underlying mantle at 1300 ˚C.

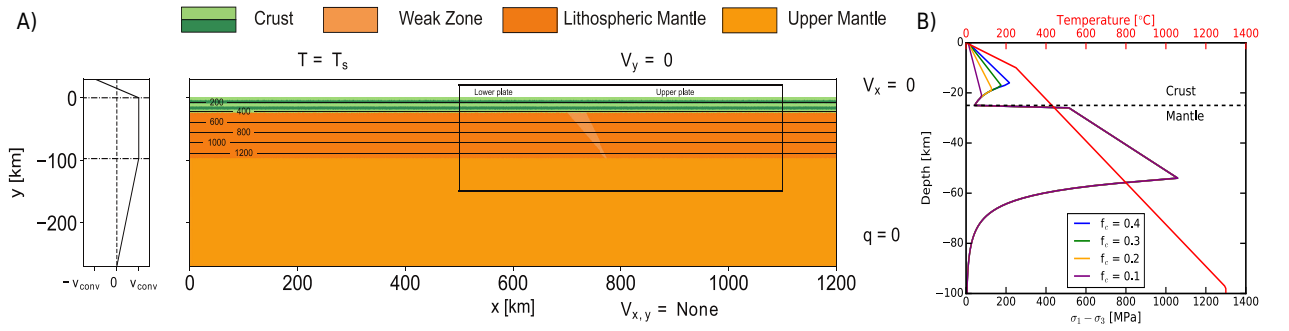

Figure 5.1: A) Initial 2D model setup of case 03fc. Temperature contours are given at 200℃ intervals. The black box (x > 700 km & x < 1100 km, y < 20km & y > -150 km) portrays the area shown in subsequent figures that display model evolution. B) 1D strength and temperature profile of the crust and mantle. The strength profiles have a constant strain rate ($\dot{\varepsilon}_{II} = 10^{-14}\ s^{-1}$) with different friction coefficients, with increasing friction coefficient resulting in a thicker viscous layer at the base of the crust.

The continental crust layer is homogenous and has a quartzite viscous rheology (Table 1), and a crustal thickness of 25 km. A single crustal layer is used to better constrain the role of the friction coefficient which may be obscured by a multi-layered crust where the layers have different frictional and viscous properties. A 45° dipping weak zone, representing a pre-existing subduction zone, is prescribed with a wet olivine rheology. The weak zone is surrounded by a dry olivine mantle, which results in deformation above the weak zone whilst also facilitating subduction of the lithosphere. To allow the evolution of topography during

the model, a 30 km 'sticky air' layer is included, with a low viscosity (10^{19} Pa s) and density (1 kg m^{-3}) to minimise shear stresses at the surface (Vogt et al., 2017a).

5.2.2. Rheological laws

Viscous deformation occurs through either dislocation or diffusion creep:

$$\eta_{disl/diff} = \frac{1}{2} A^{-\frac{1}{n}} \dot{\varepsilon}_{II}^{\frac{1-n}{n}} e^{\left(\frac{E+PV}{nRT_r}\right)} \tag{5.1}$$

where η is the viscosity, A is the pre-exponential factor, n is the stress exponent, E is the activation energy, P the pressure, V the activation volume, R the gas constant, T_r is the temperature at a given position and $\dot{\varepsilon}_{II}$ is the second invariant of strain rate. In the crust, diffusion creep is neglected due to the low temperatures and high strain rates in the model. The bulk average grain size of the crust, which is on the order of mm scale, also makes dislocation creep the dominant viscous deformation mechanism in the crust (Ranalli and Adams, 2013).

Plasticity is implemented in the model through a Drucker-Prager yield criterion (Spiegelman et al., 2016) which limits the maximum stress within the crust, resulting in an effective viscosity for the plastic flow:

$$\tau_y = C \cos\varphi + P \sin\varphi \tag{5.2.1}$$

$$\eta_p = \frac{\tau_y}{2\dot{\varepsilon}_{II}} \tag{5.2.2}$$

where τ_y is the yield stress, C is the cohesion at the surface, φ is the internal friction angle, where $sin\ sin\ \varphi$ is equivalent to the friction coefficient (f_c) and *P* is the lithostatic pressure.

Table 5.1: Initial material properties used for the visco-plastic rheology. ρ is density at the surface. A is the pre-exponential factor, n, is the stress exponent, E is the activation energy, f_c is the friction coefficient, C is the cohesion at the surface and α is the coefficient of thermal expansion.

	Crust	***Sediment***	***Mantle***		***Weak Zone***	
Rheology	*Quartzite*[a]	*Quartzite*[a]	*Olivine*[b]		*Wet Olivine*[b]	
Deformation mechanism	Dislocation	Dislocation	Dislocation	Diffusion	Dislocation	Diffusion
A (MPa^{-n} s^{-1})	1.1×10^{-34}	1.1×10^{-34}	1.1×10^{5}	1.5×10^{9}	1.6×10^{3}	2.5×10^{7}
n	4.0	4.0	3.5	1.0	3.5	1.0
Ea ($J\ mol^{-1}$)	2.23×10^{5}	2.23×10^{5}	5.30×10^{5}	3.75×10^{5}	5.20×10^{5}	3.75×10^{5}
Va ($m^3\ mol^{-1}$)	0	0	6.0×10^{-6}	6.0×10^{-6}	2.3×10^{-5}	1.0×10^{-5}
C, C_w (Pa)	10^7, 10^6	10^7, 10^6	10^7		10^7, 10^6	
f_c, $f_{c,w}$	Presented in Table 2	0.2, 0.1	0.6		0.1, 0.05	
ρ_0 ($kg\ m^{-3}$)	2700	2600	3300		3300	

[a](Gleason and Tullis, 1995) [b](Hirth and Kohlstedt, 2013)

Plastic strain weakening of the crust is implemented through a function of the accumulated plastic strain (ε), similar to previous approaches, as outlined in Ruh et al. (2014 and Vogt et al. (2017a). Both the cohesive (C) and internal friction angle (φ) strength are linearly reduced (C_w, φ_w) with incremental strain (ε) between 0.5 (ε_{min}) and 1.5 (ε_{max}):

$$C = \begin{cases} \mathrm{C} & if\ \varepsilon \leq\ \varepsilon_{min} \\ C + \dfrac{(C - C_w)}{(\varepsilon_{min} - \varepsilon_{max})}(\varepsilon - \varepsilon_{min}), & if\ \varepsilon_{min} <\ \varepsilon <\ \varepsilon_{max} \\ C_w, & if\ \varepsilon \geq\ \varepsilon_{max} \end{cases} \quad (5.3)$$

$$\varphi = \begin{cases} \varphi & if\ \varepsilon \leq\ \varepsilon_{min} \\ \varphi + \dfrac{(\varphi - \varphi_w)}{(\varepsilon_{min} - \varepsilon_{max})}(\varepsilon - \varepsilon_{min}), & if\ \varepsilon_{min} <\ \varepsilon <\ \varepsilon_{max} \\ \varphi_w, & if\ \varepsilon \geq\ \varepsilon_{max} \end{cases} \quad (5.4)$$

The effective viscosity (η) for the visco-plastic rheology is then determined through the minimum viscosity of each deformation mechanism:

$$\eta_{crust} = (\eta_p, \eta_{disl}) \quad (5.5)$$

$$\eta_{mantle} = (\eta_p, \eta_{disl}, \eta_{diff}) \quad (5.6)$$

Elasticity, that may alter the short-term stress distribution in our models, is not accounted for as orogenic wedges are assembled over geological timescales, with a visco-plastic rheology sufficiently encapsulating the long-term stress distribution (Kaus et al., 2008; Vogt et al., 2017a).

5.2.3. Surface processes

The surface is tracked using passive tracers along the boundary between the crust and sticky air. The passive tracers are advected along within the particles before being moved back to the original x coordinate (2D) or x-z coordinate (3D) along the new surface. Once back to the original position, the erosion and sedimentation rates are applied to the passive tracers to determine the new surface height:

$$dh = dt(v_s - v_e) \quad (5.7)$$

Where v_e and v_s are the erosion and sedimentation rates, respectively, dh is the change in height and dt is the timestep duration. The surface timesteps are smaller than the model CFL condition to allow accurate tracking of the surface. The surface timestep (dt) is determined using a tenth of the CFL condition, resulting in timesteps of ~11,700 years in 2D and ~23,400 in 3D for surface processes, therefore ~5 timesteps occur for surface processes for each model timestep.

To limit erosion to uplifted areas and sedimentation to basins, a condition is imposed based on the vertical position (y) of the surface compared to the original surface (y_0) (Gerya, 2019):

$$v_s = 0\ m\ yr^{-1}, v_e = v_e\ when\ y > y_0 \quad (5.8)$$

$$v_e = 0\ m\ yr^{-1}, v_s = v_s\ when\ y < y_0 \quad (5.9)$$

Erosion and sedimentation are applied through the material particles in the model. As the surface moves, new material is embedded beneath the surface as sediment that was previously sticky air, while crust or sediment material above the new surface is removed and re-assigned as sticky air.

5.3. Results

The 2D models are first presented in order of increasing friction coefficient from 0.1 to 0.4 first without and then with surface processes, focusing on the internal structure and topographic expression of each wedge to assess the role of each on the evolution of the wedge. The 3D models are then assessed to determine how changes in friction coefficient and surface processes influence the evolution of the orogen and the formation of salients and recesses.

Table 5.2: Experiments described in the text. Cases are labelled according to the friction coefficient, where 03fc represents a friction coefficient (f_c) of 0.3 with no surface processes. -SSP represents slow, and -FFP represents fast*, surface processes.*

Case Name	*f_c, $f_{c,w}$*	*Crustal material colour*	*V_e* *[mm yr^{-1}]*	*v_s* *[mm yr^{-1}]*
01fc	0.1, 0.05	Blue	0	0
01fc-SSP	0.1, 0.05	Blue	1	0.1
01fc-FSP	0.1, 0.05	Blue	0.5	0.05
02fc	0.2, 0.1	Pink	0	0
02fc-SSP	0.2, 0.1	Pink	1	0.1
02fc-FSP	0.2, 0.1	Pink	0.5	0.05
03fc	0.3, 0.15	Green	0	0
03fc-SSP	0.3, 0.15	Green	1	0.1
03fc-FSP	0.3, 0.15	Green	0.5	0.05
04fc	0.4, 0.2	Grey	0	0
04fc-SSP	0.4, 0.2	Grey	1	0.1
04fc-FSP	0.4, 0.2	Grey	0.5	0.05
01fc-04fc-3D	0.1, 0.05, 0.4, 0.2	Blue (f_c = 0.1), grey (f_c = 0.4)	0	0
01fc-SP-3D	0.1, 0.05	Blue (f_c = 0.1)	z < 150 km – 1 z > 150 km – 0.5	z < 150 km – 0.1 z > 150 km – 0.05

5.3.1. 2D models

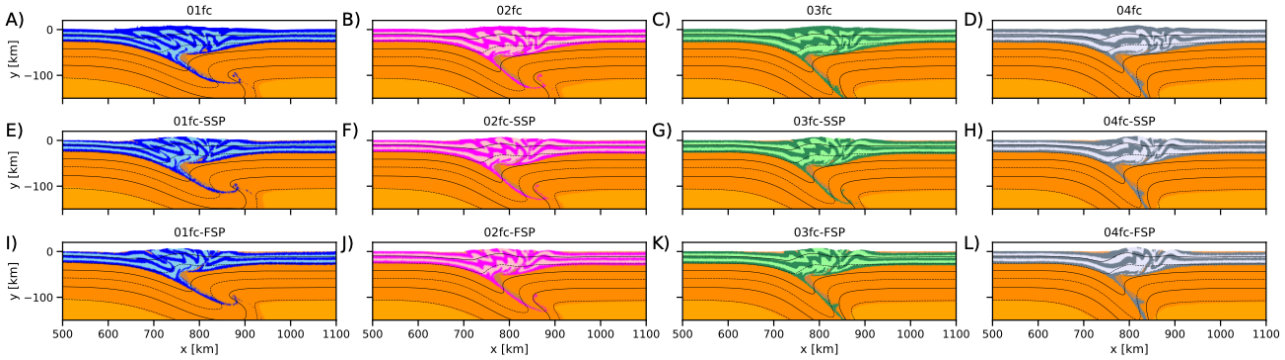

Figure 5.2: Material plots for models with different f_c values with no surface processes (A - D) or with slow (E – H) or fast (I – L) surface processes (SSP and FSP, respectively) after 450 km of convergence (t = 22.5 Myr). A clear transition from plastic-dominated features (stacking of the entire crust) in 01fc to viscous-dominated features (folding of crust) as in 04fc can be seen when looking left to right. SSP representing v_e = 0.5 mm yr^{-1} & v_s =0.05 mm yr^{-1} whilst FSP represents v_e = 1 mm yr^{-1} & v_s = 0.1 mm yr^{-1}. Regarding surface processes, the internal structural is very similar with and without surface processes, however surface processes do promote exhumation at the centre of the wedge.

The final structure of each wedge is presented in Figure 5.2, with a clear change in internal structure observed as f_c increases. The wedge in 01fc (Figure 5.2A) is characterised by the stacking of the entire crust, with deformation above the initial weak zone. The crustal stacking occurs along discrete planes with high amounts of plastic strain that extends to the base of the crust, with low strain in the areas between (Figure 5.3A). In contrast, convergence in 04fc (Figure 5.2D) is accommodated by the folding of crust, as seen by the material distribution. The amount of plastic strain localisation in the upper crust in 04fc (Figure 5.3D) is low compared to 01fc, with deformation accommodated in the viscous lower crust instead. Intermediate values of f_c (02fc - Figure 5.2B and 03fc - Figure 5.2C) show a transition between the two end members, displaying features of both, with the stacking of crust to mid-crustal levels, resembling 01fc, and flowing of the crust at the base of the orogen, comparable to 04fc. This is also seen in the plastic strain distribution, with the depth at which strain accumulates decreasing with increasing friction coefficient (Figure 5.3A-D). This is a result of the increasing friction coefficient which results in a decrease in the depth of the BD transition.

In 01fc, the influence of viscous rheology at the base of the crust is negligible and instead the entire crust is controlled by the yield strength of the crust and deforms in the plastic regime. As the friction coefficient increases, the viscous rheology becomes the dominant deformation mechanism that accommodates convergence as the thickness of the viscous layer at the base of the crust increases (Figure 5.1B). This is where our models differ from purely viscous wedges (Pusok and Kaus, 2015; Vanderhaeghe et al., 2003; Willett, 1999b), which do not exhibit crustal stacking or strain localisation as strain is not included in these models. Our models also differ from purely plastic wedges (Ruh et al., 2014, 2012) which exhibit increasing amounts of strain localisation with increasing friction coefficient, whereas our models show the opposite as viscous deformation becomes dominant, which reduces the amount of strain localisation (Figure 5.3A-D).

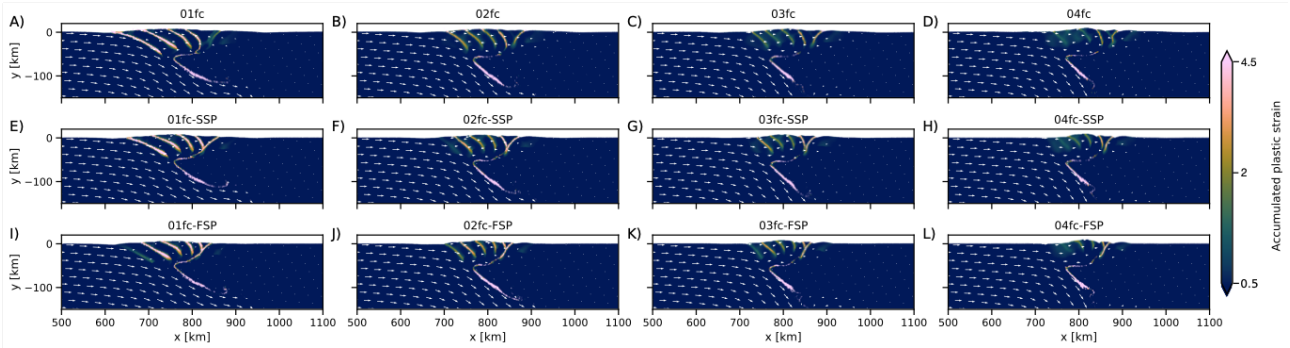

Figure 5.3: Strain plots for models with different f_c values with no surface processes (A - D) or with slow (E – H) or fast (I – L) surface processes (SSP and FSP, respectively) after 450 km of convergence (t = 22.5 Myr). A clear transition from plastic-dominated features (stacking of the entire crust), as seen in 01fc, to viscous-dominated features (folding of crust), as seen in 04fc, is observed. SSP represents v_e = 0.5 mm yr^{-1} & v_s =0.05 mm yr^{-1} whilst FSP represents v_e = 1 mm yr^{-1} & v_s = 0.1 mm yr^{-1}. surface processes, do not alter the overall internal structure much, but do reduce the distance between high strain zones and reduce the length of the wedge.

The models are repeated but include varying erosion (v_e) and sedimentation (v_s) rates to determine the role of surface processes on internal structure and on the width and thickness of the orogen. Surface processes do not alter the main deformation mechanism, resulting in similar internal structures for a given friction coefficient between models with and without surface processes. This is highlighted by the similar distribution of plastic strain for models with the same friction coefficient (Figure 5.3 – columns). However, surface processes promote exhumation at the centre of the wedge close to the initial weak zone,

exposing deep crustal material at the surface, revealed by the presence of lower crustal material at the surface in Figure 5.2E-2L. From Figure 5.2E-2L, the initial depth of material exposed at the surface after 450 km of convergence increases with increasing erosion rate, with the depth increasing from ~10 km in 01fc-SSP (Figure 5.2E) to ~20 km in 01fc-FSP (Figure 5.2I) based on the initial depth of the layers, but has negligible impact on the wedge thickness. The initial depth of material that is exposed at the surface is also dependent on the friction coefficient, with the initial depth of material exposed at the surface after 450 km of convergence increasing with decreasing friction coefficient, with material originally at a depth of ~20 km exposed at the surface in 01fc-FSP whilst material exposed at the surface in 04fc-FSP originating from a depth of ~10 km (Figure 5.2I – 2L), based on the initial depth of the layers.

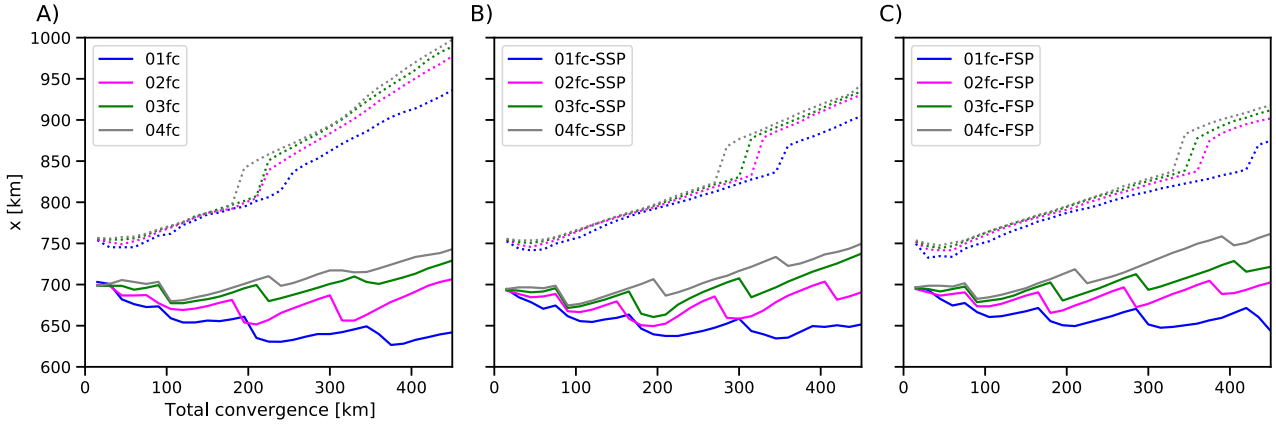

Figure 5.4: Evolution of orogens front (solid line) and rear (dotted line) position, based on the position of elevated topography (where y first exceeds 200 m at the orogens front and rear), for all 2D models. A) No surface processes, B) SSP models, c) FSP models. The distance between the front and back of the orogen represents the orogens width The model results show that both rheology and surface processes influence the width of the orogeny. The influence of rheology on orogen width increases as the amount of convergence increases.

Figure 5.4 presents the growth of topography at the front and rear of the orogen in each 2D model, highlighting the relative positions from each other, over the total convergence. Topography at the front of the orogen begins to grow at a similar location regardless of the friction coefficient or the influence of surface processes. In the models without surface processes (Figure 5.4A), the topography displays brief periods where the orogens front would converge between 01fc and 02fc, but the predominant trend is an

increase in the distance between the orogens front between each model as convergence continues. This is most pronounced between 01fc and 04fc, which diverge throughout the entire evolution of each orogen. The rear of the orogen shows a different evolution, with each model following a similar trend up to ~300 km of convergence, however the evolution of 01fc diverges from the other models after this point. This is due to the rheology of the lower crust influencing the amount of backward migration of the wedge. The role of the friction coefficient on wedge width is clear after 450 km of convergence, with a wedge width of ~300 km in 01fc and a width of ~250 km in 04fc, with a width difference of ~50 km. However, between 02fc and 04fc, the difference in wedge width is smaller, ~30 km (Figure 5.4A). Surface processes do not alter the overall growth of the orogen laterally but surface processes do restrict the wedge width. Between the models with high erosion (FSP) and no erosion, for any friction coefficient, a decrease in wedge with of ~50 km is observed (Figure 5.4A)

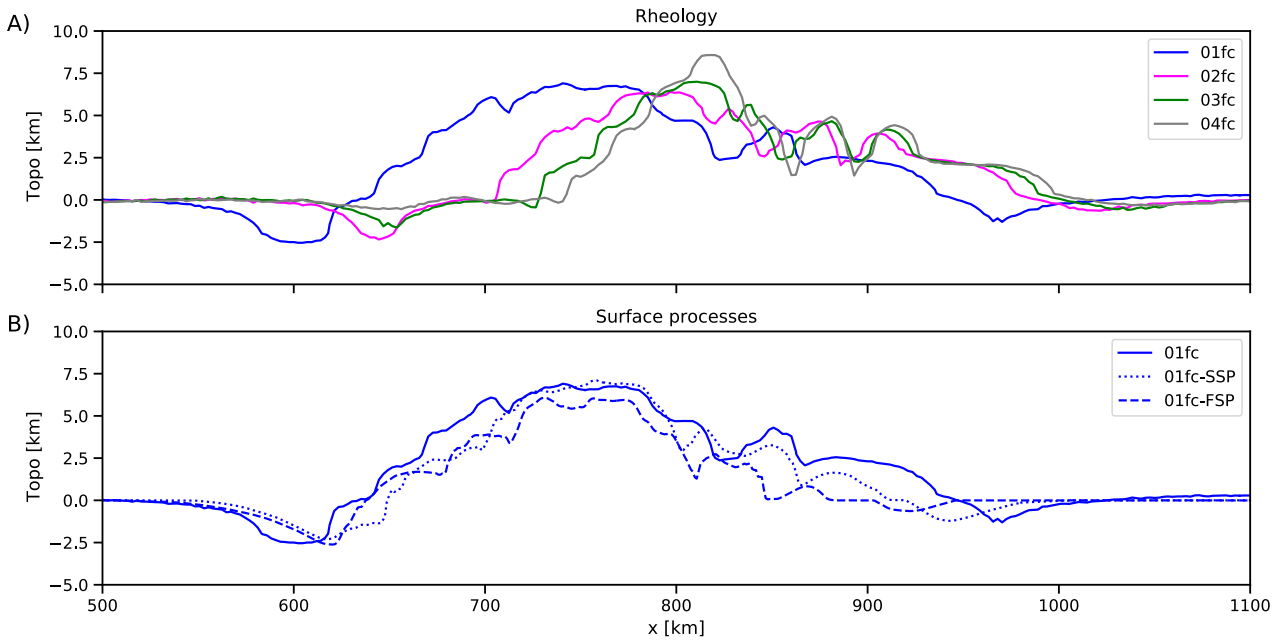

Figure 5.5: Comparison of topography due to A) rheology and B) surface processes after 450 km of convergence. Profiles taken from Fig. 3. In A) a large distance is observed at the front of the wedge between 01fc and 02fc of ~70 km, whilst erosion and sedimentation reduce the wedge with by ~50 km at the back of the wedge and ~10 km at the front of the wedge.

Figure 5.5 highlights the influence of rheology and surface processes on the final topography after 450 km of convergence. In Figure 5.5A, a different topographic distribution can be seen between each value of the friction coefficient tested. Increasing the friction coefficient results in the point of maximum topography migrating backwards, whilst also increasing the maximum height that can be supported (Figure 5.5A). This is a result of the thickness of the viscous layer in the lower crust that results in the wedge moving in the same direction as convergence. In 01fc, deformation is mainly concentrated at the front of the wedge and opposite to the direction of convergence, characteristic of plastic deformation, whilst in 04fc deformation is primarily concentrated at the back of the wedge and in the same direction as convergence. In contrast, surface processes do not have a major influence on the topographic shape but do result in a decrease in wedge width (Figure 5.5B).

The 1D strength profiles presented in Figure 5.1B are used to determine the average crustal strength (MPa). An increase in the friction coefficient increases the strength of the crust, with the average strength of the crust increasing from 46 MPa for an f_c of 0.1 to 111.3 MPa for an f_c of 0.4, with intermediate values of 71.9 MPa when f_c is 0.2 and 92.9 MPa when f_c is 0.3, with a quartzite rheology (Table 5.1) and a background strain rate of 10^{-14} s^{-1}. The increase in strength with increasing friction coefficient results in a decrease in wedge width and increase in topography, a proxy for crustal thickness, similar to previous studies that utilise a purely viscous rheology (Pusok and Kaus, 2015; Willett, 1999b) a purely plastic rheology (Ruh et al., 2012; Willett, 1999b) or viscoplastic rheology (Vogt et al., 2017b, 2017a; Willett, 1999b). This is observed in the 2D topography (Figure 5.5A) after 450 km of convergence (22.5 Myr), which shows a decrease in the wedge width and increase in topographic height with increasing friction coefficient.

Thee 2D results suggest that salients and recesses controlled by rheology can be identified based on the topography, which varies along strike (Figure 5.5A). In contrast,

erosion and sedimentation results in a decrease in wedge width but does not alter the overall topographic distribution or point of maximum topography (Figure 5.5B). These results suggest the topography can be used to identify the cause of salients and recesses in nature.

5.3.2. 3D models

5.3.2.1. Role of lateral variation in rheology

The topography in Figure 5.6A after 450 km of convergence provides insights into how the topography responds to lateral variations in rheology. Figure 5.6A shows the change in location of maximum topography along strike, in agreement with the findings from the 2D model (Figure 5.5A). Where $f_c = 0.1$ (blue material, $z > 150$ km) the peak topography occurs at x ~770 km, whilst where $f_c = 0.4$ (grey material, $z < 150$ km) the peak in topography occurs at x ~810 km. A large variation in wedge width is also observed, with displacements of ~40 km at the front of the wedge and ~10 km at the back, with a total of ~50 km difference in wedge width observed, on average (Figure 5.7). The difference in wedge width results in sharp changes in topographic height across the transition zone (y = 150 km), as observed at x = 700 km, where the topography decreases from ~6 km to ~1 km over a short distance. The topography also shows different distributions away from the transition zone, with the topography widening away from the transition zone where $f_c = 0.4$ ($y < 150$ km) whilst the topography appears to narrow away from the transition zone where $f_c = 0.1$ ($y > 150$ km).

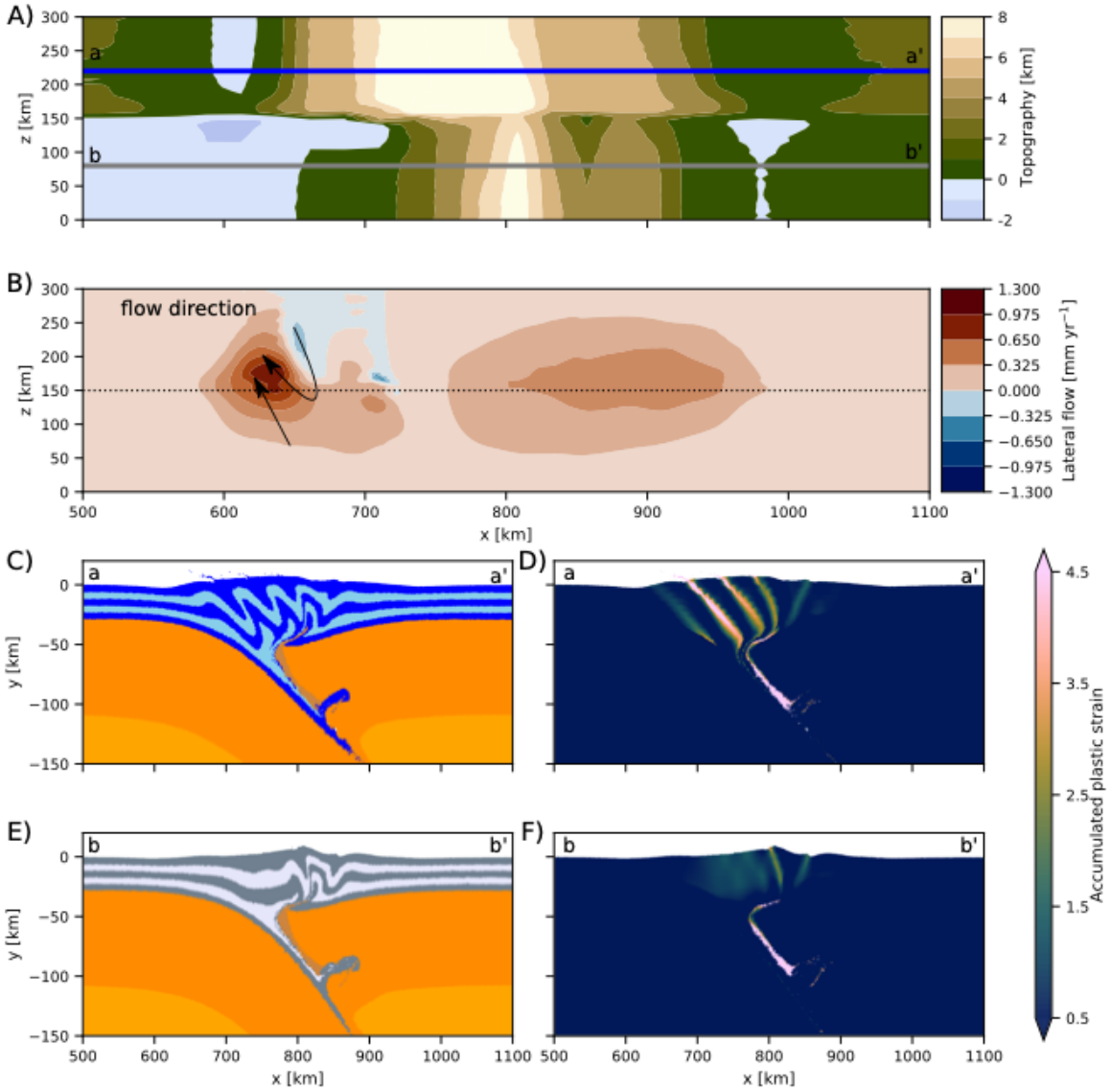

Figure 5.6: A) Plot of surface topography, B) lateral flow at a depth of ~4 km below the surface and 2D profiles of material (C and E) and accumulated plastic strain (D and D) for 01fc-04fc-3D after 450 km of convergence. The dotted lines in (A) represent the profiles taken to measure the evolution of topography in Figure 5.7 and the location of the profiles of material (C and E) and strain (D and F). The topography highlights how the location of peak topography is discontinuous along strike, with a salient forming where rheological strength is low (z > 150 km) and a recess forming where rheological strength is high (z < 150 km).

Figure 5.7 shows the evolution of elevated topography across a profile taken perpendicular to the strike of the orogen and parallel to convergence. In the 3D models, elevated topography begins to develop at a similar position but diverge as convergence is ongoing to around ~40 km after 450 km of convergence. This is due to the friction coefficient, and thus higher strength, of the crust where the friction coefficient is 0.4 restricting the outward growth of the orogen. This results in a salient forming where strength is low and a recess where strength is high Figure 5.7. At the rear of the orogen, the region of elevated

topography follows a similar path throughout the evolution of the wedge, with a constant distance of ~10 km between the elevated topography at the rear of the orogen. This results in a difference in wedge width of ~50 km between the different crustal strengths, similar to the 2D results. The models did not reach a constant difference in wedge width after 450 km of convergence but might as convergence continues.

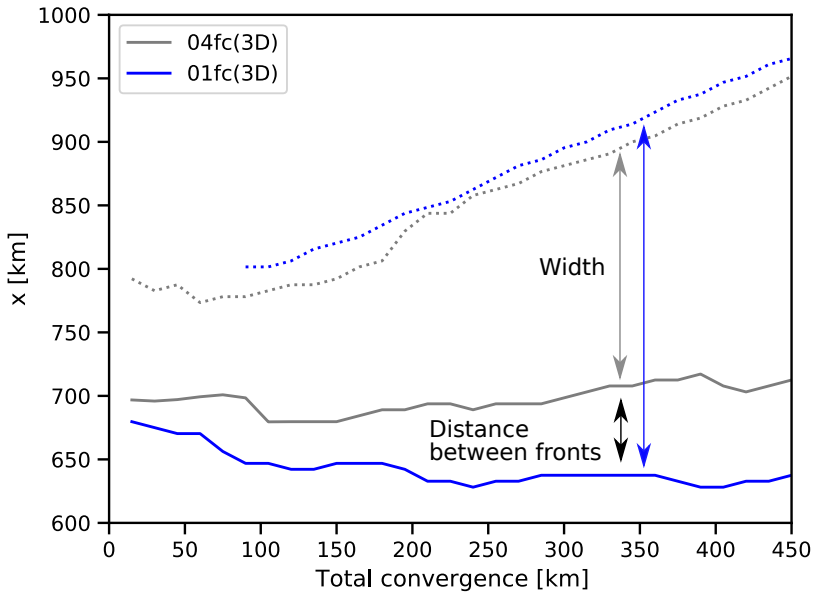

Figure 5.7: Evolution of orogens front (solid line) and rear (dotted line) over 450 km of convergence for 01fc-04fc-3D. The y axis represents the x-coordinate where the topography first (front - solid) or last (back - dotted) exceeds a height of 200 m. The grey lines represent the evolution of the topography at z = 80 km where the crust has a friction coefficient of 0.4 (04fc) and blue is measured at z = 220 km where the crust has a friction coefficient of 0.1 (01fc). The model highlights a similar evolution to the 2D models (Figure 5.4A), with the topographic fronts diverging throughout convergence to form a salient (blue) and recess (grey) in the 3D models.

5.3.2.2. Role of lateral variation in surface processes

Figure 5.8 provides insights into how the topography responds to lateral variations in surface process in case 01fc-SP-3D. Figure 5.8 shows that the position of the peak in topography does not vary along strike of the orogen, with the maximum topography located at x ~750 km, in contrast to 3D model 01fc-04fc-3D (Figure 5.6) which does show lateral variation in peak topography along strike. Another feature different to 01fc-04fc-3D in 01fc-SP-3D is how the transition occurs along strike from a low rate of surface processes (y > 150 km) to a high rate of surface processes (y < 150 km). The topography appears to narrow toward the transition zone at y = 150 km, whilst the topography and topographic fronts

appear smoother and occurs over a wider area compared to the rheological model (01fc-04fc-3D).

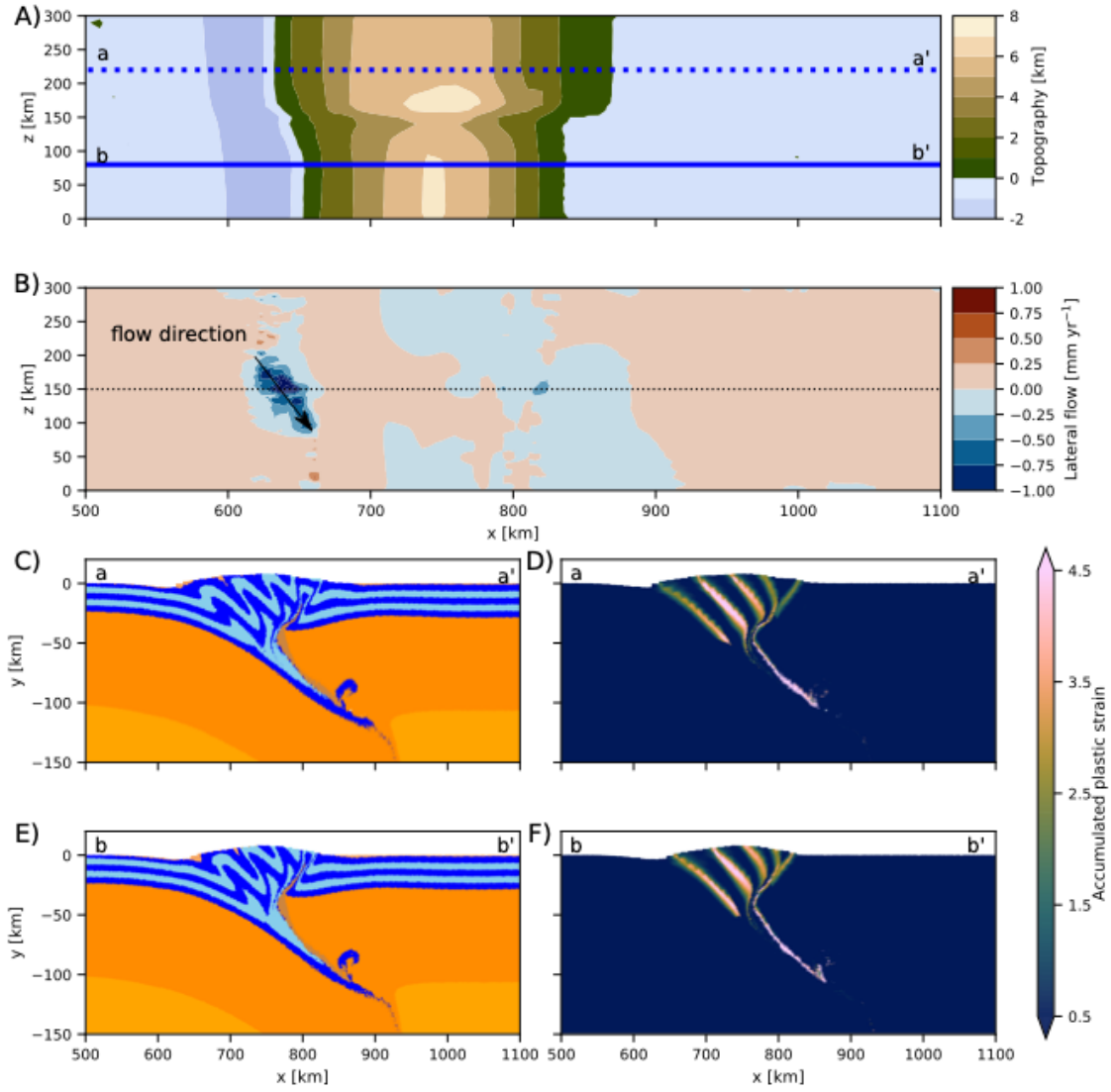

Figure 5.8: A) Plot of surface topography and B) lateral flow direction at a depth of ~4 km below the surface. 2D profiles of material (C and E) and accumulated plastic strain (D and F) for 01fc-SP-3D after 450 km of convergence. The dotted lines in (A) represent the profiles taken to measure the evolution of topography in Figure 5.9 and the 2D profiles of material (C and E) and strain (D and F). The topography highlights how the location of peak topography is continuous along strike, with a salient forming where the orogen is wide due to slow erosion rates (z > 150 km) and a recess forming where the orogen is narrow due to fast erosion rates (z < 150 km).

Figure 5.9 illustrates the evolution of the front and rear of the orogen in 01fc-SP-3D based on the topographic evolution from a profile perpendicular to the orogen which is parallel to the convergence direction. The results of the topography in the 3D is similar to the 2D models, which show an increase in the difference in wedge width as the orogen expands due to increasing erosion rates. As convergence is ongoing, there are points at

which the front of the wedge converges, this is due to widening of the orogen occurring at different times due to the lateral variation in the erosion rates. As the slow erosion rate is restricting the wedge, the fast erosion side widens due to the continued convergence which results in the fronts reaching a similar location, for example after 375 km of convergence (Figure 5.9). However, the main trend is an increase in the difference in the width of the orogen as material is eroded quicker on one side, forming a salient where surface processes are slow and a recess where they are high. The profile across the side with slow erosion (Figure 5.9 – blue) shows a wider orogen compared to the side with fast erosion (Figure 5.9 – cyan). The increase in the width mainly occurs at the front of the orogen, with a difference of ~20 km at the front of the orogen and ~10 km at the back orogen, resulting in a difference in width of ~30 km (Figure 5.8). This is expected from the 2D results, as the width of the orogen decreases when the rate of erosion increases.

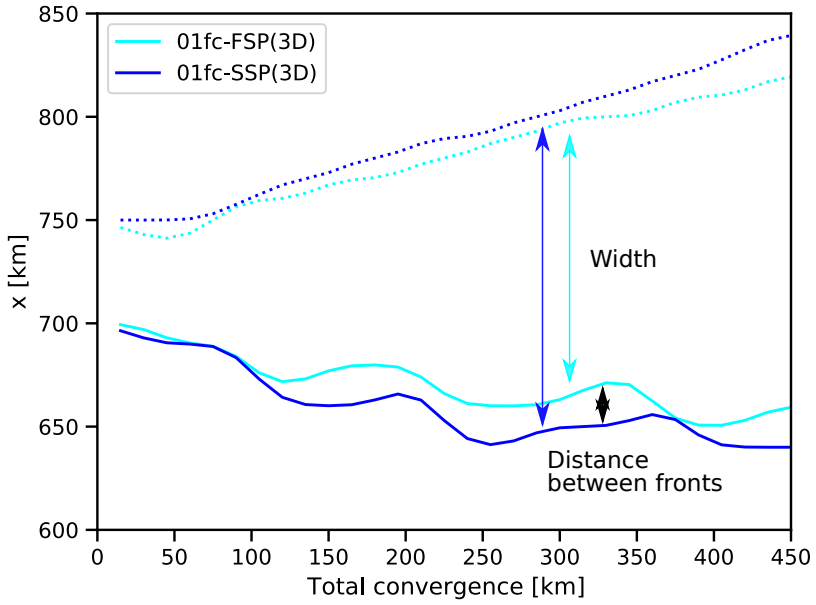

Figure 5.9: Evolution of orogens front (solid line) and rear (dotted line) over 450 km of convergence for 01fc-SP-3D, where the constant fc throughout but the erosion & sedimentation rates vary laterally. The y axis represents the x-coordinate where the topography first (front - solid) or last (back - dotted) exceeds a height of 200 m. The blue lines represent the evolution of the topography at z = 80 km where slow erosion and sedimentation rates (SSP) are applied and cyan is measured at z = 220 km, where the fast erosion and sedimentation rates (FSP) are applied. SSP represents v_e = 0.5 mm yr^{-1} & v_s =0.05 mm yr^{-1} whilst FSP represents v_e = 1 mm yr^{-1} & v_s = 0.1 mm yr^{-1} .The model highlights a similar evolution to the 2D models (Figure 5.4), with the topographic fronts diverging to form a salient (blue) and recess (grey) in the 3D models. The outward propagation of the orogen front occurs at different amounts of convergence due to varying erosion and sedimentation rates, resulting in periods where the fronts of both orogens are at a similar position (e.g. at ~375 km of convergence).

5.4. Discussion

5.4.1. Role of crustal strength on the formation of salients and recesses

We investigate the role of crustal strength by varying the friction coefficient and find a decrease in wedge width and increase in thickness and topographic height with increasing friction coefficient (Figure 5.5A). We find that while increasing the friction coefficient increases the influence of the viscous rheology in the lower crust, it also results in an overall increase in strength of the crust. This is due to the increase in strength through an increase in the friction coefficient outweighs the decrease in strength caused by the decrease in the depth of the brittle-ductile transition (Figure 5.1B). Our results are in agreement with other lithospheric-scale models (Pusok and Kaus, 2015; Vogt et al., 2017b, 2017a; Willett, 1999b) and fold-and-thrust belt models (Ruh et al., 2014, 2012) that also show an increase in crustal strength leads to a decrease in wedge width and increase in thickness and topographic height for the same amount of convergence.

The evolution of the orogen's width and internal structure is similar in the 3D model when the rheology in varied laterally (01fc-04fc-3D) and variations in rheology in the 2D models (Figure 5.4A), implying the 2D models provide appropriate insights in to the formation of salients and recesses in 3D when away from the contact between the different crustal material. The 2D results suggest that as the difference in rock strength increases laterally, the wedge width of the orogen increases. The difference in width is also dependent on the amount of convergence, which increases with convergence (Figure 5.7).

However, close to the boundary in 01fc-04fc-3D, lateral flow is observed from the strong to the weak side and from low to high topography (Figure 5.6B). The opposite occurs in the erosion and sedimentation models, where flow is induced from high to low topography (Figure 5.8B). This flow in 01fc-04fc-3D may be a result of the rheology, as the weaker

material is easier to deform so material ‘escapes’ from the strong side to the weak side. This may be due to the boundary operating as a strike-slip fault, where the strong side forms a relatively stable front that does not move whilst the weak side migrates outwards, forming a recess. This could result in lateral flow across the boundary from the strong to weak side as space is created by this movement which induces flow.

Our models do not exhibit self-organisation as predicted for the Himalayan arc by Weinberg (2016), with the distance between the fronts of the salients and recesses increasing as the amount of convergence increases. The fact that our models did not reach a steady state maximum distance between salient and recess may be because of the relatively short total convergence or the quasi-2D nature of the models. It could also be a result of the large differences in overall strength of the entire crust, with different deformation mechanisms operating to accommodate convergence and different structures forming. In the Himalayas at a large scale, major structures can be traced along the entire orogen (Searle and Treloar, 2019), suggesting that the overall strength of the crust may be similar across the orogen that may favour self-organisation. However, at local scale, the structures can vary considerably (Matin and Mukul, 2020; Roberts et al., 2020), suggesting local heterogeneities in crustal strength could be involved in the formation of salients and recesses.

If the lithospheric strength is similar, a similar evolution occurs and internal structure forms. This can be achieved through the dominant deformation mechanism. If difference rock units have a similar friction coefficient along the orogen, which is expected from laboratory experiments (Byerlee, 1978), but different viscous rheologies and plastic deformation dominates due to high velocities or a low Moho temperature (Knight et al., 2021), then a similar evolution is wedge width is expected. On the other hand, if lateral variations in rock units have similar viscous rheology and different friction coefficients and

viscous deformation dominates due to low velocities or a high Moho temperature (Knight et al., 2021), again a similar evolution is wedge width is expected. This is due to the wedge width being controlled by the strength of the crust, when the strength is similar then a similar width would arise even in different units.

5.4.2. Surface processes on salients and recesses

Surface processes form salients and recesses by restricting the outward growth of the wedge through erosion, as observed in the final topography in Figure 5.5B. The restricted wedge width is due to surface processes redistributing material across the wedge, with erosion removing material from topographic highs and sedimentation resulting in deposition of material in topographic lows. The removal of material reduces the vertical stress acting on the wedge, stopping the lateral growth of the wedge and the outward propagation of deformation, instead surface processes prolong fault activity and increase strain localisation along faults, with deformation concentrated at the centre of the orogenic wedge, which is most notable in the plastic strain distribution (see Figure 5.3) (Avouac and Burov, 1996; Dal Zilio et al., 2020; Ellis et al., 2001; Jammes and Huismans, 2012; Jaquet et al., 2017; Piccolo et al., 2017; Selzer et al., 2007) and promotes exhumation of mid-crustal material, observed in the distribution of crustal material (Figure 5.2, bottom row) (Dal Zilio et al., 2020; Jammes and Huismans, 2012; Kaus et al., 2008).

Surface processes can influence the internal structure when erosion rates are similar to uplift rates, as observed in Beaumont et al. (1996) and Willett (1999a). The rapid removal of material restricts any outward growth of the wedge, concentrating deformation and exhumation along a single back thrust. These studies demonstrate that surface processes can have a first order influence on the internal structure if erosion rates are comparable to

uplift rates. However, as the erosion rate in the models presented here is below the rate required for this, this phenomenon is not observed.

5.4.3. Identifying the causes of salients and recesses in nature

The 3D model results demonstrate how the topography can be used to identify the causes of salients and recesses in nature. When the salient and recess is rheological in nature, a change in the overall topographic shape occurs, with the location of maximum topography varying migrating in the same direction as convergence as the friction coefficient increases (Figure 5.5A). In contrast, when there are lateral variations in erosion and sedimentation rates, the topography is constant along strike, but the width of the orogen changes (Figure 5.5B).

The Himalayan arc is consistent along strike at large scale and can be defined by a small circle (Figure 5.10) (Bendick and Bilham, 2001), however at smaller scale, a sinuous front is visible, forming salients and recesses (Macedo and Marshak, 1999; Mukul, 2010). There are two types of recesses along the Himalayan front, they are either open to the foreland (e.g. Gorubathan recess) or contain intermontane, longitudinal valleys or Duns (e.g. Dehradun and Kangra recesses) (Mukul, 2010; Srivastava et al., 2017), implying different processes result in the formation salients and recesses in the region.

Deviations in topographic height along the Himalayan front are used to identify the locations of salients and recesses (Figure 5.10A), whilst the free-air gravity anomaly (Figure 5.10B) has previously been used to identify areas of different crustal strength due to areas of high strength able to support large crustal thicknesses (Koulakov et al., 2015). The salients and recesses identified in the Himalayas are in the order of ~50 km in width along the front of the orogen. Areas of thicker crust are identified by higher topography and higher

free-air gravity anomaly and correlate these areas to areas of higher crustal strength, which is required to support thicker crust (Koulakov et al., 2015).

The topography shows two clear recesses between 80 and 90 °E, however these recesses show very different features in both the topography and free-air gravity anomalies. R1, located at 84 °E and 28 °N shows multiple intermontane, longitudinal valleys in the topography that converge at the recess. The topography is consistent along R1, with a small gap due to a longitudinal valley that originate from deep within the orogen. The recess shows lower, negative free-air gravity anomalies values compared with the surrounding area, with the negative values correlating with the with the intermontane, longitudinal valleys. These distinctive features in the topography and free-air gravity anomalies suggest that the formation of R1 is due to focused erosion in the region. Another area of focused erosion, visible due to intermontane valleys, can be seen within the region of S2. However, the free-air gravity anomalies in S2 are not as low or as extensive compared to R1, suggesting that for recesses to form, similar to R1, high amounts of erosion must occur.

In contrast to R1, R2 shows different features in the topography and free-air gravity anomalies. R2 is flanked by erosional channels and longitudinal valleys, however the area behind R2 shows a lack of erosional processes operating the region, suggesting R2 is harder to erode than the surrounding area, with the topography also showing a change in topographic height across R2. The free-air gravity anomalies close to R2 are positive, suggesting that the crust is strong in that region. These features of R2 suggest that the region is of due to rheological heterogeneities rather than lateral variations in erosion rates.

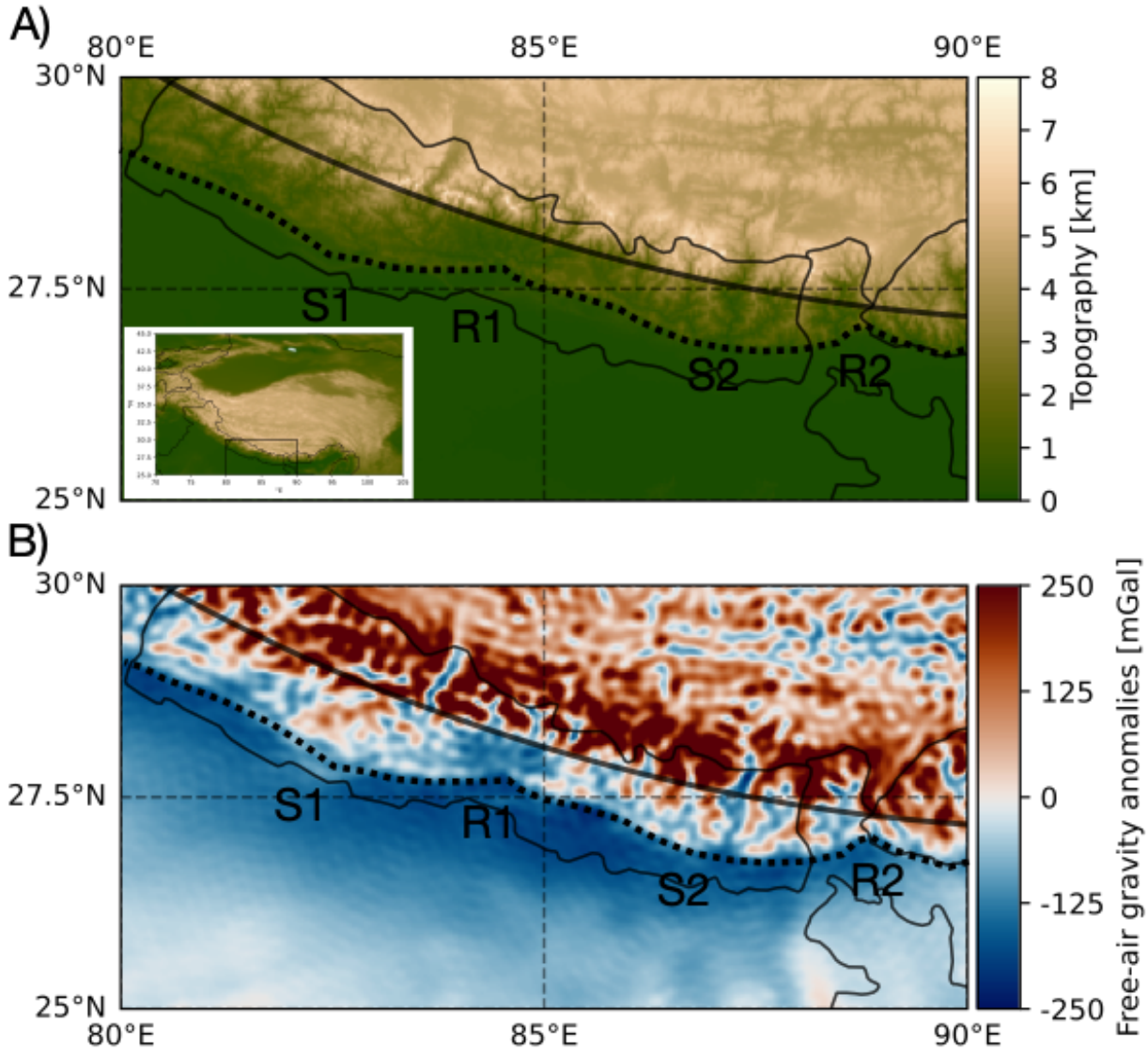

Figure 5.10: A) Topography from EarthEnv-DEM90 (Robinson et al., 2014) and B) free air gravity anomalies from WGM2012 (Balmino et al., 2012) of the Himalayan arc between 85 and 92 °E, along with the small circle arc from Bendick and Bilham (2001) that is centred at 92.6 °E, 42.4 °N with a radius of 1696 km. Two salients (S1 & S2) and recesses (R1 & R2) are marked along the orogen front but show very different topographic and free-air gravity anomaly features. The black lines represent country boundaries.

The position of R2 (Figure 5.10) marks the Gorubathan recess, with the mountain front receding to the north by ~11 km compared with the Dharan salient (S2) (Mukul, 2010; Srivastava et al., 2017), with the boundary between the two defined by the Gish Transverse Fault (GTF) (Mukul, 2010). As well as the wedge width varying across the Dharan salient and Gorubathan recess, the structures also vary significantly. Differences in structure include a thicker, better developed Munsiari thrust (MT) in the Dharan salient compared to the Gorubathan recess, as well as kilometre-scale folding observed in the Gorubathan

recess not observed in the Dharan salient (Matin and Mukul, 2020). Further evidence supporting variations in rheology between the Dharan salient and Gorubathan recess is observed in the transport direction on the Main Central Thrust Zone (MCTZ). Structural mapping and microstructural analysis around the Darjeeling-Sikkim section of the MCTZ showed a curved movement of flow, with parts of flow recording movement towards the recess and then curving around to movement away from the recess between 20 and 9 Ma and was attributed to rheological heterogeneities in the crust (Roberts et al., 2020). This is similar to the lateral flow observed in Figure 5.6B, which also shows a curved flow from the recess to the salient which then curves back towards the recess at a depth of ~4 km (Figure 5.6B). The differences in structure and flow direction across the Dharan salient and Gorubathan recess, along with a lack of large erosional features observed in the topography of the Gorubathan recess, suggest the recess is caused by lateral variations in rock strength. These features also highlight the local variations along the length of the Himalayan arc that cannot be identified at large scales.

The analysis of drainage patterns across salients and recesses in the Himalayas highlights the feedback between rock strength and surface processes, demonstrating that the formation of salients and recesses in nature is more complex, Erosion rates, measured in a coastal setting over a period of years to centuries, varies based on the lithology, with orders of erosion rates generally of the order of 10^{-3} m yr^{-1} for granitic rocks, 10^{-3} to 10^{-2} m yr^{-1} for limestone and 10^{0} to 10^{1} m yr^{-1} for Quaternary sediments (Tsuguo, 1983). These erosion rates are enhanced by the presence of discontinuities in the rocks, such as cracks, cleavages, joints, faults, and bedding planes, which can be due to the lithology or tectonic in origin, and the strength of rocks can also be further reduced due to weathering (Sunamura, 2005). These erosion rates highlight the feedback between rock type, which also relates to the rheology, and erosion, highlighting that both processes most likely occur

at the same time. However, in these situations where both the rheology and erosion rates vary laterally, rheology is most likely the dominant factor as lateral variations in strength are in the order of ~10^7 Pa (Burov, 2011), which is higher than the fluvial shear stress (Liu et al., 2020) that results in erosion and transport of material along river channels (~10^2 Pa).

5.4.4. Model limitations

The models utilised in this study are simple versions of nature's complexities, used to investigate the causes of salients and recesses. For the rheological models, we assume a homogenous crust, with the lateral heterogeneity occurring along a straight boundary. Rigids present in the Indian crust have been inferred to represent variations in rheology oblique to the orogen front (Godin et al., 2019; Godin and Harris, 2014) that are thought to result in the formation of some of the salients and recesses along the Himalayan front, whilst other heterogeneities occur within the crust throughout the orogen. Another simplification is the use of a constant velocity condition to represent sedimentation and erosion rates. Erosion rates have previously been recorded to scale with topography, with erosion rates highest at highest elevations, with a non-linear relationship between topographic height and erosion rates (Montgomery and Brandon, 2002). Erosion rates in nature combine a range of complex processes that results in variations in topography, which is seen in Figure 5.10. Future models could include these complex processes by incorporating surface process modelling by utilising the Badlands software (Salles, 2016) that can be incorporated along with geodynamic modelling in Underworld2. However, our models provide insights into the role of rheology and surface processes on the formation of salients and recesses and provides a basis for future work that incorporate detailed surface processes.

5.5. Conclusions

We used both 2D and 3D numerical models with a viscoplastic rheology to investigate the role of rheology and surface processes on the formation of salients and recesses. The main results can be summarized as follows:

1. Increasing friction coefficient results in an increase in the overall strength of the crust, but also decreases the depth of the brittle-ductile transition, increasing the thickness of the viscous lower crust. This results in a change in structural style, with high amounts of strain and crustal stacking favoured at a low friction coefficient, with viscous flow and folding of the crust favoured at a high friction coefficient. As the strength of the crust increases, the wedge width decreases.

2. Erosion and sedimentation do not alter the overall structural style of the wedge, which is determined by the friction coefficient. However, erosion does promote the exhumation of crust at the centre of the wedge, reduces the distance between shear zones and restricts the widening of the wedge by reducing the gravitational load acting on the wedge.

3. The cause of the salients and recesses can be identified from the topography. Lateral variations in rheology result in a discontinuous topographic peak along the orogen, whilst surface processes produce a continuous topographic peak along the orogen.

4. In nature, additional topographic features (e.g. drainage networks) can be used to aid in determining the cause of salients and recesses. However, this highlights the feedback between rheology and erosion, with lower strength rocks more susceptible to erosion.

5. Additional data, such as structural mapping or free-air gravity anomalies, can also be used to deduce the causes of salients and recesses in nature.

5.6. References

Avouac, J.P., Burov, E.B., 1996. Erosion as a driving mechanism of intracontinental mountain growth. J. Geophys. Res. Solid Earth 101, 17747–17769. https://doi.org/10.1029/96JB01344

Balmino, G., Vales, N., Bonvalot, S., Briais, A., 2012. Spherical harmonic modelling to ultra-high degree of Bouguer and isostatic anomalies. J. Geod. 86, 499–520. https://doi.org/10.1007/s00190-011-0533-4

Beaumont, C., Ellis, S., Hamilton, J., Fullsack, P., 1996. Mechanical model for subduction-collision tectonics of Alpine-type compressional orogens. Geology 24, 675–678. https://doi.org/10.1130/0091-7613(1996)024<0675:MMFSCT>2.3.CO;2

Bendick, R., Bilham, R., 2001. How perfect is the Himalayan arc? Geology 29, 791–794.

Beucher, R., Moresi, L., Giordani, J., Mansour, J., Sandiford, D., Farrington, R., Mondy, L., Mallard, C., Rey, P., Duclaux, G., Kaluza, O., Laik, A., Morón, S., 2019. UWGeodynamics: A teaching and research tool for numerical geodynamic modelling. J. Open Source Softw. 4, 1136. https://doi.org/10.21105/joss.01136

Burov, E.B., 2011. Rheology and strength of the lithosphere. Mar. Pet. Geol. 28, 1402–1443. https://doi.org/10.1016/j.marpetgeo.2011.05.008

Chen, L., Capitanio, F.A., Liu, L., Gerya, T.V., 2017. Crustal rheology controls on the Tibetan plateau formation during India-Asia convergence. Nat. Commun. 8, 15992. https://doi.org/10.1038/ncomms15992

Dahlen, F.A., 1984. Noncohesive critical Coulomb wedges: An exact solution. J. Geophys. Res. Solid Earth 89, 10125–10133. https://doi.org/10.1029/JB089iB12p10125

Dahlen, F.A., 1988. Mechanical energy budget of a fold-and-thrust belt. Nature 331, 335–337. https://doi.org/10.1038/331335a0

Dahlen, F.A., 1990. Critical Taper Model of Fold-And-Thrust Belts and Accretionary Wedges. Annu. Rev. Earth Planet. Sci. 18, 55–99. https://doi.org/10.1146/annurev.ea.18.050190.000415

Dal Zilio, L., Ruh, J., Avouac, J.-P., 2020. Structural Evolution of Orogenic Wedges: Interplay Between Erosion and Weak Décollements. Tectonics 39, e2020TC006210. https://doi.org/10.1029/2020TC006210

Dal Zilio, L., van Dinther, Y., Gerya, T.V., Pranger, C.C., 2018. Seismic behaviour of mountain belts controlled by plate convergence rate. Earth Planet. Sci. Lett. 482, 81–92. https://doi.org/10.1016/j.epsl.2017.10.053

Davis, D., Suppe, J., Dahlen, F.A., 1983. Mechanics of fold-and-thrust belts and accretionary wedges. J. Geophys. Res. Solid Earth 88, 1153–1172. https://doi.org/10.1029/JB088iB02p01153

Ellis, M., 1988. Lithospheric Strength in Compression: Initiation of Subduction, Flake Tectonics, Foreland Migration of Thrusting, and an Origin of Displaced Terranes. J. Geol. 96, 91–100.

Ellis, S., Wissing, S., Pfiffner, A., 2001. Strain localization as a key to reconciling experimentally derived flow-law data with dynamic models of continental collision. Int. J. Earth Sci. 90, 168–180. https://doi.org/10.1007/s005310000151

Gerya, T., 2019. Introduction to Numerical Geodynamic Modelling. Cambridge University Press.

Gleason, G.C., Tullis, J., 1995. A flow law for dislocation creep of quartz aggregates determined with the molten salt cell. Tectonophysics, 30 Years of Tectonophysics a Special Volume in Honour of Gerhard Oertel 247, 1–23. https://doi.org/10.1016/0040-1951(95)00011-B

Godin, L., Harris, L.B., 2014. Tracking basement cross-strike discontinuities in the Indian crust beneath the Himalayan orogen using gravity data – relationship to upper crustal faults. Geophys. J. Int. 198, 198–215. https://doi.org/10.1093/gji/ggu131

Godin, L., Soucy La Roche, R., Waffle, L., Harris, L.B., 2019. Influence of inherited Indian basement faults on the evolution of the Himalayan Orogen. Geol. Soc. Lond. Spec. Publ. 481, 251–276. https://doi.org/10.1144/SP481.4

Hirth, G., Kohlstedt, D., 2013. Rheology of the Upper Mantle and the Mantle Wedge: A View from the Experimentalists, in: Inside the Subduction Factory. American Geophysical Union (AGU), pp. 83–105. https://doi.org/10.1029/138GM06

Jammes, S., Huismans, R.S., 2012. Structural styles of mountain building: Controls of lithospheric rheologic stratification and extensional inheritance. J. Geophys. Res. Solid Earth 117. https://doi.org/10.1029/2012JB009376

Jaquet, Y., Duretz, T., Grujic, D., Masson, H., Schmalholz, S.M., 2017. Formation of orogenic wedges and crustal shear zones by thermal softening, associated topographic evolution and application to natural orogens. Tectonophysics. https://doi.org/10.1016/j.tecto.2017.07.021

Kaus, B.J.P., Steedman, C., Becker, T.W., 2008. From passive continental margin to mountain belt: Insights from analytical and numerical models and application to Taiwan. Phys. Earth Planet. Inter., Recent Advances in Computational Geodynamics:

Theory, Numerics and Applications 171, 235–251. https://doi.org/10.1016/j.pepi.2008.06.015

Koulakov, I., Maksotova, G., Mukhopadhyay, S., Raoof, J., Kayal, J.R., Jakovlev, A., Vasilevsky, A., 2015. Variations of the crustal thickness in Nepal Himalayas based on tomographic inversion of regional earthquake data. Solid Earth 6, 207–216. https://doi.org/10.5194/se-6-207-2015

Liu, Y., Tan, X., Ye, Y., Zhou, C., Lu, R., Murphy, M.A., Xu, X., Suppe, J., 2020. Role of erosion in creating thrust recesses in a critical-taper wedge: An example from Eastern Tibet. Earth Planet. Sci. Lett. 540, 116270. https://doi.org/10.1016/j.epsl.2020.116270

Livani, M., Scrocca, D., Arecco, P., Doglioni, C., 2018. Structural and Stratigraphic Control on Salient and Recess Development Along a Thrust Belt Front: The Northern Apennines (Po Plain, Italy). J. Geophys. Res. Solid Earth. https://doi.org/10.1002/2017JB015235

Macedo, J., Marshak, S., 1999. Controls on the geometry of fold-thrust belt salients. Geol. Soc. Am. Bull. 15.

Matin, A., Mukul, M., 2020. Himalayan cross faults affect thrust sheet geometry: An example from the Munsiari thrust sheet near the Gish Transverse fault zone, frontal Darjiling Himalaya, India. J. Asian Earth Sci. 199, 104400. https://doi.org/10.1016/j.jseaes.2020.104400

Medvedev, S., 2002. Mechanics of viscous wedges: Modeling by analytical and numerical approaches. J. Geophys. Res. Solid Earth 107, ETG 9-1. https://doi.org/10.1029/2001JB000145

Miser, H.D., 1932. Oklahoma structural salient of the Ouachita Mountains. Geol Soc Am Bull 43, 138.

Montgomery, D.R., Brandon, M.T., 2002. Topographic controls on erosion rates in tectonically active mountain ranges. Earth Planet. Sci. Lett. 201, 481–489. https://doi.org/10.1016/S0012-821X(02)00725-2

Moresi, L., Dufour, F., Mühlhaus, H.-B., 2003. A Lagrangian integration point finite element method for large deformation modeling of viscoelastic geomaterials. J. Comput. Phys. 184, 476–497. https://doi.org/10.1016/S0021-9991(02)00031-1

Moresi, L., Quenette, S., Lemiale, V., Mériaux, C., Appelbe, B., Mühlhaus, H.-B., 2007. Computational approaches to studying non-linear dynamics of the crust and mantle. Phys. Earth Planet. Inter. 163, 69–82. https://doi.org/10.1016/j.pepi.2007.06.009

Mukul, M., 2010. First-order kinematics of wedge-scale active Himalayan deformation: Insights from Darjiling–Sikkim–Tibet (DaSiT) wedge. J. Asian Earth Sci., Tectonics of the Indian Subcontinent 39, 645–657. https://doi.org/10.1016/j.jseaes.2010.04.029

Piccolo, A., Faccenda, M., Carosi, R., Montomoli, C., Visonà, D., 2017. Crustal strength control on structures and metamorphism in collisional orogens. Tectonophysics. https://doi.org/10.1016/j.tecto.2017.09.018

Pusok, A.E., Kaus, B.J.P., 2015. Development of topography in 3-D continental-collision models. Geochem. Geophys. Geosystems 16, 1378–1400. https://doi.org/10.1002/2015GC005732

Ranalli, G., Adams, M., 2013. Rheological contrast at the continental Moho: Effects of composition, temperature, deformation mechanism, and tectonic regime. Tectonophysics, Moho: 100 years after Andrija Mohorovicic 609, 480–490. https://doi.org/10.1016/j.tecto.2012.10.037

Roberts, A.G., Weinberg, R.F., Hunter, N.J.R., Ganade, C.E., 2020. Large-Scale Rotational Motion Within the Main Central Thrust Zone in the Darjeeling-Sikkim Himalaya, India. Tectonics 39. https://doi.org/10.1029/2019TC005949

Robinson, N., Regetz, J., Guralnick, R.P., 2014. EarthEnv-DEM90: A nearly-global, void-free, multi-scale smoothed, 90m digital elevation model from fused ASTER and SRTM data. ISPRS J. Photogramm. Remote Sens. 87, 57–67. https://doi.org/10.1016/j.isprsjprs.2013.11.002

Ruh, J.B., Gerya, T., Burg, J.-P., 2014. 3D effects of strain vs. velocity weakening on deformation patterns in accretionary wedges. Tectonophysics 615–616, 122–141. https://doi.org/10.1016/j.tecto.2014.01.003

Ruh, J.B., Kaus, B.J.P., Burg, J.-P., 2012. Numerical investigation of deformation mechanics in fold-and-thrust belts: Influence of rheology of single and multiple décollements. Tectonics 31. https://doi.org/10.1029/2011TC003047

Salles, T., 2016. Badlands: A parallel basin and landscape dynamics model. SoftwareX 5, 195–202. https://doi.org/10.1016/j.softx.2016.08.005

Searle, M.P., Treloar, P.J., 2019. Introduction to Himalayan tectonics: a modern synthesis. Geol. Soc. Lond. Spec. Publ. 483, 1–17. https://doi.org/10.1144/SP483-2019-20

Selzer, C., Buiter, S.J.H., Pfiffner, O.A., 2007. Sensitivity of shear zones in orogenic wedges to surface processes and strain softening. Tectonophysics 437, 51–70. https://doi.org/10.1016/j.tecto.2007.02.020

Spiegelman, M., May, D.A., Wilson, C.R., 2016. On the solvability of incompressible Stokes with viscoplastic rheologies in geodynamics. Geochem. Geophys. Geosystems 17, 2213–2238. https://doi.org/10.1002/2015GC006228

Srivastava, V., Mukul, Manas, Mukul, Malay, 2017. Quaternary deformation in the Gorubathan recess: Insights on the structural and landscape evolution in the frontal Darjiling Himalaya. Quat. Int., Earthquake and Active Tectonics of the Himalayan Convergent Boundary 462, 138–161. https://doi.org/10.1016/j.quaint.2017.05.004

Sunamura, T., 2005. Cliffs, Lithology Versus Erosion Rates, in: Schwartz, M.L. (Ed.), Encyclopedia of Coastal Science. Springer Netherlands, Dordrecht, pp. 241–243. https://doi.org/10.1007/1-4020-3880-1_72

Tsuguo, S., 1983. Processes of Sea Cliff and Platform Erosion, in: CRC Handbook of Coastal Processes and Erosion. CRC Press, pp. 233–265.

Vanderhaeghe, O., Medvedev, S., Fullsack, P., Beaumont, C., Jamieson, R.A., 2003. Evolution of orogenic wedges and continental plateaux: insights from crustal thermal-mechanical models overlying subducting mantle lithosphere. Geophys. J. Int. 153, 27–51. https://doi.org/10.1046/j.1365-246X.2003.01861.x

Vogt, K., Matenco, L., Cloetingh, S., 2017a. Crustal mechanics control the geometry of mountain belts. Insights from numerical modelling. Earth Planet. Sci. Lett. 460, 12–21. https://doi.org/10.1016/j.epsl.2016.11.016

Vogt, K., Willingshofer, E., Matenco, L., Sokoutis, D., Gerya, T., Cloetingh, S., 2017b. The role of lateral strength contrasts in orogenesis: A 2D numerical study. Tectonophysics. https://doi.org/10.1016/j.tecto.2017.08.010

Weinberg, R.F., 2016. Himalayan leucogranites and migmatites: nature, timing and duration of anatexis. J. Metamorph. Geol. 34, 821–843. https://doi.org/10.1111/jmg.12204

Willett, S.D., 1999a. Orogeny and orography: The effects of erosion on the structure of mountain belts. J. Geophys. Res. Solid Earth 104, 28957–28981. https://doi.org/10.1029/1999JB900248

Willett, S.D., 1999b. Rheological dependence of extension in wedge models of convergent orogens. Tectonophysics 305, 419–435. https://doi.org/10.1016/S0040-1951(99)00034-7

Chapter 6

Fast-to-slow convergence reconciles the long-term evolution of the Himalayan orogen

Authors: Ben S. Knight[1]*, Fabio A. Capitanio[1], Roberto F. Weinberg[1], Luca Dal Zilio[2]

Affiliations:

[1]School of Earth, Atmosphere & Environment, Monash University, Clayton, 3800

[2]Division of Geological and Planetary Sciences, California Institute of Technology (Caltech), Pasadena, CA, USA

Abstract

The collision of India and Eurasia has resulted in a range of structures divided across two main regions, the Himalayan fold and thrust belt and the Tibetan Plateau. Although these regions are well studied, previous numerical models have mainly focused on utilising a constant convergence velocity to investigate the processes forming either the Himalayan fold and thrust belt or the Tibetan plateau independently. In this study, we investigate either a constant or decreasing convergence velocity, comparable to the decreasing velocity observed between India and Asia, to investigate role of the convergence history on the long-term structural evolution of orogens. The constant velocity models replicate some structures observed in the both the Himalayas and Tibet, however the fast to slow model replicates most of the structures observed in the region. The timing and duration of processes operating in the model matched those observed in the region, producing similar structures. A switch from the high convergence velocity phases, dominated by deep burial, localised exhumation and crustal under thrusting, to slow convergence velocity phases, characterised by the cooling of the orogens interior and formation of a fold-and-thrust belt at the front of the orogen, is observed. These results highlight that the convergence history and thermal evolution are critical to the creation of the Himalayan fold-and-thrust belt and Tibetan plateau.

6.1. Introduction

Since collision of India and Asia ~50 Ma (Molnar and Tapponnier, 1975; Patriat and Achache, 1984; Zahirovic et al., 2012), ~2,600 ± 900 km of convergence has been accommodated within a broad collisional zone, resulting in the unique structures observed in the Himalayan mountain chain and the Tibetan Plateau (DeCelles et al., 2002; Guillot et al., 2003; Halim et al., 1998; Molnar and Tapponnier, 1975; Patriat and Achache, 1984). How deformation has been partitioned between the two regions and the different processes operating throughout the structural evolution of the orogen remains debated.

At the front of the orogen is the Himalayan fold-and-thrust belt (H-FAT) that has a remarkably consistent structure along the entire length of the orogen (Figure 6.1A) (DeCelles et al., 2002). The development of the H-FAT belt is well constrained, with active faulting younging from North to South (DeCelles et al., 2001; Goscombe et al., 2018). However, different processes have been suggested to accommodate convergence in the H-FAT belt, derived from the structures. These processes include: (1) the subduction of parts of or (2) the entire Indian crust (Capitanio et al., 2010) (3) that results in the ecoligitization of mafic lower crust (Pichon et al., 1992; Spain and Hirn, 1997), chronicled by the presence of (ultra-)high-pressure eclogite facies observed in the Kaghan region, north Pakistan, and in the Tso Morari complex, NW India, which underwent eclogitization between 47 and 43 Ma (Goscombe et al., 2018; Searle, 2015). Convergence has also previously been suggested to be accommodated by (4) the thrusting of Indian crust into the orogen (Avouac, 2007; Gao et al., 2016; Kohn, 2014) or (5) by return channel flow (Nelson et al., 1996; Searle, 2015), which may be driven by focused erosion at the surface (Beaumont et al., 2004, 2001). Thrusting of Indian crust is recorded in the deformation of the Lesser Himalaya Sequence (LHS), with shear zones that decrease in age to the south, with thrusting occurring on the Main Central Thrust (MCT) ~23 Ma (DeCelles et al., 2002, 2001), whilst convergence is

currently being accommodated along the Main Boundary Thrust (MBT) at the front of the orogen. Channel flow is recorded by the presence of the Greater Himalayan Crystalline Sequence (GHCS) above the MCT and South Tibetan Detachment (STD), with Monazite U–Pb ages on the emplacement of the GHCS varying between 14 to 32 Ma depending on the location (Godin et al., 2006; Goscombe et al., 2018).

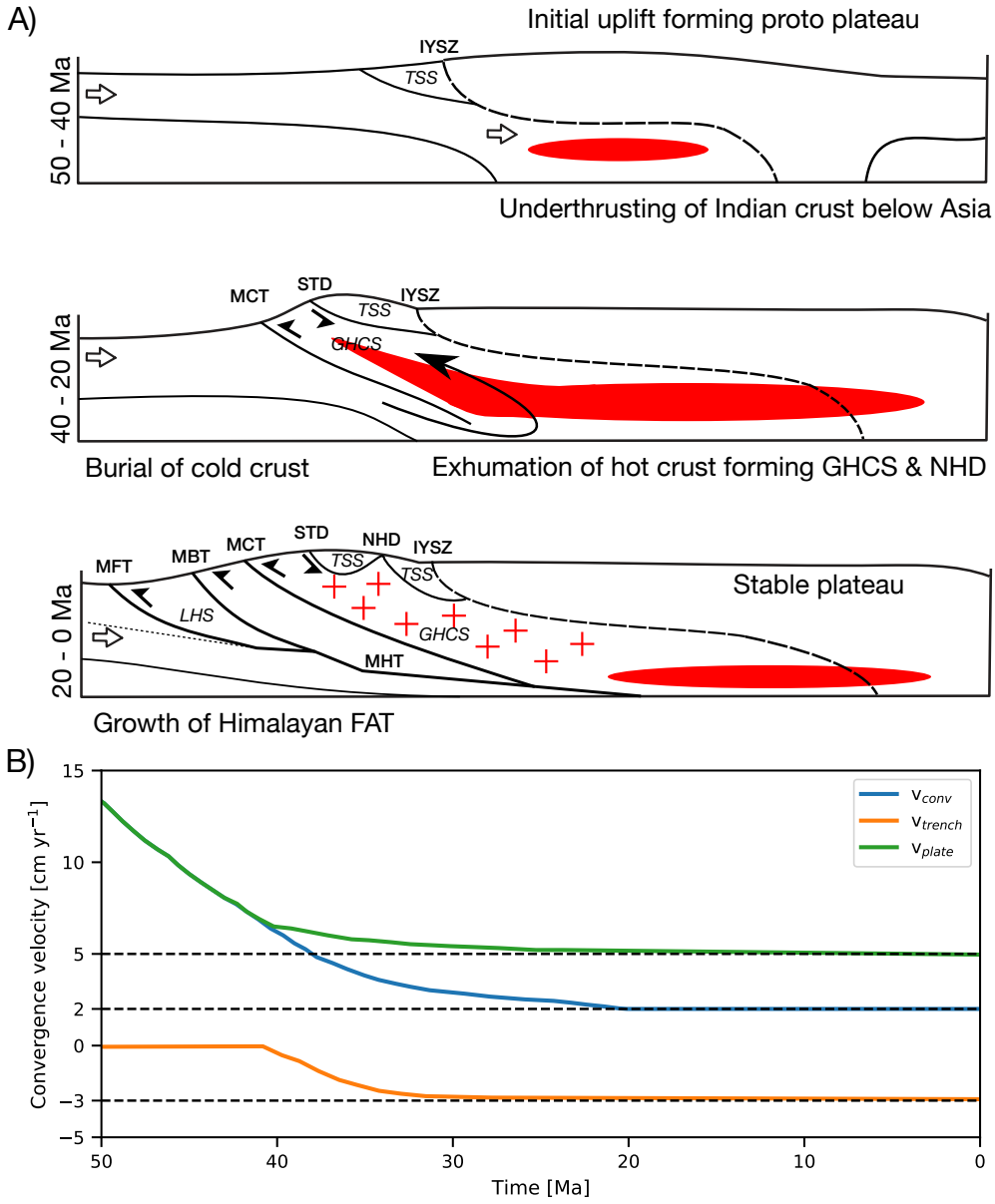

Figure 6.1: A) Schematic evolution of the Himalayas and Tibet, highlighting the formation of key structures at different times, based on various previous schematic diagrams of the evolution of the major structures (e.g. Elliott et al., 2016; Herman et al., 2010; Nelson et al., 1996; Searle, 2015; Streule et al., 2010). IYSZ – Indus Yarlung Suture Zone, NHD – Northern Himalayan Domes, MHT – Main Himalayan Thrust, STD – South Tibetan Detachment, MCT – Main Central Thrust, MBT – Main Boundary Thrust, MFT – Main Frontal Thrust, LHS – Lesser Himalayan Sequence, TSS – Tethyan Sedimentary Sequence, GHCS – Greater Himalayan Crystalline Sequence. B) Evolution of convergence, trench and plate velocity, modified from Capitanio et al. (2010). The convergence velocity (v_{conv}) is the sum of the plate velocity (v_{plate}) and trench velocity (v_{trench}).

To the North of the H-FAT belt is the Tibetan Plateau (TP) which has concurrently grown with the H-FAT belt through several proposed mechanisms: (1) under-thrusting of Indian crust and lithosphere beneath Asia (Argand, 1922; DeCelles et al., 2002; Powell, 1986), (2) viscous mid- or lower-crust flow, with minimal crust thickening (Clark et al., 2005a; Clark and Royden, 2000; Cook and Royden, 2008; Royden, 1997), with the presence of a viscous mid-crust observed in geophysical datasets (Nelson et al., 1996). (3) Rigid terrane block accretion and thickening during the subduction of Asian lithosphere (Kelly et al., 2019, 2016; Tapponnier et al., 2001, 1982; Willett and Beaumont, 1994), or through (4) homogenous, regional-scale thickening, due to the continuous Indian indentation or due to lithosphere delamination and recycling (England and Houseman, 1986; Molnar et al., 1993a), which may have occurred as late as ~9 Ma based on multiple observations from the region (Molnar et al., 1993b).

The different structures (Figure 6.1A) observed in the H-FAT belt, their age and relation to the Asian lithosphere beneath the TP suggest the processes accommodating convergence in the region has changed over time. Additionally, the convergence velocity and where the velocity is accommodated (e.g. trench retreat, within the FAT belt), has rearranged over time (Figure 6.1B) (Capitanio et al., 2010; Guillot et al., 2003). The convergence velocity may have continually decreased since collision ~50 Ma (Molnar and Stock, 2009) or may have decreased until reaching a constant velocity of ~5 cm yr^{-1} 20 Ma (Zahirovic et al., 2012), with a constant rate of shortening suggested for the Himalayan FAT belt since ~40 Ma (Guillot et al., 2003). Although each process can explain a unique structure in the region, a combination of processes, that occur at different times throughout the evolution of the orogen, are required to reconcile the diversity of structures observed within the Himalayan orogen and Tibetan Plateau within the broader context of the India-Asia convergence.

Previous numerical models have investigated the origin of plateaus, with application to Tibet (Capitanio, 2020; Capitanio et al., 2015; Chen et al., 2020, 2017; Clark et al., 2005a, 2005b; Cook and Royden, 2008; Kelly et al., 2019; Pusok and Kaus, 2015) whilst others numerical models have focused on orogenic wedges or fold-and-thrust belts, with application to the Himalayas (e.g. Beaumont et al., 2004, 2001; Burg and Schmalholz, 2008; Cattin and Avouac, 2000; Dal Zilio et al., 2020, 2019; Faccenda et al., 2009, 2008; Piccolo et al., 2017). To date, our understanding of the combined orogen-plateau formation remains relatively unexplored (Chen et al., 2020, 2017; Kelly et al., 2019, 2016) and how the structures observed in the H-FAT belt and TP are linked to the decreasing convergence velocity throughout the Cenozoic remains unknown.

In this study, a two-dimensional thermo-mechanical numerical model is used to test the role of long-term convergence on the structural evolution of the orogeny and compare model results with the structural evolution of the H-FAT belt and TP (Figure 6.1A). A decreasing convergence velocity is used as a boundary condition to show how the convergence velocity controls the long-term structuring of the orogen-plateau margin and its lithospheric evolution. The use of temperature-dependent visco-plastic crust atop a subducting lithosphere includes both stress and strain rate-dependent rheology to include the dependency on the convergence velocity and temperature on the overall strength of the crust. A comparison of the models with the Indo-Asian margin shows that deceleration of the Indian plate over the Cenozoic is key to the emergence of the main thermo-tectonics of the region, including the Indian crust under-thrusting Tibetan crust to form a plateau, the emplacement of Greater Himalayan Crystalline Sequence through channel flow at high convergence velocity and the emplacement of the Northern Himalayan Domes during exhumation of lower crustal material, followed by the formation of the Himalayan fold-and-thrust belt due to the decrease in convergence velocity that results in the thermal re-

equilibration of the orogen and stabilisation of the thermally-controlled brittle-ductile transition depth.

6.2. Methods

Collision of continental crust is modelled as a viscous fluid with an infinite Prandtl number and a low Reynolds number. The conservation of mass, momentum and energy equations are solved for an incompressible, visco-plastic fluid through the extended Boussinesq approximation in a 2D Cartesian box using the finite element, particle-in-cell (PIC) code Underworld2 (Beucher et al., 2019; Moresi et al., 2007, 2003). Underworld2 allows the tracking of distinct materials and their properties through Lagrangian particles within a Eulerian finite element grid. The full methods utilised are outlined in Chapter 2.

6.2.1. Rheology

Viscous deformation in the model is included through the constitutive equation for dislocation and diffusion creep:

$$\eta_{disl,diff} = \chi \frac{1}{2} A^{-\frac{1}{n}} \dot{\varepsilon}_{II}^{\frac{1-n}{n}} e^{\left(\frac{E+PV}{nRT_r}\right)} \quad (6.1)$$

where χ is the strength factor, η is the viscosity, A is the pre-exponential factor, n is the stress exponent, E is the activation energy, P the pressure, V the activation volume, R the gas constant, T_r is the temperature at a given position and $\dot{\varepsilon}_{II}$ is the second invariant of strain rate. All the parameters for the viscous rheology are presented in Table 3.1.

Plasticity is implemented in the model through a depth-dependent von-Mises yielding criterion (Spiegelman et al., 2016):

$$\tau_y = C \cos\varphi + P \sin\varphi \quad (6.2.1)$$

$$\eta_p = \frac{\tau_y}{2\dot{\varepsilon}_{II}} \tag{6.2.2}$$

where τ_y is the yield stress, C is the cohesion at the surface, φ is the internal friction angle, where $\sin\varphi$ is equivalent to the friction coefficient (f_c) and P is the lithostatic pressure.

Table 6.1: Initial material properties used for the viscoplastic rheology. ρ is the density at the surface. A is the pre-exponential factor, n, is the stress exponent, E is the activation energy, f_c is the friction coefficient, C is the cohesion at the surface and α is the coefficient of thermal expansion.

Material	***Sediment***	***Crust A & B***	***Crust C***	***Mantle***		***Weak Zone***	
Rheology	Quartzite[a]	Quartzite[a]	Diabase[a]	Olivine[b]		Wet Olivine[b]	
Deformation mechanism	Dislocation	Dislocation	Dislocation	Dislocation	Diffusion	Dislocation	Diffusion
Strength factor (χ)	0.5	1	1	1	1	1	1
A (MPa^{-n} s^{-1})	6.7×10^{-7}	6.7×10^{-7}	2.0×10^{-4}	1.1×10^{5}	1.5×10^{9}	1.6×10^{3}	2.5×10^{7}
n	2.4	2.4	3.4	3.5	1.0	3.5	1.0
E ($J\ mol^{-1}$)	1.56×10^{5}	1.56×10^{5}	2.60×10^{5}	5.30×10^{5}	3.75×10^{5}	5.20×10^{5}	3.75×10^{5}
V ($m^3\ mol^{-1}$)	0	0	0	6.0×10^{-6}	6.0×10^{-6}	2.3×10^{-5}	1.0×10^{-5}
C, C_w (MPa)	10, 1	10, 1	10, 1	10		10, 1	
f_c, $f_{c,w}$	0.3, 0.15	0.3, 0.15	0.3, 0.15	0.6		0.1, 0.05	
ρ_0 ($kg\ m^{-3}$)	Varied, see Table 2	2,300	2,800	3,300		3,300	

[a](Ranalli, 1995) [b](Hirth and Kohlstedt, 2003).

Both the cohesion (C) and internal friction angle (φ) are linearly reduced (C_w, φ_w) between 0.5 (ε_{min}) and 1.5 (ε_{max}) as plastic strain (ε) accumulates due to yielding of the crust:

$$C = \begin{cases} \mathrm{C} & if\ \varepsilon \leq\ \varepsilon_{min} \\ C + \dfrac{(C - C_w)}{(\varepsilon_{min} - \varepsilon_{max})}(\varepsilon - \varepsilon_{min}), & if\ \varepsilon_{min} <\ \varepsilon <\ \varepsilon_{max} \\ C_w, & if\ \varepsilon \geq\ \varepsilon_{max} \end{cases} \tag{6.3}$$

$$\varphi = \begin{cases} \varphi & if\ \varepsilon \leq\ \varepsilon_{min} \\ \varphi + \dfrac{(\varphi - \varphi_w)}{(\varepsilon_{min} - \varepsilon_{max})}(\varepsilon - \varepsilon_{min}), & if\ \varepsilon_{min} <\ \varepsilon <\ \varepsilon_{max} \\ \varphi_w, & if\ \varepsilon \geq\ \varepsilon_{max} \end{cases} \tag{6.4}$$

The effective viscosity (η) for the visco-plastic rheology is then determined through the minimum viscosity of each deformation mechanism:

$$\eta_{crust} = \min(\eta_p, \eta_{disl}) \tag{6.5}$$

$$\eta_{mantle} = \min(\eta_p, \eta_{disl}, \eta_{diff}) \tag{6.6}$$

The model neglects the role of elasticity as a visco-plastic rheology adequately encapsulates the long-term stress distribution (Kaus et al., 2008; Vogt et al., 2017). Our models also neglect diffusion creep in the crust as plastic deformation is the principal deformation mechanism at low temperatures and high strain rates and dislocation creep is dominant at increasing temperatures and high strain rates.

6.2.2. Surface processes

To investigate the role of surface processes, a linear diffusive surface is included in certain models. The surface is tracked using passive tracers along the boundary between the crust and sticky air. The passive tracers are advected along with the particles within the

model before being interpolated back to the original x coordinate (2D). Surface processes are modelled assuming the short-range transport of material as a linear flux (q_s) which is proportional to the surface slope ($\frac{dh}{dx}$) and diffusive rate (D) (Avouac, 1993; Culling, 1960):

$$q_s = -D\frac{dh}{dx} \tag{6.7}$$

The diffusive rate (D) is expressed as a unit area over unit time ($m^2\,yr^{-1}$), that determines the amount of erosion and sedimentation taking place at the surface, whilst $\frac{dh}{dx}$ represents the slope. In 2D models the surface is represented as a line (1D), which reduces the change in surface height over time ($\frac{dh}{dt}$) to:

$$\frac{dh}{dt} = \frac{dq_s}{dx} \tag{6.8}$$

As the surface diffuses, new material is embedded beneath the diffused surface as sediment that was previously sticky air, while crust or sediment material above the diffused surface is removed and re-assigned as sticky air.

6.2.3. Model setup

The 2D model is designed to simulate continental collision (Figure 6.2A). The model has a length (x) of 1792 km and a height (y) of 224 km. The grid is uniformly spaced at 512 x 64 nodes, producing a grid resolution of 3.5 km, with 30 particles per cell to track material properties. Timesteps are determined by using (half of) the Courant–Friedrichs–Lewy (CFL) condition. A cell width of 3.5 km results in timesteps of 87,500 years for a convergence velocity of 2 cm yr^{-1} and 17,500 years at a convergence velocity of 10 cm yr^{-1}. In the fast to slow models, the timestep duration increases as the convergence velocity decreases.

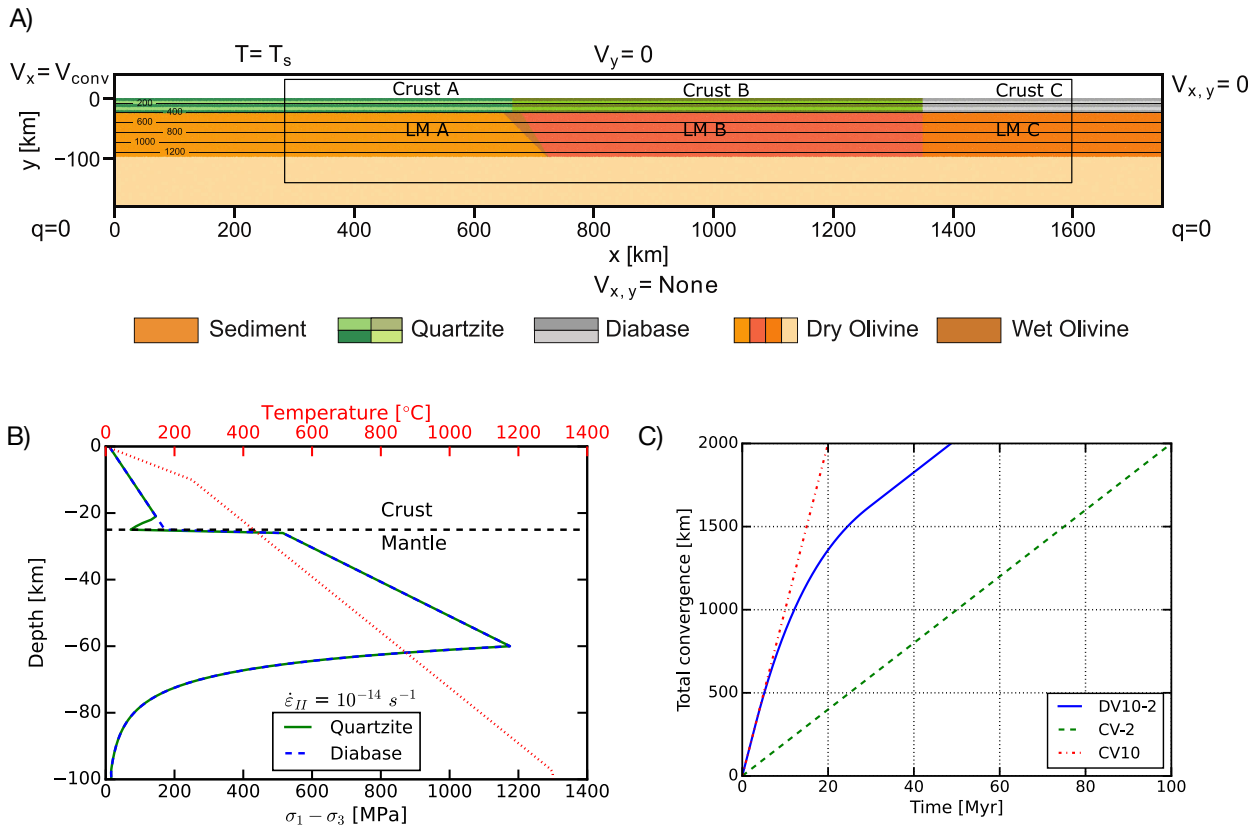

Figure 6.2: A) Model setup. The convergence velocity is applied to the left boundary, the top boundary is free slip, the right boundary no slip and the bottom boundary is unconstrained. The left, top and right boundaries have zero heat flux, whilst the temperature of the bottom boundary is unconstrained. The black box marks the area that is plotted in subsequent figures. LM = lithospheric mantle. B) Strength and temperature profile displaying the difference in strength between crust A/B (quartzite) and C (diabase). C) Total convergence against time to show how each model reaches 2000 km of convergence over the duration of the model: CV10 – fast model (10 cm yr^{-1}) for 20 Myr, CV2 – slow model (2 cm yr^{-1}) for 100 Myr, DV10-2 – decreasing velocity model (10 to 2 cm yr^{-1}) over 50 Myr.

The viscous rheology of the crust varies, with a quartzite rheology used for crust A and B, while a diabase rheology is used for crust C (Table 3.1) to represent a rigid block analogous to the rigid Tarim Basin to the NW of the Tibetan Plateau. The friction coefficient is kept constant for the different crustal blocks (f_c = 0.3, Table 3.1). A 45° dipping weak zone within the mantle lithosphere (x = 650 km) is included within the lithosphere, representing a pre-existing suture (Vogt et al., 2017). The weak zone has a wet olivine rheology and low friction coefficient (0.1), whilst the surrounding lithospheric mantle (LM) has a dry olivine rheology and high friction coefficient (0.6) (Table 3.1). The pre-existing weakness is included within the lithospheric mantle to introduce a rheological heterogeneity that facilitates

lithospheric subduction and localises deformation in the crust above (Burg and Gerya, 2005; Vogt et al., 2017; Willingshofer et al., 2013).

A constant temperature (T = 0 °C) is applied to the top boundary, with no heat flux across the side walls. The initial internal temperature distribution follows a geothermal gradient of 25 °C km^{-1} for the first 10 km and then 12 °C km^{-1} until a temperature of 1300 °C is reached at the lithosphere-asthenosphere boundary (LAB) at a depth of 97.5 km. We neglect adiabatic gradients and keep the underlying mantle at 1300 ˚C. The temperature is unconstrained on the bottom boundary to allow the temperature to evolve freely as the lithosphere subducts.

The model uses a no-slip condition on the right (v_x, v_y = 0) boundary and a free-slip condition on the top (v_y = 0) boundary. The bottom boundary is unconstrained, allowing for inflow and outflow of material, implying the model overlies an infinite half-space with an inviscid fluid (Gerya, 2009). The convergence velocity is applied on the left side wall across the crust and mantle lithosphere. Below the lithosphere (y < - 97.5 km), the velocity linearly decreases from the convergence velocity at base of the lithosphere to zero at the bottom of the left wall. Above the crust, an inflow/outflow is prescribed across the sticky air layer (y > 0 km) to allow topography to develop.

The role of the convergence history is illustrated by comparison with models run at constant velocity. Convergence velocity across the crust and mantle is either constant throughout the model (2 or 10 cm yr^{-1}), or decreases over time (10 to 2 cm yr^{-1}) to simulate 2000 km of convergence (Figure 6.2C), similar to the total amount of convergence between India and Asia since collision ~50 Ma (Guillot et al., 2003; Halim et al., 1998; Molnar and Tapponnier, 1975). The convergence velocity imposed aims to reproduce forces that are self-consistently generated by multiple driving forces, e.g. plume push, double subduction (Pusok and Stegman, 2020), which are not included in this high-resolution model.

6.3. Results

In this section we outline the main outcomes of 3 reference models that do not include internal heating or surface processes and have a reference crustal density (ρ_0) of 2800 kg m^{-3}. We also summarise the role of internal heating (9 additional models), surface process (6 additional models) and crustal density (6 additional models) on the final structure of the orogen for each convergence velocity tested, with a total of 24 models investigated (Table 6.2).

Table 6.2: Model name, total time, velocity condition and additional processes.

Model name	*Total model time [Myr]*	*Velocity condition [cm yr^{-1}]*	*Surface diffusivity (D) [m^2 yr^{-1}]*	*Internal heating rate (H_r) [μW m^{-3}]*	*Crustal density (ρ_0) [kg m^{-3}]*
CV10	20	10	0	0	2800
CV10_ρ2900	20	10	0	0	2900
CV10_ρ2700	20	10	0	0	2700
CV10_D150	20	10	150	0	2800
CV10_D300	20	10	300	0	2800
CV10_0.5H_r	20	10	0	0.5	2800
CV10_1H_r	20	10	0	1	2800
CV10_2.25H_r	20	10	0	2.25	2800
CV2	100	2	0	0	2800
CV2_ρ2900	100	2	0	0	2900

CV2_ρ2700	100	2	0	0	2700
CV2_D150	100	2	150	0	2800
CV2_D300	100	2	300	0	2800
CV2_0.5H_r	100	2	0	0.5	2800
CV2_1H_r	100	2	0	1	2800
CV2_2.25H_r	100	2	0	2.25	2800
DV10-2	50	10 to 2	0	0	2800
DV10-2_ρ2900	50	10 to 2	0	0	2900
DV10-2_ρ2700	50	10 to 2	0	0	2700
DV10-2_D150	50	10 to 2	150	0	2800
DV10-2_D300	50	10 to 2	300	0	2800
DV10-2_0.5H_r	50	10 to 2	0	0.5	2800
DV10-2_1H_r	50	10 to 2	0	1	2800
DV10-2_2.25H_r	50	10 to 2	0	2.25	2800

6.3.1. Constant convergence velocity models

6.3.1.1. Fast Convergence model - CV10

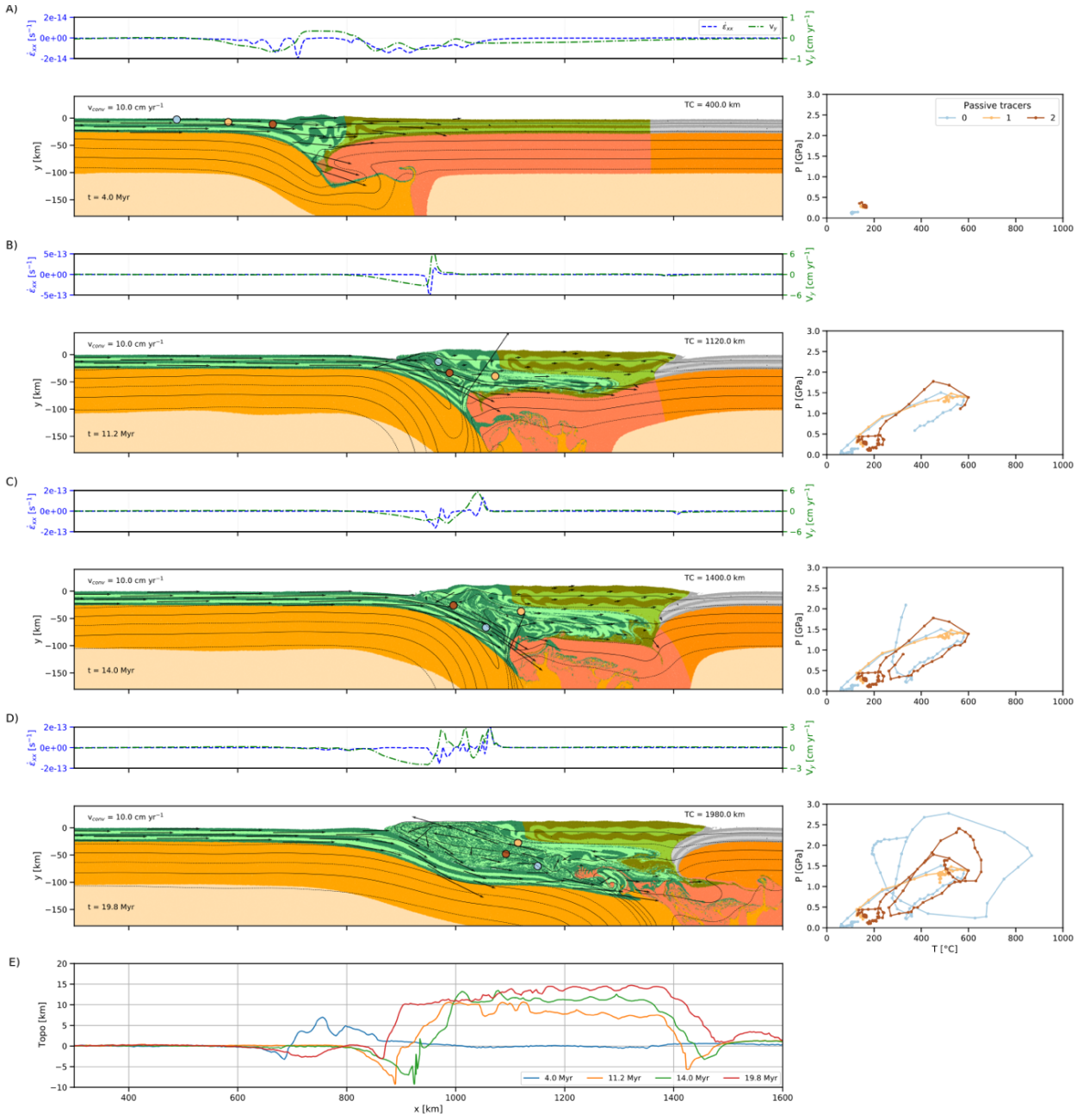

Figure 6.3: Evolution of material and passive tracers in CV10, with material plots also including temperature contours, velocity vectors and passive tracers. Boxes above material plots highlight the horizontal strain rate (□xx) and vertical velocity (vy) at y = -15 km. Boxes to the right of the material show the pressure-temperature paths of the passive tracers. A) Phase 1 – formation of initial wedge above weak zone. B) Phase 2 – migration toward the back wall and lengthening of the orogen and Phase 4 - where underthrusting of crust A below crust B occurs and return flow forms at the front of the orogen. C & D) Phase 3 – doming of the crust and exhumation of deep crustal material. E) Topography at the same intervals presented in A-D. The topography shows the different stages, with topography narrow in phase 1 before widening and forming a plateau in phase 2 and 3. During phase 4, the orogen continues to widen, with a sharp topographic gradient at the front of the orogen.

The evolution of CV10 (Figure 6.3) is dictated by the constant high convergence velocity (10 cm yr^{-1}), and is divided into 4 phases, which are defined by changes in processes accommodating convergence that results in new structures forming.

Phase 1 (0 – 4 Myr) is defined by the formation of an orogenic wedge above the pre-existing weak zone located within the lithospheric mantle (Figure 6.5A). During this phase, the crust mainly thickens to form a proto-wedge, with deformation primarily concentrated within crust A. During phase 1, the horizontal strain rates and vertical velocity are low as deformation occurs over a wide area as the initial wedge forms (Figure 6.3A). After ~5 Myr the wedge reaches a critical thickness, changing the way convergence is accommodated, with the orogen moving to a phase of lateral growth to accommodate convergence.

Phase 2 (5 – 10 Myr) is characterised by the transition from vertical to lateral growth of the orogen due to the underthrusting of crust A below crust B and the continuous subduction of cold crust to a depth of ~150 km. During this phase, crust A underthrusts ~250 km beneath crust B (Figure 6.3B) and undergoes heavy shearing while thickening progressively, reaching a thickness of up to ~50 km below crust B. During this phase, the orogen migrates backwards toward the back wall, resulting in the widening of the elevated topography, forming a wide plateau (Figure 6.3E). Lateral migration stops at ~10.5 Myr, hindered by the rigid crust C which is close to the right-side wall (Figure 6.3B).

Phase 3 (10 – 16 Myr) begins as return flow develops at the front of the orogen after ~10 Myr, due to the burial and exhumation of crust A. Phase 3 is recorded by the vertical velocity and horizontal strain rates, which shows localised deformation concentrated at the front of the orogen due to return flow. The region of return flow at the front of the orogen displays decreasing negative vertical velocity (burial) from the front of the wedge, then at the centre the vertical velocity changes to positive, representing exhumation (Figure 6.3B). The vertical velocity and horizontal strain rate distribution in the burial region is indicative of

shearing-induced flow (Couette flow) over a wide area whilst the vertical velocity pattern in the exhumation region is indicative of pressure-induced flow (Poiseuille flow) over a narrow area, with Figure 6.3B showing the burial of cold material at the front of the wedge and exhumation of hot material.

The burial and exhumation cycles due to return flow are recorded in the passive tracers. These particles experience changes in pressure that exceed 2 GPa and a temperature range of over 500 °C. Passive tracer 0 appears to record isothermal burial at low temperatures that then undergoes heating before undergoing isothermal exhumation at high temperatures across phases 2 to 4.

The start of Phase 4 is marked by the flattening of the subducting mantle lithosphere at 16 Myr (Figure 6.3C-D), with the change in subducting angle altering the stress and, consequently, the structures at the front of the orogen. The change in subduction angle of the lithosphere dilates the region of high stress at the front of the wedge, resulting in the exhumation of hot and buoyant crustal material from near the Moho in the interior of the orogen and the emplacement of highly deformed crust (Figure 6.3D) over a wide area. The broadening of the exhumation region is observed in the vertical velocity, which we interpret as different processes operating compared to phase 3. The topography at the end of the model in Figure 6.3E shows the development of a very sharp topographic gradient at the front of the orogen after 19.8 Myr.

At depth, the long-term subduction progressively removes LM B from beneath the plateau, by delamination/thermal erosion, and replace it with crust A. Due to the fast convergence velocity, crust A is rigidly underthrusted beneath the plateau, while above crust A also heats up and flows in large volumes to the surface. Interestingly, by Phase 4, LM B is completely removed and the deep crust beneath crust B undergoes heating due to closer

contact with the asthenosphere. This is illustrated in the localised isotherm resurgence and the crustal melting plume, beneath the plateau (Figure 6.3C-D).

6.3.1.2. Slow Convergence model – CV2

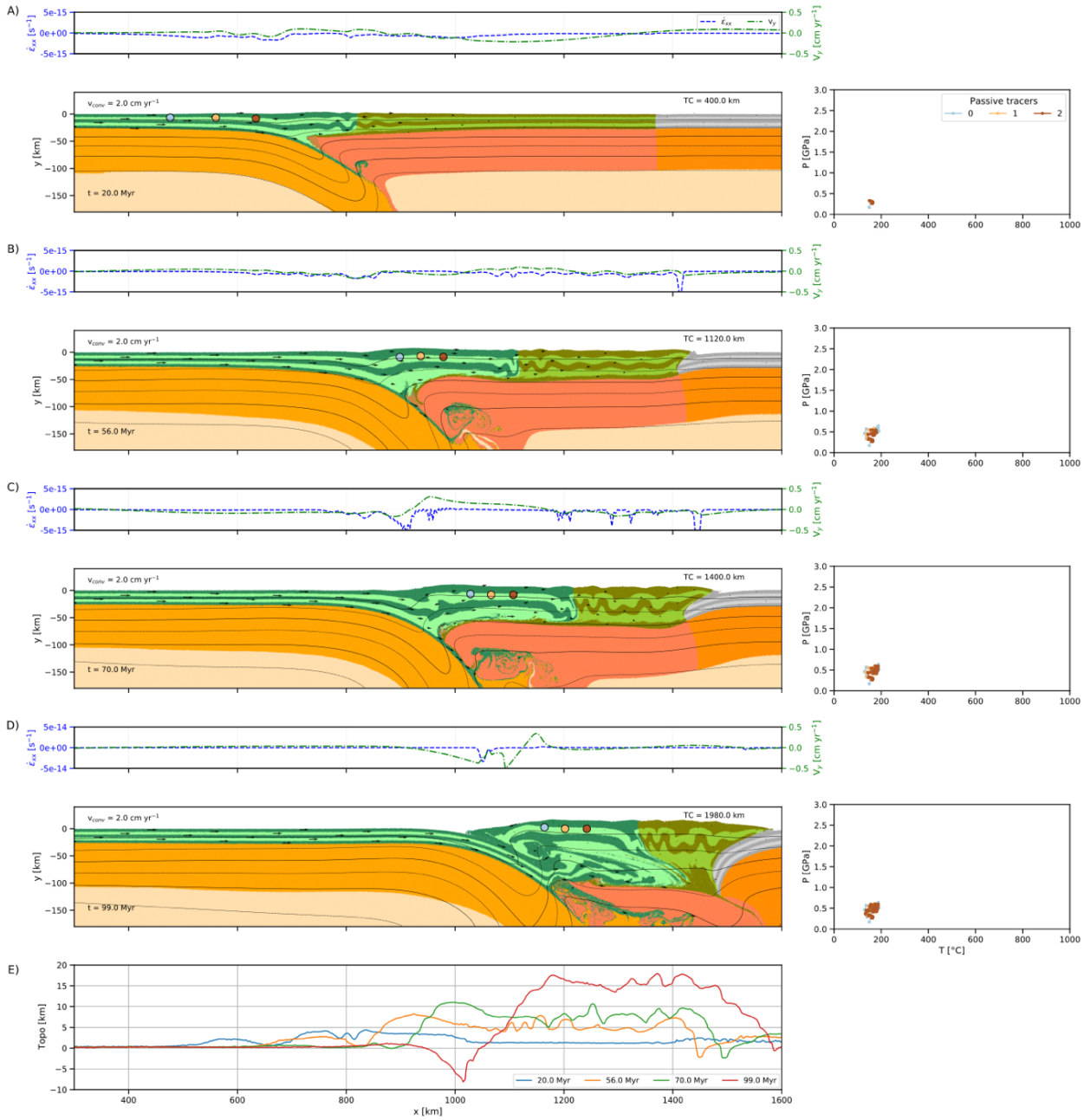

Figure 6.4: Evolution of material and passive tracers in CV2, with material plots also including temperature contours, velocity vectors and passive tracers. Boxes above material plots highlight the horizontal strain rate (ε_{xx}) and vertical velocity (v_y) at y = -15 km. Boxes to the right of the material show the pressure-temperature paths of the passive tracers. A) – D) highlight that the orogen migrates backward throughout and primarily accommodates convergence through thickening and folding of the crust. E) Topography at the same intervals presented in A-D, with the topographic height continuously increasing and migrating backward throughout the evolution of the model. A large decrease in length and increase in crustal thickness is observed between 56 and 81 Myr, concentrated in Crust B which undergoes intense shortening forming tight folds.

CV2 shares the same initial configuration and constitutive laws of CV10 (Figure 6.3) but the structural evolution of CV2 (Figure 6.4) is very different, highlighting the role of convergence velocity on the structural evolution of orogens.

During the evolution of CV2, the lithospheric mantle maintains a relatively stable dip angle throughout as the force balance between the imposed convergence velocity and slab pull remain proportionate. This results in the vertical velocity and horizontal strain rates, recorded at a depth of 15 km, remaining relatively stable throughout. This stability is also recorded by the evolution of the passive tracers, where the pressure and temperature remain relatively constant due to static passive tracers as the orogen is in a quasi-steady state throughout. In CV2, convergence is primarily accommodated through buckling, folding, and thickening of the crust. Due to 100 Myr of convergence at 2 cm yr^{-1} to reach 2000 km of shortening in CV2, thermal diffusion, rather than advection, as observed in CV10 model, controls the evolution, favouring the establishment of rather uniform geothermal gradients throughout the orogen (Figure 6.4A-D).

Phase 1 begins with large-scale crustal folding above the weak zone at the plate margin, with a minimal increase in crustal thickness or topography. After 10 Myr of convergence, crust A progressively detaches from the subducting lithosphere and the suture, migrating towards the back wall (Figure 6.4A), forming low-relief topography over a wide area (Figure 6.4E).

Phase 2 begins around ~50 Myr, after the orogen has migrated and thickened close to the rigid backstop, resulting in crust B undergoing folding as it is squeezed between crust A and crust C. At 56 Myr, the deformation style is still characterised by folding, forming large wavelength folds in crust B (Figure 6.4B). After 56 Myr the topography reaches a height of 5 km over a length of ~500 km (Figure 6.4E). As convergence is ongoing, the crust continues

to thicken as the orogen is restricted between the subducting lithosphere on the left and rigid crust C on the right.

After 81 Myr, most of the convergence is accommodated in crust B, which has been shortened from 700 km to 100 km, mainly through increasing in thickness, reaching a thickness of ~100 km (Figure 6.4C), while no underthrusting of the crust A below crust B is observed. This is reflected in the topography, which has grown to a height of ~10 km over a length of ~500 km (Figure 6.4E). During this time, minor deformation occurs at the front of the orogen in crust A through folding. The continued shortening in DV2 results in steep gradients in topography and crustal thickness developing at both the front and back of the orogen in Figure 6.4E.

Towards the end of CV2, between 81 and 100 Myr (Figure 6.4D), deformation is mainly located in crust A along shear zones that develop, whilst minor advection of crust near to the front of the orogen also occurs. Crust A also begins to underthrust below crust B, with crust A extending 50 km into crust B below the suture zone at the surface. The slow velocity results in cold geotherms compared to CV10 due to thermal diffusion. The orogen reaches a length of ~500 km with the crust thickening to ~100 km and the topography increasing to ~15 km in the interior of the orogen (Figure 6.4E) after 100 Myr.

Throughout the evolution of CV2, the subducting lithosphere maintains a relatively stable dip angle at depth, while LM B, beneath the plateau, is partially removed by thermal erosion. The slow convergence velocity allows the crust and lithospheric mantle to cool due to diffusion and stops the advection of material, with the root of the plateau cold enough to stop crustal flow. Consequently, no return flow or underthrusting occurs along with negligible exhumation in CV2.

6.3.2. Fast-to-slow convergence

6.3.2.1. DV10-2 (10 – 2 cm yr^{-1})

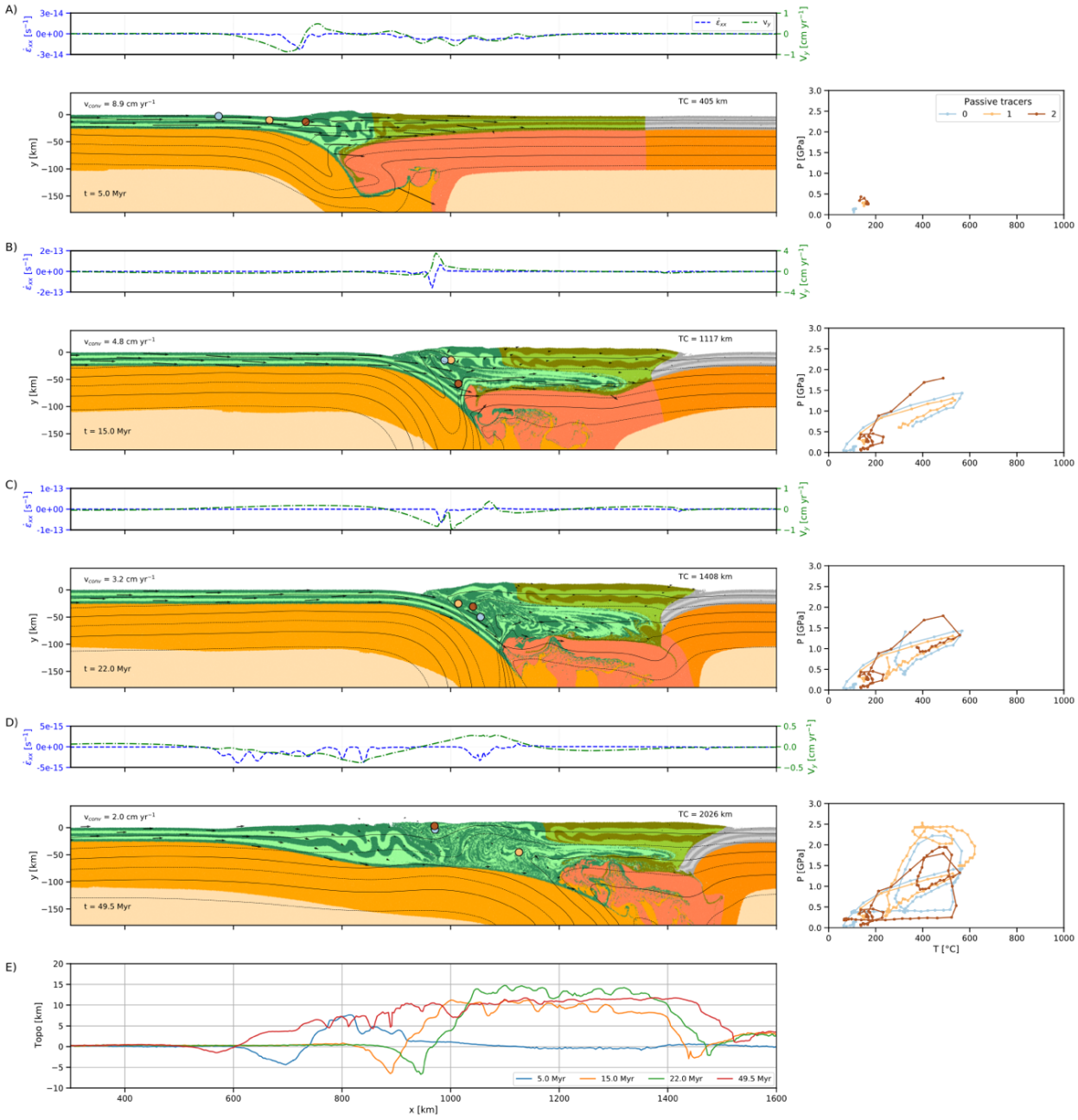

Figure 6.5: Evolution of material and passive tracers in DV10-2, with material plots also including temperature contours, velocity vectors and passive tracers. Boxes above material plots highlight the horizontal strain rate (ε_{xx}) and vertical velocity (v_y) at y = -15 km. Boxes to the right of the material show the pressure-temperature paths of the passive tracers. A) Phase 1 – formation of initial wedge above weak zone. B) Phase 2 – migration toward the back wall and lengthening of the orogen & Phase 3 - with underthrusting of crust A below crust B and return flow at the front of the orogen. C) Phase 4 - flattening of the slab, large exhumation event and relaxing of the isotherms. D) Phase 5 – FAT belt development at the front of the orogen. E) Topography at the same intervals presented in A-D. The topography shows the different stages, with phase 1 (5 Myr) very narrow before widening and forming a plateau in phase 2 and 3 (15 Myr). During phase 4 (35 Myr), the orogen lengthens slightly, before extending mainly at the front during FAT development in phase 5 (50 Myr).

The structural evolution of DV10-2 (Figure 6.5) is controlled by the decreasing convergence velocity. Unlike the previous models, which are under a constant convergence velocity and develop consistent structures, DV10-2 develops structures associated with transient processes associated with the velocity at the time, which allows the structures to be used to deduce the convergence history. The overall evolution is characterised by 1) tectonic structures that become unstable under the decreasing convergence rate, and 2) new features that emerge due to the thermal re-equilibration of the wedge. This is due to advection controlling the structural evolution at high velocity, whilst diffusion controls the structures that form at low velocities.

Phase 1 (0 – 5 Myr) is characterised by the initially high convergence velocity (10 cm yr^{-1}), with an orogenic wedge forming above the initial weak zone located within the lithospheric mantle after 5 Myr (Figure 6.5A). The initial structure and deformation during phase 1 in DV10-2 is comparable to CV10 as the two models have the same initial conditions including the same convergence velocity.

At the end of phase 1, a critical wedge thickness is reached and the orogen begins to migrate toward the back-wall at the start of phase 2, with the orogen growing laterally to accommodate convergence after 5 Myr. This is observed in the topography, with the topographic height increasing and topography occurring over a much wider area after 15 Myr compared to 5 Myr (Figure 6.5E), forming a wide plateau. The topography also displays a large change in thickness between the foreland and orogen after 15 Myr.

During phase 2 (5 – 15 Myr), crust A underthrusts below crust B, similar to the processes observed in CV10. By the end of phase 2, crust A has under-thrusted below crust B, extending ~200 km below the surface after 15 Myr (Figure 6.5B) compared to the position of the suture between the two crusts observed at the surface, creating a curved suture

geometry. This underthrusting, along with some thickening of crust B, elevates the plateau region.

During phase 3 (15 – 30 Myr), a region of return flow develops at the front of the wedge, exhuming deep hot crust to the surface. Similar to CV10, the return flow region displays velocity profiles that suggest shear driven flow (Couette flow) in the burial region and pressure-driven flow (Poiseuille flow) for exhumation (Figure 6.5B) with v_y peaking at ~4 cm yr^{-1} and temperature ranging from ~100 °C to ~700 °C across the return flow region, based on the isotherms and pressure-temperature paths of the passive tracers (Figure 6.5B). These values are much lower than the velocity or temperatures observed during phase 3 in CV10 (Figure 6.3C), due to the difference in convergence velocity. This is also observed in the pressure-temperature paths of passive tracers which show multiple phases of burial and exhumation.

Phase 4 marks the beginning of the critical transition to the dynamics of a cold wedge due to slowing convergence and the thermal re-equilibration of the wedge. In Phase 4 exhumation of deep crust occurs, similar to CV10. However, this exhumation is of a transient nature, occurring between 30 to 38 Myr, before thermal equilibration inhibits viscous flow as the region cools. The large exhumation event is driven by the same process as in CV10, i.e. the flattening of the lithospheric mantle angle beneath a thicker wedge. However, the width of the exhumed region is smaller in DV10-2 (Figure 6.5C), compared with CV10 (Figure 6.3D). The size and rate of this event is limited by the slower imposed convergence velocity, as well as a progressive cooling of the wedge, which limits the viscous flow of deeply buried crust in DV10-2.

The demise of exhumation and the cooling of the metamorphic core in Phase 4 acts as a buttress for the following evolution of the wedge, showing the critical role of the fast-to-slow transition. As convergence slows to 2 cm yr^{-1} at 32 Myr, the front of the orogen begins

to thermally re-equilibrate and a fold-and-thrust belt begins to develop (Figure 6.5C). This is reflected in the topography that shows the orogen lengthening at the front (Figure 6.5E) as the deformation propagates outward. As the large exhumation event ceases at 38 Myr, the isotherms at the front of the orogen continue to relax due to diffusion, with the fold-and-thrust belt now accommodating most of the convergence, signalling the start of phase 5 that lasts for the remainder of DV10-2 (Figure 6.5D). During phase 5 the plateau becomes relatively stable and inactive, as indicated by the low vertical velocity and horizontal strain rates in the region.

In DV10-2 LM B is progressively removed, allowing for a sustained heating of the buried lower crust beneath the plateau, in phase 4 and 5. The processes occurring in phases 1 to 4 are the same as in CV10, although the isotherms and the pressure-temperature paths in DV10-2 (Figure 6.5C-D) display lower temperatures and less pronounced crustal plutonism compared to CV10.

6.3.3. Influence of different processes during orogenesis

6.3.3.1. Role of internal heating

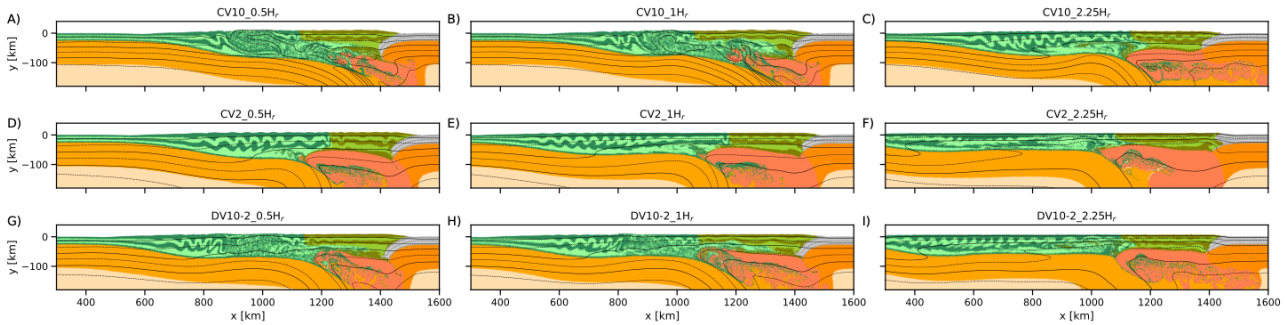

Figure 6.6: Comparison of models after 2000 km of convergence with differing amounts of internal heating rates in the crust. Left – H_r = 0.5μW m^{-3}, centre - H_r = 1 μW m^{-3}, right - H_r = 2.25 μW m^{-3}. Fast convergence models (v_{conv} = 10 cm yr^{-1}) are along the top (A – C), slow convergence models (v_{conv} = 2 cm yr^{-1}) are along the middle (D – E) and fast-to-slow convergence models (v_{conv} = 10 to 2 cm yr^{-1}) are along the bottom (G - I). The models show that increasing the internal heating rate influences the internal structure as it becomes the main heating mechanism, outweighing structures that form due to advection and diffusion, resulting in similar structures regardless of convergence velocity when high enough, observed when H_r = 2.25 μW m^{-3} (right column).

The influence of internal heating on the structural evolution of orogens was also investigated, with the final structure of each model presented in Figure 6.6. Internal heating

is an additional heating mechanism that alters the temperature distribution of the crust, influencing the structural evolution of the orogen. Our results show that the inclusion of internal heating hinders the development of structures associated with the fast and slow convergence velocity due to advection and diffusion, respectively, with internal heating becoming the dominant temperature mechanism that controls the structural evolution of the orogen when the internal heating rate is high enough.

Internal heating is incorporated as a constant rate for the crust (0.5, 1 or 2.25 $\mu W\ m^{-3}$) and mantle (0.022 $\mu W\ m^{-3}$) resulting in the crust warming whilst the lithosphere cools due to diffusion outweighing the low internal heating rate applied to the mantle. In general, internal heating causes LM B to cool over time which causes LM B to become more rigid, whilst the crust warms and becomes more viscous. This results in deformation being concentrated in Crust A, promoting the formation of a fold-and-thrust belt whilst also hindering the backward migration of the orogen due to the rigidity of LM B. Increasing the internal heating rate results in an increase in the width of the orogen and smoothing of topography, whilst also reducing the maximum crustal thickness observed within the orogen as the increase in temperature reduces the overall strength of the crust.

At a high convergence velocity (10 cm yr^{-1}) similar structures form when the internal heating is 0.5 or 1 $\mu W\ m^{-3}$ (Figure 6.6A-B) compared to the model with no internal heating (CV10). The similarities include the underthrusting of crust A below crust B form a plateau and the highly deformed region of crust where burial and exhumation occurs. However, when the internal heating rate is 2.25 $\mu W\ m^{-3}$ (Figure 6.6C), these features do not form, instead a small plateau forms due to thickening of crust B with convergence primarily accommodated in a fold-and-thrust belt at the front of the orogen. This is due to a high internal heating rate (2.25 $\mu W\ m^{-3}$) hindering advection that is required to develop sharp thermal gradients to form a region of return flow at the front of the wedge. Instead, the

temperature profile across the crust remains relatively stable due to the high internal heating rate, which results in the development of a fold-and-thrust belt.

A similar phenomenon occurs in the low convergence models (v_{conv} = 2 cm yr^{-1}) (Figure 6.6D-F). However, instead of reducing the influence of advection, the influence of cooling of the crust due to diffusion is hindered. Internal heating results in high crustal temperatures, promoting a brittle upper crust and viscous lower crust. The low internal heating rate in the mantle results in cooling due to diffusion, creating a brittle upper mantle in LM B that stops the backward migration of the crust and lithospheric mantle and promotes the formation of a fold-and-thrust belt, with deformation concentrated in crust A when the internal heating rate is 0.5 or 1 $\mu W\ m^{-3}$ (Figure 6.6D-E). When the internal heating rate of the crust is 2.25 $\mu W\ m^{-3}$ (Figure 6.6F) the crust flows due to a high internal temperature, creating viscous structures throughout the crust.

The evolution of the fast-to-slow convergence models (v_{conv} = 10 to 2 cm yr^{-1}) (Figure 6.6G-I) shows an intermediate behaviour between the fast (v_{conv} = 10 cm yr^{-1}) and slow (v_{conv} = 2 cm yr^{-1}) models with internal heating. At a low internal heating rate, the decreasing velocity model shows structures associated with both the fast and slow models. However, if internal heating is high enough (2.25 $\mu W\ m^{-3}$), then internal heating dominates the thermal evolution and hinders the development of distinctive features, resulting in a similar final structure for all models (CV10_2.25H_r, CV2_2.25H_r, DV10-2_2.25H_r) regardless of the convergence velocity (Figure 6.6 – right column).

Internal heating hinders the development of structures associated with advection at high velocity, including underthrusting of crust A below crust B, and the burial and exhumation of crust A at the front of the wedge that creates a large temperature gradient at the front of the wedge. It also hinders diffusion in the crust at low velocity, resulting in a

consistent structural evolution of the orogen regardless of the convergence velocity if internal heating is above the threshold to outweigh advection and diffusion, with the threshold varying based on the convergence velocity. At high and high to low velocity, the internal heating threshold is between 1 and 2.25 $\mu W\ m^{-3}$, whilst at low velocity, the threshold is <0.5 $\mu W\ m^{-3}$.

6.3.3.2. Role of surface processes

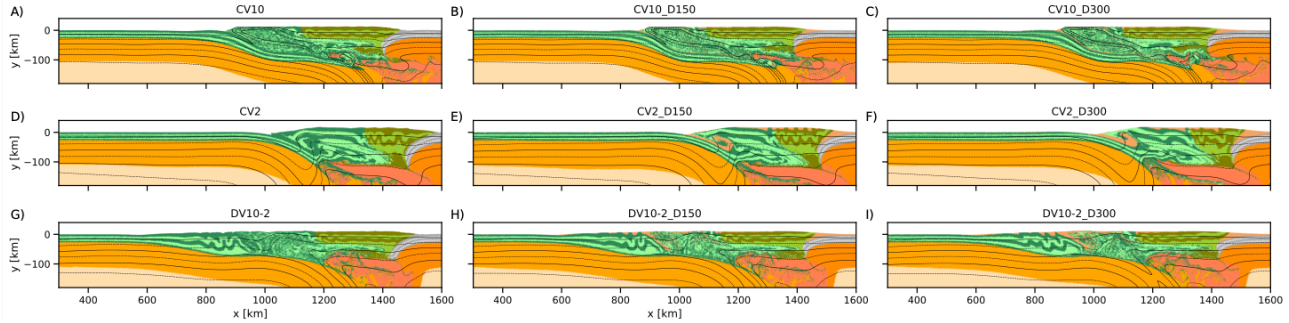

Figure 6.7: Comparison of models after 2000 km of convergence without surface processes (left) and with a surface diffusivity rate of 150 $m^2\ yr^{-1}$ (centre) and 300 $m^2\ yr^{-1}$ (right). Fast convergence models (v_{conv} = 10 cm yr^{-1}) are along the top, slow convergence models (v_{conv} = 2 cm yr^{-1}) are along the middle and fast-to-slow convergence models (v_{conv} = 10 to 2 cm yr^{-1}) are along the bottom. The models show that a surface processes, represented by a diffusive surface, do not have a major influence on the final structure of the orogen. The only major difference is the deposition of sediments across the plateau and within the fold-and-thrust belt, as well as the advection of sediments deep within the wedge in the return flow region.

The role of surface processes (Figure 6.7) was also investigated to determine how erosion and sedimentation influence the structural evolution of the orogen as focused erosion at the front of the orogen has previously been suggested to be critical to the formation of channel flow required to form the Greater Himalayan Crystalline Sequence (Beaumont et al., 2004, 2001). Figure 6.7 shows that surface processes do not have a major influence on the overall structure of the orogen over 2000 km of convergence, with the only difference being the deposition of sediments throughout the orogen.

Although focused erosion produces channel flow (Beaumont et al., 2001), our models highlight that a region of focused erosion is not required to form channel flow during orogenesis. Instead, our models show that channel flow can also form due to tectonic processes, occurring due to gravitational forces that evolve self-consistently at a high

convergence velocity. The high convergence velocity causes the burial of cold material to deep within the orogen and the exhumation of hot material from deep within the wedge towards the surface.

6.3.3.3. Role of crustal density

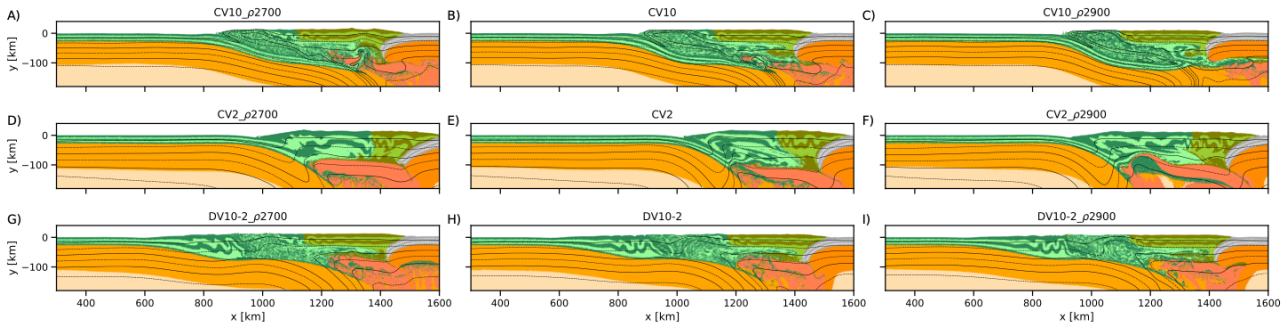

Figure 6.8: Comparison of models after 2000 km of convergence with varying crustal density. Left - ρ_0 = 2700 kg m^{-3}, centre - ρ_0 = 2800 kg m^{-3}, right - ρ_0 = 2900 kg m^{-3}. Fast convergence models (v_{conv} = 10 cm yr^{-1}) are along the top (A - C), slow convergence models (v_{conv} = 2 cm yr^{-1}) are along the middle (D – F) and fast-to-slow convergence models (v_{conv} = 10 to 2 cm yr^{-1}) are along the bottom (G – I). The models show that changes in the crustal density do not influence the overall structure of the orogen, with only minor localised variations in structure observed.

The reference density (ρ_0) of the crust was also varied to assess how the density influences the structural evolution of the orogen. Figure 6.8 shows that the density of the crust does not have a major influence on the overall structure of the orogen, with only subtle variations in structures observed.

In the fast convergence models (v_{conv} = 10 cm yr^{-1}) (Figure 6.8A-C), increasing the crustal density narrows the orogen, increases the overall crustal thickness and increases the amount of underthrusting that occurs below the orogen. The main difference is the angle of underthrusting and the angle of subducting lithosphere, both of which increase with increasing crustal density. This is due to the increase in crustal density increasing the vertical stress component whilst the horizontal stress component, due to the imposed convergence, remains the same, causing the angle of subducting lithosphere to increase. An increase in density also causes more of LM B to be removed underneath the plateau due to the increase in crust that is underthrusted below crust B.

In the slow convergence models (v_{conv} = 2 cm yr^{-1}) (Figure 6.8D-F), increasing the crustal density also narrows the orogen, increases the overall crustal thickness and increases the amount of underthrusting that occurs below the orogen. Some local variations in structure within the orogen occur, but overall, the structures remain similar regardless of crustal density due to the low convergence velocity.

In the fast-to-slow convergence models (v_{conv} = 10 to 2 cm yr^{-1}) (Figure 6.8G-I), increasing the crustal density does not vary the structures within the orogen significantly, with similar structures observed in all fast-to-slow models. The main difference occurs in the structures observed within the fold-and-thrust belt, with the dip angle of shear zones increasing with increasing crustal density. This is due to the increase in crustal density increasing the vertical stress component whilst the horizontal component remains the same across all models due to the same convergence velocity, which increases the dip angle of the shear zone.

6.4. Discussion

6.4.1. The role of velocity on the long-term structural evolution

The results presented show that the structures that develop during orogenesis are dependent on the convergence velocity and thermal evolution. At a low convergence velocity, diffusion is the dominant process controlling the thermal evolution of the wedge, whilst at high velocity advection dominates, resulting in very different structures. However, when the convergence velocity decreases, the models follow a different evolution, with advection dominating at high velocity and diffusion dominating at low velocity. Whilst some of the structures observed in the high velocity model emerge in the fast-to-slow model, the processes forming these structures are transient and strongly constrain the subsequent evolution: first, features achieved during the early, fast-convergence stage are progressively

abandoned during the wedge re-equilibration to slower, colder wedge dynamics, second, these early features exert crucial constraints on the formation of the frontal fold-and-thrust belt.

The fast convergence velocity in CV10 and the beginning of DV10-2 favours the thickening of crust over lateral flow, forming a proto-wedge above the pre-existing lithospheric weakness. As the fast convergence is maintained, underthrusting of Crust A below Crust B occurs due to the far-field forces produced by the applied convergence on the left sidewall. If these forces generating the high convergence velocity were generated by the subducting lithosphere alone, it is likely the horizontal underthrusting would not occur as the primary force direction would be vertical from the subducting lithosphere rather than horizontal.

The high convergence velocity and resultant underthrusting in our model results in a curved geometry of the suture zone, similar to generalised cross-sections of the region (Figure 6.1A). The geometry of the suture zone suggests an external driving force in the region is required to reach the high velocities observed at collision ~50 Ma. Modelling by Pusok and Stegman (2020) propose that the anomalously high velocity could only have been achieved by the arrival of the Reunion mantle plume and a double subduction system in the region prior to collision. Our results show that the high convergence velocity also results in the formation of a region of return flow at the front of the wedge, with a high velocity required to bury the rigid crust, which is not seen in CV2. The subsequent flattening of the lithosphere observed in CV10 and DV10-2 is likely due to the horizontal forces exceeding the vertical forces, resulting in the flattening of the subducting lithosphere.

In DV10-2, the cessation of burial and exhumation results in the relaxation of the isotherms. Coupled with the reduction in convergence velocity, which decreases the depth of the brittle-ductile transition, results in a fold-and-thrust belt developing at the front of the

orogen. The FAT belt has a viscous decollement that allows thrusts to propagate outwards at the front of the wedge. This is not observed in CV10 as the convergence velocity remains high and the isotherms do not diffuse and equilibrate, resulting in deformation concentrated in the highly deformed region.

CV2 has a different evolution to CV10 and DV10-2 due to the low convergence rate throughout. This is apparent in the topography, with a wide and flat orogen visible after 50 Myr (Figure 6.4A-B). However, as convergence is ongoing, the material continues to shorten, resulting in folding and thickening of crust B between ~50 and 80 Myr as the wedge can no longer migrate backwards due to crust C, which acts as a rigid backstop (Figure 6.4C). As convergence continues, thickening of crust A occurs between the subduction zone and the contact with crust B (Figure 6.4D).

The results of CV10 and CV2 show low velocity favours viscous deformation and the flow of crust, whilst high velocity favours shearing, whilst the decreasing velocity model (DV10-2) results in a unique evolution that shares similarities with CV10 at high velocity before the slowdown of convergence and subsequent thermal diffusion resulting in the formation of a FAT belt at the front of the wedge.

6.4.2. Insights into the processes occurring in the Himalayas and Tibet over time

Although some structures that emerge in CV10 and CV2 are comparable to the structures observed in the Himalayas and Tibet, we focus on the evolution of DV10-2 which replicates major structures observed in the region. More importantly, the structures that emerge in DV10-2 form at a similar time to those determined for structures observed in the Himalayas and Tibet. To compare the timing of structures between DV10-2 and those

observed in the Himalayas and Tibet, we equilibrate 0 Myr to 50 Ma, which denotes the onset of collision in the region.

6.4.2.1. Uplift of Tibetan Plateau

DV10-2 provides insights into processes that result in the uplift of the TP and the timing of uplift. DV10-2 suggests the TP formed from at a central point, with initial uplift to form a proto-wedge occurring at the onset of collision ~50 Ma close to the initial point of continental collision, with the plateau then expanding both North and South from this central point. This is in agreement with the timing of uplift in Tibet as recorded by the formation of sediment basins across the TP, with uplift in the North Qiangtang terrane and Hoh Xil basin dated between 50-30 Ma, whilst uplift in the Gyirong and Thakkhola basins to the south of the Plateau in the Himalayas have been dated as reaching their current elevation ~11 Ma (Wang et al., 2014, 2008). DV10-2 suggests that most of the uplift of the TP occurred early after collision, between 5 and 15 Myr (45 to 35 Ma), which is in agreement with Wang et al. (2008) that used magnetostratigraphy, sedimentology, paleocurrent measurements, and $^{40}Ar/^{39}Ar$ and fission-track studies to show that the centre of the TP was elevated by ~40 Ma.

As well as the timing, the model also provides insights into the processes that result in the uplift of the plateau. In DV10-2, underthrusting of crust A, equivalent to the Indian crust, below crust B, the Asian crust (Figure 6.9) is observed. Underthrusting has previously been proposed to explain the thick crust below the TP that is required to support the elevated topography in the region (Argand, 1922; DeCelles et al., 2002; Powell, 1986). In DV10-2, underthrusting occurs between 7 and 15 Myr (43 to 35 Ma), which jacks up crust B to form a plateau. Underthrusting also results in an increase in the temperature of the lower crust (Avouac, 2015; Burov, 2011), resulting in a viscous lower crust that flows (Figure 6.9), which has also been suggested as a process that could have formed of the TP (Clark et al., 2005a;

Clark and Royden, 2000; Cook and Royden, 2008; Royden, 1997). The model results also show that the formation of a thick plateau due to underthrusting does not occur when the internal heating rate of the crust is high (H_r = 2.25 μW m^{-3}) as the advection of cold material is thwarted by the high internal heating rate that increases the temperature of the crust.

During the underthrusting of crust A in DV10-2, crust B undergoes minor thickening and folding, which has also been suggested for the Tibetan crust to account for the large crustal thicknesses in the region (England and Houseman, 1986; Molnar et al., 1993a). DV10-2 does not include variations in terrane rheology within the TP, whereas previous studies have suggested the rheology may vary within the TP which results in variations in deformation age at terrane boundaries within the TP (Kelly et al., 2019, 2016).

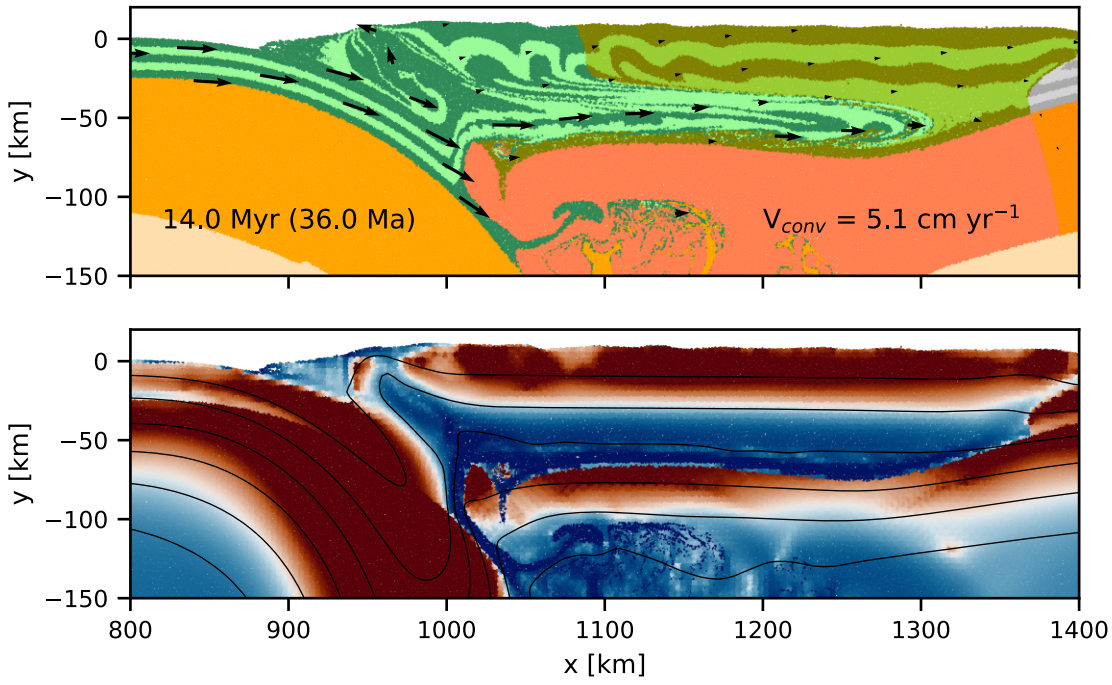

Figure 6.9: Underthrusting of crust A and the formation of a viscous lower crust to form the Tibetan Plateau in DV10-2. Top – material, bottom – viscosity.

6.4.2.2. Formation of the Himalayan FAT belt

DV10-2 also provides insights into the formation of the Himalayan FAT belt, including the formation of channel flow and the emplacement of the GHCS, doming of the crust to

form the Northern Himalayan Domes (NHD) and the formation of a fold-and-thrust belt at the front of the orogen.

In DV10-2 the front of the orogen begins to accommodate convergence as burial and exhumation occurs between 14 and 30 Myr (36 to 20 Ma). Return flow is characterised by a velocity profile that suggests burial that is driven by shearing of rigid crust at the front of the orogen (Couette flow), whilst the velocity profile close to the top boundary of the return flow region suggests pressure driven during exhumation (Poiseuille flow). The kinematics in DV10-2 are similar to kinematic indicators observed across the Greater Himalayan Crystalline Sequence (GHCS), which show top-to-south kinematic indicators and inverted metamorphic isograds in the lower part of the GHCS above the Main Central Thrust (MCT) creating a hot-on-cold sequence across the MCT (Goscombe et al., 2018; Hunter et al., 2018; Searle, 2015) whilst top-to-north kinematic indicators and right-way-up metamorphic isograds are observed in the upper part of the GHCS below the Southern Tibetan Detachment (STD) (Godin et al., 2006; Searle, 2015). Our model results in peak temperatures of ~600 °C recorded in the pressure-temperature-time (PTt) paths, similar to peak temperatures recorded in the GHCS (Avouac, 2015; Goscombe et al., 2018; Searle, 2015).

Exhumation in DV10-2 is driven by a (large) pressure gradient (Figure 6.5B) caused by the variations in topography and crustal thickness between the plateau and foreland. A large pressure gradient is required to generate channel flow (Searle, 2015), with the large pressure gradient possible in the Himalayas due to the large variation in topography and crustal thickness between the Tibetan Plateau (~5 km elevation; 65–75 km thick crust) and Indian foreland (<0.5 km elevation; ~35– 40 km thick crust) (Searle, 2015).

The various boundary conditions tested (CV10, CV2 and DV10-2) suggest that to form an area of return flow, not only is a large pressure gradient required, but the

convergence velocity must also be high enough to facilitate the amount of shearing required to bury rigid crust at the front of the orogen (Godin et al., 2006; Searle, 2015) and the internal heating rate of the crust must be low (<2.25 $\mu W\ m^{-3}$) to allow advection and the development of sharp thermal gradients. CV2 has a large variation in crustal thickness and topography (Figure 6.3E) but does not have a phase of return flow due to the low convergence velocity, whilst CV10 and DV10-2 both display a phase of return flow as the convergence velocity is adequate in both models to bury rigid crust at the front of the orogen. Our models also show that the density of the crust does not alter the formation of return flow in the fast and fast to slow models, with return flow occurring in all models tested (Figure 6.8). Our suit of models also show that focused erosion is not required to develop return flow (Beaumont et al., 2004, 2001), with return flow driven by tectonic forces (Godin et al., 2006; Searle, 2015).

The timing of return flow in DV10-2 is in agreement with PTt paths obtained from the GHCS, with evidence of burial and exhumation beginning between the South Tibet Detachment and Main Central Thrust ~38 Ma (Goscombe et al., 2018; Searle, 2015; Searle and Hacker, 2019) and ceasing once the Himalayan FAT began to develop ~18 Ma (Gao et al., 2016; Searle, 2015). Both CV10 (Figure 6.3F) and DV10-2 (Figure 6.5F) exhibit multiple burial and exhumation cycles during the evolution of the model, with the passive tracers displaying ‘yo-yo’ tectonics. ‘Yo-yo’ tectonics has been observed in PTt paths from the Niğde Massif, Turkey (Umhoefer et al., 2007) and Western Alps (Rubatto et al., 2011), however there are currently no studies suggesting ‘yo-yo’ tectonics has occurred in the GHCS.

The large exhumation of crustal material seen in phase 4 of DV10-2 between 31 and 38 Myr (Figure 6.5C) is a result of the change in subduction angle of the lithosphere, with the change in angle of subduction decreasing to sub-horizontal, which alters the stress state at the front of the orogen. This causes a decrease in the pressure gradient at the front of the orogen which was driving localised exhumation in the return flow region. The change in

pressure gradient results in the exhumation of a large amount of material, producing a highly deformed region of crust, and signals the beginning of the development of the FAT belt in DV10-2 (Figure 6.5C). However, as the large exhumation event occurs in both CV10 and DV10-2 but a FAT belt does not develop CV10, the change in pressure gradient and flattening of the subducting lithosphere does not cause the FAT belt to form. The large exhumation of crust and subsequent cooling of the highly deformed region in DV10-2 is similar in time and structure to that seen in the Northern Himalayan Domes, which were emplaced 21 – 12 Ma (Goscombe et al., 2018). The large exhumation event in DV10-2 results in rapid cooling of the orogen, similar to the large decrease in temperature from ~600 °C to ~200 °C observed at ~16 Ma in geochronological data obtained from the Everest Himalaya area (Searle, 2015) (Figure 6.10).

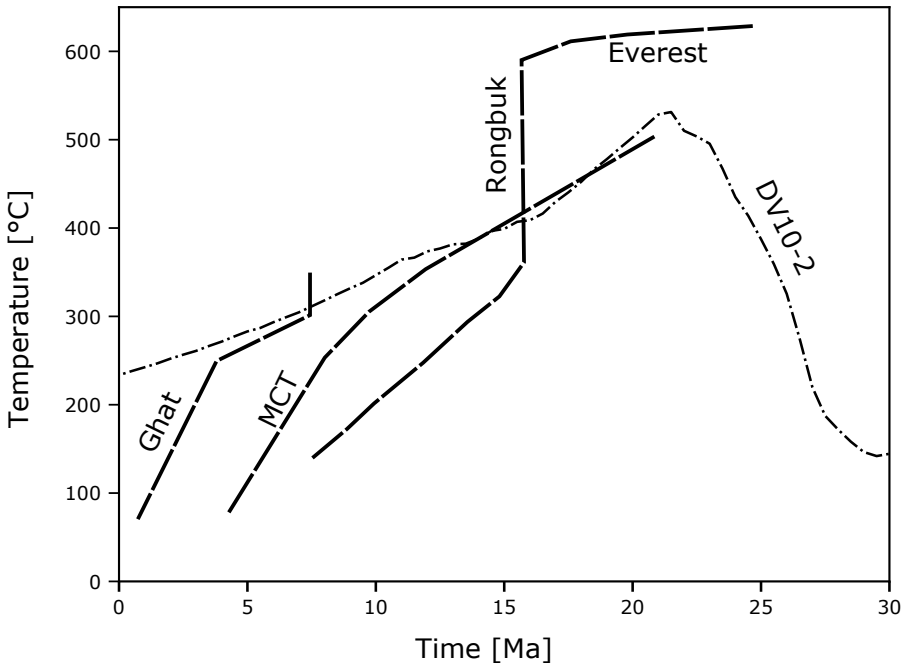

Figure 6.10: Temperature vs time diagram to compare geochronological data from the Himalayas presented in Searle (2015) with model results. Both show peak metamorphic temperatures between 20 and 25 Ma before decreasing due to the rapid exhumation and subsequent cooling of the partial molten mid-crust, as observed in phase 4 of DV10-2.

Our models also show that the burial and exhumation of crust in phase 3 and 4 is hindered by high internal heating rates. With high internal heating rates (H_r = 2.25 μW m^{-3}),

burial of cold material to deep within the crust and the exhumation of warm crust from near the Moho does not occur as the influence of advection on the temperature distribution is outweighed by the internal heating rate.

The final phase (phase 5) in the evolution of DV10-2 results in the formation of a FAT belt at the front of the orogen (Figure 6.5D). As the velocity decreases in DV10-2 at ~32 Myr (~18 Ma) to 2 cm yr^{-1}, a FAT belt begins to form as exhumation of crust occurs in the centre of the orogen. The FAT belt becomes the primary process accommodating convergence at ~38 Myr (12 Ma) when exhumation ceases. This is similar to how convergence is currently accommodated in the Himalayas, where around 2 cm yr^{-1} of the 5 cm yr^{-1} Indian plate velocity is accommodated in the H-FAT belt (Ader et al., 2012; Stevens and Avouac, 2015), with the rest accommodated through lateral extrusion in the East, which is documented by GPS measurements taken across the region (Gan et al., 2007; Liang et al., 2013).

The FAT belt develops at the front of the orogen due to the slowing of convergence and re-equilibration of the isotherms, resulting in a viscous lower crust and plastic upper crust which causes a FAT belt to begin to develop at ~32 Myr (~18 Ma). This timing of FAT belt development is close to the ages obtained for the initial development of the H-FAT belt ~20 Ma (Gao et al., 2016; Searle, 2015; Tobgay et al., 2012). As a FAT belt does not form in CV10, the thermal re-equilibration at the front of the wedge due to the decreasing convergence velocity is the main cause of the development of the FAT belt in DV10-2. The fold and thrust belt links to a viscous basal decollement, which is similar to the structure in the H-FAT, where all major faults in the H-FAT link to the Main Himalayan Thrust (MHT), which is the basal decollement, at depth (DeCelles et al., 2002, 2001; Nelson et al., 1996; Zhao et al., 1993).

There is a progressive decrease in the age of activity of the active fault and a shallowing of the decollement toward the hinterland observed in the evolution of DV10-2,

which is also in agreement to the evolution of the main thrusts within the Himalayan FAT belt (DeCelles et al., 2002, 2001; Goscombe et al., 2018). The development of shear zones and the formation of a FAT belt accommodating convergence instead of channel flow is in agreement with seismic reflection profiles, which show a single, continuous reflection visible in seismic reflection profiles that represents the MHT, which would not be visible if channel flow was operating in the region (Gao et al., 2016). The depth of the brittle-ductile transition, controlling the depth of seismicity, is mainly controlled by the temperature, with the transition occurring at a depth of ~35 km along the 400 °C isotherm.

Our models also suggest that the development of a fold-and-thrust belt is controlled by the temperature distribution within the crust, with a fold-and-thrust belt forming when there are no large temperature gradients in the crust. This occurs in the fast-to-slow convergence model due to diffusion at the low convergence rate, re-equilibrating the temperature within the wedge. A fold-and-thrust belt also occurs when internal heating is high enough, as internal heating outweighs the role of advection and diffusion, causing the isotherms to remain relatively stable throughout the evolution of the model.

Figure 6.11 shows that the final topographic shape of DV10-2 matches the topography obtained from ETOPO1 (Amante, 2009), with the orogen rising from the lowlands to the height of the plateau over a distance of ~100 km. The model also matches the shape of plateau; however a discrepancy exists between the height of the plateau in the model compared to nature, which is most likely due to the model not capturing the isostasy of the crust accurately due to a temperature-dependent density used for the entire crust.

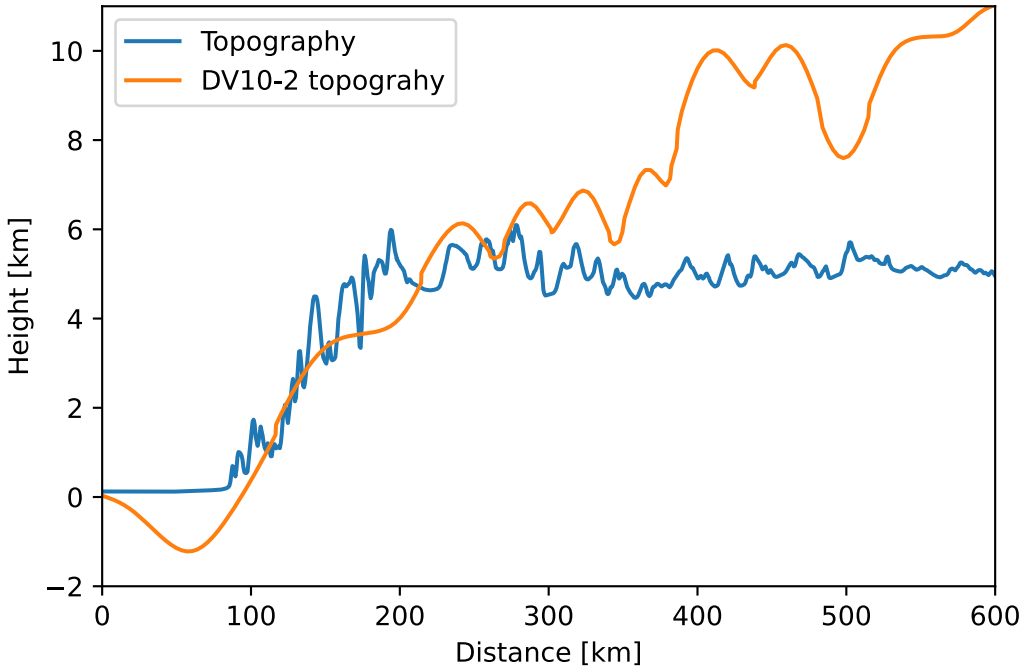

Figure 6.11: Comparison of topography at the front of the orogen between the model (DV10-2 – orange line) and nature (topography – blue line). The model matches the overall topographic shape, whilst there are discrepancies in the plateau height of ~2 km. The topography was determined between points (81, 27) and (87, 37) in the WGS84 reference frame.

6.4.3. Model limitations

Although our model reproduces major structures observed across the Himalayas and Tibet, providing insights into the processes that form these structures, there are discrepancies between the model results and nature. One major inconsistency is the length between the suture zone and front of the orogen, which incorporates the region of channel flow, doming and the fold-and-thrust belt. In DV10-2, this region occurs over a length of ~600 km, whilst in the Himalayas these features occur over a length of ~150 km in the East and ~350 km in the West (Roy and Purohit, 2018). Another inconsistency is the depth of the decollement at the front of the wedge, which occurs at the base of the crust in our models. In the Himalayas, the MHT is visible at <20 km below the Himalayan fold-and-thrust belt based on seismic imaging (Dal Zilio et al., 2021; Hubbard et al., 2016; Wang et al., 2017).

6.5. Conclusions

The structures in the Himalayan FAT belt and Tibetan Plateau document a complex structural and thermal evolution, with various processes operating throughout the evolution. Our numerical models show that the deformation of the crust during orogenesis is the product of the convergence history and thermal evolution.

Although constant velocity models replicate some structures observed in the region, only the fast to slow model reproduces most features recorded in the region at a comparable time and for a similar duration. At high velocity, underthrusting of the crust occurs to form a plateau, along with the burial of cold, rigid crust and exhumation of hot, viscous crust to form a region of return flow. As the velocity decreases and the temperature re-equilibrates, a fold-and-thrust belt develops to accommodate convergence as the stress is concentrated at the front of the orogen.

Our models also show that when internal heating is high, internal heating hinders advection and diffusion, resulting in similar structures regardless of the convergence velocity, suggesting that the average internal heating rate of the crust must be below 2.25 $\mu W\ m^{-3}$ to produce the structures observed in the region. The models also show that surface processes and the density of the crust do not alter the overall structural evolution, however they do produce localised variations in structure due to altering the forces acting on the crust.

6.6. References

Ader, T., Avouac, J.-P., Liu-Zeng, J., Lyon-Caen, H., Bollinger, L., Galetzka, J., Genrich, J., Thomas, M., Chanard, K., Sapkota, S.N., Rajaure, S., Shrestha, P., Ding, L., Flouzat, M., 2012. Convergence rate across the Nepal Himalaya and interseismic coupling on the Main Himalayan Thrust: Implications for seismic hazard. J. Geophys. Res. Solid Earth 117, n/a-n/a. https://doi.org/10.1029/2011JB009071

Amante, C. (2009). Etopo1 1 arc-minute global relief model: Procedures, data sources and analysis. National Geophysical Data Center. https://doi.org/10.7289/V5C8276M

Argand, E., 1922. La tectonique de l'Asie. Conférence faite á Bruxelles, le 10 août 1922, in: Congrès Géologique International (XIIIe Session)- Belgique 1922. Belgium, pp. 171–372.

Avouac, J.-P., 2007. 6.09 - Dynamic Processes in Extensional and Compressional Settings – Mountain Building: From Earthquakes to Geological Deformation, in: Schubert, G. (Ed.), Treatise on Geophysics. Elsevier, Amsterdam, pp. 377–439. https://doi.org/10.1016/B978-044452748-6.00112-7

Avouac, J.-P., 2015. Mountain Building: From Earthquakes to Geologic Deformation, in: Treatise on Geophysics. Elsevier, pp. 381–432. https://doi.org/10.1016/B978-0-444-53802-4.00120-2

Beaumont, C., Jamieson, R.A., Nguyen, M.H., Lee, B., 2001. Himalayan tectonics explained by extrusion of a low-viscosity crustal channel coupled to focused surface denudation. Nature 414, 738–742. https://doi.org/10.1038/414738a

Beaumont, C., Jamieson, R.A., Nguyen, M.H., Medvedev, S., 2004. Crustal channel flows: 1. Numerical models with applications to the tectonics of the Himalayan-Tibetan orogen. J. Geophys. Res. Solid Earth 109. https://doi.org/10.1029/2003JB002809

Beucher, R., Moresi, L., Giordani, J., Mansour, J., Sandiford, D., Farrington, R., Mondy, L., Mallard, C., Rey, P., Duclaux, G., Kaluza, O., Laik, A., Morón, S., 2019. UWGeodynamics: A teaching and research tool for numerical geodynamic modelling. J. Open Source Softw. 4, 1136. https://doi.org/10.21105/joss.01136

Burg, J.-P., Gerya, T.V., 2005. The role of viscous heating in Barrovian metamorphism of collisional orogens: thermomechanical models and application to the Lepontine Dome in the Central Alps. J. Metamorph. Geol. 23, 75–95. https://doi.org/10.1111/j.1525-1314.2005.00563.x

Burg, J.P., Schmalholz, S.M., 2008. Viscous heating allows thrusting to overcome crustal-scale buckling: Numerical investigation with application to the Himalayan syntaxes. Earth Planet. Sci. Lett. 274, 189–203. https://doi.org/10.1016/j.epsl.2008.07.022

Burov, E.B., 2011. Rheology and strength of the lithosphere. Mar. Pet. Geol. 28, 1402–1443. https://doi.org/10.1016/j.marpetgeo.2011.05.008

Capitanio, F.A., 2020. Current Deformation in the Tibetan Plateau: A Stress Gauge in the India-Asia Collision Tectonics. Geochem. Geophys. Geosystems 21, e2019GC008649. https://doi.org/10.1029/2019GC008649

Capitanio, F.A., Morra, G., Goes, S., Weinberg, R.F., Moresi, L., 2010. India–Asia convergence driven by the subduction of the Greater Indian continent. Nat. Geosci. 3, 136–139. https://doi.org/10.1038/ngeo725

Capitanio, F.A., Replumaz, A., Riel, N., 2015. Reconciling subduction dynamics during Tethys closure with large-scale Asian tectonics: Insights from numerical modeling. Geochem. Geophys. Geosystems 16, 962–982. https://doi.org/10.1002/2014GC005660

Cattin, R., Avouac, J.P., 2000. Modeling mountain building and the seismic cycle in the Himalaya of Nepal. J. Geophys. Res. Solid Earth 105, 13389–13407. https://doi.org/10.1029/2000JB900032

Chen, L., Capitanio, F.A., Liu, L., Gerya, T.V., 2017. Crustal rheology controls on the Tibetan plateau formation during India-Asia convergence. Nat. Commun. 8, 15992. https://doi.org/10.1038/ncomms15992

Chen, L., Liu, L., Capitanio, F.A., Gerya, T.V., Li, Y., 2020. The role of pre-existing weak zones in the formation of the Himalaya and Tibetan plateau: 3-D thermo-mechanical modeling. Geophys. J. Int. ggaa125. https://doi.org/10.1093/gji/ggaa125

Clark, M.K., Bush, J.W.M., Royden, L.H., 2005a. Dynamic topography produced by lower crustal flow against rheological strength heterogeneities bordering the Tibetan Plateau. Geophys. J. Int. 162, 575–590. https://doi.org/10.1111/j.1365-246X.2005.02580.x

Clark, M.K., Bush, J.W.M., Royden, L.H., 2005b. Dynamic topography produced by lower crustal flow against rheological strength heterogeneities bordering the Tibetan Plateau. Geophys. J. Int. 162, 575–590. https://doi.org/10.1111/j.1365-246X.2005.02580.x

Clark, M.K., Royden, L.H., 2000. Topographic ooze: Building the eastern margin of Tibet by lower crustal flow 4.

Cook, K.L., Royden, L.H., 2008. The role of crustal strength variations in shaping orogenic plateaus, with application to Tibet. J. Geophys. Res. Solid Earth 113. https://doi.org/10.1029/2007JB005457

Dal Zilio, L., Dinther, Y. van, Gerya, T., Avouac, J.-P., 2019. Bimodal seismicity in the Himalaya controlled by fault friction and geometry. Nat. Commun. 10, 48. https://doi.org/10.1038/s41467-018-07874-8

Dal Zilio, L., Hetényi, G., Hubbard, J., Bollinger, L., 2021. Building the Himalaya from tectonic to earthquake scales. Nat. Rev. Earth Environ. 2, 251–268. https://doi.org/10.1038/s43017-021-00143-1

Dal Zilio, L., Ruh, J., Avouac, J.-P., 2020. Structural Evolution of Orogenic Wedges: Interplay Between Erosion and Weak Décollements. Tectonics 39, e2020TC006210. https://doi.org/10.1029/2020TC006210

DeCelles, P.G., Robinson, D.M., Quade, J., Ojha, T.P., Garzione, C.N., Copeland, P., Upreti, B.N., 2001. Stratigraphy, structure, and tectonic evolution of the Himalayan fold-thrust belt in western Nepal. Tectonics 20, 487–509. https://doi.org/10.1029/2000TC001226

DeCelles, P.G., Robinson, D.M., Zandt, G., 2002. Implications of shortening in the Himalayan fold-thrust belt for uplift of the Tibetan Plateau. Tectonics 21, 12-1-12–25. https://doi.org/10.1029/2001TC001322

Elliott, J.R., Jolivet, R., González, P.J., Avouac, J.P., Hollingsworth, J., Searle, M.P., Stevens, V.L., 2016. Himalayan megathrust geometry and relation to topography revealed by the Gorkha earthquake. Nat. Geosci. 9, 174. https://doi.org/10.1038/ngeo2623

England, P., Houseman, G., 1986. Finite strain calculations of continental deformation: 2. Comparison with the India-Asia Collision Zone. J. Geophys. Res. Solid Earth 91, 3664–3676. https://doi.org/10.1029/JB091iB03p03664

Faccenda, M., Gerya, T.V., Chakraborty, S., 2008. Styles of post-subduction collisional orogeny: Influence of convergence velocity, crustal rheology and radiogenic heat production. Lithos 103, 257–287. https://doi.org/10.1016/j.lithos.2007.09.009

Faccenda, M., Minelli, G., Gerya, T.V., 2009. Coupled and decoupled regimes of continental collision: Numerical modeling. Earth Planet. Sci. Lett. 278, 337–349. https://doi.org/10.1016/j.epsl.2008.12.021

Gan, W., Zhang, P., Shen, Z.-K., Niu, Z., Wang, M., Wan, Y., Zhou, D., Cheng, J., 2007. Present-day crustal motion within the Tibetan Plateau inferred from GPS

measurements. J. Geophys. Res. Solid Earth 112. https://doi.org/10.1029/2005JB004120

Gao, R., Lu, Z.W., Klemperer, S.L., Wang, H.Y., Dong, S.W., Li, W.H., Li, H.Q., 2016. Crustal-scale duplexing beneath the Yarlung Zangbo suture in the western Himalaya. Nat. Geosci. 9, 555-+. https://doi.org/10.1038/ngeo2730

Gerya, T., 2009. Introduction to Numerical Geodynamic Modelling. Cambridge University Press, Cambridge. https://doi.org/10.1017/CBO9780511809101

Godin, L., Grujic, D., Law, R.D., Searle, M.P., 2006. Channel flow, ductile extrusion and exhumation in continental collision zones: an introduction. Geol. Soc. Lond. Spec. Publ. 268, 1–23. https://doi.org/10.1144/GSL.SP.2006.268.01.01

Goscombe, B., Gray, D., Foster, D.A., 2018. Metamorphic response to collision in the Central Himalayan Orogen. Gondwana Res. 57, 191–265. https://doi.org/10.1016/j.gr.2018.02.002

Guillot, S., Garzanti, E., Baratoux, D., Marquer, D., Mahéo, G., Sigoyer, J. de, 2003. Reconstructing the total shortening history of the NW Himalaya. Geochem. Geophys. Geosystems 4. https://doi.org/10.1029/2002GC000484

Halim, N., Cogné, J.P., Chen, Y., Atasiei, R., Besse, J., Courtillot, V., Gilder, S., Marcoux, J., Zhao, R.L., 1998. New Cretaceous and Early Tertiary paleomagnetic results from Xining-Lanzhou basin, Kunlun and Qiangtang blocks, China: Implications on the geodynamic evolution of Asia. J. Geophys. Res. Solid Earth 103, 21025–21045. https://doi.org/10.1029/98JB01118

Herman, F., Copeland, P., Avouac, J.-P., Bollinger, L., Mahéo, G., Fort, P.L., Rai, S., Foster, D., Pêcher, A., Stüwe, K., Henry, P., 2010. Exhumation, crustal deformation, and thermal structure of the Nepal Himalaya derived from the inversion of thermochronological and thermobarometric data and modeling of the topography. J. Geophys. Res. Solid Earth 115. https://doi.org/10.1029/2008JB006126

Hirth, G., Kohlstedt, D., 2003. Rheology of the upper mantle and the mantle wedge: A view from the experimentalists, in: Eiler, J. (Ed.), Geophysical Monograph Series. American Geophysical Union, Washington, D. C., pp. 83–105. https://doi.org/10.1029/138GM06

Hubbard, J., Almeida, R., Foster, A., Sapkota, S.N., Bürgi, P., Tapponnier, P., 2016. Structural segmentation controlled the 2015 Mw 7.8 Gorkha earthquake rupture in Nepal. Geology 44, 639–642. https://doi.org/10.1130/G38077.1

Hunter, N.J.R., Weinberg, R.F., Wilson, C.J.L., Luzin, V., Misra, S., 2018. Microscopic anatomy of a “hot-on-cold” shear zone: Insights from quartzites of the Main Central Thrust in the Alaknanda region (Garhwal Himalaya). GSA Bull. 130, 1519–1539. https://doi.org/10.1130/B31797.1

Kaus, B.J.P., Steedman, C., Becker, T.W., 2008. From passive continental margin to mountain belt: Insights from analytical and numerical models and application to Taiwan. Phys. Earth Planet. Inter., Recent Advances in Computational Geodynamics: Theory, Numerics and Applications 171, 235–251. https://doi.org/10.1016/j.pepi.2008.06.015

Kelly, S., Beaumont, C., Butler, J.P., 2019. Inherited terrane properties explain enigmatic post-collisional Himalayan-Tibetan evolution. Geology. https://doi.org/10.1130/G46701.1

Kelly, S., Butler, J.P., Beaumont, C., 2016. Continental collision with a sandwiched accreted terrane: Insights into Himalayan–Tibetan lithospheric mantle tectonics? Earth Planet. Sci. Lett. 455, 176–195. https://doi.org/10.1016/j.epsl.2016.08.039

Kohn, M.J., 2014. Himalayan Metamorphism and Its Tectonic Implications. Annu. Rev. Earth Planet. Sci. 42, 381–419. https://doi.org/10.1146/annurev-earth-060313-055005

Liang, S., Gan, W., Shen, C., Xiao, G., Liu, J., Chen, W., Ding, X., Zhou, D., 2013. Three-dimensional velocity field of present-day crustal motion of the Tibetan Plateau derived from GPS measurements. J. Geophys. Res. Solid Earth 118, 5722–5732. https://doi.org/10.1002/2013JB010503

Molnar, P., England, P., Martinod, J., 1993a. Mantle dynamics, uplift of the Tibetan Plateau, and the Indian Monsoon. Rev. Geophys. 31, 357–396. https://doi.org/10.1029/93RG02030

Molnar, P., England, P., Martinod, J., 1993b. Mantle dynamics, uplift of the Tibetan Plateau, and the Indian Monsoon. Rev. Geophys. 31, 357–396. https://doi.org/10.1029/93RG02030

Molnar, P., Stock, J.M., 2009. Slowing of India’s convergence with Eurasia since 20 Ma and its implications for Tibetan mantle dynamics. Tectonics 28. https://doi.org/10.1029/2008TC002271

Molnar, P., Tapponnier, P., 1975. Cenozoic Tectonics of Asia: Effects of a Continental Collision. Science 189, 419–426.

Moresi, L., Dufour, F., Mühlhaus, H.-B., 2003. A Lagrangian integration point finite element method for large deformation modeling of viscoelastic geomaterials. J. Comput. Phys. 184, 476–497. https://doi.org/10.1016/S0021-9991(02)00031-1

Moresi, L., Quenette, S., Lemiale, V., Mériaux, C., Appelbe, B., Mühlhaus, H.-B., 2007. Computational approaches to studying non-linear dynamics of the crust and mantle. Phys. Earth Planet. Inter. 163, 69–82. https://doi.org/10.1016/j.pepi.2007.06.009

Nelson, K.D., Zhao, W., Brown, L.D., Kuo, J., Che, J., Liu, X., Klemperer, S.L., Makovsky, Y., Meissner, R., Mechie, J., Kind, R., Wenzel, F., Ni, J., Nabelek, J., Leshou, C., Tan, H., Wei, W., Jones, A.G., Booker, J., Unsworth, M., Kidd, W.S.F., Hauck, M., Alsdorf, D., Ross, A., Cogan, M., Wu, C., Sandvol, E., Edwards, M., 1996. Partially Molten Middle Crust Beneath Southern Tibet: Synthesis of Project INDEPTH Results. Science 274, 1684–1688. https://doi.org/10.1126/science.274.5293.1684

Patriat, P., Achache, J., 1984. India–Eurasia collision chronology has implications for crustal shortening and driving mechanism of plates. Nature 311, 615–621. https://doi.org/10.1038/311615a0

Piccolo, A., Faccenda, M., Carosi, R., Montomoli, C., Visonà, D., 2017. Crustal strength control on structures and metamorphism in collisional orogens. Tectonophysics. https://doi.org/10.1016/j.tecto.2017.09.018

Pichon, X.L., Fournier, M., Jolivet, L., 1992. Kinematics, topography, shortening, and extrusion in the India-Eurasia collision. Tectonics 11, 1085–1098. https://doi.org/10.1029/92TC01566

Powell, C.McA., 1986. Continental underplating model for the rise of the Tibetan Plateau. Earth Planet. Sci. Lett. 81, 79–94. https://doi.org/10.1016/0012-821X(86)90102-0

Pusok, A.E., Kaus, B.J.P., 2015. Development of topography in 3-D continental-collision models. Geochem. Geophys. Geosystems 16, 1378–1400. https://doi.org/10.1002/2015GC005732

Pusok, A.E., Stegman, D.R., 2020. The convergence history of India-Eurasia records multiple subduction dynamics processes. Sci. Adv. 6, eaaz8681. https://doi.org/10.1126/sciadv.aaz8681

Ranalli, G., 1995. Rheology of the Earth. Springer Science & Business Media.

Royden, L.H., 1997. Surface Deformation and Lower Crustal Flow in Eastern Tibet. Science 276, 788–790. https://doi.org/10.1126/science.276.5313.788

Rubatto, D., Regis, D., Hermann, J., Boston, K., Engi, M., Beltrando, M., McAlpine, S.R.B., 2011. Yo-yo subduction recorded by accessory minerals in the Italian Western Alps. Nat. Geosci. 4, 338–342. https://doi.org/10.1038/ngeo1124

Searle, M.P., 2015. Mountain Building, Tectonic Evolution, Rheology, and Crustal Flow in the Himalaya, Karakoram, and Tibet, in: Treatise on Geophysics. Elsevier, pp. 469–511. https://doi.org/10.1016/B978-0-444-53802-4.00121-4

Searle, M.P., Hacker, B.R., 2019. Structural and metamorphic evolution of the Karakoram and Pamir following India–Kohistan–Asia collision. Geol. Soc. Lond. Spec. Publ. 483, 555–582. https://doi.org/10.1144/SP483.6

Spain, M., Hirn, A., 1997. Seismic structure and evidence for eclogitization during the Himalayan convergence. Tectonophysics, Collisional Orogens: Zones of Active Transfer Between Crust and Mantle 273, 1–16. https://doi.org/10.1016/S0040-1951(96)00285-5

Spiegelman, M., May, D.A., Wilson, C.R., 2016. On the solvability of incompressible Stokes with viscoplastic rheologies in geodynamics. Geochem. Geophys. Geosystems 17, 2213–2238. https://doi.org/10.1002/2015GC006228

Stevens, V.L., Avouac, J.P., 2015. Interseismic coupling on the main Himalayan thrust. Geophys. Res. Lett. 42, 5828–5837. https://doi.org/10.1002/2015GL064845

Streule, M.J., Strachan, R.A., Searle, M.P., Law, R.D., 2010. Comparing Tibet-Himalayan and Caledonian crustal architecture, evolution and mountain building processes. Geol. Soc. Lond. Spec. Publ. 335, 207–232. https://doi.org/10.1144/SP335.10

Tapponnier, P., Peltzer, G., Dain, A.Y.L., Armijo, R., Cobbold, P., 1982. Propagating extrusion tectonics in Asia: New insights from simple experiments with plasticine. Geology 10, 611–616. https://doi.org/10.1130/0091-7613(1982)10<611:PETIAN>2.0.CO;2

Tapponnier, P., Zhiqin, X., Roger, F., Meyer, B., Arnaud, N., Wittlinger, G., Jingsui, Y., 2001. Oblique Stepwise Rise and Growth of the Tibet Plateau. Science 294, 1671–1677. https://doi.org/10.1126/science.105978

Umhoefer, P.J., Whitney, D.L., Teyssier, C., Fayon, A.K., Casale, G., Heizler, M.T., 2007. Yo-yo tectonics in a wrench zone, Central Anatolian fault zone, Turkey. https://doi.org/10.1130/2007.2434(03)

Vogt, K., Matenco, L., Cloetingh, S., 2017. Crustal mechanics control the geometry of mountain belts. Insights from numerical modelling. Earth Planet. Sci. Lett. 460, 12–21. https://doi.org/10.1016/j.epsl.2016.11.016

Wang, C., Dai, J., Zhao, X., Li, Y., Graham, S.A., He, D., Ran, B., Meng, J., 2014. Outward-growth of the Tibetan Plateau during the Cenozoic: A review. Tectonophysics 621, 1–43. https://doi.org/10.1016/j.tecto.2014.01.036

Wang, C., Zhao, X., Liu, Z., Lippert, P.C., Graham, S.A., Coe, R.S., Yi, H., Zhu, L., Liu, S., Li, Y., 2008. Constraints on the early uplift history of the Tibetan Plateau. Proc. Natl. Acad. Sci. 105, 4987–4992. https://doi.org/10.1073/pnas.0703595105

Wang, X., Wei, S.J., Wu, W.B., 2017. Double-ramp on the Main Himalayan Thrust revealed by broadband waveform modeling of the 2015 Gorkha earthquake sequence. Earth Planet. Sci. Lett. 473, 83–93. https://doi.org/10.1016/j.epsl.2017.05.032

Willett, S.D., Beaumont, C., 1994. Subduction of Asian lithospheric mantle beneath Tibet inferred from models of continental collision. Nature 369, 642–645. https://doi.org/10.1038/369642a0

Willingshofer, E., Sokoutis, D., Luth, S.W., Beekman, F., Cloetingh, S., 2013. Subduction and deformation of the continental lithosphere in response to plate and crust-mantle coupling. Geology 41, 1239–1242. https://doi.org/10.1130/G34815.1

Zahirovic, S., Müller, R.D., Seton, M., Flament, N., Gurnis, M., Whittaker, J., 2012. Insights on the kinematics of the India-Eurasia collision from global geodynamic models. Geochem. Geophys. Geosystems 13. https://doi.org/10.1029/2011GC003883

Zhao, W., Nelson, K.D., Che, J., Quo, J., Lu, D., Wu, C., Liu, X., 1993. Deep seismic reflection evidence for continental underthrusting beneath southern Tibet. Nature 366, 557–559. https://doi.org/10.1038/366557a0

Chapter 7

Conclusions

7.1. Thesis summary

The main aim of this thesis is to provide a comprehensive study into the processes influencing the structural evolution of orogens, highlighting the role of internal heating and convergence velocity, which alter the rheological response to convergence, as well as surface processes that alter the stresses acting on the orogen. These processes are usually incorporated within geodynamic modelling of orogens, as well as other tectonic settings, but their time- and rate-dependency is ignored, altering the insights into each process effecting the orogens evolution.

7.1.1. Convergence velocity on the structure of orogens

The convergence velocity is an important parameter as it dictates, along with the temperature, the rheological response to convergence. Previous studies have considered the role of velocity (Faccenda et al., 2008; Vogt et al., 2017a, 2017b) on the structural evolution of orogenic wedges, however these models also include internal heating and surface processes.

Chapter 3 shows that the convergence velocity is an important parameter to consider when assessing the structural evolution of an orogen. The convergence velocity can result in different structures, especially if the convergence velocity decreases over time, as observed in the Himalayas (Zahirovic et al., 2012). Another important parameter to consider is the crustal thickness, which can also results in a whole range of structures as the crustal thickness changes from a thinned continental crust to a typical undeformed continental crust during collision (Bott, 1980; Capitanio et al., 2010).

At high velocity and/or thin crust, plastic deformation dominates, whilst at low velocity and/or thick crust, viscous deformation dominates. This results in different structural styles, with plastic deformation favouring crustal stacking along discrete shear zones, forming a

narrow and thick orogen. In contrast, viscous deformation results in folding of the crust and lateral flow, forming a wide and flat orogen.

Our models also show that the kinematics are key to understanding the structures of orogens. In **Chapter 6** 2000 km of convergence is modelled, representing the amount of convergence between India and Asia since collision ~50 Ma (DeCelles et al., 2002; Guillot et al., 2003; Halim et al., 1998; Molnar and Tapponnier, 1975; Patriat and Achache, 1984).

Chapter 6 shows that the decreasing convergence velocity is the critical component in the formation of all the major structures observed across the region. The decreasing velocity model can recreate the Tibetan Plateau, return flow, exhumation of deep crustal material and form a fold-and-thrust belt, with these structures emerging in the model at similar times to those observed in the region. The role of surface processes, internal heating and crustal density are also investigated, with only internal heating having a major influence on the final structure of the orogen. This is due to internal heating hindering thermal advection at high velocity and diffusion at a low velocity. This results in similar structures across the range of velocities tested when internal heating dominates.

7.1.2. The role of time-dependent processes on the structural evolution of orogens

Chapter 4 illustrates that the influence of both surface processes and internal heating on the internal structure increases with time. Both internal heating and surface processes can dominate the structural evolution of the orogen if given either (1) enough time, due to a low convergence velocity or (2) the internal heating or erosion and sedimentation rates are high enough. If internal heating dominates, the internal structure of the orogen is dominated by viscous structures as internal heating increases the temperature of the curst. If surface processes dominate, erosion stops the outward propagation of deformation by reducing the gravitational load acting on the wedge. If material is removed fast enough, deformation is

concentrated along a back-thrust which promotes exhumation of material from deep within the orogen. Chapter 4 highlights that the role of surface processes and internal heating should be considered carefully when modelling any tectonic margin, particularly if there are variations in the duration of the model.

Chapter 6 illustrates that to form all the main structures in the Himalayas, the influence of surface processes and internal heating need to be secondary to the kinematics and thermal evolution. However, if one of these processes dominates, it can control the evolution of the margin. This is seen through the role of internal heating, which results in similar structures across all convergence velocities tested by dictating the thermal evolution of the orogen, minimising the influence of advection at high velocity and diffusion at low velocity.

7.1.3. The formation of salients and recesses in the Himalayas

Salients and recesses are prominent along the fronts of multiple orogens, including the Himalayas (Macedo and Marshak, 1999). However, their formation remains debated. At local scale, field studies that assess the deformation styles across the Dharan salient and Gorubathan recess in the Himalayas suggest the salient and recess formed due to variations in rheology (Matin and Mukul, 2020). However, at the large scale, deviations in the Himalayan arc defined by a small circle have previously been attributed to surface processes, as these deviations correlate with large drainage basins (Bendick and Bilham, 2001).

The models, presented in **chapter 5** show that the causes of salients and recesses can be determined from the internal structure and topography. As the friction coefficient increases, a change in structural style is observed from plastic dominated to viscous dominated due to the shallowing of the brittle-ductile transition. This results in a more narrow and thicker wedge characterised by viscous structures as the friction coefficient increases.

Changes in friction coefficient also alter the distribution of elevated topography due to the rheological response to convergence. Surface processes result in the narrowing of the wedge whilst also promoting exhumation at the centre of the wedge, however no major change in internal structure is observed. Surface processes do not alter the overall distribution of elevated topography but does restrict the wedge width.

These insights are utilised to investigate two large-scale salients and recesses in the Himalayas. The free-air gravity anomalies and topography show contrasting features between recesses, with rheological recesses identified by high positive gravity anomalies and a lack of erosional features, identified across the Gorubathan recess, which is in agreement with field observations (Matin and Mukul, 2020). In contrast, erosional recesses were identified by high negative gravity anomalies that correlate with drainage channel is the region.

7.2. Future work on orogenesis

Orogenesis is a process that has been extensively studied for centuries in the field and decades in the lab or numerically. As computational power increases and models become more complex, it is important to continue to study orogens to decipher their complex and unique evolution. From a modelling perspective, future research directions include:

1. A strength and weakness of this thesis is the investigation of parameters influencing orogenesis independently. Further studies are required with all processes occurring at the same time to determine the conditions in which each parameter dominates, which can now be done due to the work conducted in this thesis.
2. The Incorporation various geophysical and satellite datasets within numerical models to understand the current stress distribution within the crust that results in large Earthquakes. Earthquakes pose a significant threat to life in mountain regions, from either the Earthquake or subsequent events caused by the Earthquake (e.g. landslides,

flooding). The stress distribution is influenced by the convergence velocity, changes in topography and crustal thickness as well as heterogeneities in the mantle. Satellite data provides the convergence velocity (GPS) and topography (Radar), whilst tomography provides the crust and mantle structure. Similar methods have previously been used to better understand Cenozoic intraplate volcanism in eastern Australia (Davies and Rawlinson, 2014; Rawlinson et al., 2017) and intra-plate seismicity in the central and south-eastern US (Saxena et al., 2021) however it has not yet been applied to orogens.

3. The incorporation of the convergence history of a region to better understand the structural evolution. **Chapter 6** demonstrates the importance of the convergence history on the structural evolution of the Himalayas, which can be applied to other regions. Plate constructions are available (Seton et al., 2012; Zahirovic et al., 2015, 2012) and can be used to reconstruct the collisional history of a region. This could be extended to other tectonic settings to better understand the structural evolution.
4. More complex surface processing modelling should be done to better understand the link between erosion and sedimentation and orogenesis. The drainage networks observed in the topography of the Himalayas are an example of the complex surface processes operating in the region. This can be done by incorporating surface processes through additional modelling software, such as Fastscape, LandLAB (Hobley et al., 2017) or Badlands (Salles, 2016), which can be coupled to geodynamic models run with Underworld2 by leveraging the Python3 API.

7.3. Concluding remarks

Orogenesis is a key part of plate tectonics, resulting in spectacular landscapes that have fascinated many for centuries. Orogenesis incorporates a wide range of processes that are competing to dictate the structural evolution of the orogen. Although these processes have been modelled in this thesis, they are simplistic representations of these

processes that occur in nature, whist in nature these processes are linked and provide feedback to each other, further altering the structural evolution of orogens. The models show that each process can dictate the structural evolution of the orogen if dominant, with each process producing a unique structure.

7.4. References

Bendick, R., Bilham, R., 2001. How perfect is the Himalayan arc? Geology 29, 791–794.

Bott, M.H.P., 1980. Mechanisms of Subsidence at Passive Continental Margins, in: Dynamics of Plate Interiors. American Geophysical Union (AGU), pp. 27–35. https://doi.org/10.1029/GD001p0027

Capitanio, F.A., Morra, G., Goes, S., Weinberg, R.F., Moresi, L., 2010. India–Asia convergence driven by the subduction of the Greater Indian continent. Nature Geoscience 3, 136–139. https://doi.org/10.1038/ngeo725

Davies, D.R., Rawlinson, N., 2014. On the origin of recent intraplate volcanism in Australia. Geology 42, 1031–1034. https://doi.org/10.1130/G36093.1

DeCelles, P.G., Robinson, D.M., Zandt, G., 2002. Implications of shortening in the Himalayan fold-thrust belt for uplift of the Tibetan Plateau. Tectonics 21, 12-1-12–25. https://doi.org/10.1029/2001TC001322

Faccenda, M., Gerya, T.V., Chakraborty, S., 2008. Styles of post-subduction collisional orogeny: Influence of convergence velocity, crustal rheology and radiogenic heat production. Lithos 103, 257–287. https://doi.org/10.1016/j.lithos.2007.09.009

Guillot, S., Garzanti, E., Baratoux, D., Marquer, D., Mahéo, G., Sigoyer, J. de, 2003. Reconstructing the total shortening history of the NW Himalaya. Geochemistry, Geophysics, Geosystems 4. https://doi.org/10.1029/2002GC000484

Halim, N., Cogné, J.P., Chen, Y., Atasiei, R., Besse, J., Courtillot, V., Gilder, S., Marcoux, J., Zhao, R.L., 1998. New Cretaceous and Early Tertiary paleomagnetic results from Xining-Lanzhou basin, Kunlun and Qiangtang blocks, China: Implications on the geodynamic evolution of Asia. Journal of Geophysical Research: Solid Earth 103, 21025–21045. https://doi.org/10.1029/98JB01118

Hobley, D.E.J., Adams, J.M., Nudurupati, S.S., Hutton, E.W.H., Gasparini, N.M., Istanbulluoglu, E., Tucker, G.E., 2017. Creative computing with Landlab: an open-source toolkit for building, coupling, and exploring two-dimensional numerical models of Earth-surface dynamics. Earth Surf. Dynam. 5, 21–46. https://doi.org/10.5194/esurf-5-21-2017

Macedo, J., Marshak, S., 1999. Controls on the geometry of fold-thrust belt salients. Geological Society of America Bulletin 15.

Matin, A., Mukul, M., 2020. Himalayan cross faults affect thrust sheet geometry: An example from the Munsiari thrust sheet near the Gish Transverse fault zone, frontal Darjiling Himalaya, India. Journal of Asian Earth Sciences 199, 104400. https://doi.org/10.1016/j.jseaes.2020.104400

Molnar, P., Tapponnier, P., 1975. Cenozoic Tectonics of Asia: Effects of a Continental Collision. Science 189, 419–426.

Patriat, P., Achache, J., 1984. India–Eurasia collision chronology has implications for crustal shortening and driving mechanism of plates. Nature 311, 615–621. https://doi.org/10.1038/311615a0

Rawlinson, N., Davies, D.R., Pilia, S., 2017. The mechanisms underpinning Cenozoic intraplate volcanism in eastern Australia: Insights from seismic tomography and geodynamic modeling. Geophysical Research Letters 44, 9681–9690. https://doi.org/10.1002/2017GL074911

Salles, T., 2016. Badlands: A parallel basin and landscape dynamics model. SoftwareX 5, 195–202. https://doi.org/10.1016/j.softx.2016.08.005

Saxena, A., Choi, E., Powell, C.A., Aslam, K.S., 2021. Seismicity in the central and southeastern United States due to upper mantle heterogeneities. Geophysical Journal International 225, 1624–1636. https://doi.org/10.1093/gji/ggab051

Seton, M., Müller, R.D., Zahirovic, S., Gaina, C., Torsvik, T., Shephard, G., Talsma, A., Gurnis, M., Turner, M., Maus, S., Chandler, M., 2012. Global continental and ocean basin reconstructions since 200Ma. Earth-Science Reviews 113, 212–270. https://doi.org/10.1016/j.earscirev.2012.03.002

Vogt, K., Matenco, L., Cloetingh, S., 2017a. Crustal mechanics control the geometry of mountain belts. Insights from numerical modelling. Earth and Planetary Science Letters 460, 12–21. https://doi.org/10.1016/j.epsl.2016.11.016

Vogt, K., Willingshofer, E., Matenco, L., Sokoutis, D., Gerya, T., Cloetingh, S., 2017b. The role of lateral strength contrasts in orogenesis: A 2D numerical study. Tectonophysics. https://doi.org/10.1016/j.tecto.2017.08.010

Zahirovic, S., Müller, R.D., Seton, M., Flament, N., 2015. Tectonic speed limits from plate kinematic reconstructions. Earth and Planetary Science Letters 418, 40–52. https://doi.org/10.1016/j.epsl.2015.02.037

Zahirovic, S., Müller, R.D., Seton, M., Flament, N., Gurnis, M., Whittaker, J., 2012. Insights on the kinematics of the India-Eurasia collision from global geodynamic models. Geochemistry, Geophysics, Geosystems 13. https://doi.org/10.1029/2011GC003883